



UNIVERSITEIT  
STELLENBOSCH  
UNIVERSITY

**The Tectono-Metamorphic Evolution of the Theespruit  
Formation in the Tjakastad Schist Belt and Surrounding Areas  
of the Barberton Greenstone Belt, South Africa**



by  
**Johann F.A. Diener**

*Thesis presented in partial fulfilment of the requirements for the degree of*

**Master of Science**

*at the University of Stellenbosch*

Supervised by Prof. Gary Stevens and Prof. Alex Kisters

December 2004

## Declaration

I, the undersigned, hereby declare that the work contained in this thesis is my own original work and that I have not previously in its entirety or in part submitted it at any other university for a degree.

Signature: .....

Date: .....



## Abstract

The southern portions of the Early- to Mid-Archaean Barberton granitoid-greenstone terrain of South Africa consists of a high-grade metamorphic granitoid-gneiss terrain that is juxtaposed against the low-grade metamorphic supracrustal sequence of the Barberton Greenstone Belt. The boundary of the two different crustal domains corresponds to the Theespruit Formation, an amphibolite-facies, highly tectonized mélange of metabasites, felsic volcanics and rare, aluminous clastic sediments that occurs along the granitoid-greenstone margins. Amphibolite-facies lithologies in the Theespruit Formation are characterized by strongly prolate mylonitic fabrics that formed in a constrictional tectonic regime. Away from the granitoid-greenstone margin and towards the central parts of the greenstone belt, these rocks grade to, and are overprinted by, greenschist-facies S-L mylonites that formed during non-coaxial deformation. Both peak and retrograde minerals define, and are aligned parallel to, the fabrics in these rocks, indicating that shearing was initiated under peak metamorphic conditions and continued during retrogression. S-C' fabric relationships indicate that shearing occurred in an extensional tectonic regime and that, during deformation, the gneiss terrain was uplifted relative to the greenstone belt. Peak metamorphic assemblages of grt-st-bt-chl-pl-qtz and ky-st-bt-ms-pl-qtz in metasediments and grt-ep-hbl-pl-qtz in amphibolite constrain peak metamorphic conditions of  $7.4 \pm 1.0$  kbar and  $560 \pm 20$  °C that were attained during the main accretionary episode in the Barberton terrain at  $3229 \pm 25$  Ma. Peak assemblages in all rocks are pre-tectonic and were deformed and re-equilibrated during retrogression, resulting in these being minimum estimates of peak metamorphic conditions. Petrographic evidence and retrograde pressure-temperature estimates indicate that retrogression involved near-isothermal decompression of ca. 4 kbar prior to cooling into the greenschist-facies. The style and timing of metamorphism in the Theespruit Formation is similar to that of the granitoid-gneiss terrain, suggesting that the Theespruit Formation shares a geological history with the gneiss terrain and that it is allochthonous to the greenstone belt. The main deformational and fabric-forming event exhibited in the Theespruit Formation occurred during the exhumation of the granitoid-gneiss terrain subsequent to peak metamorphism. Consequently, the juxtaposition of this terrain against

the greenstone belt was achieved by tectonic underplating and core complex formation at ca. 3.23 Ga. The occurrence of high-grade constrictional mylonites that are overprinted by low-grade non-coaxial mylonites as well as extension in an overall compressional tectonic regime is consistent with exhumation by extensional orogenic collapse. Burial of the high-grade terrain to depths of 25 – 30 km is only possible in a relatively cold and rigid crustal environment, while the extremely low apparent geothermal gradients of ca. 20 °C/km preserved in this terrain suggest that burial and exhumation occurred rapidly, within a time-span of ca. 15 – 20 Ma. These parameters strongly suggest that metamorphism occurred in response to a lateral plate tectonic process that was operational in the Barberton terrain at 3230 Ma.





## Uittreksel

Die suidelike dele van die Vroeg- tot Middel-Argeïese Barberton graniet-groensteen terrein van Suid-Afrika bestaan uit 'n hoë-graad metamorfe graniet-gneiss terrein wat die lae-graad metamorfe groenstone van die Barberton Groensteen Gordel begrens. Die grens tussen die twee verskillende kors-domeine hang saam met die Theespruit Formasie, 'n amfiboliet-fasies, getektoniseerde melange van metabasiete, felsiese vulkaniese gesteentes en skaars, alumineuse klastiese sedimente wat langs die graniet-groensteen kontakte voorkom. Amfiboliet-fasies gesteentes in die Theespruit Formasie word gekenmerk deur sterk prolaat milonitiese maakselformings wat in 'n vernouende tektoniese omgewing gevorm het. Hierdie rotse word weg van die graniet-groensteen kontak en na die sentrale dele van die groensteen gordel oordruk en vervang deur groenskis-fasies S-L miloniete wat tydens nie-koaksiale vervorming gevorm het. Beide piek en retrograad minerale definieer, en is georiënteer parallel aan die maakselforming in die rotse, wat daarop dui dat skuifskur onder piek metamorfe toestande begin het en volgehou het tydens retrogressie. S-C' maakselformings dui daarop dat skuifskur in 'n verlengende tektoniese omgewing plaasgevind het en dat die gneiss terrein opgehef is relatief tot die groensteengordel tydens vervorming. Piek metamorfe versamelings van grt-st-bt-chl-pl-qtz en ky-st-bt-ms-pl-qtz in metasedimente en grt-ep-hbl-pl-qtz in amfiboliet bepaal piek metamorfe toestande van  $7.4 \pm 1.0$  kbar en  $560 \pm 20$  °C wat bereik is gedurende die hoofase van akkresie in die Barberton terrein teen  $3229 \pm 25$  Ma. Die piek metamorfe versamelings in alle rotse is pre-tektonies en is gevorm en geherekwilbreer tydens retrogressie, wat maak dat die beramings minimum skattings van piek metamorfe toestande is. Petrografiese getuies asook druk-temperatuur beramings dui daarop dat retrogressie gepaard gegaan het met byna-isotermiese drukverligting van naastebly 4 kbar voor afkoeling tot in die groenskis-fasies. Die styl en tydsberekening van metamorfose in die Theespruit Formasie is vergelykbaar met metamorfose in die graniet-gneiss terrein, wat daarop dui dat die Theespruit Formasie 'n geologiese geskiedenis met die gneiss terrein deel en allochtoon is tot die groensteen gordel. Die hoofase van vervorming en maakselforming in die Theespruit Formasie het plaasgevind gedurende die herontbloting van die graniet-gneiss terrein na piek metamorfose. Gevolglik is die

teenplasing van dié terrein teen die groensteen gordel vermag deur tektoniese onderplasing en kernkompleksvorming teen ongeveer 3.23 Ga. Die verskynsel van hoë-graadse vernoude miloniete wat oordruk word deur lae-graadse nie-koaksiale miloniete asook verlenging in 'n algeheel saamdrukkende tektoniese omgewing dui daarop dat herontbloting plaasgevind het deur middel van verlengende orogenetiese ineenstorting. Die begrawing van die hoë-graadse terrein tot dieptes van 25 – 30 km is net moontlik in 'n relatief koel en star kors-omgewing, terwyl die uitermate lae geotermiese gradiente van ongeveer 20 °C/km wat in die terrein behoue gebly het daarop dui dat begrawing en herontbloting vinnig geskeid het, binne 'n tydsverloop van ongeveer 15 – 20 Ma. Hierdie beperkings is 'n sterk aanduiding dat metamorfose plaasgevind het as gevolg van 'n laterale plaattektoniese proses wat werksaam was in die Barberton terrein teen 3230 Ma.



## Acknowledgements

The Barberton project is financially supported by the National Research Foundation under grant number NRF 2050238 awarded to Alex Kisters. I received further financial support under a Prestigious and Equity Scholarship from the NRF (NRF 2060045). The financial support of the NRF is gratefully acknowledged.

I cannot claim that the ideas and concepts presented here are merely my own, they are the product of a continued collaboration and exchange of ideas among all participants in the Barberton project. I'd like to thank Gary Stevens and Alex Kisters for introducing me to Barberton and giving me the opportunity to get thrown in at the deep end by getting involved in the project as part of my Honours studies. Their continued encouragement and support during all aspects of the project was indispensable, particularly in keeping track of the bigger picture while I was fighting my way through all the different aspects and finer details of these fascinating rocks. I'd like to thank the land-owners in the Tjakastad area for access to their land and their hospitality during field work. Thanks to Marc and Sarah for putting up with me, Mike for ensuring that I was always deadly with the laser and Neil and Esmé for letting the probe run smoothly. Janus made sure that I didn't work too hard and got out once in a while.

## Contents

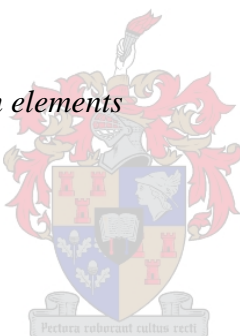
<b>Declaration</b>	<b>ii</b>
<b>Abstract</b>	<b>iii</b>
<b>Uittreksel</b>	<b>v</b>
<b>Acknowledgements</b>	<b>vii</b>
<b>Contents</b>	<b>viii</b>
<b>List of Figures</b>	<b>xiii</b>
<b>List of Tables</b>	<b>xvi</b>
<b>Chapter 1: Introduction</b>	<b>1</b>
1.1 Introduction	1
1.2 Aims of the study	3
<b>Chapter 2: Regional Geology</b>	<b>5</b>
2.1 Introduction	5
2.2 Greenstone stratigraphy	5
2.2.1 <i>Sandspruit Formation</i>	8
2.2.2 <i>Theespruit Formation</i>	8
2.2.3 <i>Komati Formation</i>	9
2.3 The relationship of the Theespruit and Komati Formations and the significance of the Komati Fault	9
2.4 Granitoid-gneiss geology	11
2.4.1 <i>Pre-3.5 Ga plutonism</i>	11
2.4.2 <i>Early TTG plutonism at ca. 3.45 Ga</i>	12
2.4.3 <i>Late TTG plutonism at ca. 3.23 Ga</i>	12
2.4.4 <i>The ca. 3.1 Ga granodiorite-monzon granite-syenite suite</i>	13
2.5 Proposed models for the geological evolution of the Barberton Greenstone Belt	13
2.5.1 <i>Early models</i>	13



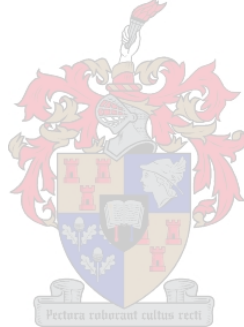
2.5.2 <i>Recent models</i>	14
2.5.2.1 <i>D<sub>1</sub> deformation</i>	14
2.5.2.2 <i>D<sub>2</sub>/D<sub>3</sub> and subsequent deformational events</i>	15
<b>Chapter 3: Lithology and Petrography</b>	<b>17</b>
3.1 Introduction	17
3.2 Felsic schist and agglomerate	20
3.3 Mafic rocks	26
3.3.1 <i>Amphibolite petrography</i>	27
3.3.2 <i>Chlorite schist and retrograde amphibolite petrography</i>	30
3.4 Ultramafic rocks	31
3.5 Chert	31
3.6 Intrusive rocks	32
3.7 Locality 62105	33
<b>Chapter 4: Structure</b>	<b>37</b>
4.1 Introduction	37
4.2 Fabric development in the greenstones	37
4.3 Fabric development in the granitoids	44
4.4 Strain	45
4.4.1 <i>Low-strain amphibolite</i>	45
4.4.2 <i>Amphibolite-facies mylonites</i>	46
4.4.3 <i>Greenschist-facies mylonites</i>	49
4.5 Kinematics	49
4.6 Locality 61602	53
<b>Chapter 5: Whole-rock geochemistry</b>	<b>56</b>
5.1 Introduction	56
5.2 Analytical procedures	56
5.2.1 <i>Major- and trace elements</i>	56
5.2.2 <i>Rare earth elements</i>	57



5.3 Felsic schist	57
5.3.1 Major elements	59
5.3.2 Trace elements	59
5.3.3 Rare earth elements	60
5.3.4 Possible protoliths	60
5.4 Amphibolite and chlorite schist	67
5.4.1 Major elements	67
5.4.2 Trace elements	70
5.4.3 Possible protoliths	70
<b>Chapter 6: Mineral Chemistry</b>	<b>72</b>
6.1 Introduction	72
6.2 Analytical procedures	72
6.2.1 Major elements	72
6.2.2 Trace- and rare earth elements	73
6.3 Felsic schist mineral chemistry	73
6.3.1 Garnet	78
6.3.2 Staurolite	86
6.3.3 Aluminosilicates	86
6.3.4 Biotite	86
6.3.5 Chlorite	87
6.3.6 Plagioclase	88
6.4 Amphibolite	88
6.4.1 Garnet	88
6.4.2 Amphibole	95
6.4.3 Epidote	95
6.4.4 Plagioclase	96
<b>Chapter 7: Estimation of metamorphic conditions</b>	<b>97</b>
7.1 Implications of garnet zoning profiles	97
7.2 Peak metamorphic assemblages	98



7.2.1 <i>Clastic metasediments</i>	98
7.2.2 <i>Amphibolite</i>	101
7.3 Estimation of peak metamorphic conditions via THERMOCALC	102
7.3.1 <i>Introduction</i>	102
7.3.2 <i>Results</i>	102
7.4 Petrogenetic grids and pseudosections	105
7.4.1 <i>Clastic metasediments</i>	105
7.4.2 <i>Amphibolite</i>	109
7.4.3 <i>Correlation between THERMOCALC estimates and     petrogenetic grids</i>	109
7.5 Estimation of retrograde metamorphic conditions	109
<b>Chapter 8: Timing of metamorphism and deformation</b>	<b>111</b>
8.1 Introduction	111
8.2 Sample selection	112
8.2.1 <i>Tj 3</i>	113
8.2.2 <i>Tj 18</i>	115
8.3 Methodology	116
8.4 Results	118
<b>Chapter 9: Discussion</b>	<b>121</b>
9.1 The pressure-temperature path	121
9.2 Comparative styles of metamorphism	124
9.3 The timing of deformation relative to metamorphism	127
9.4 Kinematics of exhumation	128
9.5 Regional context and a model for the exhumation of the southern terrain	132
9.6 The rotation and re-orientation of fabrics	135
9.7 The significance of felsic rocks in the Theespruit Formation	139
9.8 The significance of the Theespruit Formation as a basal mélange	143
9.9 The preservation of D <sub>1</sub> fabrics	145



<b>Chapter 10: Conclusions</b>	<b>147</b>
10.1 Conclusions	147
10.2 Implications for Archaean crustal evolution	148
<b>References</b>	<b>151</b>
<b>Appendices</b>	<b>170</b>
Appendix 1: Geological map of the Tjakastad Schist Belt and surrounding areas of the Barberton Greenstone Belt, South Africa	170
Appendix 2.1: Table of standards for XRF analysis	171
Appendix 2.2: Table of standards for SEM-ED analysis	173
Appendix 2.3: Table of standards for LA-ICP-MS analysis	174
Appendix 3.1: Felsic schist mineral chemistry	175
Appendix 3.2: Mafic rock mineral chemistry	196



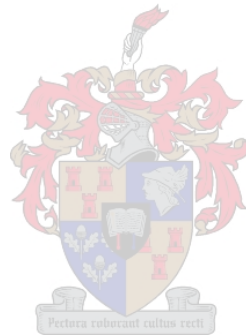


## List of Figures

2.1:	Geological map of the Barberton granitoid-greenstone terrain	6
2.2:	Stratigraphic column of the Barberton Supergroup	7
3.1:	Sample locality map of the Tjakastad Schist Belt	18
3.2:	Field photographs of felsic agglomerate	21
3.3:	Photomicrographs of garnet from felsic schist	23
3.4:	Photomicrographs of felsic schist	24
3.5:	Photomicrographs of amphibolite	29
3.6:	Field photographs of serpentinite and intrusive breccia	33
3.7:	Sketch map of locality 62105	34
3.8:	Photomicrograph of felsic schist from locality 62105	36
3.9:	Photomicrograph of garnet-quartz mylonite	36
4.1:	Field photographs illustrating transposition folding	38
4.2:	Structural map of the Tjakastad Schist Belt and surrounding areas	39
4.3:	Photographs and sketches of tectonization in the Tjakastad Schist Belt	40
4.4:	Field photographs of fabric development in the mylonites	42
4.5:	Stereographic projections of foliations and lineations	43
4.6:	Field photograph of fabric development in the granitoids	44
4.7:	Flinn diagram	46
4.8:	Map indicating the location and extent of the different strain regimes in the Theespruit Formation	47
4.9:	Field photographs of strained rocks	48
4.10:	Photographs of shear fabrics present in the Theespruit Formation	50
4.11:	Sketch map of locality 61602	54
5.1:	Harker diagrams of various felsic rocks from the Barberton terrain	63
5.2:	REE profiles of felsic rocks from the Barberton terrain	64

5.3:	Harker diagrams of mafic rocks from the Theespruit and Komati Formations	69
5.4:	Komatiite classification diagram	71
6.1:	Elemental maps of garnet in felsic schist	80
6.2:	Major-, trace- and REE zoning profiles of garnet from sample Tj 18	82
6.3:	Major element zoning profiles of garnet from sample 62601C	83
6.4:	Chondrite-normalized REE profiles of garnet from sample Tj 18	84
6.5:	Backscatter image of two generations of chlorite in felsic schist	87
6.6:	Major element zoning profiles of garnet from amphibolite	93
7.1:	AFM diagram showing the equilibration of metamorphic assemblages	100
7.2:	Pressure-temperature plot of THERMOCALC estimates	104
7.3:	Petrogenetic grid showing the position of reactions that formed the peak assemblages in felsic schist	106
7.4:	AFM diagram showing the bulk-rock compositional control on peak assemblages in felsic schist	107
7.5:	Pseudosections showing the stability field of the peak assemblages in garnet-bearing and kyanite-bearing felsic schist	108
7.6:	Backscatter image of a site of garnet breakdown in felsic schist	110
8.1:	Photomicrographs of titanite in sample Tj 3	114
8.2:	Backscatter images of complex titanite grains in sample Tj 18	116
8.3:	U-Pb Concordia diagram for titanite from sample Tj 3	119
9.1:	Pressure-temperature diagram of the stability fields of kyanite-staurolite and sillimanite-staurolite coexistence	122
9.2:	Proposed pressure-temperature path for lithologies of the Tjakastad Schist Belt	123

9.3:	Pressure-temperature diagram and map summarizing the available metamorphic data from the southern Barberton terrain	125
9.4:	The unfolding of fabrics to their original orientation	130
9.5:	The sense of displacement in mylonites along the southern margin of the Barberton Greenstone Belt	131
9.6:	The development of constrictional fabrics in the Lower Plate rocks	134
9.7:	Evolutionary model for the exhumation of the high-grade terrain	137
9.8:	The apparent reverse sense of displacement during steepening of the fabrics	139



## List of Tables

3.1:	Location and description of samples collected	18
4.1:	Location and description of shear fabrics that are visible in outcrop or hand sample	52
5.1:	Whole-rock major-, trace- and rare earth element composition of felsic rocks investigated	58
5.2:	Average whole-rock compositions of felsic rocks from the southern part of the Barberton terrain	62
5.3:	Whole-rock major- and trace element composition of mafic rocks investigated	68
6.1:	Major element composition of minerals in felsic schist	74
6.2:	Major element composition of minerals in amphibolite	89
7.1:	Equilibrium assemblages in felsic schist and amphibolite	101
7.2:	THERMOCALC pressure-temperature estimates	103
8.1:	U-Pb isotopic data for titanite from sample Tj 3	119

# **CHAPTER 1: INTRODUCTION**

## 1.1 Introduction

Granitoid-greenstone terrains are a dominant feature of the Archaean crust and are preserved in most cratonic areas on earth, affording scientists the opportunity to investigate the processes that shaped the Earth's early crust. One of the more pertinent and enigmatic topics in the Earth Sciences is the question as to what extent the models of modern crustal evolution and tectonic processes are applicable to the Archaean. Did the Earth's crust evolve in a fundamentally different way during the Archaean or are Archaean geological processes comparable, or at least similar, to modern geological processes? This question remains the topic of much debate and difference of opinion (e.g. Davies, 1992, 1995; Condie, 1994; Hamilton, 1998; De Wit, 1998; Kusky and Polat, 1999; Marshak, 1999), and it is only through the continued and refined investigation of all aspects of Archaean crustal evolution that we are able to shed new light on these issues. One of the core aspects of this ongoing debate is the complex and often controversial nature of the relationship between greenstone belts and the surrounding granitoids (e.g. Ridley et al., 1997). In most granitoid-greenstone terrains, the supracrustal greenstone component exhibits polyphase deformation but only very low metamorphic grades. In stark contrast, the surrounding granitoids are mostly made up of complex banded gneisses, suggesting that these rocks were subjected to much higher strain intensities at higher metamorphic grades (Ridley et al., 1997).

The Early- to Mid-Archaean Barberton granitoid-greenstone terrain of South Africa is one of the best preserved examples of Archaean geology in the world and has served as a type locality of Archaean rock types and geological processes (e.g. Viljoen and Viljoen, 1969a,b; Anhaeusser, 1973, 1984; De Wit, 1982; De Ronde and De Wit, 1994; Lowe, 1994). Like most granitoid-greenstone terrains, the Barberton terrain consists of a low-grade supracrustal greenstone sequence that is surrounded by a higher-grade complex granitoid-gneiss terrain. To the southwest of the Barberton Greenstone Belt, the granitoid-gneiss terrain contains numerous large greenstone remnants that afford the

unique opportunity to quantitatively estimate the conditions of metamorphism of this terrain. A recent investigation of these remnants revealed that they were subjected to high-grade regional metamorphism, with pressure-temperature estimates of 8 – 11 kbar and 650 to 700°C (Dziggel et al., 2002). These estimates are considerably higher than known estimates of metamorphic conditions in the main body of the Barberton Greenstone Belt. Peak pressure-temperature conditions of metamorphism in the Barberton Greenstone Belt are estimated at less than 4 kbar and ca. 520 °C close to the base of the greenstone sequence (Cloete, 1991, 1999) and ca. 320 °C in the central portions of the belt (Xie et al., 1997). Despite evidence to suggest different ages of peak metamorphism in the greenstone belt and granitoid-gneiss terrain (refer to Chapter 2), these studies provide quantitative evidence to confirm that the Barberton granitoid-greenstone terrain consists of two components that experienced contrasting tectono-metamorphic evolutionary histories and that must have been tectonically juxtaposed at some point during their history.

A recent investigation of a section where these contrasting metamorphic grades are developed in association with the margin of the Stolzburg Pluton (Fig. 2.1) has proposed the presence of an extensional detachment similar to those found in metamorphic core complexes (e.g. Davis, 1980; Lister and Davis, 1989) to account for the juxtaposition of the two different crustal domains (Kisters et al., 2003). Kisters et al. (2003) also suggested that amphibolite-facies portions of the greenstone belt exposed along the margins of the Theespruit Pluton (Fig. 2.1) occur below the extensional detachment and are likely to constitute part of the high-grade granitoid-gneiss terrain. Previous studies have viewed the higher-grade greenstones developed along the southern margin of the Barberton Greenstone Belt as the metamorphic sole of an ophiolite that was metamorphosed and amalgamated with the greenstone belt along the Komati Fault (De Wit et al., 1983, 1987; Armstrong et al., 1990; De Ronde and De Wit, 1994) or the consequence of contact metamorphism associated with shearing during the diapiric intrusion of the TTG plutons (Anhaeusser, 1984).

## 1.2 Aims of this study

Despite the fact that metamorphic petrology has made an indispensable contribution to our understanding of younger tectonic processes (e.g. Miyashiro, 1961; Ernst, 1973, 1975, 1988; Chopin, 1984; Smith, 1984; Hubbard, 1989), the recent studies of Cloete (1991, 1999), Stevens et al. (2002) and Dziggel et al. (2002) are among the first to apply metamorphic petrology to help solve the problems of Archaean crustal evolution. The current study aims to utilize a detailed investigation of metamorphic petrology in combination with a structural investigation and geochronology to help clarify the conflicting interpretations of the high-grade rocks along the southern margin of the Barberton Greenstone Belt. The study focuses on the Theespruit Formation in the Tjakastad Schist Belt and the areas around the Theespruit Pluton (Fig 2.1) and encompasses sections of the farms Boekenhoutrand 722 JT, Tjakastad 730 JT, Theespruit 156 IT, Theeboom 729 JT and Honingklip 154 IT. This area straddles the metamorphic break between the low-grade greenstones and high-grade gneiss terrain and also coincides with the occurrence of the extensional detachment identified by Kisters et al. (2003) and the Komati Fault, interpreted as a terrain amalgamation structure by De Wit et al. (1983, 1987), Armstrong et al. (1990) and De Ronde and De Wit (1994). Detailed knowledge of the tectono-metamorphic history of this area has the potential to further elucidate the nature of the high-grade- to low-grade transition that lies close to the granitoid-greenstone contact and continue to develop our understanding of Archaean tectonics in the Barberton Greenstone Belt.

The specific aims of this study are to:

- 1) Document and describe the structural geology of the area, including a detailed kinematic analysis of fault rocks and strain analysis of fabrics.
- 2) Perform a detailed investigation of the metamorphic history of the area. This involves petrography as well as bulk-rock and mineral chemistry analysis with the ultimate aim of providing a quantitative pressure-temperature estimate of metamorphic conditions.

3) Carry out a geochronological analysis on selected samples to establish the timing of metamorphic and deformational events.

4) Construct a model for the evolution of the southern margin of the Barberton Greenstone Belt, based on the structural, metamorphic and geochronological results.





## **CHAPTER 2: REGIONAL GEOLOGY**

### 2.1 Introduction

The Barberton granitoid-greenstone terrain of Southern Africa straddles the border between South Africa and Swaziland (Fig. 2.1 inset). The Barberton terrain occurs on the eastern edge of the Kaapvaal Craton and forms the oldest (pre-3.0 Ga) nucleus of the craton (De Wit et al., 1992). The terrain consists of a supracrustal greenstone component surrounded by a complex granitoid-gneiss terrain. The greenstones consist of mafic and ultramafic lavas as well as clastic sediments that have experienced complex, polyphase deformation and zeolite- to greenschist-facies metamorphism (Hall, 1918; Visser, 1956; Ramsay, 1963; Viljoen and Viljoen, 1969a,b; Williams and Furnell, 1979; Fripp et al., 1980; De Wit et al., 1983; De Ronde and De Wit, 1994; Cloete, 1991, 1999). The granitoid-gneiss terrain is made up of a suite of tonalite-trondhjemite-granodiorite (TTG) plutons and syenogranites that are the result of various magmatic episodes (Hall, 1918; Robb and Anhaeusser, 1983; Anhaeusser and Robb, 1983a; Kamo and Davis, 1994; Kröner et al., 1991, 1996; Yearron, 2003). Because of the absence of index fossils and easily identifiable, correlateable lithological units in most of the Barberton stratigraphy, detailed geochronology has proven to be an important and often invaluable tool in resolving the complex geological evolution of the Barberton terrain (Tegtmeyer and Kröner, 1987; Armstrong et al., 1990; Kröner et al., 1991, 1996; Kamo and Davis, 1994).

### 2.2 Greenstone stratigraphy

The greenstone sequence in the Barberton Greenstone Belt has officially been named the Barberton Supergroup by SACS (1980) and the stratigraphy is subdivided into three groups. These are the oldest, predominantly volcanic Onverwacht Group which is overlain by the younger Fig Tree and Moodies Groups. These younger groups consist mainly of clastic sediments. The formations that constitute the Barberton greenstone stratigraphy as well as their lithological characteristics and important geochronological constraints are summarized in Figure 2.2.

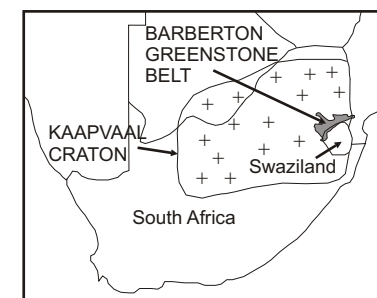
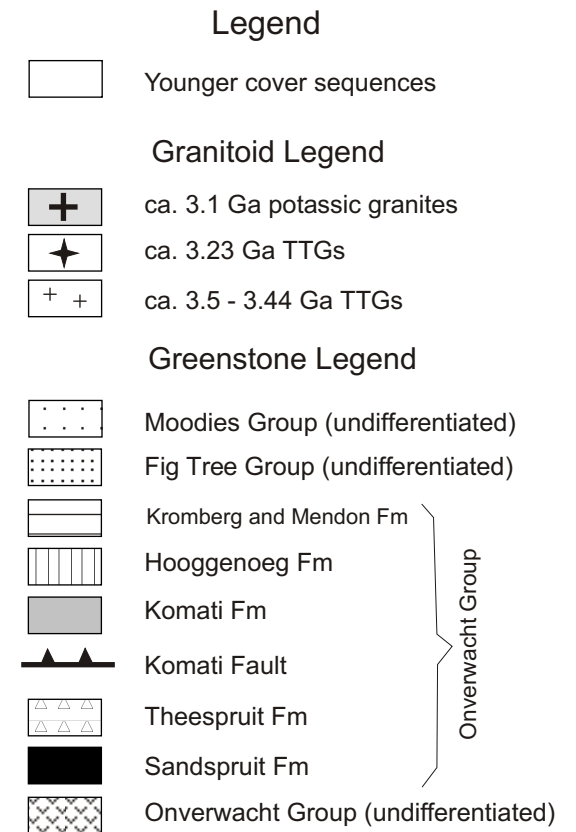
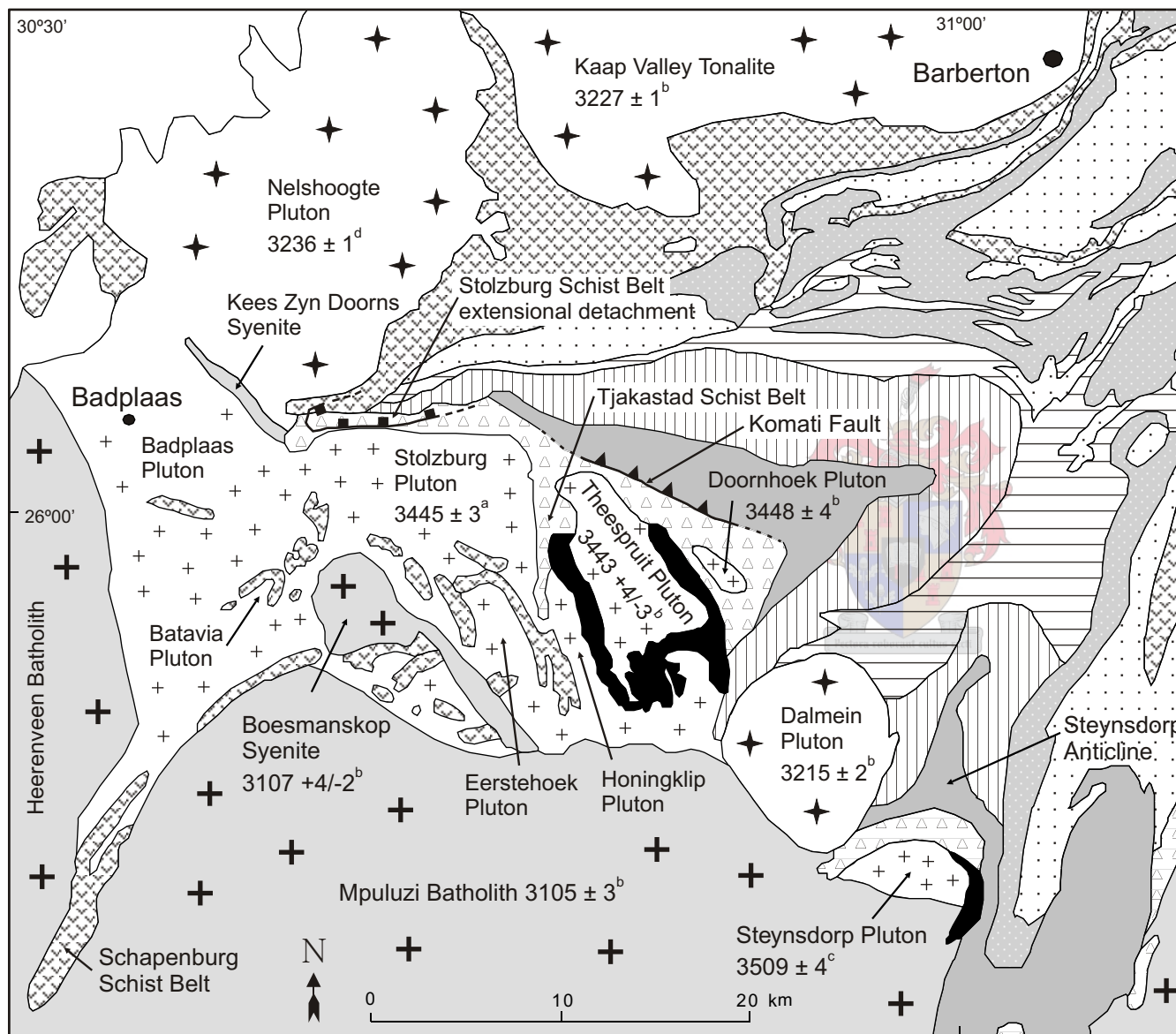


**Figure 2.1:** Geological map of the southern Barberton granitoid-greenstone terrain (modified after Anhaeusser et al., 1981; Kröner et al., 1996). Cited ages are crystallization ages of the granitoid rocks and are from (a) Kröner et al., 1991; (b) Kamo and Davis, 1994; (c) Kröner et al., 1996 and (d) De Ronde and Kamo, 2000.

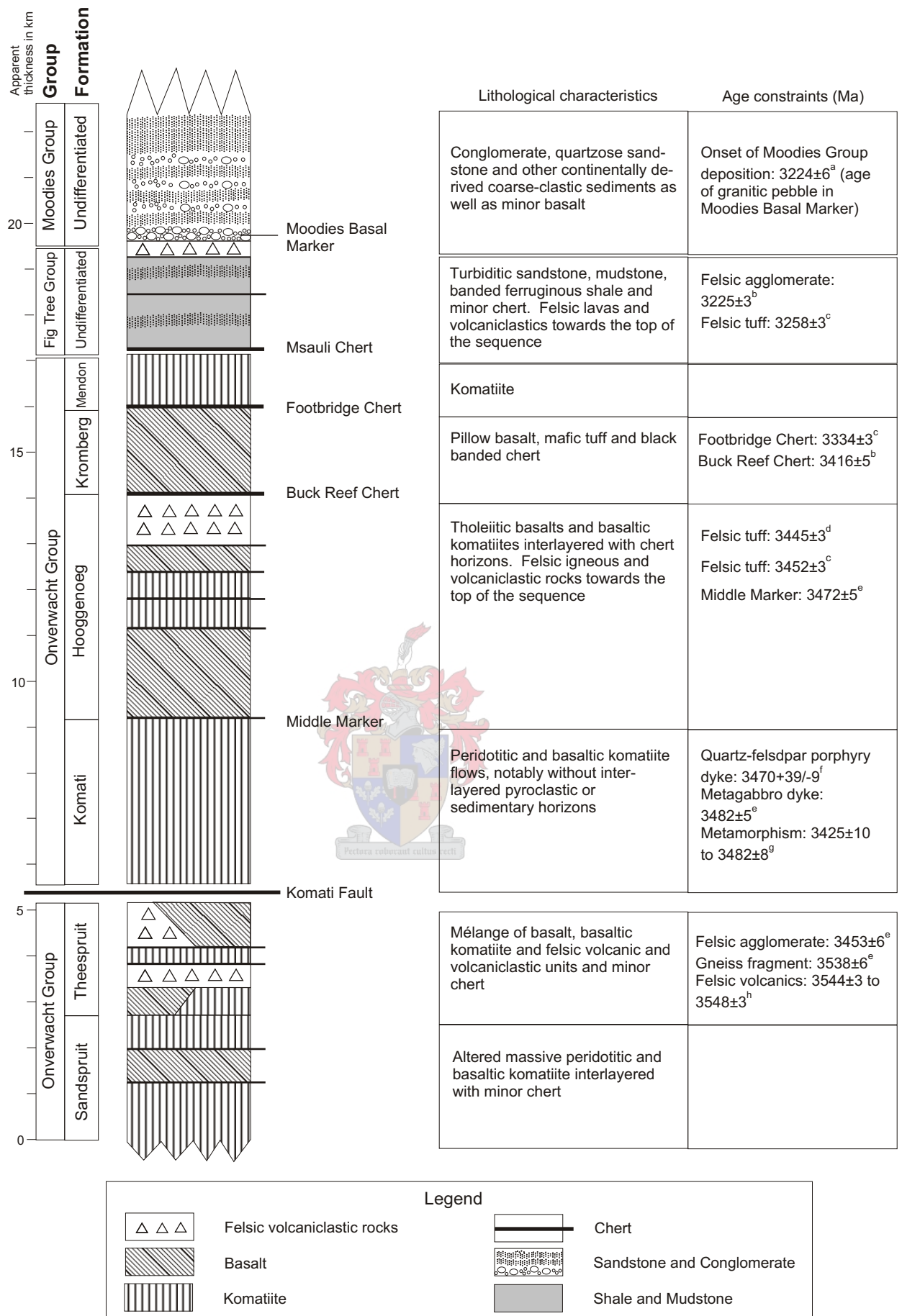


**Figure 2.2:** Simplified stratigraphic column of the Barberton Supergroup (modified after Lowe and Byerly, 1999). Cited ages are from (a) Tegtmeier and Kröner, 1987; (b) Kröner et al., 1991; (c) Byerly et al., 1996; (d) Kröner et al., 1992; (e) Armstrong et al., 1990; (f) Kamo and Davis, 1994; (g) Lopez-Martinez et al., 1992 and (h) Kröner et al., 1996.

As the present research focuses on the southern margin of the Barberton Greenstone Belt and only encompasses the lower formations of the greenstone sequence, these units will be discussed in further detail. The lowermost units of the Barberton Supergroup are the Sandspruit, Theespruit and Komati Formations which constitute the lower part of the Onverwacht Group (SACS, 1980). The lithologies of the Onverwacht Group were first described in detail by the Viljoen brothers when they investigated the greenstone stratigraphy in the southern parts of the Barberton Greenstone Belt (Viljoen and Viljoen, 1969a,b,c), and their work still forms the basis of the Onverwacht stratigraphy.

### *2.2.1 Sandspruit Formation*

The Sandspruit Formation consists of massive peridotitic and basaltic komatiite interlayered with minor chert horizons. These rocks were subjected to greenschist- to amphibolite-facies metamorphic grades and crop out mainly as chlorite-actinolite schists and massive amphibolites (Viljoen and Viljoen, 1969b). The Sandspruit Formation is estimated to be ~ 2.1 km thick in its type section, to the south of the Theespruit Pluton (Fig. 2.1; Viljoen and Viljoen, 1969b). Currently, this formation occurs mainly as greenstone remnants preserved in the TTG terrain to the south of the Barberton Greenstone Belt, where these rocks are isolated from the main body of the greenstone belt (Viljoen and Viljoen, 1969b).

### *2.2.2 Theespruit Formation*

The Theespruit Formation contains a mélange of basalt, basaltic komatiite as well as sericitic and aluminous schists and agglomerates (Viljoen and Viljoen, 1969b; Lowe and Byerly, 1999). The sericitic and aluminous rocks have been interpreted to represent altered felsic volcanic and pyroclastic units and are usually associated with thin black-banded chert horizons (Viljoen and Viljoen, 1969b; De Wit et al., 1983, 1987). These felsic rocks are characteristic of the Theespruit Formation and are, apart from a similar unit in the upper Hooggenoeg Formation (Fig. 2.2), unknown in the remainder of the Onverwacht Group (Viljoen and Viljoen, 1969b,c; De Wit et al., 1987). The Theespruit

Formation occurs as an up to 2 km thick, laterally continuous unit along the granitoid-greenstone contact in the south of the Barberton Greenstone Belt (Viljoen and Viljoen, 1969b). These rocks have experienced upper-greenschist- to amphibolite-facies metamorphism, with the higher metamorphic grades occurring close to the granitoid contacts and the grade decreasing rapidly away from the plutons and towards the centre of the greenstone belt (Viljoen and Viljoen, 1969b).

### 2.2.3 Komati Formation

The Theespruit Formation is overlain by the Komati Formation, a 3.5 km thick succession of peridotitic and basaltic komatiites (Viljoen and Viljoen, 1969b). Characteristically, the Komati Formation does not contain any pyroclastic or sedimentary horizons interlayered with the komatiite flows (Viljoen and Viljoen, 1969b; Lowe and Byerly, 1999; Dann, 2000). The Middle Marker, a thin, laterally continuous chert unit defines the top of the Komati Formation and separates it from the overlying Hooggenoeg Formation (Viljoen and Viljoen, 1969c). Cloete (1999) investigated metamorphism in the Komati and Hooggenoeg Formations and concluded that the Komati Formation was subjected to maximum pressure-temperature conditions of ca. 3 – 4 kbar at 520°C in a static (burial) metamorphic environment. Whole-rock and amphibole-  $^{40}\text{Ar}/^{39}\text{Ar}$  ages ranging from  $3425 \pm 10$  to  $3486 \pm 8$  Ma (Lopez-Martinez et al., 1992) obtained from the Komati Formation are considered to reflect the timing of this metamorphic event. The Komati Formation has a minimum emplacement age of  $3482 \pm 5$  Ma (Armstrong et al., 1990), which suggests that emplacement and metamorphism occurred almost synchronously (Lopez-Martinez et al., 1992; De Ronde and De Wit, 1994).

## 2.3 The relationship of the Theespruit and Komati Formations and the significance of the Komati Fault

The upper formations of the Onverwacht Group are separated from the Sandspruit and Theespruit Formations by the Komati Fault (Figs. 2.1 and 2.2; Viljoen and Viljoen, 1969a,b; De Wit et al., 1983, 1987; Armstrong et al., 1990; De Ronde and De Wit, 1994;

Lowe and Byerly, 1999) and the stratigraphic position of the Theespruit Formation relative to the Komati Formation has not been fully resolved. Dating of felsic volcanoclastics from the Theespruit Formation type locality to the east of the Theespruit Pluton has revealed that these units have a depositional age of  $3453 \pm 6$  Ma (Armstrong et al., 1990), which is substantially younger than the  $3482 \pm 5$  Ma age obtained for the structurally overlying Komati Formation during the same study. It was also shown that the Theespruit Formation contains older gneissose fragments, dated at  $3538 \pm 6$  Ma (Armstrong et al., 1990) and  $3538 \pm 4/-2$  Ma (Kamo and Davis, 1994), and interpreted to be tectonically imbricated portions of the underlying basement (Armstrong et al., 1990). However, dating of felsic metavolcanics from the Steynsdorp Anticline (Fig. 2.1) has shown that these rocks have ages of  $3544 \pm 3$  to  $3548 \pm 3$  Ma (Kröner et al., 1996), which are substantially older than the Komati Formation. It can thus be concluded that, at least locally, the mélangé-like Theespruit Formation contains units that are both older and younger than the overlying Komati Formation (Armstrong et al., 1990).

The importance of the Komati Fault as a significant structural break is further emphasized as it juxtaposes the relatively high-grade metamorphic and intensely deformed rocks of the Sandspruit and Theespruit Formations against the low-grade metamorphic, relatively intact Komati through Mendon Formations (Lowe et al., 1999). The Komati Fault has been interpreted as a sole thrust along which the Onverwacht Group was tectonically emplaced onto the granitoid-gneiss basement, which includes the Sandspruit and Theespruit Formations (e.g. De Wit et al., 1987, 1992; Armstrong et al., 1990; De Ronde and De Wit., 1994). Recent pressure-temperature estimates of metamorphic conditions obtained from greenstone remnants preserved in the southern granitoid-gneiss terrain (Dziggel et al., 2002) implies that a structural and metamorphic break equivalent to a crustal column of more than 20 km is present between the high-grade terrain and the low-grade Onverwacht Group. Significantly, peak metamorphism in this terrain occurred during D<sub>2</sub> (see below) and post-dates the intrusion of the ca. 3.45 Ga TTG suite into this terrain by more than 200 Ma (Dziggel et al., 2002). This implies that the terrain as a whole was reactivated subsequent to TTG emplacement and tectonically buried to mid- to lower crustal depths before exhumation and juxtaposition



against the greenstone belt. A recent investigation of the Stolzberg Schist Belt on the boundary between the two terrains (Fig. 2.1) identified structural features that suggest that juxtaposition was accomplished by extensional detachment faulting and core-complex formation (Kisters et al., 2003). Kisters et al. (2003) suggested that the Komati Fault could represent the eastwards continuation of this extensional detachment, which conflicts with previous interpretations of the Komati Fault as a major thrust fault (e.g. De Wit et al., 1983, 1987; De Ronde and De Wit, 1994). These conflicting interpretations highlight the importance of the Komati Fault as a major structural break that is central to any model that attempts to explain the geological evolution of the Barberton terrain.

## 2.4 Granitoid-gneiss geology

The Barberton Greenstone Belt is surrounded on all sides by a complex suite of tonalite-trondhjemite-granodiorite (TTG) plutons and gneisses as well as a suite of syeno-granitic plutons and batholiths. Geochemical and geochronological studies have revealed that the granitoids are the result of a complex and prolonged magmatic history that can be broadly divided into four magmatic episodes (Robb and Anhaeusser, 1983; Kamo and Davis, 1994; Kröner et al., 1991, 1996; Yearron, 2003). The main characteristics of each magmatic episode are briefly discussed below, and the location and ages of specific plutons and batholiths are presented in Figure 2.1.

### 2.4.1 *Pre-3.5 Ga plutonism*

The oldest granitoid-gneisses preserved in the eastern Kaapvaal Craton belong to the Ancient Gneiss Complex that occurs to the south of the Barberton terrain (Hunter et al., 1984; Kröner and Tegtmeier, 1994). The Ngwane Gneiss is considered to be the oldest component of the Ancient Gneiss Complex and phases of this gneiss have been dated at  $3521 \pm 23$  Ma and  $3490 \pm 3$  Ma (Kröner and Tegtmeier, 1994).

The earliest plutonic event recognized in the Barberton granitoid-greenstone terrain is the emplacement of the Steynsdorp Pluton at  $3509 \pm 4$  Ma (Kröner et al., 1996). The

Steynsdorp Pluton is a composite, strongly gneissose trondhjemite (Kisters and Anhaeusser, 1995a) that outcrops in the core of the Steynsdorp Anticline (Fig. 2.1) in the south of the Barberton Greenstone Belt.

#### *2.4.2 Early TTG plutonism at ca. 3.45 Ga*

An early magmatic event at ca. 3.45 Ga resulted in the emplacement of the Doornhoek, Stolzburg and Theespruit Plutons at  $3448 \pm 4$ ,  $3445 \pm 3$  and  $3443^{+4/-3}$  Ma respectively (Kröner et al., 1991; Kamo and Davis, 1994). These trondhjemite plutons occur along the southwestern margin of the Barberton Greenstone Belt (Fig. 2.1) and are spatially and geochemically associated with other intrusions such as the Batavia, Eerstehoek and Honingklip Plutons, which constitute the TTG terrain to the southwest of the greenstone belt (Robb and Anhaeusser, 1983; Yerron, 2003).

Although the early TTG plutons have well-constrained ca. 3.45 Ga crystallization ages, some of these plutons also consistently yield ca. 3.2 Ga ages that are interpreted to represent the timing of a metamorphic event that affected the southwestern TTG terrain (Kamo and Davis, 1994). The Stolzburg Pluton has yielded ages of  $3255 \pm 6$ ,  $3237 \pm 6$  and  $3201 \pm 2$  Ma (Kamo and Davis, 1994), and likewise, a titanite age of  $3215 \pm 3$  Ma was extracted from the Doornhoek Pluton during the same study. The 3509 Ma Steynsdorp Pluton has also yielded a titanite age of  $3190 \pm 2$  Ma (Kamo and Davis, 1994).

#### *2.4.3 Late TTG plutonism at ca. 3.23 Ga*

A subsequent episode of TTG magmatism occurred at ca. 3.23 Ga and resulted in the emplacement of the Nelshoogte, Kaap Valley and Dalmein Plutons at  $3236 \pm 1$ ,  $3227 \pm 1$  and  $3215 \pm 2$  Ma respectively (Kamo and Davis, 1994, De Ronde and Kamo, 2000). The Nelshoogte and Kaap Valley Plutons are respectively trondhjemitic and tonalitic in composition (Robb and Anhaeusser, 1983; Anhaeusser, 2001; Yerron, 2003) and were emplaced along the northern margin of the Barberton Greenstone Belt. The Dalmein



Pluton is a granodiorite (Robb, 1983; Yearron, 2003) that occurs in the south of the Barberton Greenstone Belt (Fig. 2.1).

#### 2.4.4. *The ca. 3.1 Ga granodiorite-monzogranite-syenite suite*

A phase of potassic magmatism at 3107 to 3105 Ma (Kamo and Davis, 1994) led to the emplacement of voluminous granodioritic, monzogranitic, syenogranitic and syenitic plutons in the Barberton granitoid-greenstone terrain. The Mpuluzi, Piggs Peak and Heerenveen Batholiths as well as the Boesmanskop and Kees Zyn Doorns Syenites were emplaced to the south and west of the Barberton Greenstone Belt (Fig. 2.1). To the north of the belt, the Stentor and Salisbury Kop Plutons as well as the Nelspruit Batholith were contemporaneously emplaced. The Mpuluzi, Heerenveen, Piggs Peak and Nelspruit Batholiths occur as large, laterally extensive, granodioritic to monzogranitic (Yearron, 2003) sheet-like bodies and are thought to be associated with the stabilization and consolidation of this part of the Kaapvaal Craton (De Wit et al., 1992).

## 2.5 Proposed models for the geological evolution of the Barberton Greenstone Belt

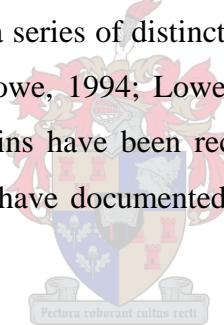
### 2.5.1 *Early models*

Early workers developed their models for the geological evolution of the Barberton Greenstone Belt based largely on field evidence and without the benefit of detailed, high-precision geochronology. They considered the greenstone sequence to represent a fairly intact stratigraphy, without significant structural breaks or repetitions (Viljoen and Viljoen, 1969a,b). The bulk of the deformation in the belt was thought to be the result of a single episode of crustal shortening that produced upright folding and steep thrusting (Visser, 1956; Ramsay, 1963). The intense deformation along the granite-greenstone contacts and the arcuate, dome-and-keel outcrop pattern of the greenstone belt were interpreted to be the result of progressive deformation resulting from the diapiric ascent of intrusive granitoids (Anhaeusser, 1973, 1984). The diapiric model invokes gravity-driven, predominantly vertical tectonics by which the denser greenstones are infolded

between the hot, buoyant diapirs. These early workers also noted that the bulk of the greenstone belt exhibits low zeolite- to greenschist-facies metamorphic grades while the margins of the belt close to the granitoid contacts display higher amphibolite-facies metamorphic grades (Hall, 1918). These higher metamorphic grades were interpreted to be the result of a contact metamorphic effect resulting from the diapiric emplacement of the granitoid magmas (Anhaeusser, 1973, 1984).

### 2.5.2 *Recent models*

Subsequent detailed structural and geochronological investigations have revealed that the Barberton Greenstone Belt has a complex, polyphase tectonic history (Williams and Furnell, 1979; Fripp et al., 1980; De Wit, 1982; De Wit et al., 1983; De Ronde and De Wit, 1994; Kamo and Davis, 1994; Lowe et al., 1985, 1999; Lowe, 1994, 1999) and that the greenstone belt is made up of a series of distinct structural and stratigraphic domains (De Ronde and De Wit, 1994; Lowe, 1994; Lowe et al., 1999). Three deformational episodes and two structural domains have been recognized by De Ronde and De Wit (1994), while Lowe et al. (1999) have documented five deformational events and four structural domains.



#### 2.5.2.1 *D<sub>1</sub> deformation*

The first extensive deformational event recognized by both De Ronde and De Wit (1994) and Lowe et al. (1999) and hereafter referred to as D<sub>1</sub>, occurred at ca. 3445 Ma and affected the lithologies of the Onverwacht Group. The Sandspruit and Theespruit Formations, which occur to the south of the Komati Fault, were most strongly affected and experienced intense deformation and metamorphism (Lowe et al., 1999). These formations are considered to have formed the roof rocks to the early TTG plutons, which were emplaced contemporaneously with D<sub>1</sub> (De Ronde and De Wit, 1994; Lowe et al., 1999). The Onverwacht rocks to the north of the Komati Fault were less affected by D<sub>1</sub>, although hypabyssal felsic intrusives and volcanics, believed to be high-level equivalents of the TTG suite (De Wit et al., 1987; Armstrong et al., 1990), were emplaced into the

Hooggenoeg Formation at this time. It has been proposed that the upper formations of the Onverwacht Group (primarily the Komati and Hooggenoeg Formations) were thrust onto the synkinematically emplaced TTG basement (which included the Sandspruit and Theespruit Formations) along the Komati Fault during  $D_1$  (De Wit et al., 1983, 1987; Armstrong et al., 1990; De Ronde and De Wit, 1994). Other workers have proposed that this thrusting event might have occurred during the later  $D_2$  deformational episode (see below; Lowe et al., 1999).

#### *2.5.2.2 $D_2/D_3$ and subsequent deformational events*

The main deformational event manifested in the Barberton Greenstone Belt occurred from 3229 – 3226 Ma (Kamo and Davis, 1994; De Ronde and Kamo, 2000) and broadly corresponds to the  $D_2$  and  $D_3$  events of De Ronde and De Wit (1994) and Lowe et al. (1999). This compressional event, hereafter referred to as  $D_2$ , is characterized by northwest-directed thrusting and upright folding, resulting in the northeast-southwest trending structural grain of the Barberton Greenstone Belt (Kamo and Davis, 1994, De Ronde and De Wit, 1994; De Ronde and Kamo, 2000).

A second phase of voluminous TTG plutonism, resulting in the emplacement of the Nelshoogte and Kaap Valley Plutons along the northern margin of the greenstone belt, occurred simultaneously with  $D_2$  (Kamo and Davis, 1994; De Ronde and Kamo, 2000). The equilibration of the peak metamorphic assemblages in the greenstone remnants preserved in the TTG terrain to the southwest of the Barberton Greenstone Belt and in the Schapenburg Schist Belt (Fig. 2.1) occurred contemporaneous with  $D_2$  (Dziggel et al., 2002; Stevens et al., 2002). Furthermore, the onset of Moodies Group deposition at 3224 Ma (Fig. 2.2; Tegtmeier and Kröner, 1987) is also within the timeframe of  $D_2$ .

The occurrence of widespread deformation, high-grade metamorphism and voluminous plutonism all point to the fact that  $D_2$  is a major accretionary episode and it has been proposed that the northern and southern domains of the Barberton Greenstone Belt were

amalgamated along the Saddleback-Inyoka Fault system during this tectonic episode (De Ronde and De Wit, 1994; Kamo and Davis, 1994).

The Dalmein Pluton truncates regional  $D_2$  structures in the Onverwacht Anticline and Kromberg Syncline (Robb, 1983; Kamo and Davis, 1994; Lowe et al., 1999), indicating that, at least in this part of the belt, the  $D_2$  accretionary event must have ceased prior to the emplacement of the Dalmein Pluton at  $3215 \pm 2$  Ma (Kamo and Davis, 1994).

Whereas other workers have viewed the  $D_2$  deformational episode essentially as a continuum, Lowe et al. (1999) have identified two additional deformational episodes,  $D_4$  and  $D_5$ , which affect the whole of the Barberton Greenstone Belt and occurred prior to 3215 Ma. These deformational episodes tighten earlier  $D_2$  folds and re-orientate  $D_2$  thrusts to their current subvertical orientation.

The shear zone-hosted gold mineralization in the northern part of the Barberton Greenstone Belt is proposed to have coincided with a later episode of deformation that occurred from ca. 3126 - 3084 Ma (De Ronde et al., 1991; De Ronde and De Wit, 1994). Although the emplacement of voluminous, sheet-like potassic granites at 3107 - 3105 Ma is traditionally considered to have been largely anorogenic (De Wit et al., 1992), recent investigations have revealed that the emplacement of the Mpuluzi and Heerenveen Batholiths were accommodated by a hitherto unrecognized deformational event that affected the Barberton terrain at 3.1 Ga (Westraat et al., 2005; Belcher and Kisters, in review). This event is responsible for the widespread tectonic fabrics present in the ca. 3.1 Ga plutonic suite that have also been observed by Robb et al. (1983) and Jackson and Robertson (1983).

## **CHAPTER 3: LITHOLOGY AND PETROGRAPHY**

### 3.1 Introduction

The greenstones of the Tjakastad Schist Belt and the areas around the Stolzburg and Theespruit Plutons consist almost exclusively of lithologies belonging to the Theespruit Formation (Fig. 2.1; Appendix 1; Viljoen and Viljoen, 1969a,b; Anhausser et al., 1981). It is only the southernmost parts of the Tjakastad Schist Belt that contain greenstone lithologies belonging to the Sandspruit Formation. The Stolzburg and Theespruit Plutons that bound the Tjakastad Schist Belt are both part of the early TTG suite that intruded the Theespruit Formation at ca. 3.45 Ga (Viljoen and Viljoen, 1969a; De Wit et al., 1983; Kröner et al., 1991; Kamo and Davis, 1994; Lowe and Byerly, 1999). A striking feature of the Tjakastad Schist Belt is the presence of unusually thick units of felsic schist, the like of which is unknown anywhere else in the Theespruit Formation (Kisters and Anhaeusser, 1995b). These units are particularly attractive from a petrological perspective because their locally aluminous compositions might allow them to generate mineral assemblages useful in constraining the conditions of metamorphism. Rock types with compositions suited to the generation of low-variance metamorphic mineral assemblages are quite rare in primitive crust, as greenstone sequences predominantly consist of mafic and ultramafic volcanic rocks. These rocks usually contain mineral phases that are stable over a wide range of pressure – temperature conditions, causing them to be of limited use in constraining precise metamorphic conditions (Will et al., 1990; Spear, 1993; Wilkins, 1997). The position of localities as well as the rock types sampled during this study is presented in Figure 3.1 and Table 3.1 and includes samples for which geochemical data are available.

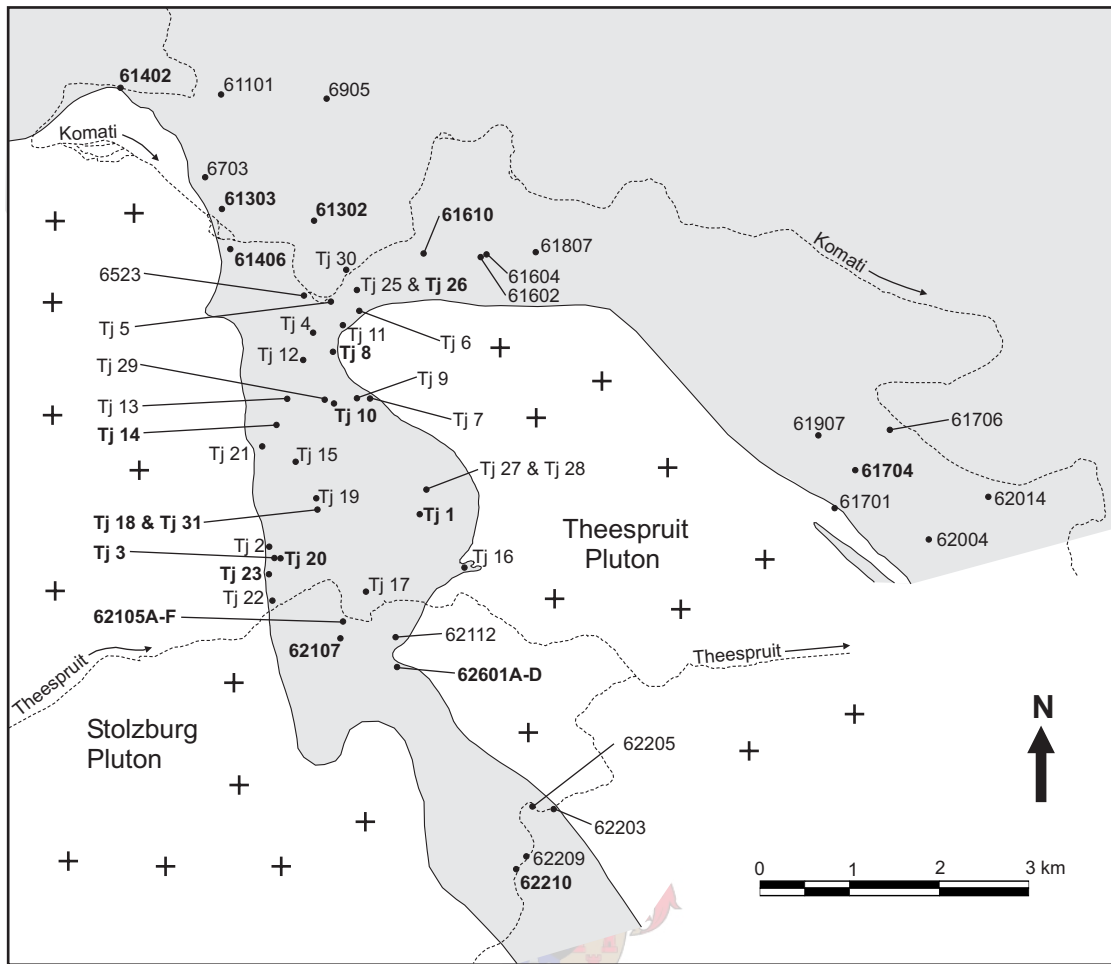


**Figure 3.1:** Map showing the location of outcrops that were sampled during this study. Bold numbers are samples that are referred to in the text or samples for which geochemical data are available.

**Table 3.1:** Location and description of samples collected. Bold entries are samples that are referred to in the text or samples for which geochemical data are available.

<b>Sample</b>	<b>Latitude</b>	<b>Longitude</b>	<b>Sample description</b>
<b>Tj 1</b>	<b>26°00'10.8"S</b>	<b>30°47'28.8"E</b>	<b>low-strain agglomerate</b>
Tj 2	26°00'23.6"S	30°46'33.7"E	felsic schist
<b>Tj 3</b>	<b>26°00'27.4"S</b>	<b>30°46'36.2"E</b>	<b>garnet amphibolite</b>
Tj 4	25°59'06.1"S	30°46'50.2"E	rodded felsic schist
Tj 5	25°58'53.6"S	30°46'54.9"E	chlorite schist
Tj 6	25°58'59.1"S	30°47'09.9"E	chlorite schist
Tj 7	25°59'29.8"S	30°47'10.1"E	amphibolite
<b>Tj 8</b>	<b>25°59'12.9"S</b>	<b>30°46'57.1"E</b>	<b>quartz-sericite schist</b>
Tj 9	25°59'29.6"S	30°47'05.3"E	felsic schist
<b>Tj 10</b>	<b>25°59'30.8"S</b>	<b>30°46'56.1"E</b>	<b>garnet amphibolite</b>

**Table 3.1:** continued

<b>Sample</b>	<b>Latitude</b>	<b>Longitude</b>	<b>Sample description</b>
Tj 11	25°59'05.5"S	30°47'01.0"E	aplite dyke
Tj 12	25°59'16.2"S	30°46'46.2"E	micaceous felsic schist
Tj 13	25°59'30.4"S	30°46'40.4"E	micaceous felsic schist
<b>Tj 14</b>	<b>25°59'39.7"S</b>	<b>30°46'36.4"E</b>	<b>epidote-amphibolite</b>
Tj 15	25°59'52.3"S	30°46'43.4"E	coarse-grained felsic schist
Tj 16	26°00'31.1"S	30°47'42.1"E	amphibolite with aplite veinlets
Tj 17	26°00'39.5"S	30°47'09.4"E	banded iron formation
<b>Tj 18</b>	<b>26°00'09.5"S</b>	<b>30°46'51.3"E</b>	<b>garnet-staurolite-biotite felsic schist</b>
Tj 19	26°00'06.8"S	30°46'51.3"E	amphibolite
<b>Tj 20</b>	<b>26°00'27.3"S</b>	<b>30°46'36.8"E</b>	<b>epidote-amphibolite</b>
Tj 21	25°59'46.9"S	30°46'31.5"E	garnet felsic schist
Tj 22	26°00'43.1"S	30°46'33.8"E	garnet amphibolite with aplite veinlets
<b>Tj 23</b>	<b>26°00'33.7"S</b>	<b>30°46'33.0"E</b>	<b>biotite-muscovite felsic schist</b>
Tj 24	26°00'33.7"S	30°46'33.0"E	garnet-biotite felsic schist
Tj 25	25°58'51.4"S	30°47'06.4"E	chlorite-muscovite schist
<b>Tj 26</b>	<b>25°58'51.4"S</b>	<b>30°47'06.4"E</b>	<b>chlorite-zoisite schist</b>
Tj 27	26°00'03.0"S	30°47'30.0"E	sheared felsic schist with plagioclase porphyroclasts
Tj 28	26°00'03.0"S	30°47'30.0"E	sheared felsic schist with plagioclase porphyroclasts
Tj 29	26°59'30.3"S	30°46'54.1"E	coarse-grained actinolite-chlorite schist
Tj 30	25°58'43.2"S	30°47'01.0"E	chlorite-muscovite schist
<b>Tj 31</b>	<b>26°00'10.2"S</b>	<b>30°46'51.5"E</b>	<b>garnet amphibolite</b>
6523	25°58'52.9"S	30°46'47.2"E	rodded amphibolite
6703	25°58'10.8"S	30°46'11.0"E	garnet felsic schist
6905	25°57'41.3"S	30°46'54.1"E	aplite dyke
61101	25°57'39.6"S	30°46'16.2"E	sheared felsic schist with plagioclase porphyroclasts
<b>61302</b>	<b>25°58'25.7"S</b>	<b>30°46'50.2"E</b>	<b>chlorite schist</b>
<b>61303</b>	<b>25°58'21.9"S</b>	<b>30°46'16.4"E</b>	<b>garnet felsic schist</b>
<b>61402</b>	<b>25°57'37.7"S</b>	<b>30°45'40.2"E</b>	<b>quartz-sericite schist</b>
<b>61406</b>	<b>25°58'36.1"S</b>	<b>30°46'20.7"E</b>	<b>garnet amphibolite</b>
61602	25°58'39.0"S	30°47'51.0"E	silicified chlorite schist
61604	25°58'38.4"S	30°47'51.6"E	retrograde amphibolite
<b>61610</b>	<b>25°58'38.4"S</b>	<b>30°47'28.7"E</b>	<b>chlorite-quartz-magnetite-garnet mylonite</b>
61701	26°00'09.2"S	30°49'58.1"E	gneissose Theespruit Pluton
<b>61704</b>	<b>25°59'56.1"S</b>	<b>30°50'05.7"E</b>	<b>garnet-chlorite schist</b>
61706	25°59'41.3"S	30°50'18.7"E	serpentinite
61807	25°58'37.2"S	30°48'09.1"E	retrograde amphibolite
61907	25°59'43.5"S	30°49'52.1"E	low strain felsic tuff
62004	26°00'21.0"S	30°50'32.0"E	felsic schist
62014	26°00'05.8"S	30°50'53.3"E	felsic schist/chert
<b>62105A</b>	<b>26°00'50.3"S</b>	<b>30°47'02.3"E</b>	<b>garnet-quartz-amphibole mylonite</b>
62105B	26°00'50.3"S	30°47'02.3"E	kyanite-mica schist
62105C	26°00'50.3"S	30°47'02.3"E	kyanite-mica schist
62105D	26°00'50.3"S	30°47'02.3"E	quartz-muscovite-chlorite felsic schist
<b>62105E</b>	<b>26°00'50.3"S</b>	<b>30°47'02.3"E</b>	<b>garnet-staurolite-biotite felsic schist</b>
<b>62105F</b>	<b>26°00'50.3"S</b>	<b>30°47'02.3"E</b>	<b>garnet-staurolite-biotite felsic schist</b>
62105G	26°00'50.3"S	30°47'02.3"E	kyanite felsic schist
<b>62107</b>	<b>26°00'57.1"S</b>	<b>30°47'00.4"E</b>	<b>garnet amphibolite</b>

**Table 3.1:** continued

<b>Sample</b>	<b>Latitude</b>	<b>Longitude</b>	<b>Sample description</b>
62112	26°00'56.4"S	30°47'20.9"E	leucocratic amphibolite
62203	26°01'57.7"S	30°48'17.5"E	Theespruit Pluton with small greenstone enclaves
62205	26°01'56.9"S	30°48'09.3"E	serpentine
62209	26°02'15.5"S	30°48'07.9"E	garnet amphibolite
<b>62210</b>	<b>26°02'20.2"S</b>	<b>30°48'04.0"E</b>	<b>amphibolite</b>
<b>62601A</b>	<b>26°01'07.1"S</b>	<b>30°47'21.1"E</b>	<b>garnet amphibolite</b>
62601B	26°01'07.1"S	30°47'21.1"E	staurolite-tourmaline felsic schist
<b>62601C</b>	<b>26°01'07.1"S</b>	<b>30°47'21.1"E</b>	<b>garnet-staurolite-biotite felsic schist</b>
<b>62601D</b>	<b>26°01'07.1"S</b>	<b>30°47'21.1"E</b>	<b>kyanite-staurolite-biotite felsic schist</b>

### 3.2 Felsic schist and agglomerate

In outcrop, the felsic schists have a light yellow- to pale brown colour and these rocks weather to yellow-brown soils. Texturally these rocks vary from well-foliated, fine-grained muscovite-quartz-biotite schists to medium-grained quartz-sericite schists and massive agglomerates. The agglomerate units are matrix-supported and contain angular and rounded fragments and cobbles of felsic volcanic rocks (Fig 3.2a) and, in one instance, a polymict assemblage consisting of felsic volcanics as well as amphibolite, black chert and banded gneiss (Fig. 3.2b and c; De Wit et al., 1983). The fragments vary in size from 5 to 20 cm in diameter and are suspended in a matrix of medium- to fine-grained quartz-sericite. The felsic schist units generally occur as 20 – 50 m thick continuous horizons, although these units can reach thicknesses of more than 1000 m in the western part of the Tjakastad Schist Belt (Appendix 1).

Felsic schist that contains metamorphic index minerals such as garnet, staurolite, biotite, kyanite, sillimanite, muscovite and chlorite are occasionally encountered. Accessory phases identified in these samples include ilmenite, apatite, titanite, tourmaline, rutile, zircon, monazite and allanite.



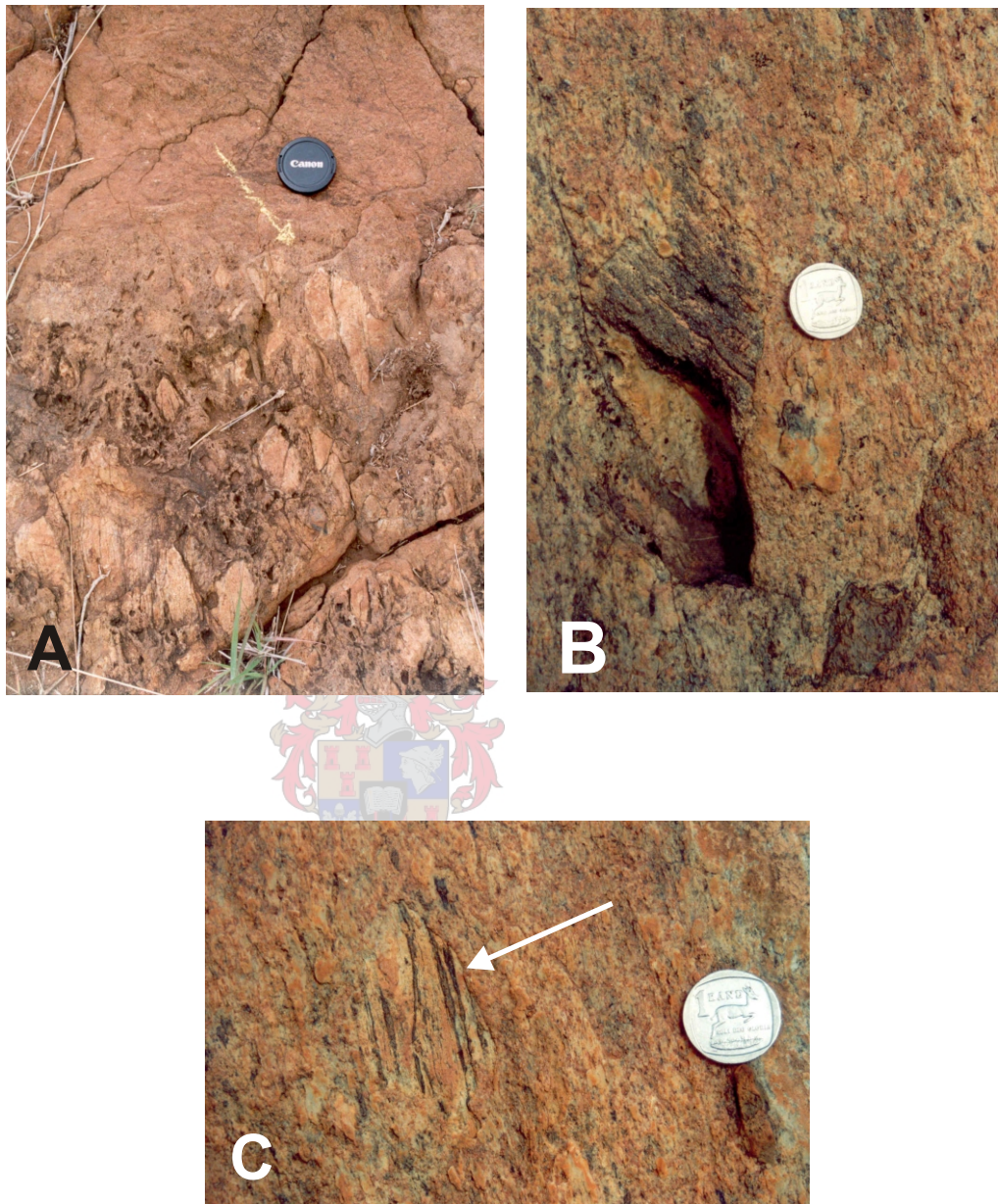


**Figure 3.2:** (a) Photograph of a typical felsic agglomerate displaying rounded clasts of felsic volcanic material. Note the presence of a steeply dipping bedding contact between this unit and a finer-grained felsic schist, oblique view. (b) and (c): Close-up of clasts of amphibolite (b) and banded gneiss (c) preserved in felsic agglomerate, profile view.

Garnet occurs as large (2 – 3,5 mm) subhedral porphyroblasts that consist of highly poikilitic cores and thin inclusion-free rims. Although it is not typical, two samples (62601C and 62105E) contain abundant small (<1 mm) garnet grains that exhibit the same petrographic zoning as the large porphyroblasts. Quartz and ilmenite constitute the majority of the inclusions in garnet but biotite, chlorite and rutile are also present. Garnet typically exhibits a fairly simple petrographic zoning that only consists of a single core – rim relationship (Fig. 3.3a and b). The bulk of garnet growth seems to have occurred prior to or very early during deformation as the prominent schistose fabric exhibited in these rocks wraps around the garnet porphyroblasts. This argument is supported by the observations that garnet grains are generally slightly flattened in the schistosity (Fig. 3.3a), exhibit well-developed pressure shadows and strong alignment parallel to the subvertical rodding lineation (refer to Chapter 4; Fig. 4.4d). Features that would indicate syntectonic garnet growth, such as spiraling inclusion trails, are absent in garnet from felsic schist samples. A single, large snowball garnet that can be interpreted as a  $\sigma$ - or  $\delta$ -object (after Simpson and Schmid, 1983) is found in sample 62105F (Fig. 3.3c). A later episode of garnet growth resulted in the formation of overgrowths that are confined to the pressure shadow sites. These overgrowths are anhedral and occur as roughly triangular ‘wings’ that are connected to the garnet porphyroblast, or as rounded, distinct grains that seem to have nucleated in the pressure shadow (Fig. 3.3 d, e and f). This later growth episode is most likely syn- to late tectonic.

Staurolite is a distinctive component of the mineral assemblage in these samples and occurs as anhedral, elongated porphyroblasts that are 3 - 10 mm long. Inclusions in staurolite consist almost exclusively of ilmenite that is always present as strongly aligned prismatic grains, while quartz, tourmaline and garnet are only subordinately present. Staurolite crystals are plastically deformed, strongly elongated and have a grain-shape preferred orientation parallel to the schistosity (Fig. 3.4a and b). Some of the deformed grains are boudinaged (Fig. 3.4a) while others are well-developed  $\sigma$ -objects that have been used to infer the sense of shear (refer to Chapter 4; Fig. 4.10c). In some samples, staurolite is extensively replaced by muscovite and is only present as relict, anhedral grains contained in a matrix of muscovite and chlorite (Fig. 3.4c).



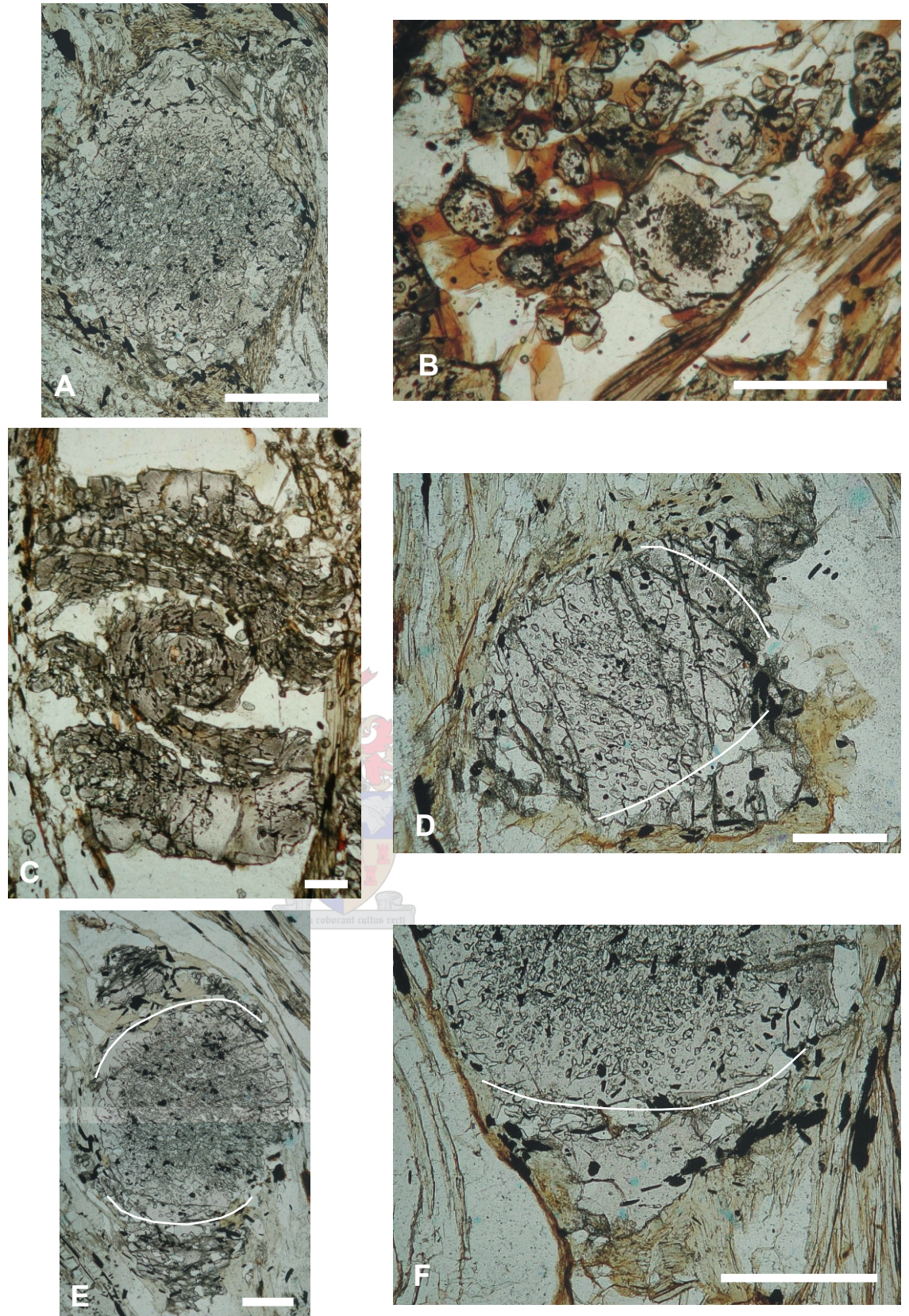


**Figure 3.3:** Photomicrographs illustrating the occurrence and paragenesis of garnet in felsic schists. **(a):** Slightly flattened garnet porphyroblast that is typical of garnet in felsic schist (from sample Tj 18). Garnet consists of a large, poikilitic core that contains inclusions of quartz and ilmenite and a thin, inclusion-free rim. **(b):** Small garnet porphyroblasts from sample 62601C exhibiting the same zonation as typical large garnet porphyroblasts. **(c):** Massive snowball garnet from sample 62105F. **(d and e):** Garnet grains displaying overgrowths that are confined to the pressure shadow sites of these grains. **(f):** Close-up of a typical, anhedral, triangular overgrowth in the pressure shadow of a large garnet porphyroblast. Photographs (d), (e) and (f) are from sample Tj 18. All photographs are taken in plane-polarized light. Scale bar is 0.5 mm long.



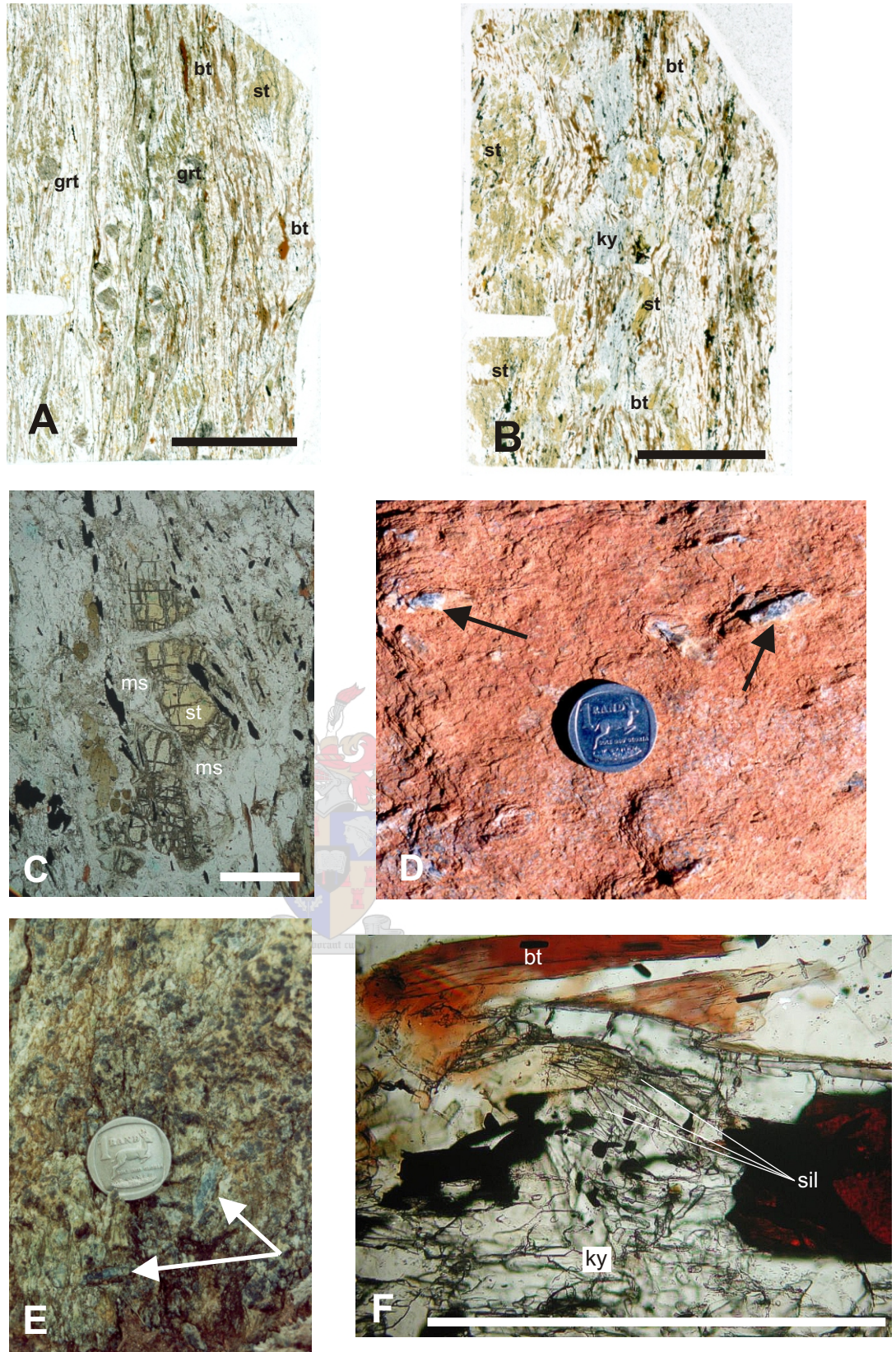


**Figure 3.4:** Photographs illustrating the occurrence of metamorphic index minerals in felsic schists. **(a):** Photograph of a thin section of garnet-staurolite-bearing felsic schist showing the alignment of staurolite parallel to the schistosity that is defined by biotite. Note how the fabric wraps around garnet porphyroblasts (from sample 62105F). **(b):** Thin section photograph of kyanite-staurolite-bearing felsic schist showing the alignment of staurolite and kyanite parallel to the schistosity defined by biotite. Note the large grains of kyanite and staurolite in the centre of the photograph that displays prominent boudinage (from sample 62601D). **(c):** Photomicrograph of relic staurolite islands preserved in a matrix of muscovite (from sample Tj 18). **(d and e):** Field photographs of kyanite occurrences. Kyanite is associated with staurolite in (e). **(f):** Photomicrograph of orientated sillimanite overgrowths on kyanite (from sample 62601D). All photomicrographs are taken in plane-polarized light. Scale bar in (a) and (b) is 10 mm long; scale bar in (c) and (f) is 0.5 mm long. Mineral abbreviations are after Kretz (1983).

The occurrence of kyanite in the Barberton Greenstone Belt has previously only been documented by De Wit et al. (1983) when they described the presence of kyanite in felsic schist to the east of the Theespruit Pluton. The current investigation has revealed that kyanite is present at a few localities in the Tjakastad Schist Belt (Appendix 1). Kyanite is abundant in some samples and occurs as large, 10 – 30 mm long grains that have a typical bladed crystal shape (Fig. 3.4d and e). Kyanite usually has a grain- shape preferred orientation parallel to the pervasive subvertical lineation, although this is not always the case. In some samples (such as locality 62105; see section 3.7), kyanite is confined to distinct bands that are intercalated with kyanite-free quartz-muscovite-chlorite zones. Kyanite, like staurolite, contains aligned inclusions of ilmenite and displays evidence of plastic deformation as well as boudinage (Fig. 3.4b). One sample (62601D) contains reaction textures of staurolite breaking down to form kyanite. This sample contains large, ductilely deformed kyanite porphyroblasts that are strongly aligned parallel to the schistosity. This sample also contains fibrous sillimanite that occurs along the kyanite grain boundaries and overprints the kyanite in an apparently late- to post-tectonic fashion (Fig. 3.4f).

Biotite and chlorite are the dominant minerals that define the schistosity in most felsic schist samples. Biotite has a deep-red colour and is usually medium- to coarse-grained, although biotite inclusions in garnet are small, equidimensional and randomly orientated. Biotite grains are generally inclusion-free and are intimately associated with chlorite. The biotite in most samples shows variable replacement by a retrogressive generation of chlorite and varies from being present as pristine biotite in some samples to only occurring as relic grains enveloped by chlorite.

More than one generation of chlorite is present in most felsic schist samples. The first generation of chlorite occurs as fine- to medium-grained crystals that are finely interleaved with biotite and defines the same schistose fabric as biotite. A second generation of chlorite occurs as a breakdown product of garnet and biotite and can be aligned parallel to the schistosity or have a random orientation. Chlorite is also common as small inclusions in garnet.



Muscovite is not a common constituent of the garnet-staurolite-bearing felsic schists and only occurs in these samples as fine-grained fibrous muscovite, replacing minerals such as staurolite and biotite. Few samples, most notably samples that are kyanite-bearing, do contain medium- to coarse-grained muscovite as part of the matrix assemblage.

Plagioclase is found in almost all of the felsic schist samples investigated and typically occurs as small, recrystallized grains in quartz-plagioclase bands. Plagioclase usually contains few inclusions of quartz, but large grains with inclusions of aligned ilmenite needles as well as biotite and quartz are occasionally encountered. In these cases, plagioclase is strongly recrystallized and displays evidence of plastic deformation, with the intermittent development of  $\sigma$ -clasts (refer to Chapter 4; Fig. 4.10b).

Ilmenite is present in almost all felsic schist samples and is the dominant opaque phase in these samples. Ilmenite occurs as small, subhedral, elongate grains that sometimes contain cores and overgrowths of rutile and titanite. Ilmenite is regularly distributed throughout most samples and is found as inclusions in most mineral phases as well as discrete, aligned grains in the rock matrix. Tourmaline is an accessory phase that is found in all garnet-, staurolite- or kyanite-bearing samples. Titanite and rutile are commonly found in close association with ilmenite, but there are rare cases where rutile and titanite occur as discrete grains. Apatite, zircon, monazite and allanite occur as matrix phases and as inclusions in garnet, but the presence of these minerals is rare and sporadic.

### 3.3 Mafic rocks

Most of the mafic rocks in the study area occur as hornblende-plagioclase amphibolite, but garnet-bearing amphibolite, epidote-amphibolite as well as chloritic schists are also common. Amphibolite has a very dark olive green to black colour in outcrop and weathers to deep red soils. These rocks are generally coarse-grained and massive and do not normally display textural or chemical banding. Igneous features such as pillow

structures are only locally preserved in amphibolite (e.g. locality 62203; Fig. 3.5a). Amphibolite primarily occurs as massive, fairly continuous units along the contacts of the Stolzburg and Theespruit Plutons and reaches thicknesses of 200 m to more than 500 m. In contrast, amphibolite horizons on the western side of the Tjakastad Schist Belt crop out as boudinaged intercalations in the massive felsic schist and are rarely more than 50 m thick. To the north and east, away from the plutons and towards the central parts of the greenstone belt, amphibolite grades into well-foliated chloritic schist, which constitutes the dominant mafic rock type in these more distant areas (Viljoen and Viljoen, 1969b). Compositionally, these schists vary from chlorite schist to chlorite-actinolite- and chlorite-carbonate schists. Certain chlorite schist units display evidence of an amphibolite-facies history such as small, meter-scale relic pods of pristine amphibolite or pseudomorphed coarse-grained amphibolite textures. In cases where the amphibolite-facies pre-history of the chlorite schists can be recognized, these rocks are referred to as retrograde amphibolite.

### *3.3.1 Amphibolite petrography*

Garnet-bearing amphibolite contains garnet grains that occur as 2 – 4 mm subhedral porphyroblasts that are generally less poikilitic than garnet from felsic schists. Ilmenite and quartz constitute the bulk of the inclusion assemblage and epidote, zoisite and titanite are also found as inclusions in garnet. Garnet normally shows a weakly developed petrographic zonation, with small, randomly orientated inclusions concentrated in the core of the crystal and gradually diminishing towards the rim. Garnet from these samples does not show petrographic evidence of overgrowths or complex growth zonation (Fig. 3.5b). Garnet is generally only slightly flattened and elongated parallel to the tectonic fabric, but a few samples (62107 and 62601A) contain strongly deformed garnet crystals. In these samples, the garnet shows well-developed euhedral crystal faces, but is also strongly elongated and zoned (Fig. 3.5c and d). The petrographic zones are not concentric, but rather consist of a thin band that runs from end to end along the long axis of the crystal. This core band is relatively inclusion-free and only contains inclusions of strongly aligned ilmenite needles. In contrast, the garnet rims on both sides of this

central band contain abundant inclusions of randomly orientated quartz and ilmenite. Most garnet crystals do not show well-developed pressure shadows, but the matrix fabric usually deflects and wraps around garnet porphyroblasts (Fig. 3.5a, b and c). This, along with the slight flattening exhibited by most grains would indicate that garnet growth was most likely early-tectonic. Garnet breakdown textures are rare, but are spectacularly developed in sample 61406. This sample contains large (8 – 12 mm) garnet porphyroblasts that have an anhedral, resorped crystal shape. The anhedral garnets are enveloped by a corona of coarse-grained plagioclase-chlorite-quartz that pseudomorphs the original euhedral garnet crystal shape (Fig. 3.5e).

Epidote is found in most garnetiferous amphibolites, where it typically occurs as small, anhedral grain aggregates in the matrix of these samples. Epidote – and occasionally zoisite – is also commonly found as small, rounded inclusions in garnet. Zoisite is only present as inclusions within garnet and is not found in the amphibolite matrix. Epidote, plagioclase and quartz define the leucocratic bands in samples of banded amphibolite and are intercalated with melanocratic bands that consist exclusively of hornblende.

Olive-green, strongly pleochroic hornblende is the major constituent of all amphibolite samples and is the dominant fabric-forming mineral in these samples. Hornblende is present as sub- to euhedral prismatic grains that are typically 1 – 4 mm in length. The hornblende grains contain evenly distributed inclusions of ilmenite, titanite and small, rounded quartz grains. Hornblende is not found as inclusions in other phases and is confined to the sample matrix. Petrographic zoning as well as reaction textures are generally absent, although the post-tectonic breakdown of hornblende to chlorite is occasionally observed (Fig. 3.5f).

Plagioclase is the other ubiquitous constituent of all amphibolites and occurs as relatively small, anhedral, recrystallized grains that are usually intergrown with quartz. The grains are generally inclusion-free and only occasionally contain fine inclusions of quartz. Plagioclase is exclusively a matrix phase and regularly shows signs of sericitization.



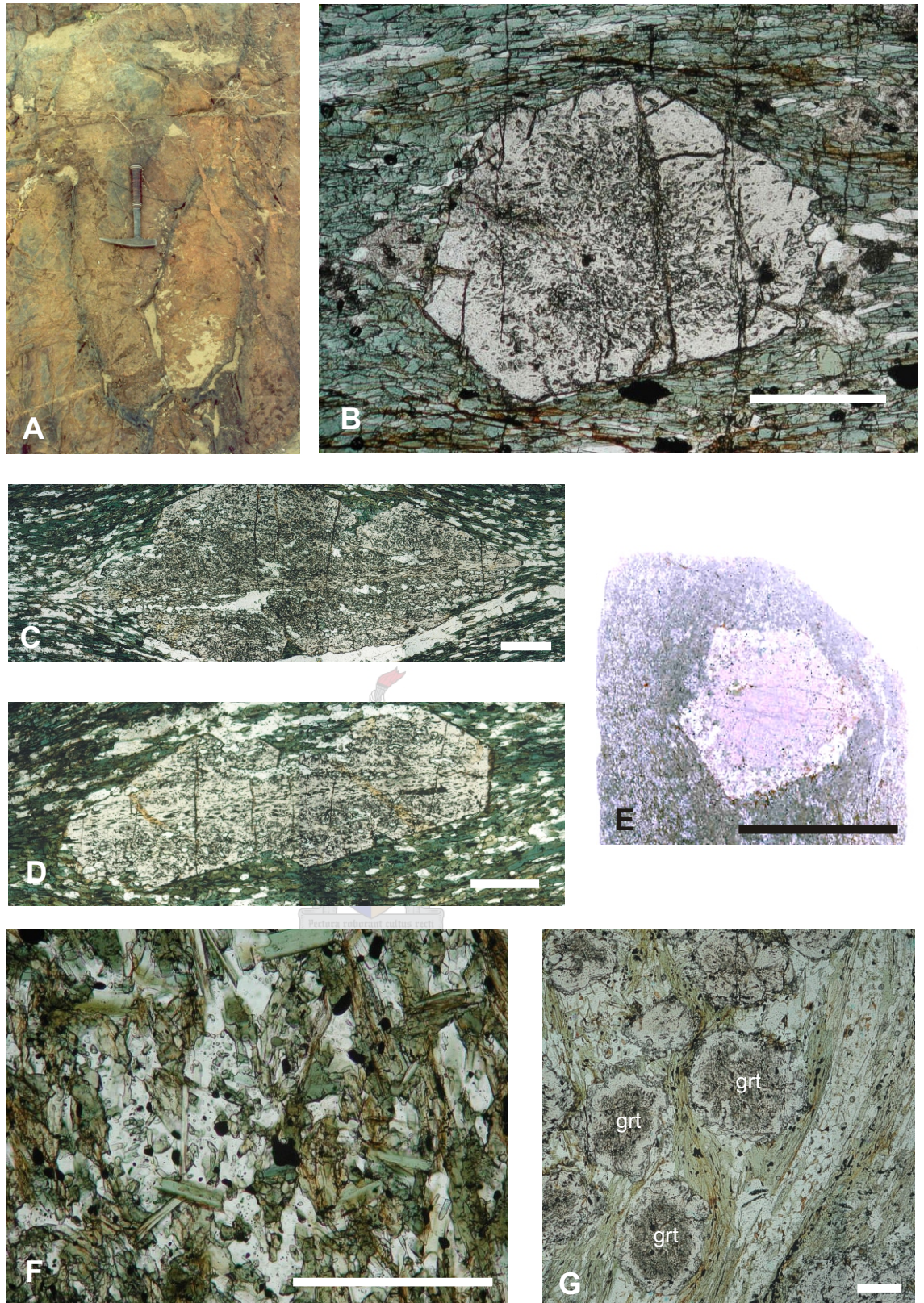


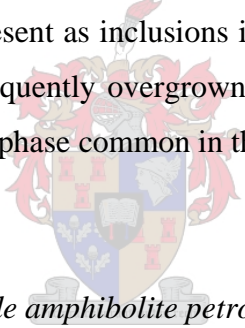
**Figure 3.5:** Photographs illustrating the occurrence and paragenesis of mineral assemblages in amphibolite. **(a):** Amphibolite displaying well-developed pillow structures. Note the slight flattening of the pillow at the head of the hammer, plan view. **(b):** Photomicrograph of typical garnet from amphibolite, consisting of a poikilitic core that grades into an inclusion-free rim. Note the euhedral crystal shape and slight attenuation in the foliation (from sample 62601A). **(c and d):** Severely flattened, euhedral garnets that exhibit a core band that contains aligned inclusions of ilmenite, enveloped by poikilitic rims that contain randomly orientated inclusions of quartz and ilmenite (from sample 62107). **(e):** Anhedral garnet exhibiting a corona of plagioclase-chlorite-quartz that pseudomorphs the euhedral garnet shape (from sample 61406). **(f):** Randomly orientated chlorite overgrowing aligned hornblende and plagioclase in the matrix of sample 61406. **(g):** Abundant small, poikilitic garnet porphyroblasts in a matrix of well-foliated chlorite, muscovite and quartz (from sample 61704). All photomicrographs are taken in plane-polarized light. Scale bar is 0.5 mm, apart from (e), where the scale bar is 10 mm.



Quartz is found in most amphibolite samples and is present as fairly small, anhedral, dynamically recrystallized grains. Quartz occurs as inclusions in phases such as garnet and hornblende and also occurs in the matrix, where it is associated with plagioclase.

Chlorite is relatively rare in most of the amphibolite samples investigated and is only found as a minor product of hornblende breakdown. A single sample (61406) contains abundant chlorite as a product of garnet and hornblende breakdown. The matrix of this sample consists of aligned hornblende, plagioclase, quartz and epidote and is overprinted by large, randomly orientated blades of chlorite (Fig. 3.5f).

Ilmenite is the most common accessory phase found in the amphibolites and is present as small, subhedral, prismatic grains. Ilmenite occurs as inclusions in almost all other mineral phases as well as the amphibolite matrix. Euhedral titanite grains are also common in these rocks and are present as inclusions in garnet and hornblende as well as the matrix. Titanite grains are frequently overgrown around a core crystal of ilmenite. Apatite is the only other accessory phase common in the amphibolite samples and allanite is sporadically encountered.



### *3.3.2 Chlorite schist and retrograde amphibolite petrography*

Most mafic schists consist primarily of chlorite and strongly aligned actinolite that defines the fabric in these rocks. Variable amounts of quartz, muscovite, plagioclase and epidote are also present. Accessory minerals are ilmenite, titanite and apatite while magnetite is locally present. Garnet is found at only two localities and is not characteristic of these rocks. Sample 61610 contains highly poikilitic, strongly anhedral, deformed and resorped garnet, while sample 61704 is a chlorite-muscovite-quartz schist that also contains abundant, highly poikilitic garnet grains (Fig. 3.5g).

Retrograde amphibolite consists of chlorite, highly sericitized plagioclase, quartz and epidote. Typical amphibolite-facies minerals such as hornblende and anorthite-rich plagioclase are absent, but these units commonly preserve amphibolite-facies textures.

The high degree of alteration suffered by these rocks is indicated by the presence of calcite and siderite, which occur as large anhedral crystals that overprint and replace phases such as epidote and zoisite.

### 3.4 Ultramafic rocks

Serpentinized ultramafic rocks are an important constituent of the Theespruit Formation. These rocks occur as thin, continuous bands as well as irregularly shaped bodies, pods and lenses (Viljoen and Viljoen, 1969b). The ultramafic slivers consist of highly foliated, soft, blue-gray talc-carbonate schists. These schists also occur as envelopes around more competent, massive pink-red serpentinite pods and lenses (Fig. 3.6a).

Little attention was paid to the petrography of the ultramafic rocks as these rocks are pervasively altered and commonly consist of serpentine, talc, dolomite, siderite and chlorite, while relic pyroxene and olivine are present in some samples. In samples of serpentinite, olivine occurs as small, round, highly fractured grains in a matrix of serpentine. Pyroxene is present as large (3 – 8 mm) skeletal grains that are enveloped in serpentine, and occasionally, chlorite. Fine-grained serpentine is the dominant constituent of most ultramafic samples, while large grains of carbonate phases such as dolomite and siderite are also common. Talc-carbonate schists do not contain any relic olivine or pyroxene and consist of talc, serpentine, chlorite, siderite, calcite and dolomite in variable proportions. 3 – 5 mm-sized crystals of euhedral magnetite are present in talc-carbonate schist at some localities.

### 3.5 Chert

The distinction between felsic schist and chert is not always immediately obvious as these two lithologies are intimately associated (Viljoen and Viljoen, 1969b) and in some cases felsic schist grades laterally into chert and vice versa. However, a few prominent chert horizons occur in the study area. These bands are continuous and can be traced for

more than 5 km and are generally 1 – 3 m thick. They are composed of sugary, recrystallized white chert, black banded chert as well as green fuchsitic chert.

### 3.6 Intrusive rocks

The Stolzburg and Theespruit Plutons are fine- to medium-grained plagioclase-quartz-hornblende trondhjemites that were intruded into the Sandspruit and Theespruit Formations (Viljoen and Viljoen, 1969a,b; Robb and Anhaeusser, 1983; De Wit et al., 1983; Kisters and Anhaeusser, 1995b). Although the intrusive contacts were subsequently tectonized (Fripp et al., 1980, Kisters and Anhaeusser, 1995b), primary intrusive relationships are locally preserved. These indicate that intrusion was by multiple mechanisms that include ductile wall rock deformation, stoping, assimilation as well as ring dyke formation and intrusive breccias (Fig. 3.6b; Kisters and Anhaeusser, 1995b).

A small, elongated gabbroic body occurs to the north of the Komati River, where the Tjakastad Schist Belt joins the bulk of the Barberton Greenstone Belt. The gabbro crosscuts all the lithologies and fabrics and does not contain any tectonic fabrics. It is thus considered to be a late, post-tectonic feature.

Late dolerite-dabase dyke swarms are intrusive into the Tjakastad Schist Belt as well as the surrounding trondhjemite plutons. These dykes are generally less than 50 m wide, are laterally continuous, have a subvertical orientation and form prominent ridges. The dyke swarms mostly define a northwest-southeast trend.

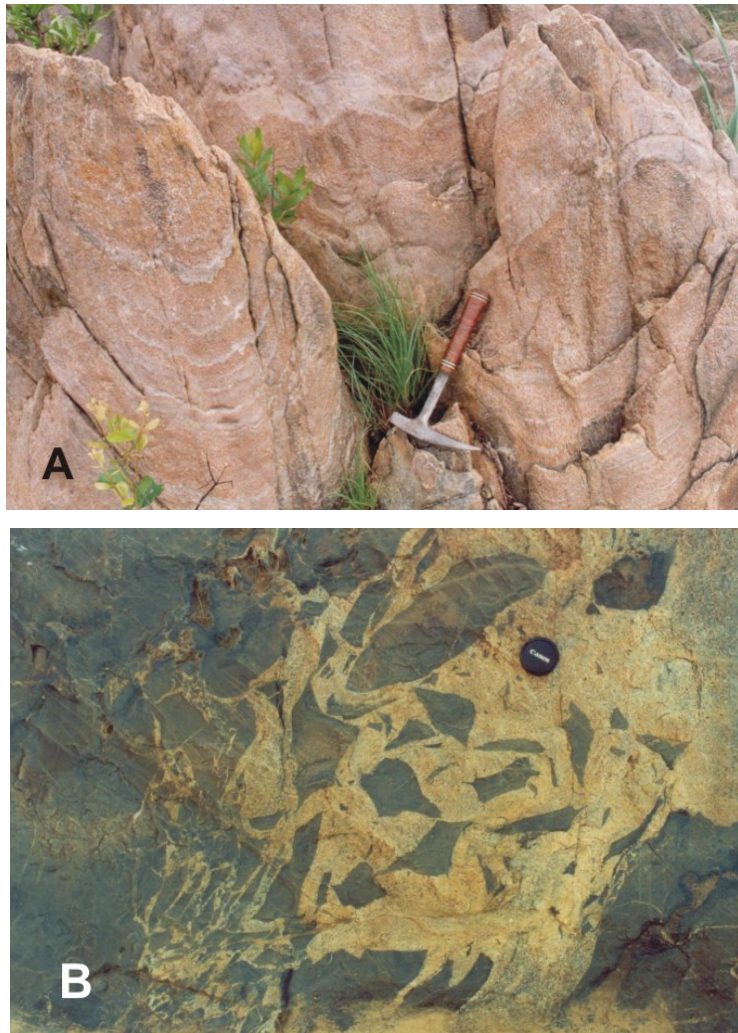


**Figure 3.6:** Photographs of serpentinite and intrusive breccia. **(a):** Photograph of serpentinite showing the preservation of primary compositional banding, profile view. **(b):** Well-developed intrusive breccia of trondhjemite into amphibolite from the intrusive aureole of the Theespruit Pluton, plan view.

### 3.7: Locality 62105

Locality 62105 is found to the south of the Theespruit River in the Tjakastad Schist Belt (Fig. 3.7) and illustrates most of the petrographically significant rock types that were used to characterize the metamorphic evolution of the area. This locality occurs on the contact between a large felsic schist unit to the west and an amphibolite unit to the east (Fig. 3.7). The felsic schist displays horizons that contain abundant kyanite as well as horizons that are garnet- and staurolite-bearing.

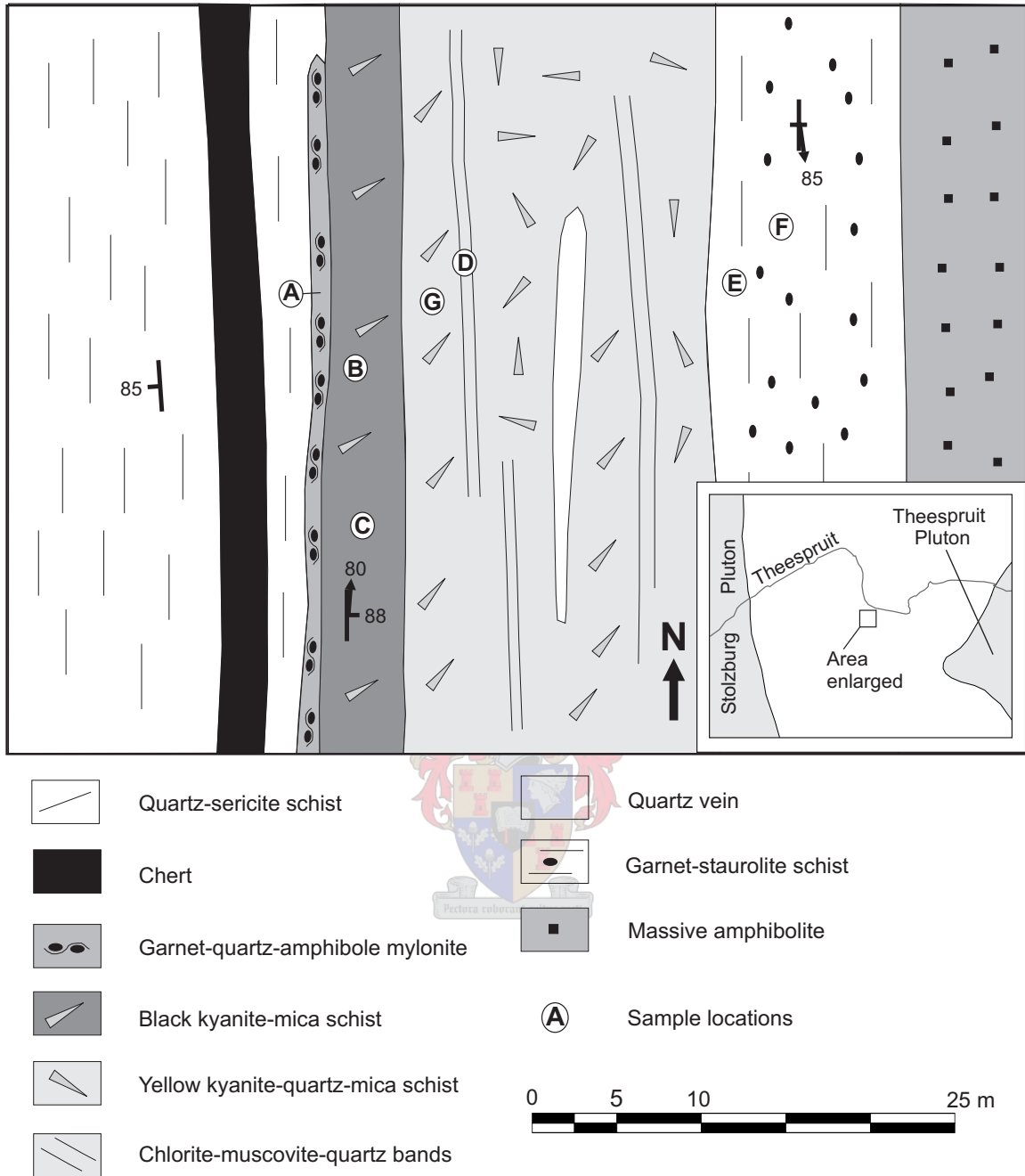


**Figure 3.7:** Sketch map of locality 62105 highlighting the diverse mineral assemblages that are present in the lithologies at this locality. The locations of samples referred to in the text are also shown.

Two kyanite-bearing lithologies are present, the first of which is an extremely dark, fine-grained silicified kyanite-biotite-muscovite schist. Kyanite in this sample occurs as 20 – 30 mm long needle-shaped grains that are strongly aligned parallel to the subvertical

mineral rodding lineation. The second kyanite-bearing horizon is a yellow-brown kyanite-quartz-biotite-muscovite schist that contains abundant 10 – 15 mm bladed kyanite crystals. Kyanite is confined to discrete bands in this horizon and crystals in certain bands have a grain-shape preferred orientation parallel to the subvertical lineation, while kyanite crystals in other bands have a completely random orientation. Kyanite-bearing bands are intercalated with kyanite-free bands on a centimeter- to meter-scale (Fig. 3.7). The kyanite-free bands consist of a matrix of quartz, muscovite, chlorite and plagioclase that contains relic crystals of highly retrogressed staurolite and biotite (Fig. 3.8). In addition, a second generation of chlorite is present as large porphyroblasts that have a random orientation and overprint the schistose matrix assemblage (Fig. 3.8).

A garnet-staurolite-bearing horizon is present to the east of the kyanite-bearing horizons. This unit contains large garnet and staurolite porphyroblasts contained in a matrix of well-foliated biotite and chlorite as well as quartz and plagioclase.

A very unusual rock type that can best be described as a quartz-garnet-amphibole mylonite has only been found at this locality. This unit is about 20 cm thick and is not laterally continuous but occurs as a thin intercalated horizon in felsic schist (Fig. 3.7). This rock contains abundant large (5 – 10 mm) garnet porphyroblasts that are contained in 0,5 to 3 mm thick bands of coarse-grained, strongly aligned hornblende and cummingtonite. The garnet-amphibole bands are interleaved with 1 - 3 mm thick, extremely coarse-grained, recrystallized quartz ribbons (Fig. 3.9). Garnet porphyroblasts are complex and consist of a large euhedral core overgrown by a wide subhedral rim. Significantly, the sample does not contain any plagioclase or epidote and hornblende is only present as a matrix phase, while cummingtonite is found as garnet inclusions and in the matrix. Exsolution lamellae of hornblende in cummingtonite as well as cummingtonite in hornblende are occasionally present in the matrix grains.



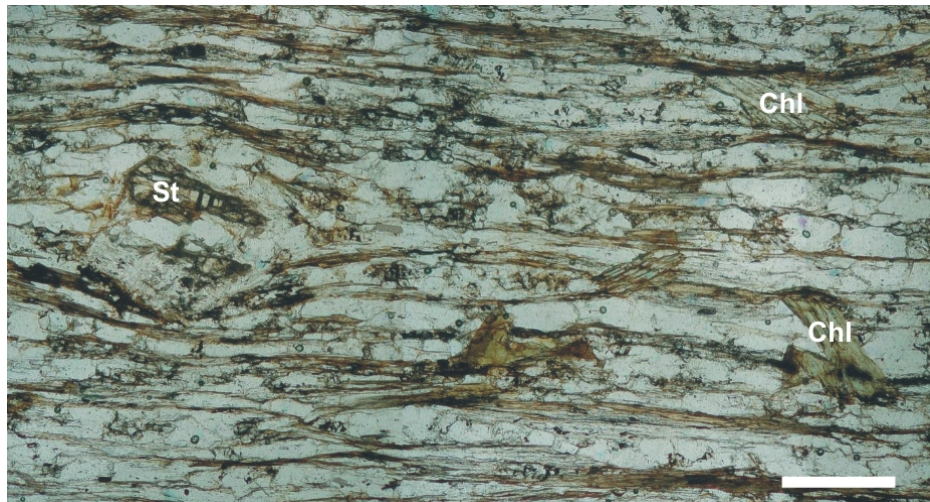


**Figure 3.8:** Photomicrograph of sample 62105D illustrating the occurrence of relic staurolite (st) grains in a matrix of well-foliated chlorite-muscovite-quartz-plagioclase that also contains a second generation of chlorite (chl) that overprints the foliation. Scale bar is 0.5 mm, plane polarized light.



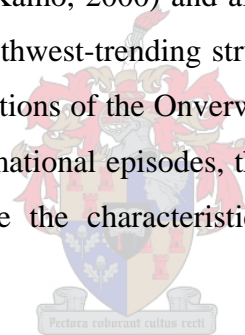
**Figure 3.9:** Photomicrograph of sample 62105A illustrating the coarse-grained banded texture of this sample. The clear bands consist of coarse-grained recrystallized quartz, while the green bands consist of hornblende and cummingtonite and also contain massive garnet porphyroblasts. Scale bar is 10 mm long.



## **CHAPTER 4: STRUCTURE**

### 4.1 Introduction

The tectonic and mélangé-like nature of the Theespruit Formation has been documented by a number of workers, indicating that this formation consists of a series of structurally juxtaposed blocks (e.g. De Wit et al., 1983). It has also been suggested that at least two major episodes of deformation have affected the rocks of the Onverwacht Group (De Ronde and De Wit, 1994; Lowe et al., 1999). The first of these deformational episodes ( $D_1$ ) occurred at ca. 3.45 Ga and most intensely affected the rocks of the Sandspruit and Theespruit Formations (De Ronde and De Wit, 1994; Lowe et al., 1999). The second deformational episode,  $D_2$ , occurred at ca. 3.23 Ga (De Ronde and De Wit, 1994; Kamo and Davis, 1994; De Ronde and Kamo, 2000) and affected the whole of the greenstone belt, resulting in the northeast-southwest-trending structural grain of folds and thrusts in the belt. Because the lower formations of the Onverwacht Group are the only lithologies that show evidence of both deformational episodes, these formations potentially afford a unique opportunity to investigate the characteristics of two Early-Archaean fabric-forming events.



### 4.2 Fabric development in the greenstones

Original bedding ( $S_0$ ) is preserved in isolated outcrops within the Tjakastad Schist Belt and is the earliest fabric recognized in these rocks. Primary features such as pillow structures in amphibolite (refer to Chapter 3; Fig. 3.5a), compositional banding in serpentinite (refer to Chapter 3; Fig. 3.6a) as well as bedding contacts between felsic schist and agglomerate (refer to Chapter 3; Fig. 3.2a) can be observed. However, these bedding relationships are only found in localized, low-strain areas and are not typical of the lithologies in the Tjakstad Schist Belt. Most bedding features have been transposed into a subvertical mylonitic foliation ( $S_1$ ) that contains numerous centimeter- to meter-scale isoclinal, intrafolial folds ( $F_1$ ) that refold  $S_0$  (Fig. 4.1a,b,c and d).

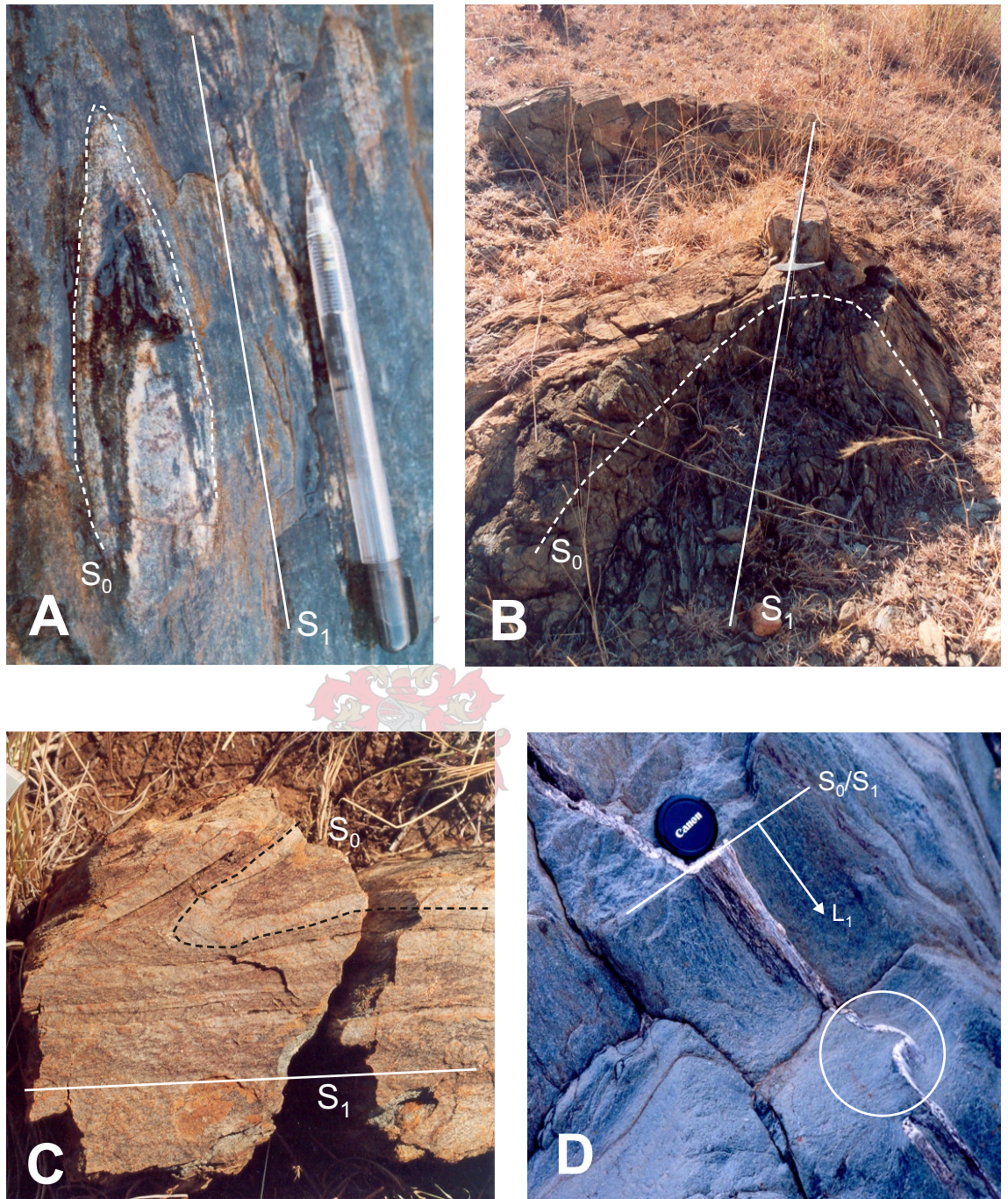


**Figure 4.1:** Photographs illustrating the occurrence of isoclinal intrafolial folds ( $F_1$ ) that re-fold  $S_0$  into the  $S_1$  mylonitic foliation. **(a):** Plan view of a small rootless isoclinal fold in amphibolite. **(b):** Meso-scale isoclinal fold in felsic schist. **(c):** Plan view of small-scale isoclinal fold in felsic schist. **(d):** Three-dimensional outcrop of folded quartz veins in chlorite schist. Note the orientation of the fold axial plane parallel to  $S_1$  and the plunge of the fold axis parallel to  $L_1$  (circled).

These folds are also recognized on a tens-of-meters map scale (Fig. 4.2). Some pavements (e.g. locality Tj 18) consist of fine, tectonically intercalated units of felsic schist and amphibolite. These intercalations are less than 50 cm wide, terminate within 10 – 20 m along strike and are imbricated against each other in a highly disorderly fashion (Fig. 4.3). Because of the intense tectonization and transposition of primary bedding features into the  $S_1$  tectonic fabric, this composite fabric will be referred to as  $S_0/S_1$ .

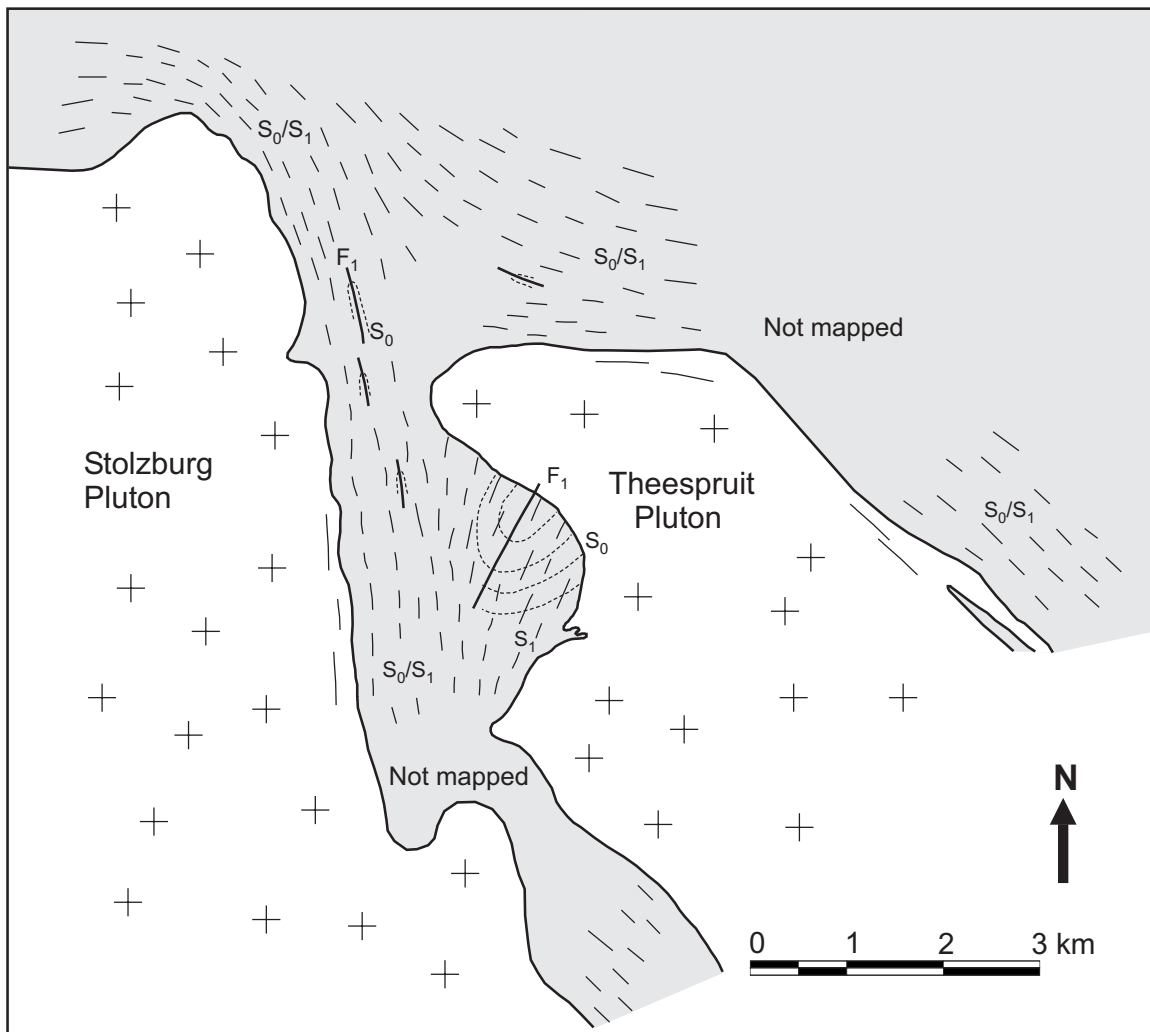


**Figure 4.2:** Structural map of the Tjakastad Schist Belt and surrounding areas showing the occurrence of isoclinal  $F_1$  folds that transpose original bedding ( $S_0$ ) into the mylonic foliation ( $S_1$ ) commonly exhibited by these rocks. Note that the trend of the composite transposition fabric ( $S_0/S_1$ ) is roughly concordant with the margins of the Stolzburg and Theespruit Plutons.



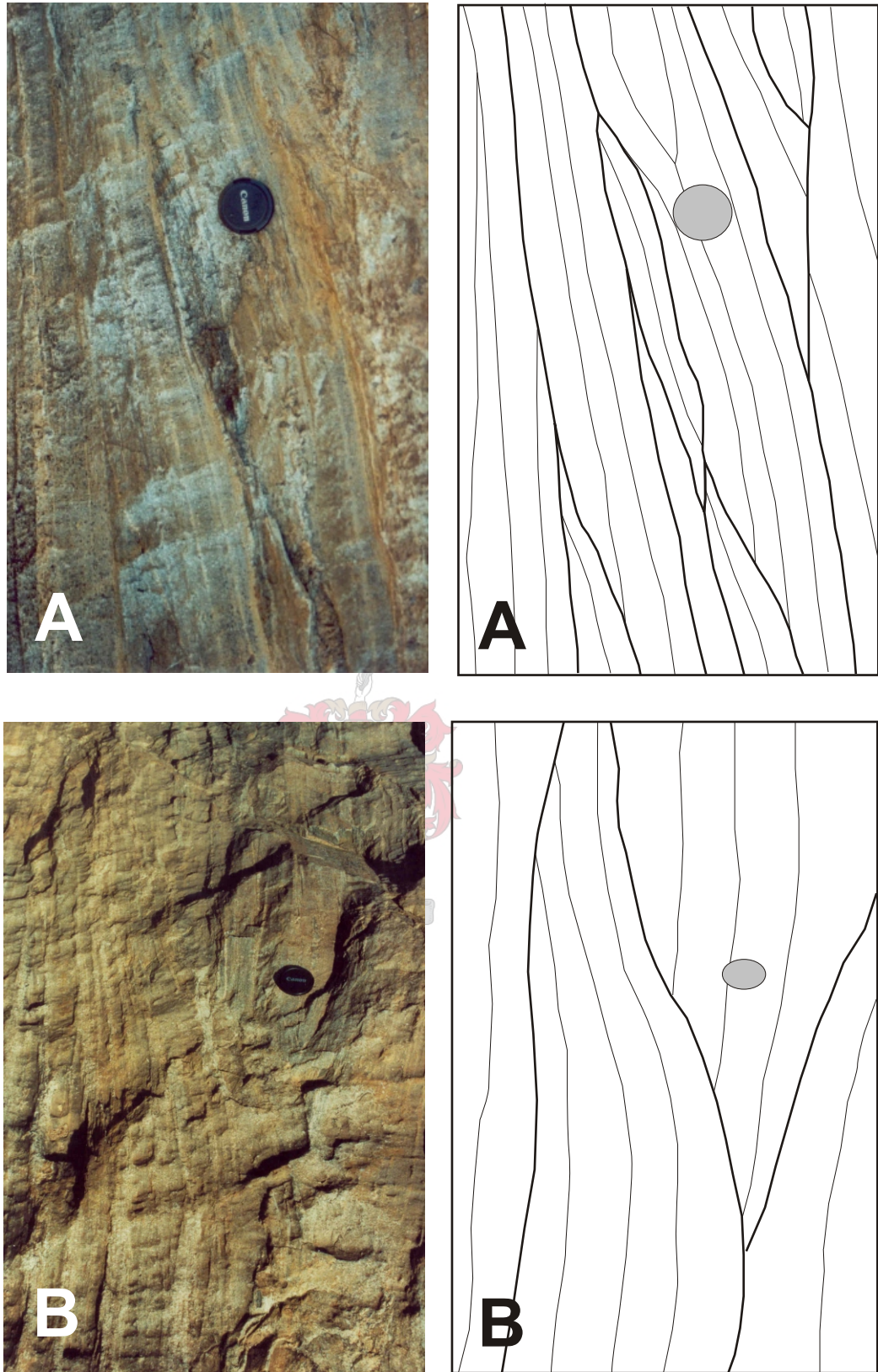


**Figure 4.3:** (a) and (b): Photographs and line drawings highlighting the tectonization of lithologies in the Theespruit Formation and the tectonic nature of contacts between different litho-tectonic units. Note the low angles at which the transposed compositional banding in different units is truncated against each other. Plan view, from locality Tj 18.

$S_0/S_1$  is an amphibolite- to greenschist-facies fabric that is defined by the alignment of metamorphic minerals in the different lithologies. In felsic schists, the fabric is defined by the preferred orientation of biotite, chlorite and muscovite, while kyanite, staurolite, plagioclase and quartz have a grain-shape preferred orientation parallel to the fabric. Deformed cobbles and clasts in agglomerate are orientated parallel to  $S_0/S_1$  (Fig. 4.4a). The grain-shape preferred orientation and alignment of hornblende, plagioclase and quartz characterizes  $S_0/S_1$  in amphibolite, while chlorite defines the fabric in chlorite schist. Associated with  $S_0/S_1$  is a pervasively developed mineral stretching lineation ( $L_1$ ).  $L_1$  is present in the  $S_1$  foliation planes (Fig. 4.4b, c and d) and usually has a subvertical down-dip orientation but also occurs as an intermediate- to steep southerly plunging lineation (Fig. 4.5).  $L_1$  is defined by rodded quartz in felsic schist and agglomerate, while metamorphic minerals such as kyanite and garnet in felsic schist and hornblende in amphibolite are strongly aligned parallel to  $L_1$  (Fig. 4.4d). The fold axes of  $F_1$  folds are aligned and orientated parallel to  $L_1$ . In most cases,  $L_1$  is the strongest fabric element developed in these mylonites, but fabric development is heterogeneous and varies from being a planar ( $S > L$ ) fabric to an almost pure linear ( $L \gg S$ ) fabric (refer to section 4.4).

$S_0/S_1$  is usually orientated parallel to the margins of the Stolzberg and Theespruit Plutons and appears to be concordant with the pluton margins (Figs. 4.2 and 4.5). In the western part of the Tjakastad Schist Belt,  $S_0/S_1$  has a north-south orientation that deflects to the west around the Stolzberg Pluton to join the east-west trending fabric in the Stolzberg Schist Belt (De Wit et al., 1983; Kisters et al., 2003). The fabrics in the Stolzberg Schist Belt are continuous to the east and can be traced to the north and east of the Theespruit Pluton, where these fabrics are concordant with the margins of the Theespruit Pluton. The area to the immediate northwest of the Theespruit Pluton does not exhibit a well-developed fabric and the rocks in this area are characterized by a relatively weak, though heterogeneously developed subvertical linear fabric. As a result, the north-south trend of  $S_0/S_1$  in the Tjakastad Schist Belt cannot be continuously traced to the east-west trend of this fabric to the north of the Theespruit Pluton (Fig. 4.2).



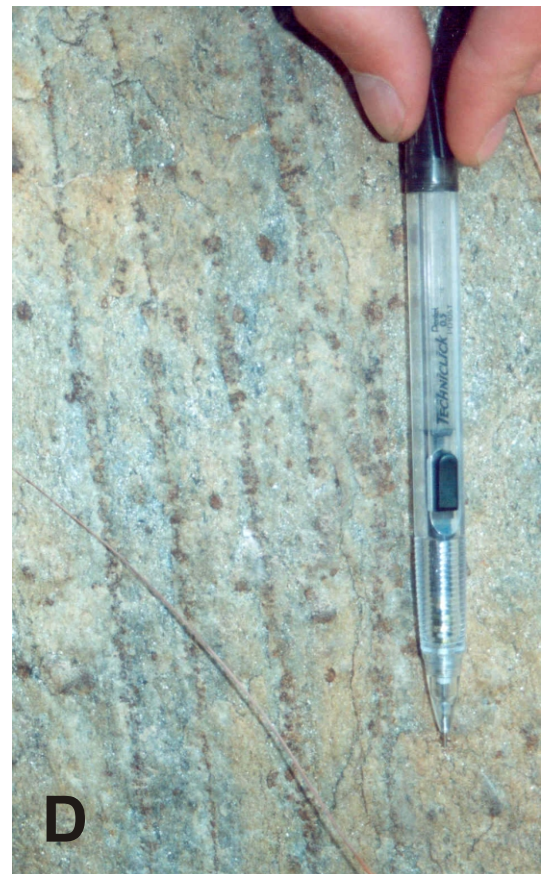


**Figure 4.4:** Photographs illustrating fabric development in the lithologies of the Theespruit Formation. **(a):** Plan view of flattened clasts in felsic agglomerate that are aligned parallel to  $S_0/S_1$ . From the central parts of the Tjakastad Schist Belt. **(b)** and **(c):** Profile view onto the foliation plane of typical felsic schist showing the development of pervasive steep- to subvertically plunging quartz rodding fabrics ( $L_1$ ). **(d):** Profile view onto the foliation plane of garnet-bearing felsic schist where garnet grains define a subvertical lineation parallel to the quartz rodding fabric ( $L_1$ ).

The eastern part of the Tjakastad Schist Belt occurs as a large embayment within the Theespruit Pluton. The lithologies in this area define a large-scale, isoclinal  $F_1$  fold that closes to the southwest. Both limbs of the fold are truncated by the Theespruit Pluton and the fold displays an axial planar fabric that is indistinguishable from  $S_1$ . In this area,  $S_1$  trends north-northeast and appears to be truncated by the Theespruit Pluton (Fig. 4.2).

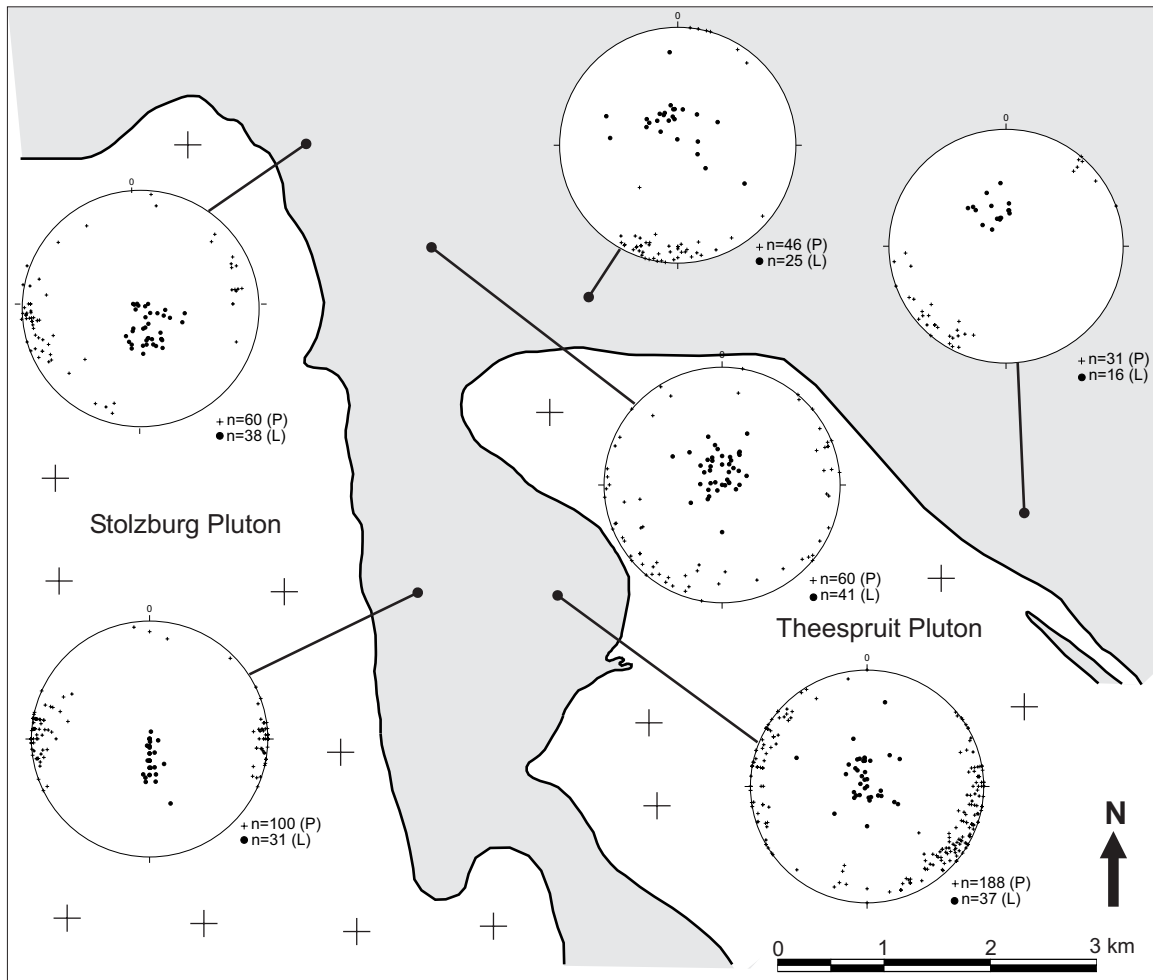


**Figure 4.5:** Equal-area lower-hemisphere stereographic projections of poles to foliations ( $S_1$ ; crosses) and lineations ( $L_1$ ; solid dots) in the Theespruit Formation.



### 4.3 Fabric development in the granitoids

Early workers described characteristic concentric foliation patterns in most of the granitoids and gneisses that surround and intrude the Barberton Greenstone Belt (Viljoen and Viljoen, 1969a; Anhaeusser et al., 1981; Robb and Anhaeusser, 1983). An investigation of the Stolzberg and Theespruit Plutons could not confirm the occurrence of these foliation patterns, but revealed that these plutons contain a persistent, although heterogeneously developed, steeply plunging mineral rodding fabric. This fabric is similar to that identified by Kisters et al. (2003) in the northern parts of the Stolzberg Pluton and is defined by rodded quartz and quartz-plagioclase aggregates that plunge at steep- to subvertical angles to the east (Fig. 4.6). Unlike in the Stolzberg Schist Belt (Kisters et al., 2003), the margins of the Stolzberg and Theespruit Plutons do not show the development of a pervasive, strongly gneissose fabric. A gneissose fabric is, however, present along the western margin of the Stolzberg Pluton and along the northeastern margin of the Theespruit Pluton (De Wit et al., 1983; Kisters and Anhaeusser, 1995b). The fabric appears within 50 m of the granite-greenstone interface and is orientated parallel to the pluton margins. Although this fabric appears to be gneissose in plan view, it is still a strongly prolate fabric that is orientated parallel to the pervasive rodding fabric recorded in the bulk of the plutons.



**Figure 4.6:** Photograph of the typical subvertical rodding fabric that is heterogeneously developed in the Stolzberg and Theespruit Plutons. Note that the fabric is hardly recognizable in plan view and that it is only visible and well-developed in profile sections.



## 4.4 Strain

The deformation that affected the Theespruit Formation resulted in the development of a heterogeneous, complex strain record that is contained in these lithologies. In an attempt to document the strain manifested in these rocks, strain markers such as pillows and ocelli in mafic and ultramafic rocks as well as clasts in agglomerate horizons were measured wherever possible. Like most strain markers, ocelli and agglomerate clasts only provide a rough estimate of the finite strain experienced by the rocks as the effects of strain partitioning cannot be accounted for. Strain partitioning is caused by competency contrasts between different lithologies – such as between felsic schist and amphibolite – and can also occur within a single rock unit and even between clasts and the host matrix.

In cases where quantitative strain markers are absent, a qualitative estimate of strain was made from the weathering pattern of outcrops as well as the development and intensity of planar and linear fabric elements. All quantitative finite strain measurements are presented on a Flinn diagram (Fig. 4.7; Flinn, 1962), which allows the distinction of three broad strain regimes that are present in the rocks of the Tjakastad Schist Belt and the surrounding areas. The location and extent of these regimes is presented Figure 4.8 and the characteristics of each regime are discussed below.

### *4.4.1 Low-strain amphibolite*

The first strain regime is found in amphibolite-facies rocks close to the margins of the Stolzburg and Theespruit Plutons (Fig. 4.8). These rocks are only slightly deformed and ocelli in these rocks have aspect ratios that vary from 3:1:1 (weakly prolate) to 3:3:2 (weakly oblate), with an average of ca. 8:4:3. A similar strain regime is found in the rocks of the Sandspruit Formation in the extreme south of the Tjakastad Schist Belt. Amphibolite in this area contains easily recognizable pillows that are slightly flattened and have aspect ratios of 5:3:1 to 3:3:1 (Fig. 4.9a).

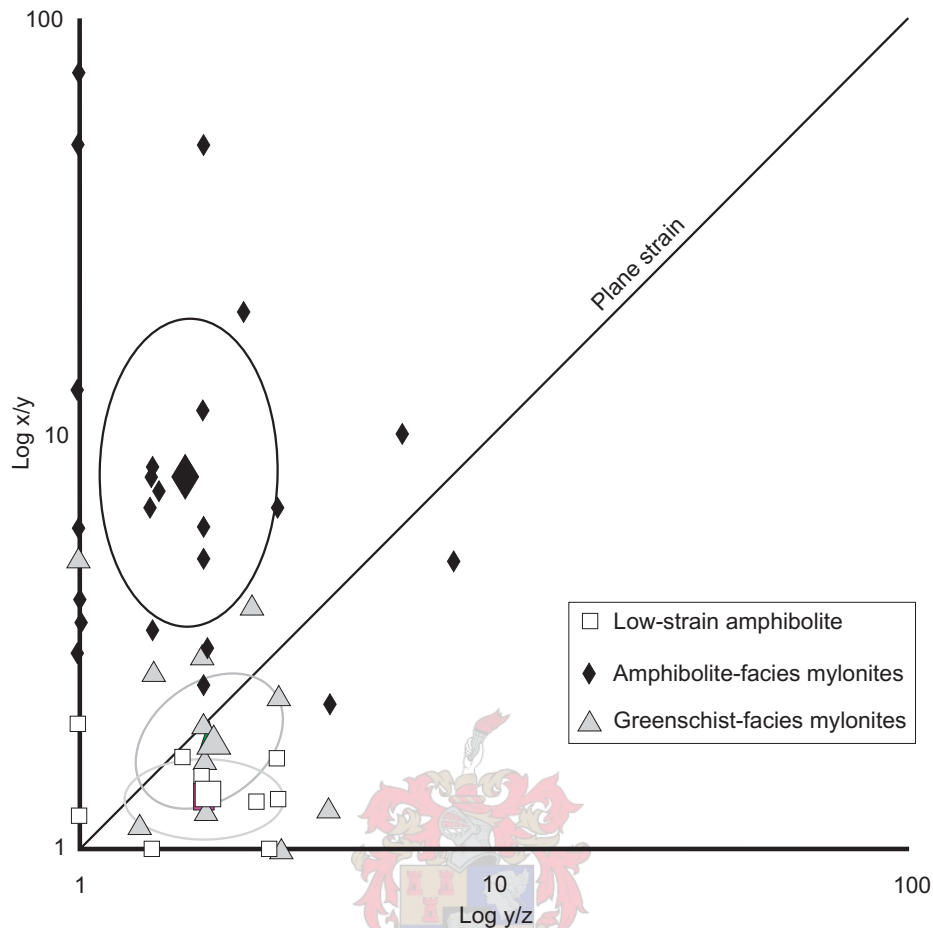


**Figure 4.7:** Flinn diagram (Flinn, 1962) illustrating the distinction of three strain regimes in the Theespruit Formation. Each datapoint represents at least four measurements of strain markers in a single outcrop. Large symbols indicate the average of values in each strain regime and ellipses define the extent of the most common recurring values for each regime.

#### 4.4.2 Amphibolite-facies mylonites

The second strain regime is characterized by highly deformed, strongly prolate amphibolite-facies- and retrograde amphibolite mylonites. Retrograde amphibolites are included in this strain regime because they exhibit the same style and intensity of strain as amphibolite-facies mylonites. Rocks of this strain domain occur in the western half of the Tjakastad Schist Belt as well as to the north and east of the Stolzburg and Theespruit Plutons. Away from the plutons, the contact between the low-strain amphibolites of the first regime and the strongly deformed amphibolites of this domain is abrupt and occurs

within 50 – 500 m from the pluton margins (Fig 4.8). Northeast of the Theespruit Pluton, this abrupt transition corresponds to the Komati Schist Zone (Williams and Furnell, 1979; De Wit et al., 1983; Dann, 2000).

Strain markers in mylonites of this regime have aspect ratios that vary from weakly oblate (9:4:1) to highly prolate (100+:2:1), with an average intensity of ca. 25:3:2 (Fig. 4.7). In the Tjakastad Schist Belt, the strain varies from slightly prolate (5:3:1) along the

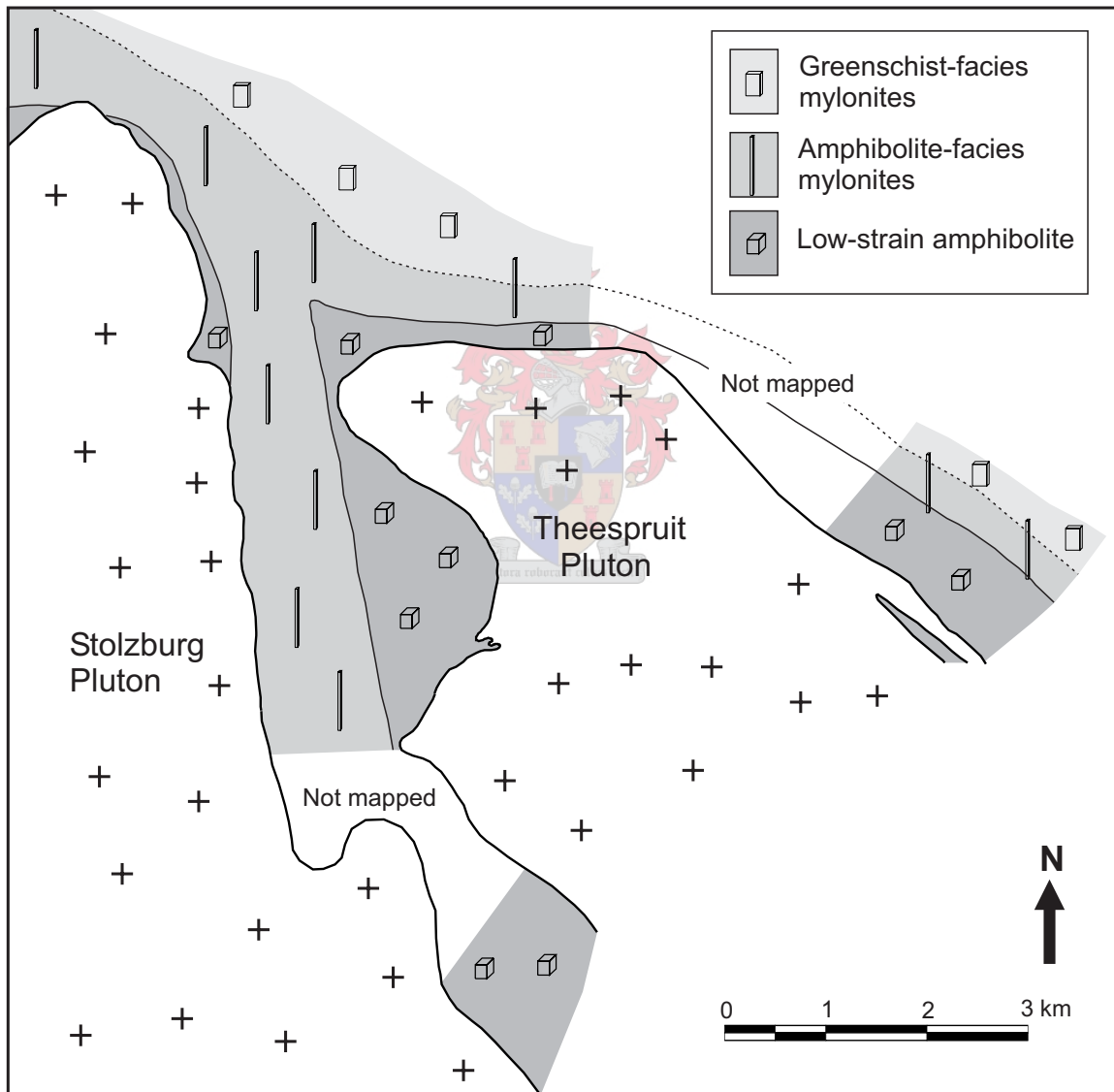


**Figure 4.8:** Map indicating the location and extent of the different strain regimes distinguished in the Theespruit Formation.

margins of the Stolzburg Pluton and becomes strongly prolate and more intense (ca. 50+:1:1) towards the central parts of the belt (Fig. 4.9b). The amphibolite-facies mylonites in the Komati Schist Zone have similar aspect ratios and intensities as in the central parts of the Tjakastad Schist Belt. The strongly prolate fabrics that are present in these mylonites indicate that deformation of these rocks occurred in a constrictional tectonic regime.

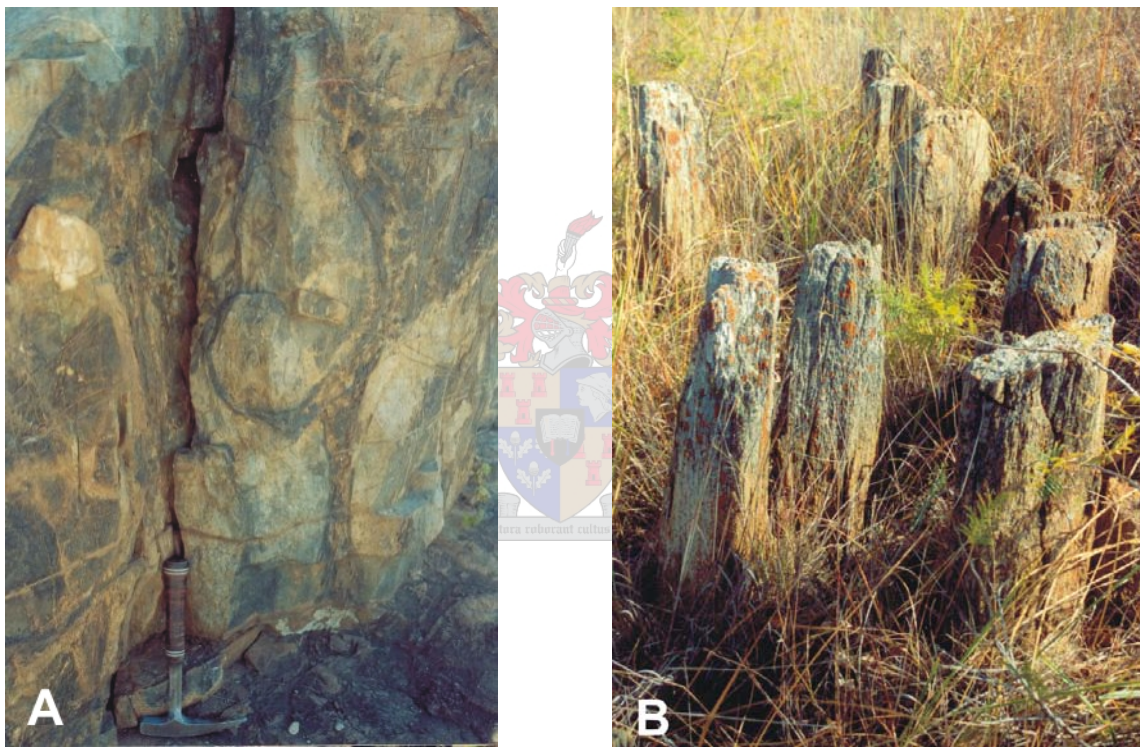


**Figure 4.9:** (a): Vertical outcrop of amphibolite belonging to the ‘low-strain amphibolite’ strain regime, displaying weakly deformed pillow structures. (b): Photograph of severely rodded felsic schist that is typical of rocks belonging to the ‘amphibolite-facies mylonite’ strain regime.

#### 4.4.3 Greenschist-facies mylonites

The prolate amphibolite- and retrograde amphibolite-facies mylonites of the Komati Schist Zone grade into, and are overprinted by, greenschist-facies mylonites away from the plutons and towards the central parts of the Barberton Greenstone Belt. Strain markers in these mylonites indicate prolate (5:1:1) to oblate (5:4:1) strain, but are generally close to plane strain with an average of ca. 4:2:1 (Fig. 4.7).

The relationship between all three strain domains is demonstrated at locality 61602 to the north of the Theespruit Pluton. A detailed description of this locality is presented in section 4.6.

#### 4.5 Kinematics

Kinematic indicators such as S-C and S-C' fabrics (Berthé et al., 1979; Simpson and Schmid, 1983) and winged porphyroclasts ( $\sigma$ - and  $\delta$ -clasts, after Simpson and Schmid, 1983) can be used to infer the sense of movement that occurred during shearing. These fabrics are particularly useful in highly tectonized areas and in the absence of a well-developed stratigraphy because they allow the determination of a relative displacement direction without utilizing stratigraphic features such as displaced marker horizons.

Outcrop-scale kinematic indicators are fairly rare in the strongly prolate mylonites that characterize the bulk of the study area. However, thin sections orientated in the sense-of-shear plane (perpendicular to the foliation and parallel to the lineation) do reveal the presence of microscale shear sense indicators in both amphibolite and felsic schists (Fig. 4.10a). S-C' fabric relationships (also termed extensional crenulation cleavage) are the predominant shear fabric encountered in all rock types and these fabrics are generally only exhibited by finer-grained and highly schistose samples of felsic schist and amphibolite.  $\sigma$ -objects such as deformed plagioclase clasts and staurolite porphyroblasts in felsic schist (Fig. 4.10b and c) as well as garnet porphyroblasts in amphibolite (Fig. 4.10d), are present in certain sections.



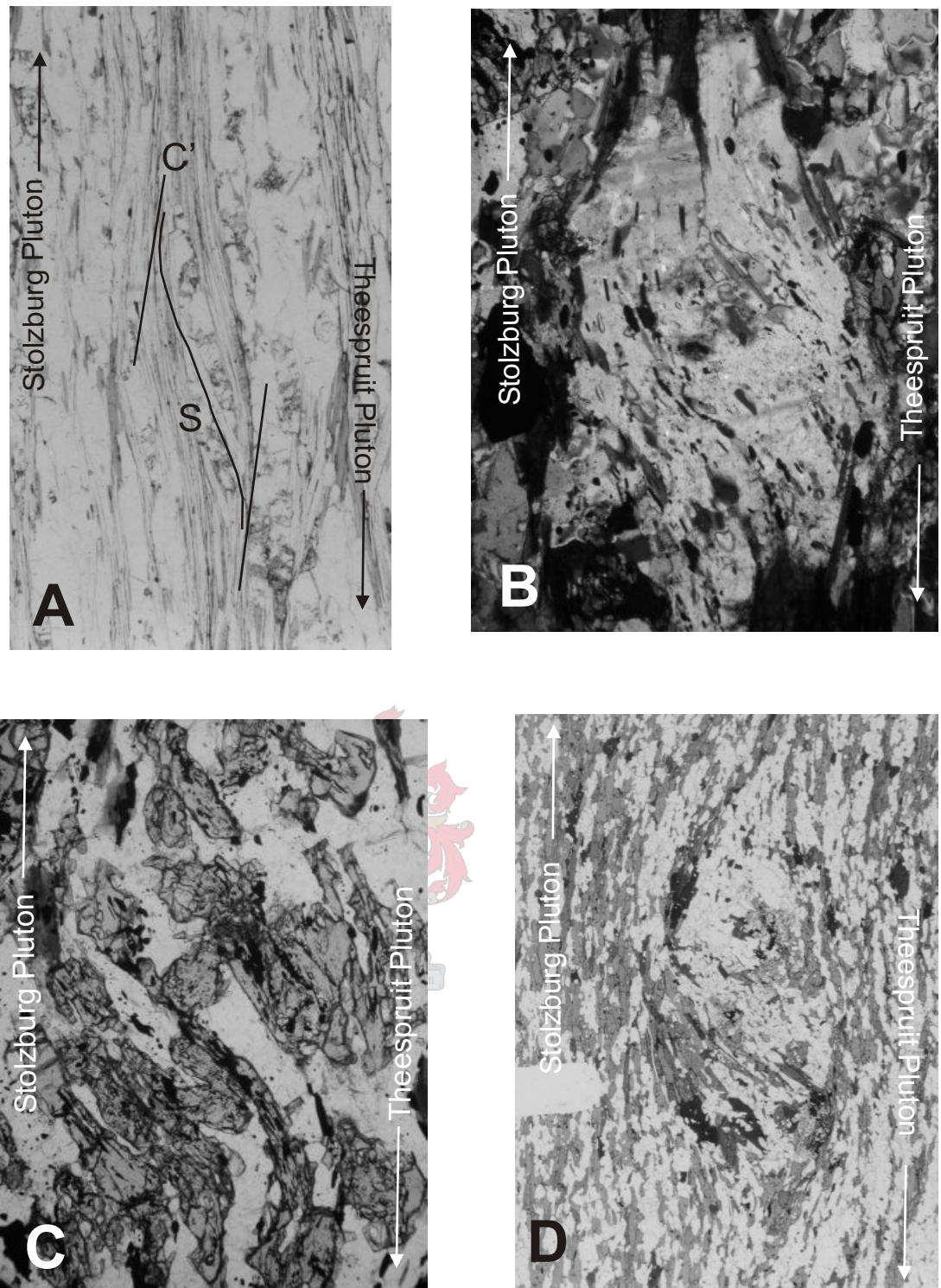


**Figure 4.10: (a-d):** Photographs of the variety of shear sense indicators encountered in the lithologies of the Theespruit Formation. **(a):** Photomicrograph of S-C' fabric defined by muscovite in felsic schist from locality Tj 23. Orientated section looking north; field of view is 5 mm across; plane-polarized light. **(b):** Photomicrograph of plagioclase object in sample 62601D. Orientated section looking north; field of view is 1.5 mm across; crossed nicols. **(c):** Photomicrograph of staurolite object from sample 61601D. Orientated section looking north; field of view is 1.5 mm across; plane-polarized light. **(d):** Photomicrograph of garnet-plagioclase aggregate (object) in amphibolite from locality Tj 3. Orientated section looking north; field of view is 10 mm across; plane-polarized light.

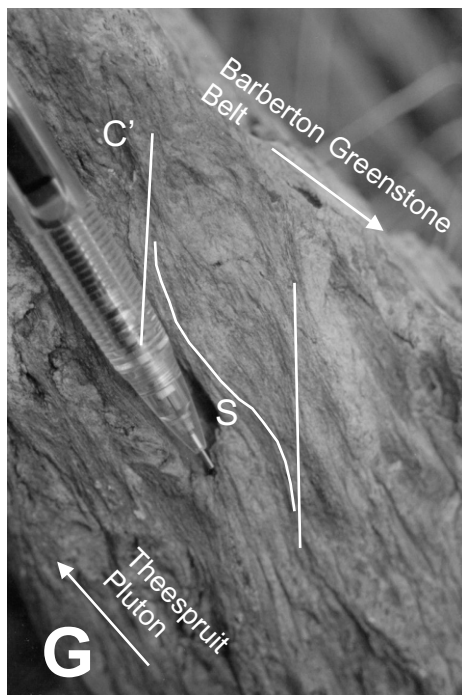
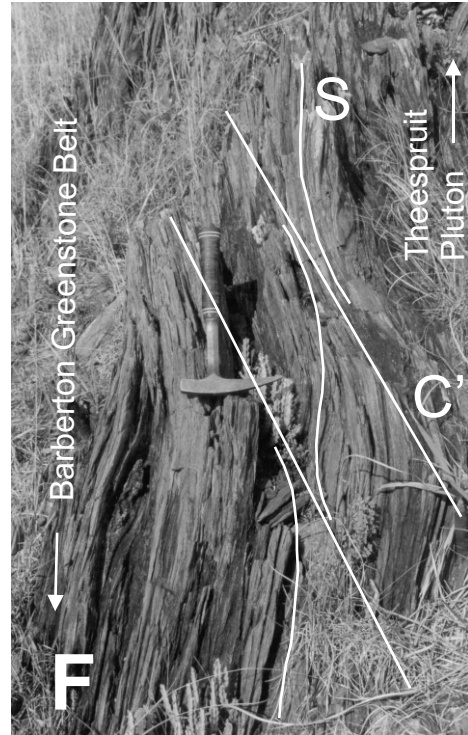
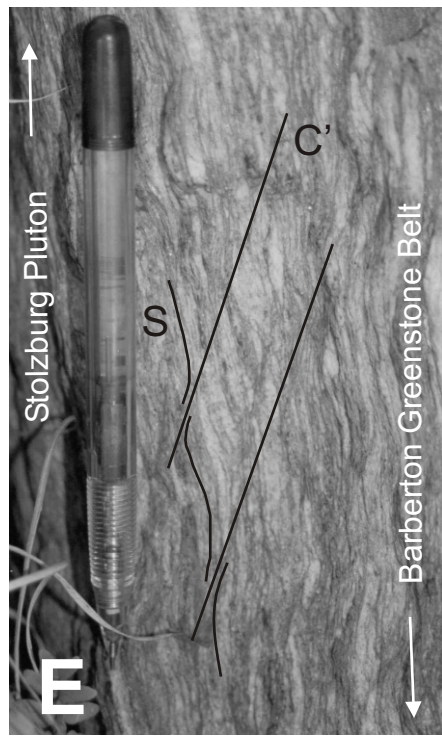


**Figure 4.10: (e-h):** continued. **(e):** Photograph of an S-C' fabric defined by agglomerate clasts in agglomerate from locality 6504. Photograph is orientated vertically and looks north, with the Stolzberg Pluton to the left and the Barberton Greenstone Belt to the right. **(f):** Photograph of S-C' fabric in chlorite schist from locality 62015. Photograph is orientated vertically and looks south-east, with the Theespruit Pluton to the right and the Barberton Greenstone Belt to the left. **(g):** Photograph of S-C' fabric defined by chlorite-muscovite in felsic schist from locality 61602. Photograph is orientated vertically and looks west, with the Theespruit Pluton to the left and the greenstone belt to the right. **(h):** Photograph of S-C' fabric defined by chlorite in silicified chlorite schist from locality 61602. Photograph has a vertical orientation and looks to the west, with the Theespruit Pluton to the left and the greenstone belt to the right.



Outcrop-scale shear fabrics have been observed in samples of agglomerate and felsic schist as well as chlorite schist (Fig. 4.10e, f and g) and these indicators consist exclusively of S-C' fabric relationships. Table 4.1 presents the GPS co-ordinates of localities that display shear fabrics that are visible in outcrop or hand sample.

In the Tjakastad Schist Belt, shear sense indicators consistently point to a Stolzberg Pluton-up – Theespruit Pluton-down sense of displacement. This displacement vector is associated with a slight dextral (Stolzberg Pluton-to-the-north – Theespruit Pluton-to-the-south) strike-slip component. The steep- to subvertical southerly plunging orientation of the L<sub>1</sub> lineation correlates with this inferred sense of movement.

The area to the northeast of the Stolzberg Pluton is almost completely devoid of kinematic indicators and only a single agglomerate horizon displays well-developed S-C' fabrics. These fabrics indicate a Stolzberg Pluton-up – greenstone belt-down sense of movement with an associated dextral strike-slip component.

**Table 4.1:** Location of localities where shear fabrics are visible in outcrop or hand sample. The table presents the type of shear fabric present as well as the sense of movement indicated by the fabric. 'Normal' indicates a granite-up – greenstone-down sense of displacement, while 'Reverse' indicates an opposite greenstone-up – granite-down sense of displacement. Mineral abbreviations are after Kretz (1983).

Locality	Latitude	Longitude	Rock type	Fabric type	Defining minerals	Sense of movement	Figure
Tj 3	26°00'27.4"S	30°46'36.2"E	amphibolite	σ clasts	grt-pl	normal	5.4d
Tj 13	25°59'30.4"S	30°46'40.4"E	micaceous felsic schist	S-C'	ms-bt	normal	
Tj 23	26°00'33.7"S	30°46'33.0"E	micaceous felsic schist	S-C'	ms-bt	normal	5.4a
6504	25°58'35.9"S	30°46'24.3"E	agglomerate	S-C'	qtz clasts	normal	5.4e
6613	25°58'13.6"S	30°46'15.6"E	agglomerate	S-C'	qtz clasts	normal	
61602	25°58'39.0"S	30°46'24.3"E	felsic schist	S-C'	chl-ms	both	5.4g
61602	25°58'39.0"S	30°46'24.3"E	talc-carbonate schist	S-C'	chl-tlc	normal	
61602	25°58'39.0"S	30°46'24.3"E	retrograde amphibolite	S-C'	chl	normal	
61602	25°58'39.0"S	30°46'24.3"E	silicified chlorite schist	S-C'	chl	reverse	5.4h
61706	25°59'41.3"S	30°50'18.7"E	serpentinite	S-C'	chl-srp-sd	normal	
61913	25°59'35.0"S	30°50'03.8"E	chlorite schist	S-C'	chl	normal	
62015	26°00'06.6"S	30°50'55.2"E	chlorite schist	S-C'	chl	normal	5.4f
62105	26°00'50.3"S	30°47'02.3"E	kyanite felsic schist	S-C'	bt	normal	
62105	26°00'50.3"S	30°47'02.3"E	garnet-staurolite schist	S-C'	bt	normal	
n/a	25°59'16.1"S	30°46'36.3"E	micaceous felsic schist	S-C'	ms	normal	

To the north and east of the Theespruit Pluton, the felsic, chloritic and ultramafic schists in the Komati Schist Zone display intermittently developed S-C' fabrics that predominantly point to a Theespruit Pluton-up – greenstone belt-down sense of displacement (Fig. 4.10f and g). However, these schists also occasionally contain fabrics that indicate an opposite greenstone-up – granite-down sense of movement (Fig. 4.10h). Both senses of shear are present in some outcrops and locality 61602 to the north of the Theespruit Pluton illustrates the relationship of these two fabric types.

#### 4.6 Locality 61602

Locality 61602 is about 100 m north of the margin of the Theespruit Pluton. The lithology between this locality and the pluton margin consists of massive, relatively undeformed amphibolite. At this locality there is an abrupt increase in the intensity of deformation that corresponds with the transition from massive, low-strain amphibolite to highly sheared retrograde amphibolite. The retrograde amphibolite consists of highly sericitized plagioclase, fine-grained quartz, epidote, chlorite and calcite. No hornblende is found in these samples but the rocks exhibit a coarse-grained, sheared amphibolite texture and contain pods of massive low-strain, pristine amphibolite (Fig. 4.11). In addition to pods of fresh amphibolite, the retrograde amphibolite zone also contains intercalated, highly sheared lenses of felsic schist, chlorite schist as well as dolomitized talc-carbonate schist and serpentinite. All of the lenses, pods and intercalated units are truncated and tectonically imbricated against each other at low angles. Prominent chert horizons are also associated with this shear zone on a regional scale. Away from the pluton, the retrograde amphibolite grades into a zone of chlorite schist. This transition is marked by the gradual disappearance of amphibolite textures and a simultaneous increase in the chlorite content as well as the schistosity exhibited by the lithologies. The foliation in these rocks trends east-west and is subvertical, while lineations plunge to the northwest at steep angles (Fig. 4.11).

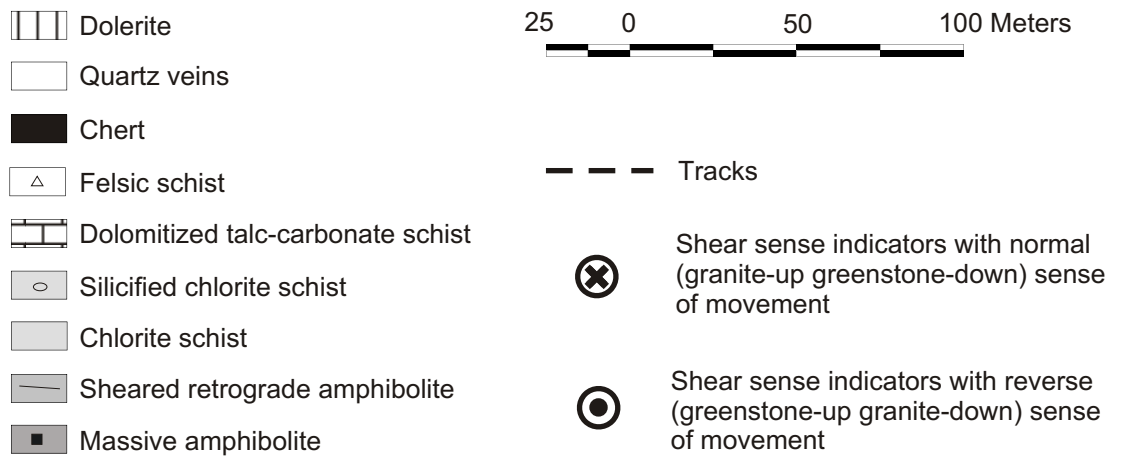
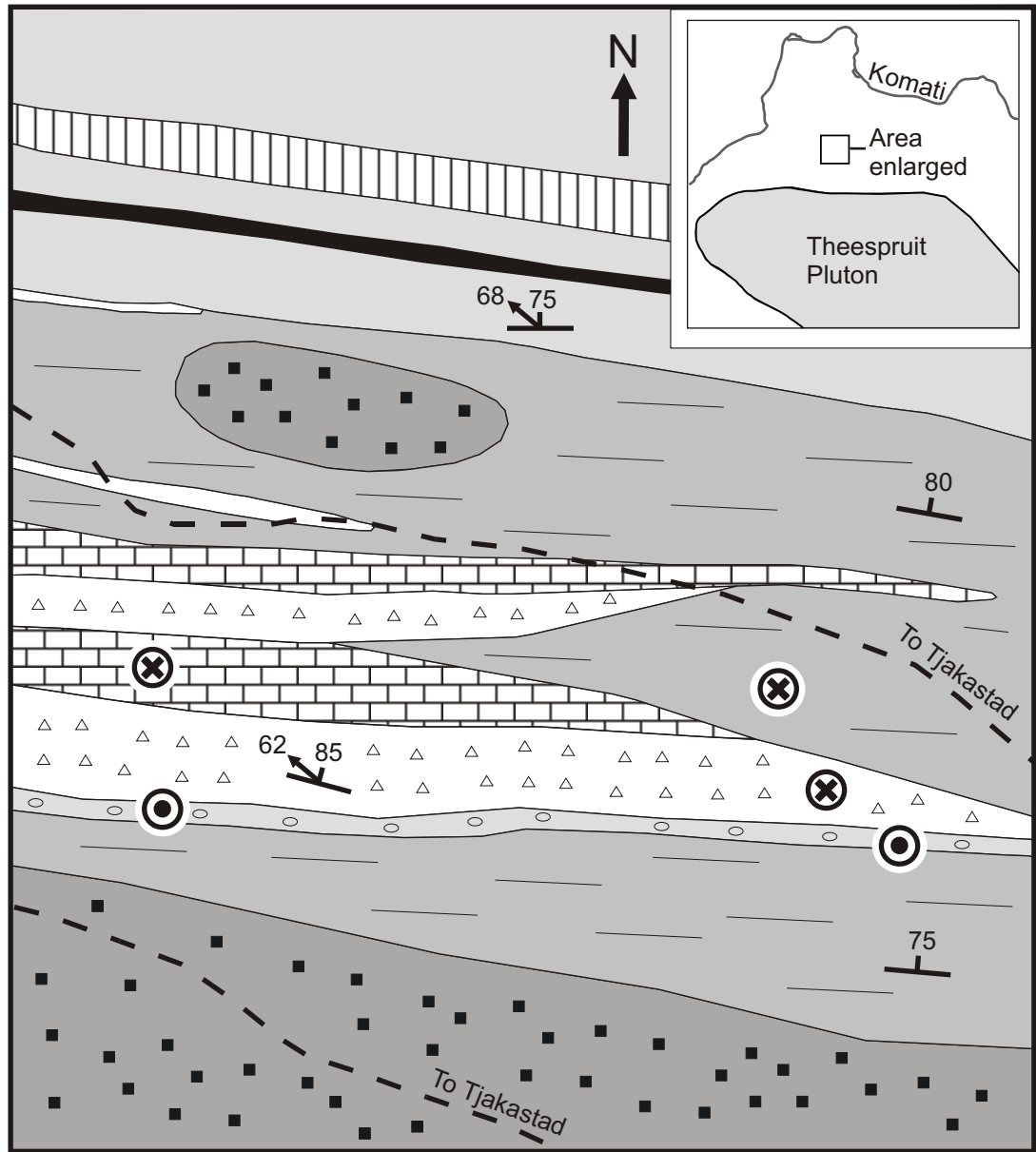


**Figure 4.11:** Sketch map of locality 61602 showing the lithologies and kinematic indicators present at this locality. Note the very discontinuous strike extent of most lithological units and the manner in which units are truncated against each other. Also note the presence of relic amphibolite pods preserved in retrograde amphibolite.

Kinematic indicators from retrograde amphibolite, felsic schist and dolomitized serpentinite indicate a normal (granite-up – greenstone-down) sense of displacement. Shear fabrics that indicate a reverse (greenstone-up – granite-down) sense of movement are found in felsic schist and a prominent silicified chlorite schist horizon that is located close to the base of the shear zone. This thin horizon exhibits well-developed S-C' fabrics that consistently point to a reverse sense of displacement (Fig. 4.10h).

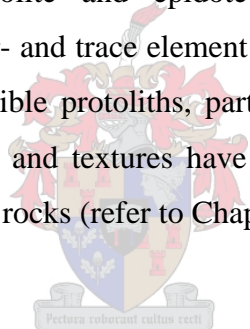
No clear chronology of events could be established in localities where shear fabrics indicate both senses of shear. However, it is significant to note that the fabrics indicating a normal (granite-up – greenstone-down) sense of movement are present in amphibolite-, retrograde amphibolite- and greenschist-facies lithologies, while the fabrics that indicate a reverse sense of movement are only present in greenschist-facies lithologies.

An investigation of the Komati Fault type locality (Viljoen and Viljoen, 1969b; De Wit, et al., 1983) revealed that this fault displays pervasive brittle fabrics that contrast with the ductile and ductile-brittle fabrics found in the Tjakastad Schist Belt and the Stolzburg Schist Belt (Kisters et al., 2003). These brittle fabrics contain kinematic indicators but are not conclusive as fabrics that point to a normal sense of movement as well as fabrics that suggest a reverse sense of movement are encountered.

## **CHAPTER 5: WHOLE-ROCK GEOCHEMISTRY**

### 5.1 Introduction

Samples targeted for detailed metamorphic study were analyzed to establish their bulk-rock composition, as the mineral paragenesis in metamorphic rocks is a function of pressure and temperature as well as the bulk composition. Specifically, the differences in bulk-rock chemistry between the quartz-sericite schists and more unique garnet-, staurolite- or kyanite-bearing samples were investigated. All of these rocks have previously been categorized as felsic metavolcanics (e.g. Viljoen and Viljoen, 1969b) but the different mineral parageneses exhibited by these two suites is likely related to bulk-rock chemical differences. The whole-rock chemical differences between garnet-bearing amphibolite, garnet-free amphibolite and epidote-amphibolite samples were also investigated. The bulk-rock major- and trace element composition of these metamorphic rocks might help to identify possible protoliths, particularly as almost all evidence of igneous or sedimentary structures and textures have been obliterated by the pervasive tectonic fabrics developed in these rocks (refer to Chapter 4).



### 5.2 Analytical procedures

#### *5.2.1 Major- and trace elements*

Samples were crushed with a sledgehammer and jaw crusher and milled in a Siebtechnik swing mill prior to the preparation of a fused disc for major element analysis and a pressed briquette for trace element analysis. X-ray fluorescence (XRF) analysis was performed on a Philips 1404 wavelength dispersive spectrometer located at the University of Stellenbosch. The instrument is fitted with a Rh tube and six analyzing channels and was operated at 50 kV and 50 mA for major element analysis and at 60 kV and 40 mA for trace element analysis. Sample matrix effects were corrected by applying theoretical alpha factors and measured line overlap factors to the raw intensities measured with SuperQ Philips software. Major- and trace element calibration was performed using



accepted international standards AGV-1, BHVO-1, JG-1, JB-1, GSP-1, SY-2, SY-3, STM-1, NIM-G, NIM-S, NIM-N, NIM-P, NIM-D, BCR, GA, GH, DRN and BR. A comparison of the measured and actual chemical composition of whole-rock standards that were analyzed as unknowns is presented in Appendix 2.1 and serves as a reflection of the absolute error associated with the whole-rock chemical compositions determined by XRF during this study.

### 5.2.2 Rare earth elements

Whole-rock rare earth element (REE) analysis was performed by laser ablation – inductively coupled plasma – mass spectrometry (LA-ICP-MS) at the University of Cape Town. Analysis was performed on fused beads that were prepared using a clean, REE free flux. Beads were mounted in epoxy and polished to ensure a smooth, flat surface suitable for analysis. The instrument used was a Cetac LSX-200 laser probe that utilizes a frequency-quadrupled Nd-YAG laser (266 nm wavelength), coupled to a Perkin Elmer / Sciex Elan 6000 ICP-MS. A stationary spot size of 200  $\mu\text{m}$  and pulse rate of 5 Hz was used during analysis. Si values (determined by XRF analysis) were used as the internal standard and the instrument was calibrated using NIST SRM 610 and NIST SRM 612 glass standards (Pearce et al., 1996).

### 5.3 Felsic schist

Most of the felsic schist samples investigated have essentially the same mineralogy and consist of quartz, muscovite, plagioclase and chlorite in variable proportions (refer to Chapter 3). Five samples that are representative of the variety of textures and grain sizes exhibited by these rocks were selected for analysis. This group consists of samples Tj 1, Tj 8, Tj 23, 61402 and 62105D and is hereafter collectively referred to as ‘mineralogically simple’ felsic schists. Felsic schists with characteristic metamorphic mineral assemblages include two garnetiferous schists (61303 and Tj 21), a kyanite-bearing sample (62105G), two staurolite-garnet-biotite schists (Tj 18 and 62105F) and one staurolite-kyanite-biotite schist (62601D). The staurolite-bearing schists (Tj 18,

62105F and 62601D) are collectively referred to as ‘mineralogically complex’ felsic schists because of their characteristic mineral assemblages. The major-, trace- and rare earth element composition of the felsic schists investigated is presented in Table 5.1.

**Table 5.1:** Whole-rock major-, trace- and rare earth element composition of felsic rocks investigated.

Sample Type	Tj 1 aggl	Tj 8 qtz-ser schist	Tj 23 mica schist	61402 qtz-ser schist	62105D chl-ms schist	61303 grt felsic schist	Tj 21 grt-chl schist	62105G ky-qtz schist	62105F grt-stau schist	Tj 18 grt-stau schist	62601D ky-stau schist
<b>SiO<sub>2</sub></b>	75.77	74.57	69.49	74.10	75.12	81.01	61.18	75.58	65.11	65.42	68.68
<b>TiO<sub>2</sub></b>	0.17	0.14	0.16	0.16	0.16	0.12	0.29	0.14	2.13	1.78	2.29
<b>Al<sub>2</sub>O<sub>3</sub></b>	13.14	12.93	16.11	12.95	13.62	9.10	17.13	13.77	15.04	13.05	16.80
<b>Fe<sub>2</sub>O<sub>3</sub></b>	1.80	1.82	2.15	1.25	2.30	3.70	6.34	1.89	8.14	8.24	5.69
<b>MnO</b>	0.04	0.04	0.06	0.04	0.04	0.05	0.14	0.04	0.21	0.28	0.08
<b>MgO</b>	2.40	3.92	3.28	3.89	2.47	1.18	5.95	3.49	4.15	4.29	3.02
<b>CaO</b>	0.13	0.01	0.51	0.02	0.10	0.03	1.56	0.30	1.01	1.42	0.63
<b>Na<sub>2</sub>O</b>	1.49	0.90	1.89	1.18	1.41	0.97	2.41	0.92	1.40	1.15	1.16
<b>K<sub>2</sub>O</b>	1.94	1.45	1.93	3.51	2.72	2.24	1.67	1.87	1.33	0.76	1.38
<b>P<sub>2</sub>O<sub>5</sub></b>	0.03	0.01	0.04	0.04	0.02	0.03	0.06	0.04	0.06	0.04	0.03
<b>LOI%</b>	1.71	1.90	2.22	1.27	1.23	1.14	2.09	1.28	1.19	1.84	1.10
<b>Total</b>	98.80	98.74	98.00	98.44	99.21	99.57	98.99	99.33	99.89	98.51	100.97
<b>Mg#<sup>a</sup></b>	73	81	75	86	68	39	65	79	50	51	51
<b>Ba</b>	1009	1259	613	654	702	169	613	215	19	61	33
<b>Rb</b>	101	129	150	111	82	51	150	65	53	54	47
<b>Sr</b>	44	72	76	66	70	39	76	89	115	108	108
<b>Y</b>	23	15	33	12	31	9	33	26	22	16	24
<b>Zr</b>	176	163	207	125	154	66	207	128	70	90	83
<b>Nb</b>	23	17	31	22	26	16	31	22	15	15	19
<b>V</b>	0	6	3	15	17	14	3	16	274	360	244
<b>Cr</b>	15	14	15	14	17	15	15	18	629	539	589
<b>Ni</b>	125	14	16	14	12	16	16	20	179	184	140
<b>Cu</b>	18	15	23	14	20	25	23	15	63	64	46
<b>Zn</b>	33	45	39	21	20	24	39	46	36	212	21
<b>Co</b>	4	4	5	3	5	8	5	4	21	21	13
<b>La</b>	64.16	38.70	100.95	18.42	43.87				12.90	8.61	16.73
<b>Ce</b>	75.43	53.81	124.85	36.04	81.85				27.30	14.16	37.60
<b>Pr</b>	8.70	5.19	15.00	2.75	7.47				4.05	2.36	5.51
<b>Nd</b>	27.44	18.18	49.52	8.70	25.93				19.74	11.09	26.09
<b>Sm</b>	3.50	3.43	7.58	1.32	4.66				5.18	2.80	6.34
<b>Eu</b>	0.08	0.08	0.84	0.02	0.75				1.72	1.19	2.17
<b>Gd</b>	3.78	5.59	5.31	1.03	4.23				4.82	2.64	5.79
<b>Tb</b>	0.97	1.08	0.85	0.27	0.72				0.80	0.56	1.02
<b>Dy</b>	4.04	4.17	4.71	1.11	4.20				4.38	3.48	5.73
<b>Ho</b>	1.23	0.60	0.90	0.25	0.86				0.85	0.79	1.18
<b>Er</b>	3.11	1.61	2.66	0.65	2.78				2.06	2.08	2.70
<b>Tm</b>	0.27	0.14	0.37	0.11	0.40				0.32	0.37	0.46
<b>Yb</b>	5.25	1.71	3.14	0.70	2.85				2.02	2.53	2.21
<b>Lu</b>	0.94	0.80	0.47	0.19	0.43				0.31	0.44	0.33

<sup>a</sup> Mg # calculated as 100 x Mg/(Mg+Fe)

### 5.3.1 Major elements

Mineralogically simple felsic schist samples have a relatively constant major element composition and record values of 69.49 – 75.77 % SiO<sub>2</sub>, 12.93 – 16.11 % Al<sub>2</sub>O<sub>3</sub>, 1.25 – 2.30 % Fe<sub>2</sub>O<sub>3</sub>, 2.40 – 3.92 % MgO, 0.01 – 0.51 % CaO, 0.90 – 1.89 % Na<sub>2</sub>O and 1.45 – 3.51 % K<sub>2</sub>O (Table 7.1). Mineralogically complex felsic schist samples also have comparatively constant major element concentrations and record values of 65.11 – 68.68 % SiO<sub>2</sub>, 13.05 – 16.80 % Al<sub>2</sub>O<sub>3</sub>, 5.69 – 8.24 % Fe<sub>2</sub>O<sub>3</sub>, 3.02 – 4.29 % MgO, 0.63 – 1.42 % CaO, 1.15 – 1.40 % Na<sub>2</sub>O and 0.76 – 1.38 % K<sub>2</sub>O. The other three samples analyzed (61303, Tj 21 and 62105G) have more variable and erratic major element concentrations and are therefore excluded from the following discussion.

Although very few samples were analyzed, contrasts and systematic variations in the bulk-rock major chemical composition of mineralogically simple and mineralogically complex felsic schists can be identified (Table 5.2; Fig. 5.1) and include a significant enrichment in Ti, Fe, Mn and Ca in mineralogically complex felsic schists relative to mineralogically simple samples. These rocks also have higher concentrations of Al and Mg and are simultaneously depleted in Si, Na and K relative to mineralogically simple schists. Furthermore, the Mg-numbers of these schists are near to 50, which is significantly lower than mineralogically simple schists that have Mg-numbers of 68 to 86 (Table 5.1). The slightly higher Al concentration and considerably lower Mg-numbers as well as the more mafic character of the mineralogically complex samples are considered to be the most likely factors that favor the stabilization of minerals such as staurolite and garnet in these rocks.

### 5.3.2 Trace elements

The fundamentally different nature of the mineralogically simple and mineralogically complex felsic schists is further highlighted by the trace element compositions of these samples. Similar to the major element concentrations, mineralogically simple felsic schists have comparable concentrations of most trace elements. Mineralogically complex

samples also have relatively constant values for the concentration of most trace elements (Table 5.1). The concentrations of some of the ferromagnesian transition trace elements such as V, Cr, Ni, Cu and Co in mineralogically complex samples are similar to concentrations found in amphibolite and other mafic rocks (see below) and are considerably higher than values from mineralogically simple schists (Table 5.1). Mineralogically complex samples are further enriched in Sr, but are depleted in Rb, Y, Nb and Zr relative to mineralogically simple felsic schists. Mineralogically simple schists are highly enriched in Ba and these samples have Ba concentrations of up to 1259 ppm (Table 5.1).

### *5.3.3 Rare earth elements*

REE profiles of mineralogically simple and mineralogically complex felsic schists further emphasize the fundamental differences between these two suites. Very little variation exists between the different samples that constitute each suite, but stark contrasts are apparent between the two suites. Mineralogically simple samples have chondrite-normalized (Taylor and McLennan, 1985) REE profiles that exhibit an enrichment in light REEs, a pronounced negative Eu anomaly and flat, relatively undepleted heavy REE values. In contrast, mineralogically complex samples have extremely flat profiles for both light and heavy REEs and exhibit a slight positive Eu anomaly (Fig. 5.2a).

### *5.3.4 Possible protoliths*

De Wit et al. (1987) proposed that the felsic rocks present in the Theespruit and Hooggenoeg Formations of the Onverwacht Group are shallow-crustal and extrusive equivalents of the TTG plutons that intrude and surround the Barberton Greenstone Belt. These workers showed that the Hooggenoeg Formation consists of intrusive and extrusive rocks with tonalitic and trondhjemitic affinities that are geochemically comparable to the ca. 3.45 Ga TTG plutonic suite that occurs to the south of the greenstone belt. The petrological and geochemical characteristics of the TTG plutonic suite have been extensively investigated by Robb and Anhaeusser (1983) and recently by

Yearron (2003). Table 5.2 presents the major-, trace- and rare earth element concentrations of the mineralogically simple and mineralogically complex felsic schists investigated during this study and compares it to felsic igneous rocks from the Hooggenoeg Formation (De Wit et al., 1987), the Steynsdorp, Stolzburg, Theespruit and Doornhoek Plutons (Yearron, 2003) and greywacke from the Fig Tree Group (Toulkeridis et al., 1999).

The mineralogically simple felsic schists have major element compositions that are, apart from higher Mg values and lower values of Ca and Na, largely indiscernible from felsic rocks of the Hooggenoeg Formation and the ca. 3.45 Ga TTG plutons (Fig. 5.1). The trace element compositions of these suites are, apart from a depletion of Sr in the mineralogically simple schists, also relatively comparable (Table 5.2). However, the REE profiles of mineralogically simple schists differ significantly from those of felsic rocks in the Hooggenoeg Formation and the ca. 3.45 Ga TTG suite (Fig. 5.2b). Rocks from the Hooggenoeg Formation as well as the Stolzburg and Theespruit Plutons have very similar REE profiles that are characterized by enrichment in light REEs, a systematic depletion in heavy REEs and no Eu anomaly. In contrast, the mineralogically simple schists from the Theespruit Formation have REE profiles that are characterized by light REE enrichment, a negative Eu anomaly and a flat heavy REE profile. This is very similar to REE profiles of the Doornhoek and Steynsdorp Plutons as well as phases of the Ngwane Gneiss (Fig. 5.2c; Hunter et al., 1984; Kröner and Tegtmeier, 1994; Yearron, 2003).

A number of contrasts are apparent when the major- and trace element composition of the mineralogically complex samples is compared to the felsic igneous rocks of the Hooggenoeg Formation and the TTG plutonic suite (Table 5.2; Fig. 5.1). These include significant relative enrichment in ferromagnesian elements (Ti, Fe, Mn and Mg) and depletion in Ca and Na. The mineralogically complex schists are highly enriched in the transition trace elements V, Cr, Ni, Cu and Zn and are relatively depleted in Ba, Rb, Sr and Zr (Table 5.2). Furthermore, the REE profiles of these samples differ markedly from those of the felsic igneous rocks and TTG plutons.



**Table 5.2:** Average whole-rock major-, trace- and rare earth element concentrations from various felsic rocks occurring in the southern part of the Barberton Greenstone Belt. Data for the Hooggenoeg Formation are from De Wit et al. (1987); data for the TTG plutons are from Yearron (2003) and data for Fig Tree greywacke are from Toulkeridis et al. (1999).

	This study				Felsic rocks from the Hooggenoeg Formation				TTG plutons				Fig Tree Group greywacke
	Min. Simple FS		Min. Complex FS		trond	trond	tonal	tonal	Steyns-	Stolz-	Thee-	Doorn-	
	avg	stdev	avg	stdev	intr	extr	intr	extr	dorp	burg	spruit	hoek	
n	5		3	4	4	3	5	6	26	6	11	11	
SiO <sub>2</sub>	73.81	2.49	66.40	1.97	73.28	72.39	64.80	63.80	69.61	71.46	71.77	72.41	64.32
TiO <sub>2</sub>	0.16	0.01	2.07	0.26	0.21	0.29	0.68	0.59	0.36	0.26	0.19	0.20	0.54
Al <sub>2</sub> O <sub>3</sub>	13.75	1.35	14.96	1.88	13.90	15.30	16.28	15.78	15.56	15.22	15.19	15.00	11.97
Fe <sub>2</sub> O <sub>3</sub> <sup>a</sup>	1.86	0.40	7.36	1.45	1.80	2.35	5.64	5.32	2.76	1.77	1.72	2.18	8.51
MnO	0.04	0.01	0.19	0.10	0.04	0.05	0.07	0.09	0.04	0.04	0.03	0.03	0.17
MgO	3.19	0.74	3.82	0.70	1.06	1.86	2.44	2.73	0.95	0.66	0.74	0.58	5.84
CaO	0.16	0.21	1.02	0.39	0.90	2.27	1.85	2.24	2.53	1.75	2.18	2.31	2.29
Na <sub>2</sub> O	1.37	0.37	1.24	0.14	5.11	0.22	6.42	5.61	4.36	6.35	5.29	4.24	1.75
K <sub>2</sub> O	2.31	0.81	1.16	0.35	3.45	5.09	1.37	3.60	2.39	2.05	1.91	2.24	1.90
P <sub>2</sub> O <sub>5</sub>	0.03	0.01	0.04	0.02	0.08	0.12	0.31	0.67	0.17	0.08	0.06	0.06	0.09
Mg# <sup>b</sup>	77	7	51	0	54	61	46	50	41	43	46	35	49
Ba	847	278	38	21					433	486	237	256	250
Rb	115	26	51	4	55	107	37	69	92	51	82	85	98
Sr	66	13	110	4	133	34	198	516	461	622	479	159	78
Y	23	9	21	4	4	5	9	21	11	5	12	18	17
Zr	165	30	81	10	122	141	174	249	186	100	102	147	117
Nb	24	5	16	2	4	6	8	7	8	5	9	10	7
V	8	7	293	60					28	17	17	17	35
Cr	15	1	586	45					48		18	8	484
Ni	36	50	168	24					18		21	5	320
Cu	18	4	58	10					13	2		9	27
Zn	32	11	90	106					60	41	44	37	90
Co	4	1	18	5									28
La	53.22	31.26	12.74	4.06	16.23	17.07	30.32	68.23	29.41	14.39	17.94	16.92	17.27
Ce	74.40	33.53	26.35	11.75	24.14	21.74	42.00	92.71	50.52	25.54	38.26	34.21	33.78
Nd	25.95	15.13	18.97	7.53	11.20	13.20	27.38	58.12	17.56	10.67	15.39	12.07	14.87
Sm	4.10	2.29	4.77	1.81	1.98	2.40	6.11	12.80	2.36	2.20	1.66	2.20	2.97
Eu	0.35	0.40	1.69	0.49	0.56	0.62		3.61	0.64	0.60	0.52	0.50	0.71
Gd	3.99	1.81	4.42	1.62					2.31	1.17	1.45	2.35	2.70
Tb	0.78	0.31	0.79	0.23	0.18	0.27	0.60	1.17	0.33	0.19	0.20	0.46	0.49
Yb	2.73	1.71	2.25	0.26	0.36	0.62	1.30	2.26	0.91	0.41	0.40	1.40	1.71
Lu	0.57	0.30	0.36	0.07	0.08	0.11	0.21	0.27	0.15	0.05	0.07	0.19	0.26

<sup>a</sup> All Fe recalculated as Fe<sub>2</sub>O<sub>3</sub>

<sup>b</sup> Mg # calculated as 100 x Mg/(Mg+Fe)

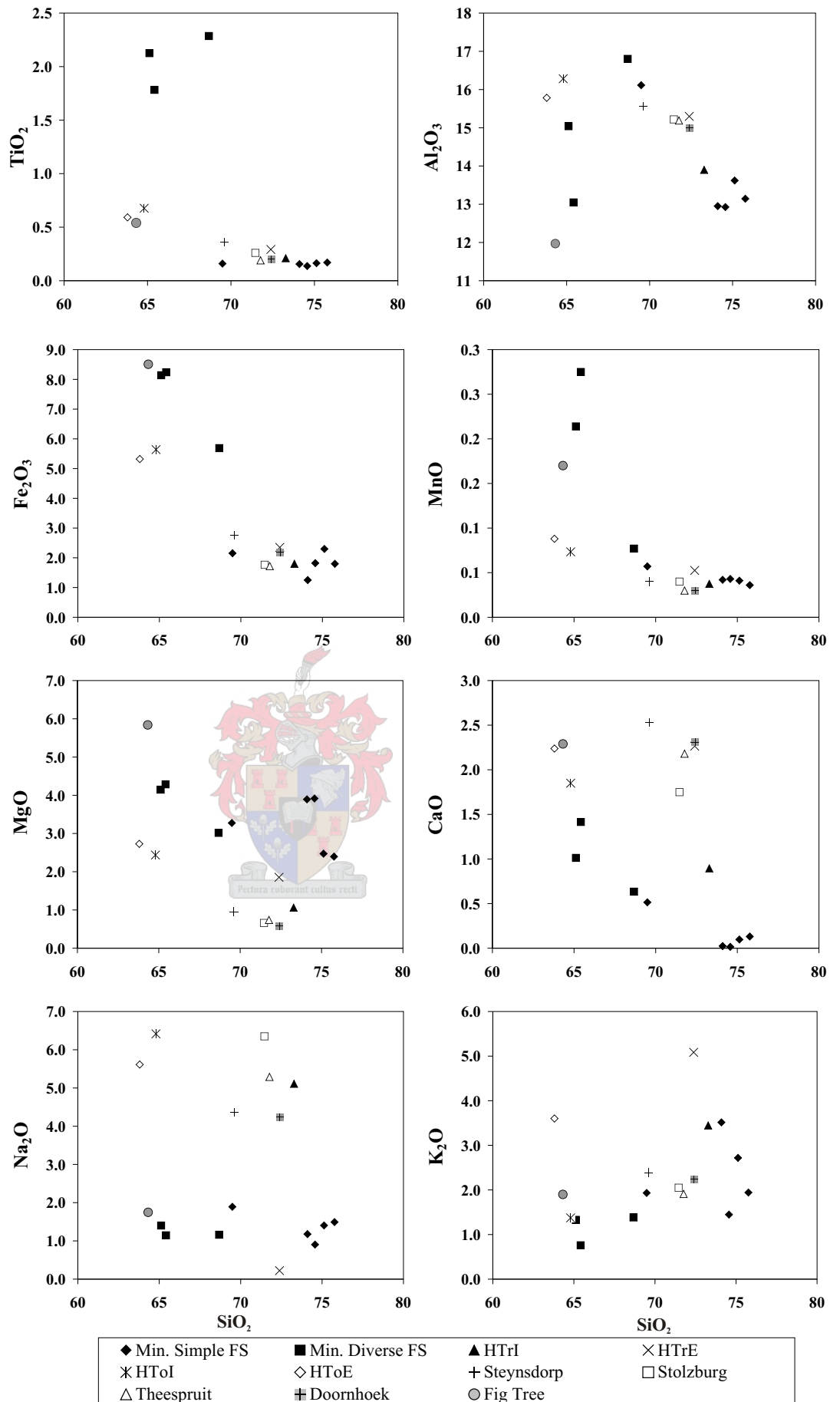


**Figure 5.1:** Major element Harker diagrams of felsic rocks investigated during the current study compared to felsic igneous rocks from the Hooggenoeg Formation (from De Wit et al., 1987), early TTG plutons (from Yearron, 2003) and Fig Tree Group sediments (from Toulkeridis et al., 1999). HTrI, HTrE, HTol and HTolE refer to tonalitic and trondhjemitic intrusive and extrusive rocks of the Hooggenoeg Formation; Min. Simple FS and Min. Diverse FS refer to felsic schists from the current study.

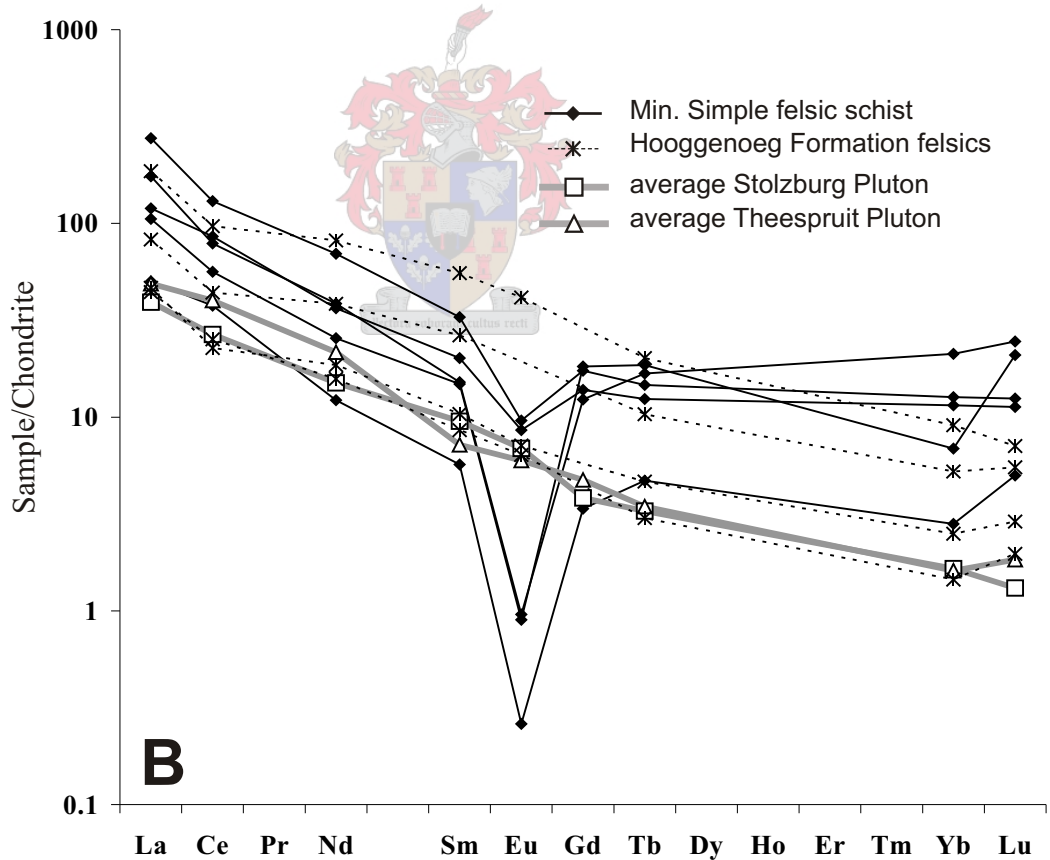
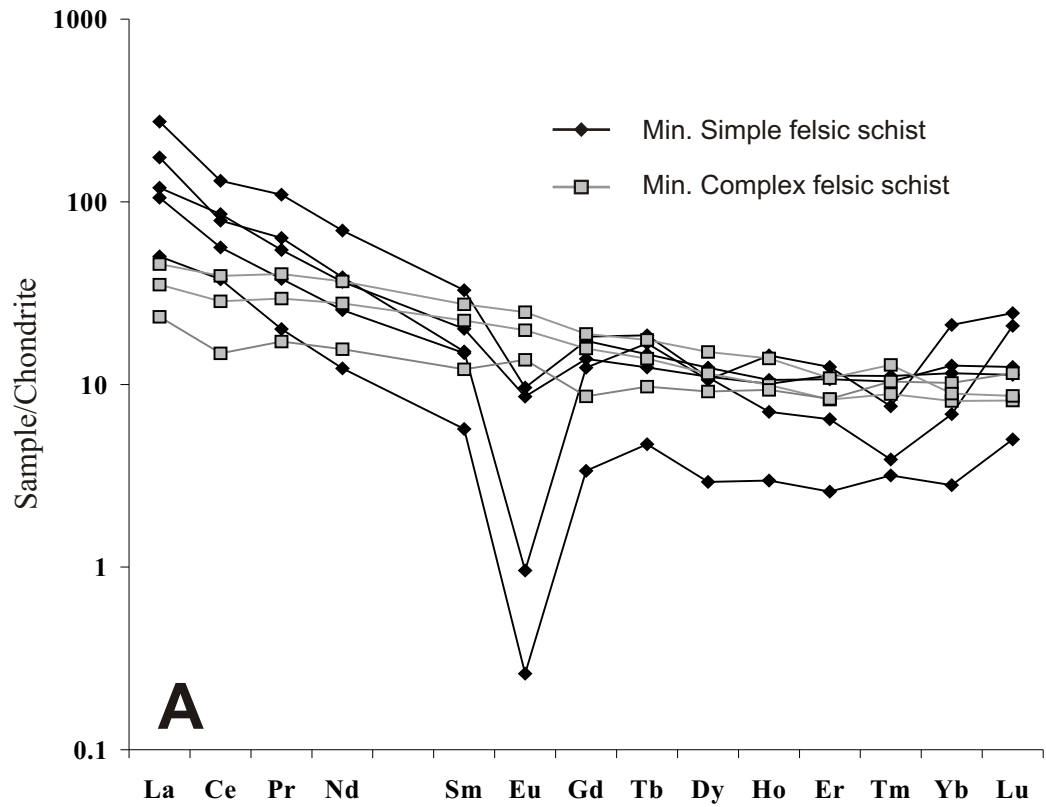


**Figure 5.2: (a):** Chondrite-normalized (Taylor and McLennan, 1985) REE profiles of mineralogically simple and mineralogically complex felsic schists. Note the extremely flat profile of mineralogically complex samples compared to the profile of mineralogically simple samples, which show LREE enrichment, a pronounced negative Eu anomaly and flat HREE profiles. **(b):** REE profiles of mineralogically simple felsic schist compared to felsic rocks of the Hooggenoeg Formation (from De Wit et al., 1987) and the Stolzburg and Theespruit Plutons (from Yearron, 2003). Note the good correlation between rocks from the Hooggenoeg Formation with the Stolzburg and Theespruit Plutons and the contrast between these rocks and the mineralogically simple felsic schists.

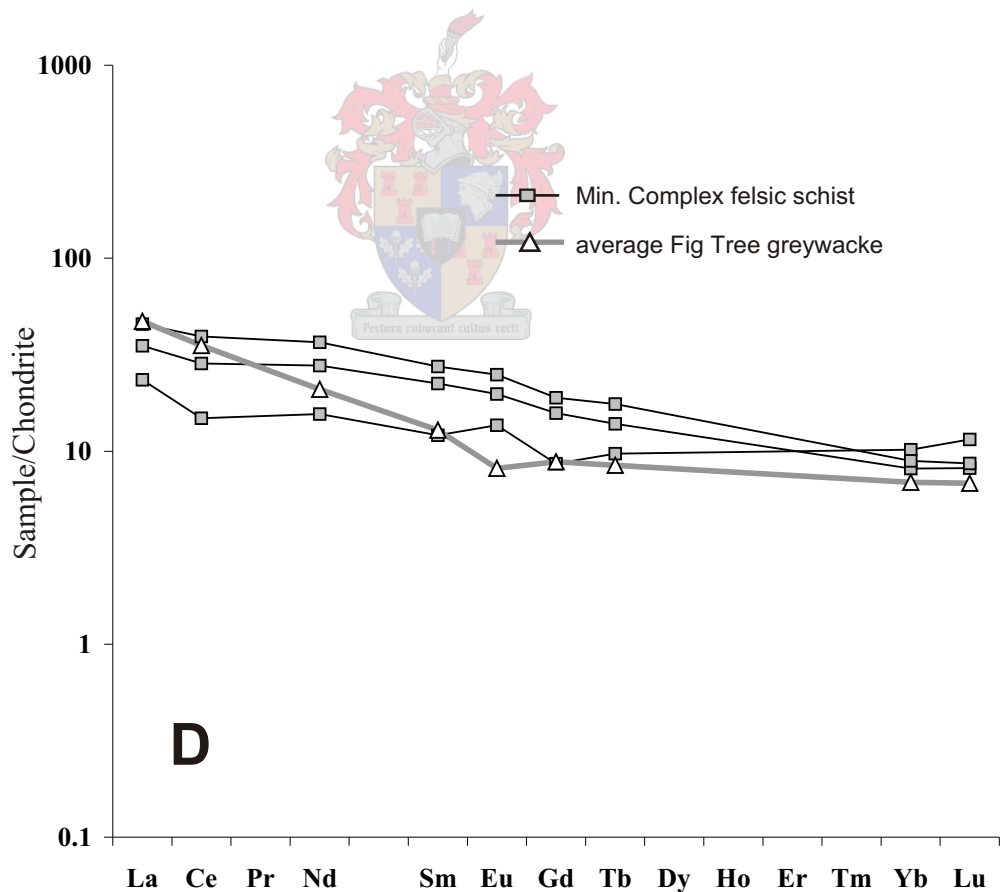
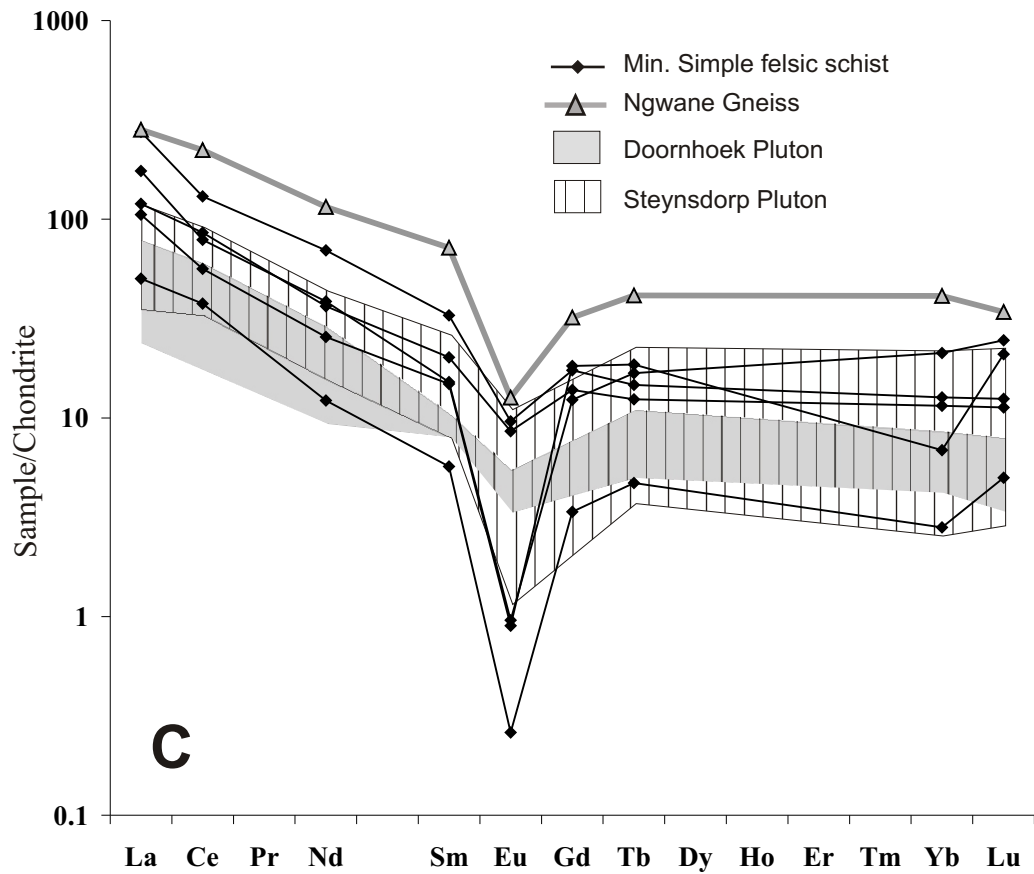


**Figure 5.2:** (c): REE profiles of mineralogically simple felsic schist compared to the Doornhoek and Steynsdorp Plutons (from Yearron, 2003) and phases of the Ngwane Gneiss (from Kröner and Tegtmeier, 1994 and Hunter et al., 1984). (d): REE profiles of mineralogically complex felsic schist compared to average Fig Tree Group greywacke (from Toulkeridis et al., 1999)

Anomalously high values of the transition trace elements are a characteristic phenomenon of many Archaean clastic sediments (McLennan and Taylor, 1984) and have been reported in Fig Tree Group greywackes (Toulkeridis et al., 1999) and metasediments from greenstone xenoliths preserved in the southern gneiss terrain of the Barberton Greenstone Belt (Dziggel et al., 2002). The cause of this enrichment is not unequivocally understood, but is most likely an indication that these rocks were derived from a source that contains an ultramafic component (McLennan and Taylor, 1984). The chemical characteristics of the mineralogically complex felsic schists are consistent with the characteristics of sediments derived from a mixed source that contains a significant mafic to ultramafic volcanic component. The REE profiles of these samples correlate well with the profiles of other Archaean sediments, such as Fig Tree Group greywacke (Fig. 5.2d; McLennan and Taylor, 1984; Toulkeridis et al., 1999). It should be noted that the REE profiles of the mineralogically complex samples are flatter than those of Fig Tree sediments and are not enriched in light REEs and also display slight positive Eu anomalies, compared to slight negative Eu anomalies in Fig Tree sediments. This could be an indication that the mineralogically complex schists were derived almost exclusively from mafic volcanics, rather than a mixed mafic and felsic igneous source (McLennan and Taylor, 1984). Additionally, the ubiquitous presence of tourmaline (a boron-bearing phase) in these schists indicates that interaction with seawater must have taken place at some stage, most likely during sedimentation (e.g. Harriss, 1969; Ishikawa and Nakamura, 1993; Chaussidon and Appel, 1997). The anomalously high Ti content of these samples (more than 2 wt % TiO<sub>2</sub>) might indicate that a detrital Ti-rich phase such as ilmenite was concentrated during sedimentation.

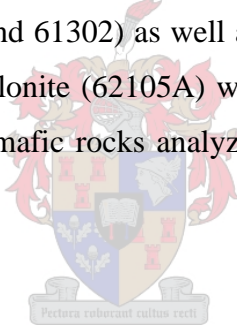
In summary, whole-rock geochemistry has revealed that most of the felsic schist and agglomerate units that occur in the Theespruit Formation are of volcanic origin. These units have a close geochemical affinity to the Steynsdorp Pluton and Ngwane Gneiss and differ from felsic units in the Hooggenoeg Formation and the ca. 3.45 Ga TTG suite that occurs to the south of the Barberton Greenstone Belt. The Theespruit Formation also contains clastic sedimentary horizons that have been derived from a source consisting almost exclusively of mafic volcanics. The sedimentary units do not constitute a



significant volumetric portion of the felsic lithologies, but are an important component as they contain suitable metamorphic mineral parageneses that are indispensable to unraveling the metamorphic history of this part of the Barberton Greenstone Belt.

#### 5.4 Amphibolite and chlorite schist

The main purpose of the bulk-rock geochemical analysis of mafic rocks sampled during this study is to establish the whole-rock geochemistry of these rocks and to constrain any chemical parameters that might control the stability of metamorphic minerals, particularly garnet, in these rocks. Consequently, representative samples of the different mineralogical suites were analyzed. These include four samples of garnet-bearing amphibolite (samples Tj 3, Tj 10, 62107 and 62601A), a sample of hornblende-plagioclase amphibolite (62210) and two samples of epidote-amphibolite (Tj 14 and Tj 20). Two chlorite schists (Tj 26 and 61302) as well as a leucocratic amphibolite (Tj 31) and a garnet-quartz-amphibole mylonite (62105A) were also analyzed. The major- and trace element composition of the mafic rocks analyzed is presented in Table 5.3 and is discussed below.



##### 5.4.1 Major elements

Diagrams showing the variation of major elements against Si are presented in Figure 5.3 and highlight the differences in the chemical composition of various amphibolites. Garnet-bearing amphibolite samples are relatively enriched in Al and Fe, but are simultaneously depleted in Mg and Ca relative to epidote-amphibolite. The garnet-epidote-free sample (62210) has concentrations that are intermediate to the two end-member groups for these elements. Similarly, garnet-bearing samples have low Mg-numbers of 20 to 52, compared to the high Mg-numbers of 65 to 71 from epidote-amphibolite samples. The large spread in Mg-numbers for garnet-bearing samples is likely caused by the extremely low concentrations of MgO in these rocks (1.91 – 6.71 wt %), as the low absolute concentration accentuates even slight relative differences in MgO concentration.

The major element results indicate that high Al<sub>2</sub>O<sub>3</sub> (more than 10 wt %) and low CaO (less than 10 wt %) as well as Mg-numbers lower than 50 are the bulk-rock chemical parameters that control the stability of garnet in the amphibolite samples investigated.

**Table 5.3:** Whole-rock major- and trace element analysis of mafic rocks investigated.

<b>Sample Type</b>	Tj 10 grt amph	Tj 3 grt amph	62107 grt amph	62601A grt amph	Tj 31 leuco- amph	62105A grt-amph mylonite	62210 amph	Tj 14 epidote- amph	Tj 20 epidote- amph	Tj 26 chl-zoi schist	61302 chl schist
<b>SiO<sub>2</sub></b>	56.93	54.23	56.35	51.08	56.23	65.64	49.24	51.48	53.06	52.91	50.79
<b>TiO<sub>2</sub></b>	1.16	1.14	1.71	1.58	0.93	0.60	1.73	0.39	0.51	0.67	1.14
<b>Al<sub>2</sub>O<sub>3</sub></b>	13.27	15.28	12.78	14.64	19.08	4.89	12.04	7.21	8.77	15.64	12.99
<b>Fe<sub>2</sub>O<sub>3</sub></b>	14.81	13.31	14.82	12.20	6.98	16.76	14.77	10.90	11.73	13.68	11.95
<b>MnO</b>	0.18	0.19	0.58	0.60	0.17	1.06	0.29	0.20	0.21	0.15	0.18
<b>MgO</b>	1.91	3.91	3.94	6.71	3.61	5.46	7.88	13.64	11.13	11.46	9.24
<b>CaO</b>	5.63	7.74	7.82	9.60	7.44	2.76	10.87	12.51	11.60	1.90	10.55
<b>Na<sub>2</sub>O</b>	2.78	2.90	1.07	0.95	2.44	0.71	1.96	1.01	1.05	0.68	2.36
<b>K<sub>2</sub>O</b>	0.32	0.55	0.34	1.72	0.42	0.15	0.30	0.33	0.30	0.60	0.28
<b>P<sub>2</sub>O<sub>5</sub></b>	0.45	0.12	0.20	0.22	0.23	0.02	0.15	0.05	0.07	0.07	0.12
<b>LOI%</b>	1.51	2.32	1.02	1.11	1.55	0.97	1.03	1.49	1.36	2.02	1.06
<b>Total</b>	99.09	99.69	100.73	100.54	99.26	99.06	100.38	99.47	99.38	100.01	100.83
<b>Mg#<sup>a</sup></b>	20	37	35	52	51	39	51	71	65	62	61
<b>Ba</b>	199	249	8	74	155	13	21	148	113	41	1
<b>Rb</b>	9	24	14	54	26	4	7	24	18	25	3
<b>Sr</b>	148	125	66	71	238	44	285	66	67	26	170
<b>Y</b>	41	26	36	28	35	23	27	10	14	35	25
<b>Zr</b>	124	102	33	42	228	0	93	24	44	44	36
<b>Nb</b>	9	10	16	14	18	13	11	3	6	7	7
<b>V</b>	0	450	276	216	101	124	260	260	271	366	155
<b>Cr</b>	15	43	718	788	80	334	850	695	417	449	763
<b>Ni</b>	23	26	210	208	57	17	241	196	148	186	226
<b>Cu</b>	107	107	122	113	69	131	127	101	104	87	103
<b>Zn</b>	83	49	49	80	94	301	55	61	113	70	46
<b>Co</b>	43	37	46	36	17	61	46	31	33	46	35

<sup>a</sup> Mg# calculated as 100 x Mg/(Mg+Fe)

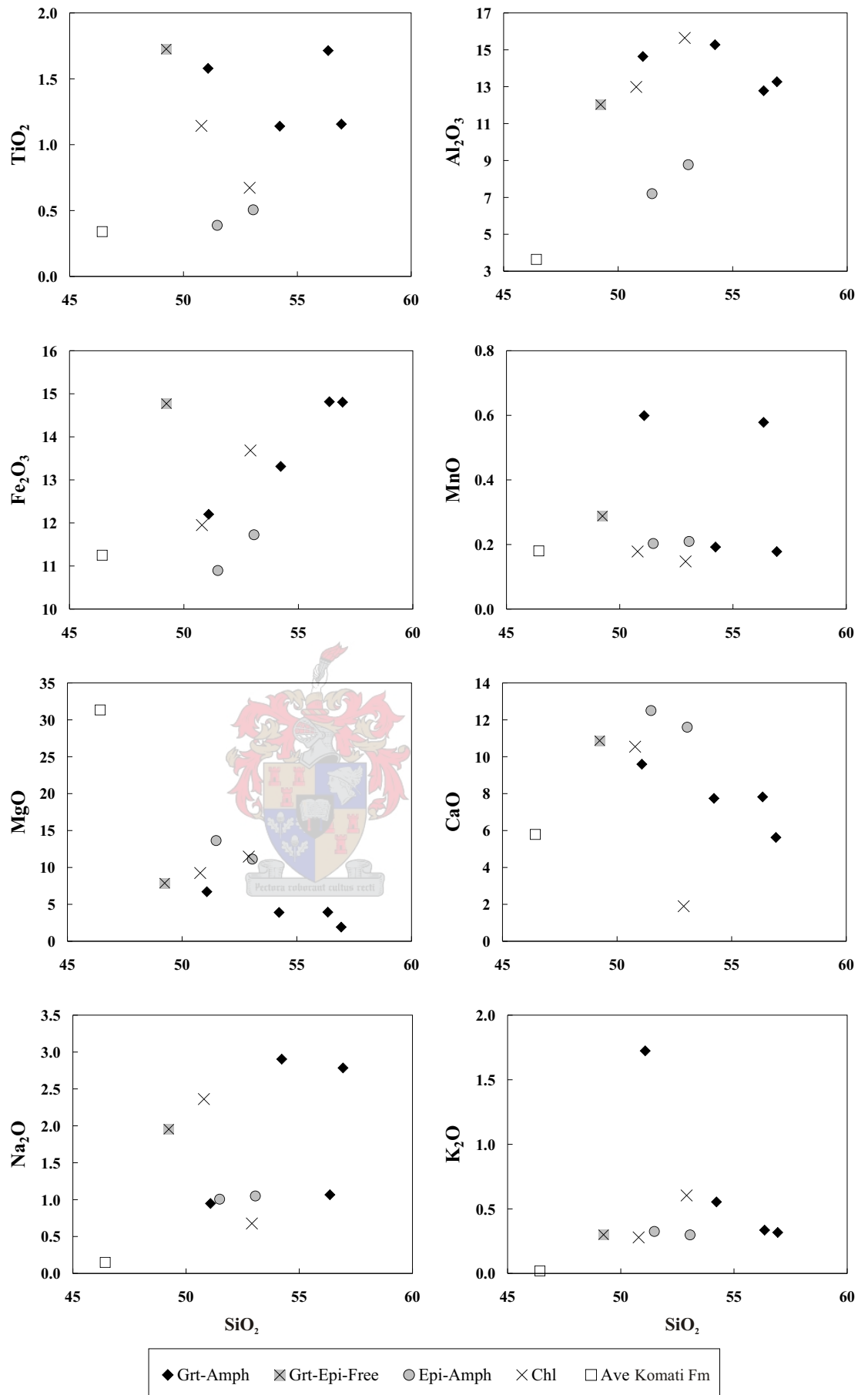


**Figure 5.3:** Major element Harker diagrams of garnet-bearing amphibolite, garnet-free amphibolite, epidote-amphibolite and chlorite schist investigated during this study compared to the average composition of ultramafic rocks from the Komati Formation (from Smith and Erlank, 1982).

#### 5.4.2 Trace elements

Most mafic samples have comparable trace element concentrations, including high values of the transition trace elements V, Cr, Ni, Cu and Co and low concentrations of the large-ion lithophile elements such as Ba and Rb (Table 5.3). A notable exception is sample Tj 10, which is severely depleted in V, Cr and Ni relative to other mafic rocks analyzed.

#### 5.4.3 Possible protoliths

Only the epidote-amphibolite samples conform to all the chemical criteria required to be classified as komatiites ( $\text{SiO}_2 < 53\%$ ,  $\text{MgO} > 9\%$ ,  $\text{K}_2\text{O} < 0,9\%$ ,  $\text{TiO}_2 < 0,9\%$  and  $\text{CaO}/\text{Al}_2\text{O}_3 > 1$ ; Brooks and Hart, 1974). Epidote-amphibolite samples plot in the field of basaltic komatiites on a komatiite classification diagram (Fig. 5.4; Viljoen et al., 1982), while the garnet-epidote-free amphibolite and chlorite schist samples plot close to the basalt-komatiite transition. Garnet-bearing samples plot well within the tholeiite basalt field. Figure 5.3 highlights the major element differences between mafic rocks investigated in this study and average ultramafic rocks from the Komati Formation (Smith and Erlank, 1982) and shows that these samples are not directly comparable to samples from the Komati Formation. This supports the observation of early workers that the mafic rocks in the Theespruit Formation consist largely of basalt and basaltic komatiite and are not as primitive as the peridotitic komatiite found in the Komati Formation (Viljoen and Viljoen, 1969b).

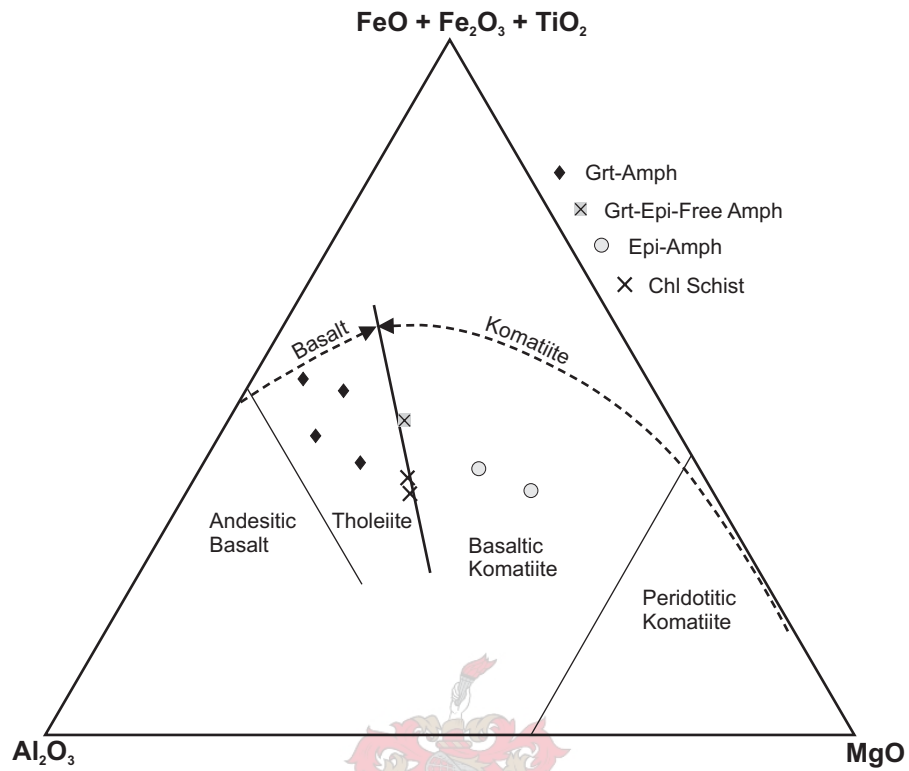


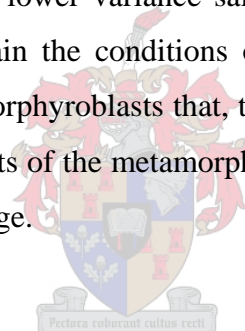
**Figure 5.4:**  $\text{FeO} + \text{Fe}_2\text{O}_3 + \text{TiO}_2 - \text{Al}_2\text{O}_3 - \text{MgO}$  diagram used for the classification of komatiite (after Viljoen et al., 1982). Garnet-bearing amphibolite samples plot in the field of tholeiite basalt, while garnet-free amphibolite and chlorite schists plot close to the transition between tholeiite basalt and basaltic komatiite. Only epidote-amphibolite samples plot within the field of basaltic komatiite.



## **CHAPTER 6: MINERAL CHEMISTRY**

### 6.1 Introduction

One of the primary objectives of any metamorphic petrological investigation is to establish the chemical composition of the minerals that constitute the metamorphic assemblage. These compositions can be used to quantitatively estimate the pressure and temperature of metamorphism by applying a variety of geothermobarometric techniques. Porphyroblasts that grew during progressive metamorphism often exhibit chemical zonation that might assist in identifying different metamorphic episodes or provide clues to the nature of the metamorphic path that the rock was subjected to. The samples selected for mineral chemical analysis are felsic schists and more mineralogically diverse varieties of amphibolite, as these lower variance samples contain mineral assemblages that have the potential to constrain the conditions of metamorphism. Many of these samples contain relatively large porphyroblasts that, through zoning patterns or inclusion characteristics, might reveal aspects of the metamorphic history that are not preserved by the current metamorphic assemblage.



### 6.2 Analytical procedures

#### *6.2.1 Major elements*

Major element mineral chemical analyses were performed on a LEO scanning electron microscope coupled to a Link ISIS energy dispersive spectrometry system at the University of Stellenbosch. The microscope operating conditions were set at an accelerating voltage of 20 kV with a beam current of 120  $\mu\text{A}$  and a probe current of 1,50 nA. Acquisition time was set at 50 seconds and spectra were processed by ZAF corrections and quantified using natural mineral standards. Mineral compositions were recalculated to mineral stoichiometries and the stoichiometric results were used to evaluate the quality of the analytical data. Furthermore, mineral standards with a known chemical composition were treated as unknowns and analyzed using the same instrument-

and calibration set-up employed for unknowns. For example, a plagioclase standard not used in the plagioclase analytical routine was analyzed with the same set-up used for unknown plagioclase and the measured chemical composition was compared to the actual, published composition. A comparison of the measured and actual chemical compositions of selected mineral standards used to test the accuracy of the analytical technique is presented in Appendix 2.2 and serves as a reflection of the absolute error associated with the determination of mineral compositions during this study. The mineral compositions presented in this chapter represent the average of at least three repeat analyses of the same mineral generation in a single sample. Only analyses that produced cation totals within 0.05 to 0.1 (depending on the number of cations) of the ideal stoichiometric number for each cation site were used in the calculations. For example, garnet: Si =  $3 \pm 0.05$ ; Al =  $2 \pm 0.05$ ; Fe+Mg+Mn+Ca =  $3 \pm 0.1$ ; total cations =  $8 + 0.05/-0.1$  and plagioclase: Al+Si =  $4 \pm 0.03$  and Ca+Na =  $1 \pm 0.03$ .

### 6.2.2 Trace- and rare earth elements

Transition trace element and REE concentrations of three garnet grains in sample Tj 18 were determined by LA-ICP-MS analysis at the Memorial University of Newfoundland. A detailed description of this instrument and the analytical- and data processing techniques used in the trace element analysis is presented in Horn et al. (1997). Analyses were calibrated against USGS reference material BCR2-G and Si (measured by electron microprobe) was used as an internal standard. BCR2-G was also routinely analyzed during the procedure to monitor instrument precision and accuracy and the results correlate well with the long-term averages reported for this instrument (Appendix 2.3).

### 6.3 Felsic schist mineral chemistry

The composition and calculated stoichiometry of minerals from felsic schist samples are summarized in Table 6.1 and the complete dataset is presented in Appendix 3.1. The mineral chemistries reflect the generally reduced redox state of these rocks and most Fe-Mg-bearing minerals do not contain significant amounts of Fe<sup>3+</sup> (Droop, 1987).

**Table 6.1:** Major element content and structural formulae for representative mineral analyses from felsic schist. Mineral stoichiometries are calculated by the number of oxygen-equivalent anions in the mineral formula.

Sample Mineral Generation	Tj 18 garnet core	Tj 18 garnet rim	Tj 18 garnet o\growth	Tj 18 garnet b\down	Tj 18 staurolite matrix	Tj 18 biotite matrix	Tj 18 biotite incl in grt	Tj 18 chlorite matrix	Tj 18 chlorite b\down	Tj 18 plag matrix	Tj 18 plag b\down	Tj 18 muscovite b\down	Sample Mineral Generation	62601C garnet core	62601C garnet peak
SiO <sub>2</sub>	36.92	37.21	37.44	36.62	29.63	39.69	39.86	30.03	30.14	58.84	60.22	48.61	SiO <sub>2</sub>	36.08	36.54
TiO <sub>2</sub>	0.00	0.09	0.08	0.13	0.62	1.32	0.97	0.02	0.02	0.00	0.00	0.50	TiO <sub>2</sub>	1.08	0.58
Al <sub>2</sub> O <sub>3</sub>	20.80	20.94	20.94	20.71	56.15	18.50	18.62	25.30	23.19	26.08	25.16	37.01	Al <sub>2</sub> O <sub>3</sub>	19.81	20.61
Cr <sub>2</sub> O <sub>3</sub>	0.00	0.00	0.00	0.00	0.35	0.00	0.00	0.00	0.00	0.00	0.00	0.00	Cr <sub>2</sub> O <sub>3</sub>	0.00	0.00
V <sub>2</sub> O <sub>5</sub>	0.00	0.00	0.00	0.00	0.28	0.00	0.00	0.00	0.00	0.00	0.00	0.00	V <sub>2</sub> O <sub>5</sub>	0.00	0.00
ZnO	0.00	0.00	0.00	0.00	1.13	0.00	0.00	0.00	0.00	0.00	0.00	0.00	ZnO	0.00	0.00
FeO	31.43	31.94	32.62	31.73	11.55	16.93	16.88	27.91	31.93	0.00	0.00	1.31	FeO	32.17	31.24
MnO	7.13	5.42	2.38	7.71	0.42	0.00	0.00	0.39	0.45	0.00	0.00	0.00	MnO	5.07	5.28
MgO	1.67	1.91	2.12	0.81	0.10	13.96	14.13	16.20	12.44	0.00	0.00	0.62	MgO	2.25	2.69
CaO	2.05	2.48	4.42	2.32	0.00	0.00	0.00	0.00	0.00	7.80	6.94	0.00	CaO	3.54	3.09
Na <sub>2</sub> O	0.00	0.00	0.00	0.00	0.00	0.00	0.00	0.00	0.00	7.18	7.57	0.45	Na <sub>2</sub> O	0.00	0.00
K <sub>2</sub> O	0.00	0.00	0.00	0.00	0.00	9.55	9.59	0.63	1.30	0.10	0.11	11.45	K <sub>2</sub> O	0.00	0.00
<b>Total</b>	<b>100.01</b>	<b>100.00</b>	<b>100.00</b>	<b>100.01</b>	<b>98.47</b>	<b>99.94</b>	<b>100.04</b>	<b>100.48</b>	<b>100.09</b>	<b>100.00</b>	<b>100.00</b>	<b>99.95</b>	<b>Total</b>	<b>100.00</b>	<b>100.03</b>
<b>Anions</b>	<b>12</b>	<b>12</b>	<b>12</b>	<b>12</b>	<b>23</b>	<b>11</b>	<b>11</b>	<b>14</b>	<b>14</b>	<b>8</b>	<b>8</b>	<b>11</b>	<b>Anions</b>	<b>12</b>	<b>12</b>
Si	3.02	3.03	3.02	3.02	Si 3.98	Si IV 2.81	Si IV 2.82	Si IV 2.75	2.85	Si 2.63	2.68	Si 3.09	Si	2.96	2.97
						Al IV 1.19	Al IV 1.18	Al IV 1.25	1.15	Al 1.37	1.32	Al IV 0.91			
Al	2.01	2.01	1.99	2.01	Al 8.89	Σ IV 4.00	Σ IV 4.00	Σ IV 4.00	4.00	Σ 4.00	4.00	Σ IV 4.00	Al	1.91	1.98
Ti	0.00	0.01	0.01	0.01	Fe <sup>2+</sup> 1.30	Al VI 0.36	Al VI 0.38	Al VI 1.48	1.43	Ca 0.37	0.33	Al VI 1.86	Ti	0.07	0.04
Cr	0.00	0.00	0.00	0.00	Mg 0.02	Ti 0.07	Ti 0.05	Ti 0.00	0.00	Na 0.62	0.65	Ti 0.02	Cr	0.00	0.00
Fe <sup>2+</sup>	2.15	2.17	2.20	2.19	Zn 0.11	Cr 0.00	Cr 0.00	Cr 0.00	0.00	K 0.01	0.01	Fe <sup>2+</sup> 0.07	Fe <sup>2+</sup>	2.21	2.13
Mn	0.40	0.30	0.13	0.44	Mn 0.04	Fe <sup>2+</sup> 1.00	Fe <sup>2+</sup> 1.00	Fe <sup>2+</sup> 2.14	2.57	Σ 1.00	0.99	Mg 0.06	Mn	0.29	0.30
Mg	0.20	0.23	0.25	0.10	V 0.02	Mn 0.00	Mn 0.00	Mn 0.02	0.03			Σ VI 2.01	Mg	0.27	0.33
Ca	0.18	0.22	0.38	0.20	Cr 0.04	Mg 1.48	Mg 1.49	Mg 2.21	1.75	Σ cat 5.00	4.99		Ca	0.31	0.27
					Ti 0.06	Σ 2.91	Σ 2.92	Ca 0.00	0.00			Na 0.06			
Σ cat	7.97	7.96	7.98	7.97	Σ 1.59			Na 0.00	0.00	XAn 0.37	0.34	K 0.93	Σ cat	8.02	8.00
								K 0.07	0.16	XAb 0.62	0.66	Σ 0.98			
XPy	0.07	0.08	0.09	0.03	Σ cat 14.46			Σ 5.92	5.94				XPy	0.09	0.11
XAlm	0.73	0.74	0.74	0.75		Σ cat 7.77	Σ cat 7.78					Σ cat 6.99	XAlm	0.72	0.70
XSpss	0.14	0.10	0.04	0.15				Σ cat 9.92	9.94				XSpss	0.09	0.10
XGrss	0.06	0.07	0.13	0.07		Mg# 59.51	Mg# 59.87					XPa 0.06	XGrss	0.10	0.09
Fe/Fe+Mg	0.91	0.90	0.90	0.96				Mg# 50.84	40.50				Fe/Fe+Mg	0.89	0.87

**Note:** XPy, XAlm, XSpss and XGrss as defined by Spear (1993). XAn = Ca/(Ca+Na), XAb = Na/(Ca+Na), XPa = Na/(Na+K), Mg# = 100 x Mg/(Mg+Fe)

**Table 6.1:** continued

Sample	62601C	62601C	62601C	62601C	62601C	62601C	62601C	62601C	Sample	62105F	62105F	62105F	62105F	62105F
Mineral	garnet	staurolite	biotite	biotite	chlorite	chlorite	plag	Mineral	garnet	garnet	staurolite	biotite	biotite	
Generation	o\growth	matrix	matrix	inclusion	matrix	inclusion	matrix	Generation	peak	o\growth	matrix	inclusion	matrix	
SiO <sub>2</sub>	35.84	29.14	39.64	40.28	30.30	31.36	62.71	SiO <sub>2</sub>	36.80	37.81	29.30	41.22	39.99	
TiO <sub>2</sub>	0.61	0.63	1.36	1.15	0.09	0.19	0.00	TiO <sub>2</sub>	0.00	0.24	0.55	1.04	1.21	
Al <sub>2</sub> O <sub>3</sub>	19.84	54.61	18.17	18.80	26.01	26.33	23.41	Al <sub>2</sub> O <sub>3</sub>	20.80	20.24	55.19	18.48	18.22	
Cr <sub>2</sub> O <sub>3</sub>	0.00	0.10	0.12	0.10	0.14	0.11	0.00	Cr <sub>2</sub> O <sub>3</sub>	0.00	0.00	0.29	0.07	0.21	
V <sub>2</sub> O <sub>5</sub>	0.00	0.20	0.00	0.00	0.00	0.00	0.00	V <sub>2</sub> O <sub>5</sub>	0.00	0.00	0.21	0.00	0.00	
ZnO	0.00	0.11	0.00	0.00	0.00	0.00	0.00	ZnO	0.00	0.00	0.20	0.00	0.00	
FeO	31.91	14.38	18.28	14.27	26.80	21.03	0.00	FeO	30.60	30.17	13.57	11.39	17.27	
MnO	7.42	0.35	0.14	0.15	0.23	0.20	0.00	MnO	5.81	6.86	0.53	0.24	0.25	
MgO	1.39	0.50	12.45	15.30	16.32	20.66	0.00	MgO	2.22	1.60	0.18	17.77	13.26	
CaO	2.99	0.00	0.00	0.00	0.00	0.00	4.59	CaO	3.97	3.08	0.00	0.00	0.00	
Na <sub>2</sub> O	0.00	0.00	0.00	0.00	0.00	0.00	9.21	Na <sub>2</sub> O	0.00	0.00	0.00	0.00	0.00	
K <sub>2</sub> O	0.00	0.00	10.26	10.49	0.12	0.12	0.08	K <sub>2</sub> O	0.00	0.00	0.00	10.15	10.37	
<b>Total</b>	<b>99.99</b>	<b>99.59</b>	<b>100.43</b>	<b>100.51</b>	<b>100.00</b>	<b>100.01</b>	<b>100.00</b>	<b>Total</b>	<b>100.20</b>	<b>100.00</b>	<b>99.31</b>	<b>100.35</b>	<b>100.76</b>	
<b>Anions</b>	<b>12</b>	<b>23</b>	<b>11</b>	<b>11</b>	<b>14</b>	<b>14</b>	<b>8</b>	<b>Anions</b>	<b>12</b>	<b>12</b>	<b>23</b>	<b>11</b>	<b>11</b>	
Si	2.97	Si 3.96	Si IV 2.83	2.82	Si IV 2.76	2.77	Si 2.78	Si 2.99	3.08	Si 3.97	Si IV 2.84	2.83	2.83	
			Al IV 1.17	1.18	Al IV 1.24	1.23	Al 1.22				Al IV 1.16	1.17	1.17	
Al	1.94	Al 8.74	Σ IV 4.00	4.00	Σ IV 4.00	4.00	Σ 4.00	Al 1.99	1.94	Al 8.81	Σ IV 4.00	4.00	4.00	
Ti	0.04	Fe <sup>2+</sup> 1.63	Al VI 0.36	0.37	Al VI 1.55	1.52	Ca 0.22	Ti 0.00	0.01	Fe <sup>2+</sup> 1.54	Al VI 0.35	0.36	0.36	
Cr	0.00	Mg 0.10	Ti 0.07	0.06	Ti 0.01	0.01	Na 0.79	Cr 0.00	0.00	Mg 0.04	Ti 0.05	0.06	0.06	
Fe <sup>2+</sup>	2.21	Zn 0.01	Cr 0.01	0.01	Cr 0.01	0.01	K 0.00	Fe <sup>2+</sup> 2.08	2.05	Zn 0.02	Cr 0.00	0.01	0.01	
Mn	0.42	Mn 0.03	Fe <sup>2+</sup> 1.09	0.84	Fe <sup>2+</sup> 2.04	1.56	Σ 1.01	Mn 0.33	0.39	Mn 0.05	Fe <sup>2+</sup> 0.66	1.02	1.02	
Mg	0.17	V 0.02	Mn 0.01	0.01	Mn 0.01	0.01		Mg 0.27	0.19	V 0.02	Mn 0.01	0.01	0.01	
Ca	0.27	Cr 0.01	Mg 1.32	1.60	Mg 2.21	2.72	Σ cat 5.01	Ca 0.35	0.27	Cr 0.03	Mg 1.83	1.40	1.40	
		Ti 0.06	Σ 2.86	2.87	Ca 0.00	0.00				Ti 0.06	Σ 2.90	2.87	2.87	
Σ cat	8.02	Σ 1.87			Na 0.00	0.00	XAn 0.21	Σ cat 8.01	7.94	Σ 1.75				
			K 0.93	0.94	K 0.01	0.01	XAb 0.78				K 0.89	0.94	0.94	
XPy	0.06	Σ cat 14.57			Σ 5.84	5.84		XPy 0.09	0.07	Σ cat 14.53				
XAlm	0.72		Σ cat 7.80	7.81				XAlm 0.69	0.71		Σ cat 7.80	7.80	7.80	
XSpss	0.14				Σ cat 9.84	9.84		XSpss 0.11	0.13					
XGrss	0.09		Mg# 54.83	65.64				XGrss 0.11	0.09		Mg# 73.55	57.77	57.77	
Fe/Fe+Mg	0.93				Mg# 52.04	63.64		Fe/Fe+Mg 0.89	0.91					

**Note:** XPy, XAlm, XSpss and XGrss as defined by Spear (1993). XAn = Ca/(Ca+Na), XAb = Na/(Ca+Na), XPa = Na/(Na+K), Mg# = 100 x Mg/(Mg+Fe)

**Table 6.1:** continued

Sample Mineral Generation	62105F chlorite matrix	62105F chlorite inclusion	62105F plag peak	62105F plag matrix	Sample Mineral Generation	62601D staurolite matrix	62601D kyanite matrix	62601D sill matrix	62601D biotite matrix	62601D muscovite matrix	62601D plag matrix	Sample Mineral Generation	62105D staurolite relic					
SiO <sub>2</sub>	30.90	31.26	59.94	62.04	SiO <sub>2</sub>	29.35	34.83	37.43	40.51	49.90	61.96	SiO <sub>2</sub>	29.84					
TiO <sub>2</sub>	0.17	0.12	0.00	0.00	TiO <sub>2</sub>	0.68	0.00	0.00	1.40	0.29	0.00	TiO <sub>2</sub>	0.25					
Al <sub>2</sub> O <sub>3</sub>	26.24	27.19	25.52	23.99	Al <sub>2</sub> O <sub>3</sub>	54.97	64.81	62.53	18.30	36.40	24.06	Al <sub>2</sub> O <sub>3</sub>	56.47					
Cr <sub>2</sub> O <sub>3</sub>	0.13	0.05	0.00	0.00	Cr <sub>2</sub> O <sub>3</sub>	0.14	0.37	0.04	0.32	0.00	0.00	Cr <sub>2</sub> O <sub>3</sub>	0.00					
V <sub>2</sub> O <sub>5</sub>	0.00	0.00	0.00	0.00	V <sub>2</sub> O <sub>5</sub>	0.12	0.00	0.00	0.00	0.00	0.00	V <sub>2</sub> O <sub>5</sub>	0.01					
ZnO	0.00	0.00	0.00	0.00	ZnO	0.11	0.00	0.00	0.00	0.00	0.00	ZnO	2.58					
FeO	24.90	20.31	0.00	0.00	FeO	13.86	0.00	0.00	14.82	0.87	0.00	FeO	10.39					
MnO	0.29	0.35	0.00	0.00	MnO	0.25	0.00	0.00	0.13	0.00	0.00	MnO	0.44					
MgO	17.33	20.77	0.00	0.00	MgO	0.52	0.00	0.00	14.66	0.00	0.00	MgO	0.17					
CaO	0.00	0.00	6.56	5.16	CaO	0.00	0.00	0.00	0.00	0.00	5.25	CaO	0.00					
Na <sub>2</sub> O	0.00	0.00	7.88	8.76	Na <sub>2</sub> O	0.00	0.00	0.00	0.00	1.90	8.68	Na <sub>2</sub> O	0.00					
K <sub>2</sub> O	0.06	0.00	0.10	0.06	K <sub>2</sub> O	0.00	0.00	0.00	10.52	10.53	0.06	K <sub>2</sub> O	0.00					
<b>Total</b>	<b>100.02</b>	<b>100.05</b>	<b>100.00</b>	<b>100.00</b>	<b>Total</b>	<b>99.63</b>	<b>100.00</b>	<b>100.00</b>	<b>100.64</b>	<b>99.89</b>	<b>100.01</b>	<b>Total</b>	<b>97.55</b>					
<b>Anions</b>	<b>14</b>	<b>14</b>	<b>8</b>	<b>8</b>	<b>Anions</b>	<b>23</b>	<b>5</b>	<b>5</b>	<b>11</b>	<b>11</b>	<b>8</b>	<b>Anions</b>	<b>23</b>					
Si IV	2.78	2.75	Si	2.67	2.75	Si	3.97	Si	0.94	1.01	Si IV	2.84	Si	3.16	Si	2.75	Si	4.01
Al IV	1.22	1.25	Al	1.34	1.25						Al IV	1.16	Al IV	0.84	Al	1.26		
Σ IV	4.00	4.00	Σ	4.01	4.00	Al	8.77	Al	2.07	1.99	Σ IV	4.00	Σ IV	4.00	Σ	4.00	Al	8.95
						Cr	0.01	0.00	0.00									
Al VI	1.57	1.57	Ca	0.31	0.24	Fe <sup>2+</sup>	1.57				Al VI	0.35	Al VI	1.87	Ca	0.25	Fe <sup>2+</sup>	1.17
Ti	0.01	0.01	Na	0.68	0.75	Mg	0.11	Σ cat	3.02	3.00	Ti	0.07	Ti	0.01	Na	0.75	Mg	0.03
Cr	0.01	0.00	K	0.01	0.00	Zn	0.01				Cr	0.02	Fe <sup>2+</sup>	0.05	K	0.00	Zn	0.25
Fe <sup>2+</sup>	1.88	1.50	Σ	1.00	1.00	Mn	0.02				Fe <sup>2+</sup>	0.87	Mg	0.00	Σ	1.00	Mn	0.04
Mn	0.02	0.02				V	0.01				Mn	0.01	Σ VI	1.93			V	0.00
Mg	2.33	2.73	Σ cat	5.01	5.00	Cr	0.02				Mg	1.53			Σ cat	5.00	Cr	0.00
Ca	0.00	0.00				Ti	0.07				Σ	2.85	Na	0.23			Ti	0.02
Na	0.00	0.00	XAn	0.31	0.24	Σ	1.80						K	0.85	XAn	0.25	Σ	1.52
K	0.01	0.00	XAb	0.68	0.75						K	0.94	Σ	1.08	XAb	0.75		
Σ	5.81	5.83				Σ cat	14.55										Σ cat	14.49
Σ cat	9.81	9.83									Σ cat	7.79	Σ cat	7.01				
Mg#	55.36	64.57									Mg#	63.81	XPa	0.21				

**Note:** XPy, XAlm, XSps and XGrss as defined by Spear (1993). XAn = Ca/(Ca+Na), XAb = Na/(Ca+Na), XPa = Na/(Na+K), Mg# = 100 x Mg/(Mg+Fe)



**Table 6.1:** continued

Sample	62105D	62105D	62105D	62105D	62105D	Sample	Tj 23	Tj 23	Tj 23	Sample	Tj 8	Tj 8	
Mineral	biotite	muscovite	chlorite	chlorite	plag	Mineral	muscovite	biotite	plag	Mineral	sericite	chlorite	
Generation	relic	matrix	post-tect	matrix	matrix	Generation	matrix	matrix	matrix	Generation	matrix	matrix	
SiO <sub>2</sub>	40.75	49.01	30.65	34.10	64.94	SiO <sub>2</sub>	50.70	41.56	65.51	SiO <sub>2</sub>	50.20	33.50	
TiO <sub>2</sub>	1.45	0.45	0.07	0.06	0.00	TiO <sub>2</sub>	0.31	0.82	0.00	TiO <sub>2</sub>	0.58	0.06	
Al <sub>2</sub> O <sub>3</sub>	19.00	38.16	27.19	27.37	21.88	Al <sub>2</sub> O <sub>3</sub>	34.61	18.14	21.59	Al <sub>2</sub> O <sub>3</sub>	37.28	27.68	
Cr <sub>2</sub> O <sub>3</sub>	0.01	0.00	0.01	0.04	0.00	Cr <sub>2</sub> O <sub>3</sub>	0.00	0.00	0.00	Cr <sub>2</sub> O <sub>3</sub>	0.00	0.00	
V <sub>2</sub> O <sub>5</sub>	0.00	0.00	0.00	0.00	0.00	V <sub>2</sub> O <sub>5</sub>	0.00	0.00	0.00	V <sub>2</sub> O <sub>5</sub>	0.00	0.00	
ZnO	0.00	0.00	0.00	0.00	0.00	ZnO	0.00	0.00	0.00	ZnO	0.00	0.00	
FeO	14.13	0.63	21.84	19.06	0.00	FeO	1.31	13.10	0.00	FeO	0.64	12.94	
MnO	0.12	0.00	0.28	0.22	0.00	MnO	0.00	0.00	0.00	MnO	0.00	0.03	
MgO	15.03	0.00	19.91	17.95	0.00	MgO	0.84	15.52	0.00	MgO	0.05	25.70	
CaO	0.00	0.00	0.00	0.00	2.88	CaO	0.00	0.00	2.71	CaO	0.00	0.00	
Na <sub>2</sub> O	0.00	2.44	0.00	0.00	10.26	Na <sub>2</sub> O	1.31	0.34	10.13	Na <sub>2</sub> O	2.44	0.00	
K <sub>2</sub> O	10.22	9.53	0.08	1.22	0.05	K <sub>2</sub> O	10.92	10.52	0.07	K <sub>2</sub> O	8.92	0.14	
<b>Total</b>	<b>100.70</b>	<b>100.22</b>	<b>100.04</b>	<b>100.02</b>	<b>100.00</b>	<b>Total</b>	<b>100.01</b>	<b>100.00</b>	<b>100.00</b>	<b>Total</b>	<b>100.10</b>	<b>100.03</b>	
<b>Anions</b>	<b>11</b>	<b>11</b>	<b>14</b>	<b>14</b>	<b>8</b>	<b>Anions</b>	<b>11</b>	<b>11</b>	<b>8</b>	<b>Anions</b>	<b>11</b>	<b>14</b>	
Si IV	2.83	Si	3.08	Si IV	2.72	2.98	Si	2.86	Si	3.14	Si IV	2.84	
Al IV	1.17	Al IV	0.92	Al IV	1.28	1.02	Al	1.14	Al IV	0.86	Al IV	1.16	
Σ IV	4.00	Σ IV	4.00	Σ IV	4.00	4.00	Σ	4.00	Σ IV	4.00	Σ IV	4.00	
Al VI	0.39	Al VI	1.90	Al VI	1.57	1.79	Ca	0.14	Al VI	1.89	Al VI	1.60	
Ti	0.08	Ti	0.02	Ti	0.00	0.00	Na	0.88	Ti	0.03	Ti	0.00	
Cr	0.00	Fe <sup>2+</sup>	0.03	Cr	0.00	0.00	K	0.00	Fe <sup>2+</sup>	0.03	Cr	0.00	
Fe <sup>2+</sup>	0.82	Mg	0.00	Fe <sup>2+</sup>	1.62	1.39	Σ	1.01	Mg	0.01	Fe <sup>2+</sup>	0.92	
Mn	0.01	Σ VI	1.96	Mn	0.02	0.01	Σ VI	1.96	Mn	1.96	Mn	0.00	
Mg	1.56			Mg	2.63	2.34	Σ cat	5.01	Mg	1.62	Σ cat	4.99	
Σ	2.86	Na	0.30	Ca	0.00	0.00	Na	0.16	Σ	2.82	Σ cat	4.99	
		K	0.76	Na	0.00	0.00	XAn	0.13	Na	0.30	Ca	0.00	
K	0.91	Σ	1.06	K	0.01	0.14	XAb	0.86	K	0.71	Na	0.00	
				Σ	5.86	5.68			Σ	1.01	K	0.01	
Σ cat	7.76	Σ cat	7.02								Σ	5.78	
				Σ cat	9.86	9.68			Σ cat	6.97		Σ cat	9.78
Mg#	65.46	XPa	0.28						XPa	0.29			
				Mg#	61.90	62.67			Mg#	67.86			
											Mg#	77.97	

**Note:** XPy, XAlm, XSpss and XGrss as defined by Spear (1993). XAn = Ca/(Ca+Na), XAb = Na/(Ca+Na), XPa = Na/(Na+K), Mg# = 100 x Mg/(Mg+Fe)

### 6.3.1 Garnet

Garnet is almandine-rich and consists of 69 – 75 % almandine, 7 – 11 % pyrope, 9 – 15 % spessartine and 6 – 13 % grossular, while Fe/Fe+Mg ratios vary between 0.89 and 0.96. Most garnet crystals examined during the petrographic investigation seem to be the result of a single growth episode and consist of a poikilitic core and thin, inclusion-free rim. However, grains that exhibit more complex zoning patterns and multiple growth episodes are also present in most samples (refer to Chapter 3). Qualitative chemical maps of Ca, Mg, Fe and Mn in garnet from sample Tj 18 and 62601C indicate that there is a strong correlation between petrographic and chemical zonation in garnet (Fig. 6.1). This is confirmed by profiles that plot the compositional variations along a traverse across the porphyroblasts (Figs. 6.2 and 6.3).

The zoning profiles exhibited by the garnets are characteristic of growth zoning (Spear, 1993) and modification of the profile by diffusion zoning is considered to be negligible. Both chemical maps and zoning profiles indicate that the felsic schist experienced two episodes of garnet growth. The first episode is manifested in all grains as a poikilitic core and thin, inclusion-free rim. The second generation resulted in the overgrowths that are confined to the pressure shadow sites of certain grains. The first generation has a relatively homogeneous concentration of Ca and Mg and these elements exhibit flat zoning profiles (Figs. 6.2 and 6.3). Fe shows an increase from the core towards the rim, while Mn is relatively enriched in the core and steadily decreases towards the rim in garnet from sample Tj 18 (Fig. 6.2). Mn in garnet from sample 62601C has a constant concentration across the core and rim of the first generation (Fig 6.3).

The major element concentration in second-generation garnet is more variable and differs significantly from the first generation. The most striking contrast is exhibited by Ca, which shows a sharp increase to almost double the values of the first generation (13 – 18 % grossular compared to 5 – 7 % in the first generation). In most garnet grains, grossular reaches a maximum in garnet that grew early during the second generation and then decreases slightly towards the outer edge. Fe shows an abrupt decrease in early second-

generation garnet, but then increases to values that are comparable with the first generation. Garnet from sample Tj 18 exhibits comparable values of Mg and Mn in both generations, with Mg showing a slight increase and Mn decreasing towards the grain boundary. Garnet from sample 62601C displays the opposite trend, with Mg steadily decreasing and Mn sharply increasing towards the grain boundary. The Fe/Fe+Mg ratio of first-generation garnet is constant and similar to the value of second-generation garnet. However, garnet from sample Tj 18 shows a slight decrease in the Fe/Fe+Mg ratio towards the grain boundary, while garnet from sample 62601C displays a steady increase towards the outer edge.

Zoning profiles of the transition trace elements Sc, V, Cr and Co in garnet from sample Tj 18 indicate that these elements have erratic concentrations. However, there is a systematic, two- to threefold increase in V and Cr in second-generation garnet compared to first-generation garnet. Conversely, Sc is relatively depleted in second-generation garnet while Co has similar concentrations in both generations.

REE zoning profiles of garnet from sample Tj 18 show distinctly different concentrations of these elements in the different garnet generations. The heavy REEs (Gd through Lu) are depleted in second-generation garnet relative to first-generation garnet by a factor of 20 or more. Notably, the middle REEs Sm and Eu have comparable concentrations in both generations. The concentrations of the light REEs (La, Ce, Pr and Nd) are below detection limits and could not be investigated. Interestingly, the REEs exhibit a zonation that is not expressed by the major elements or the transition metals. The additional zone is defined by a tenfold decrease in the concentration of the heavy REEs in the core of first-generation garnet and is best illustrated by the profile of garnet #1 (Fig. 6.2a). Garnet #2 exhibits a similar zonation, but could not be readily analyzed because of abundant inclusions.

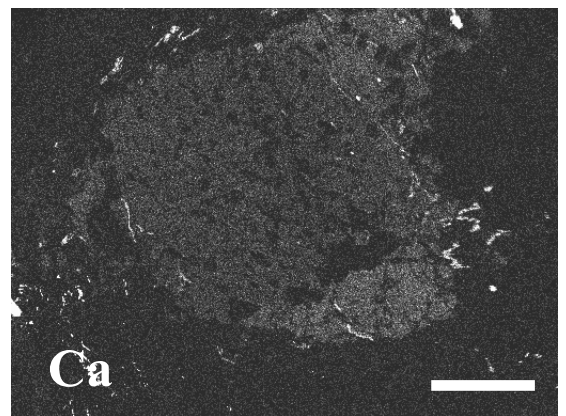
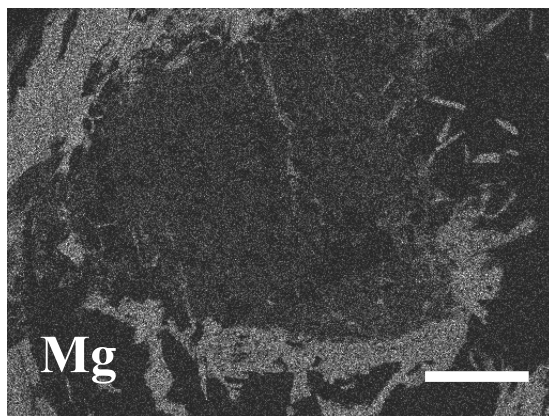
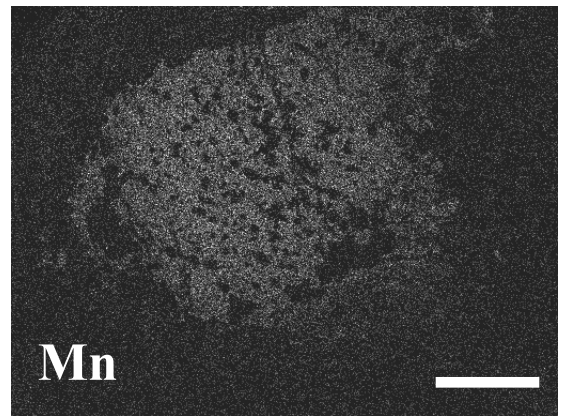
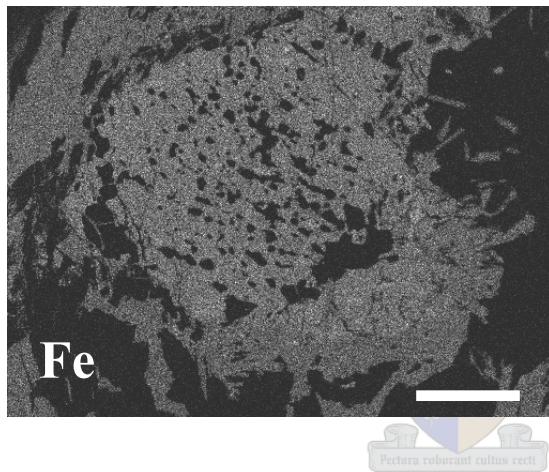
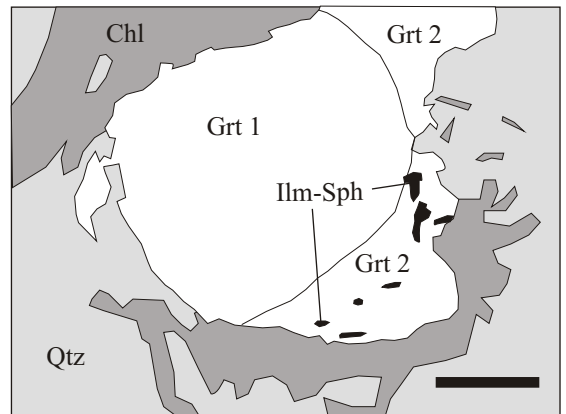
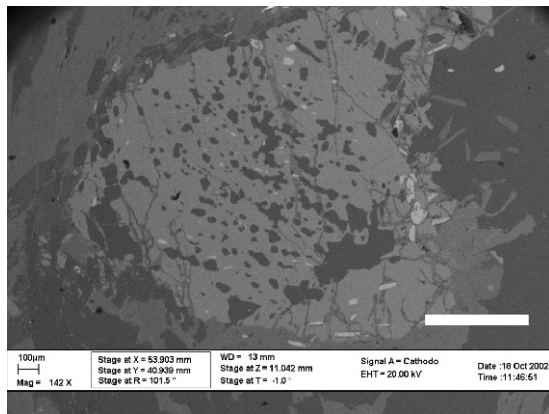


**Figure 6.1a:** Backscatter image, sketch and major element maps of garnet from sample Tj 18, illustrating the strong correlation between petrographic and chemical zonation patterns, most notably in Ca and Mn. Scale bar is 0.5 mm.



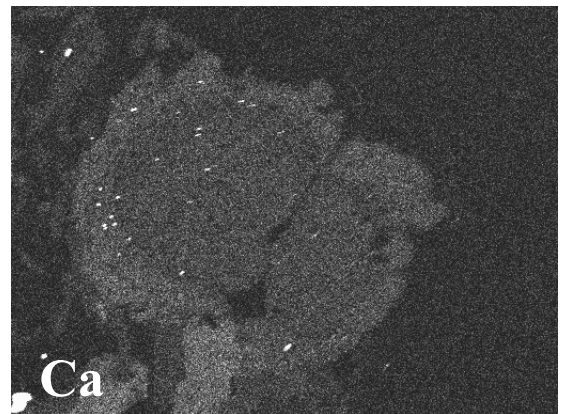
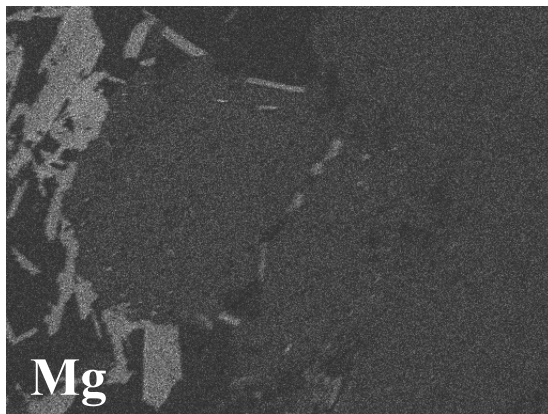
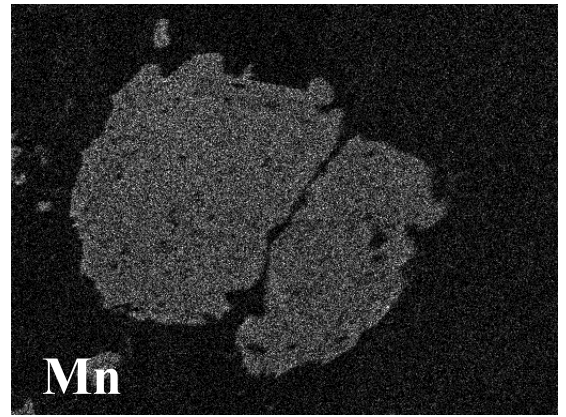
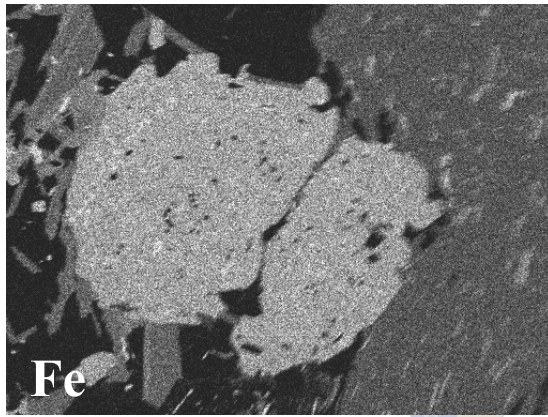
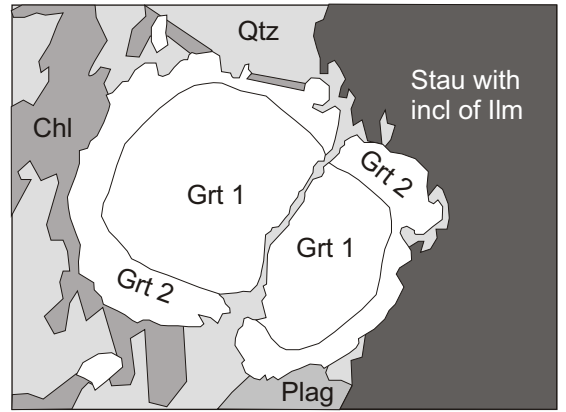
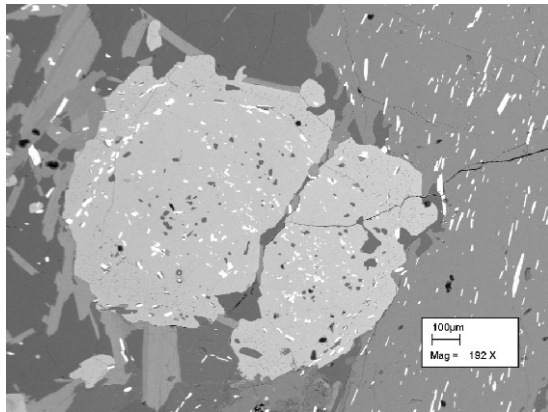


**Figure 6.1b:** Backscatter image, sketch and major element maps of garnet from sample 62601C. Note the correlation between petrographic and chemical zonation patterns, most notably in Ca.



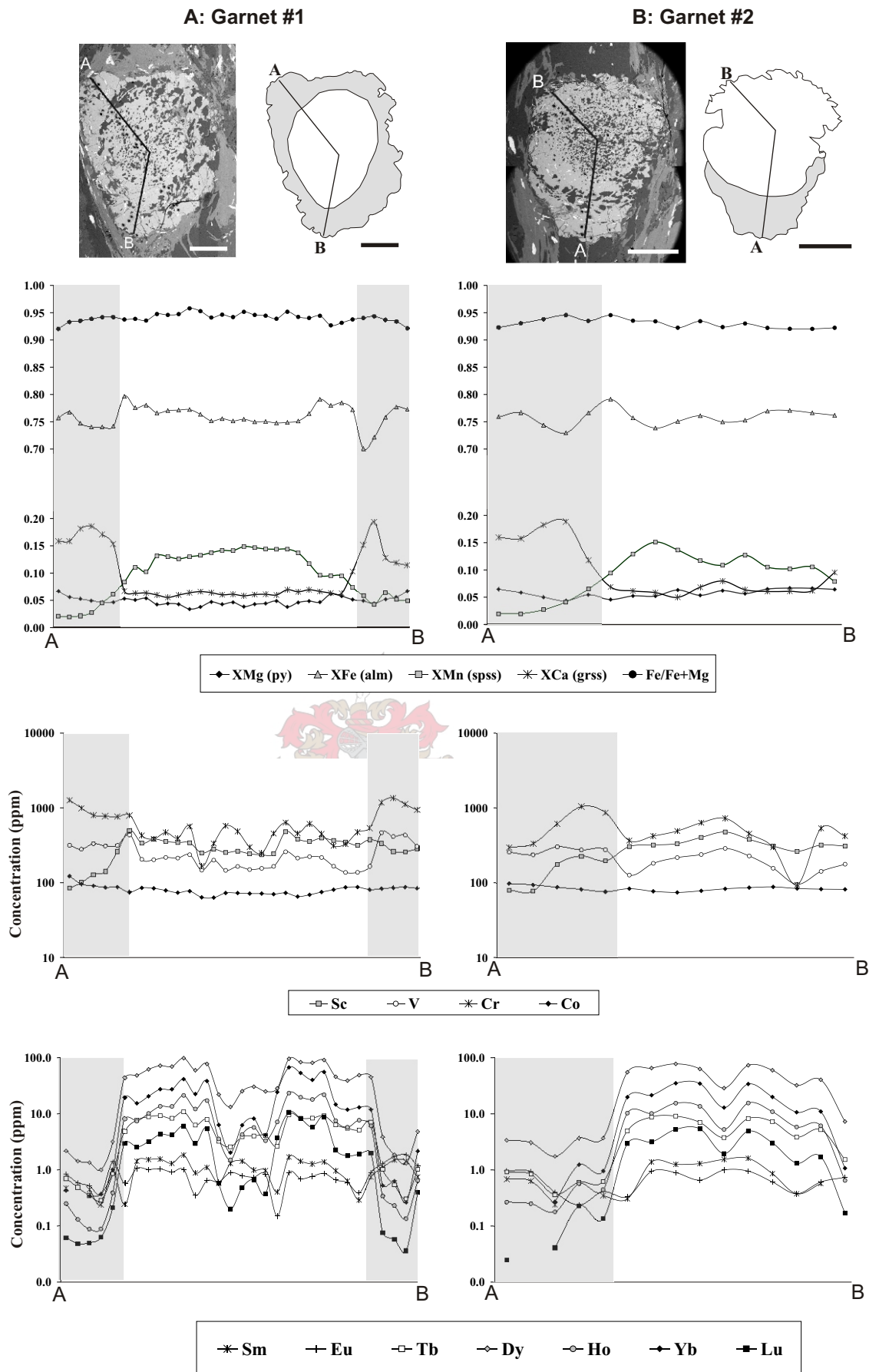


**Figure 6.2a and b:** Major-, trace- and rare earth element zonation patterns of two garnets from sample Tj 18. The location of each traverse is indicated in the photographs and all profiles are plotted from A to B. Scale bar is 0.5 mm.

**C: Garnet #3**

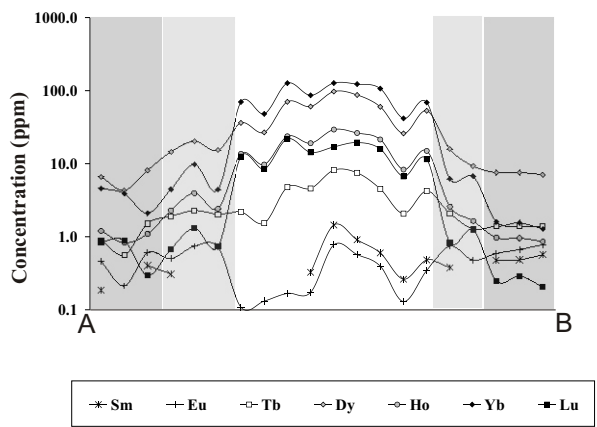
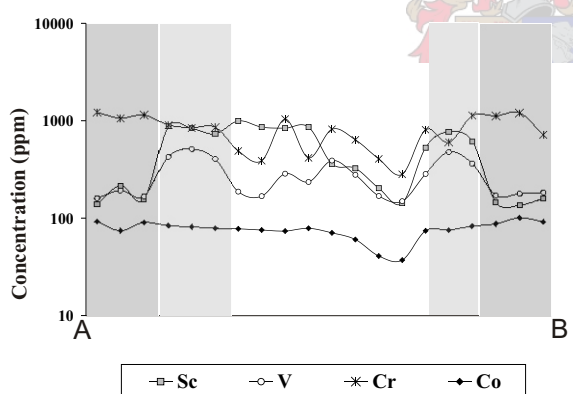
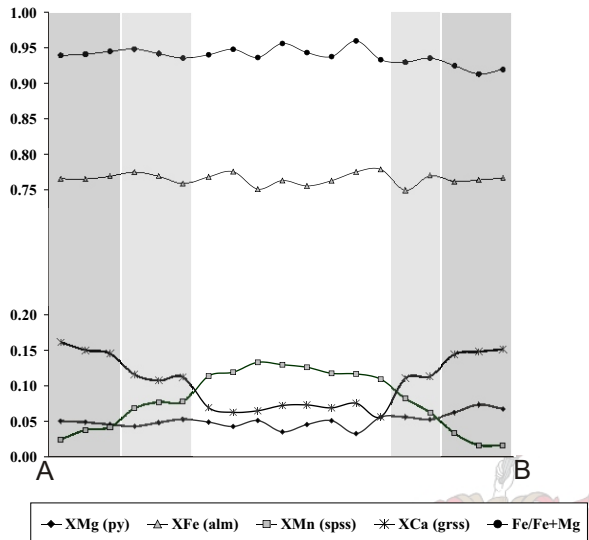
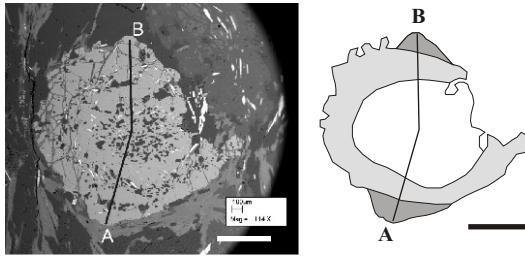


**Figure 6.2c:** (continued) Major-, trace- and rare earth element zonation profiles of a garnet from sample Tj 18. Scale bar is 0.5 mm long.

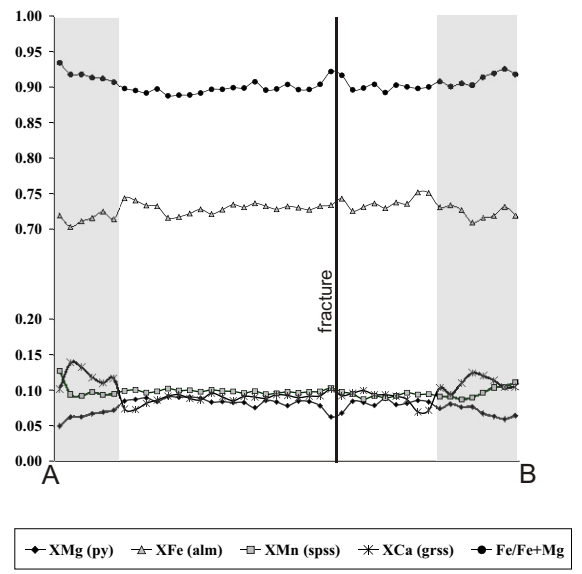
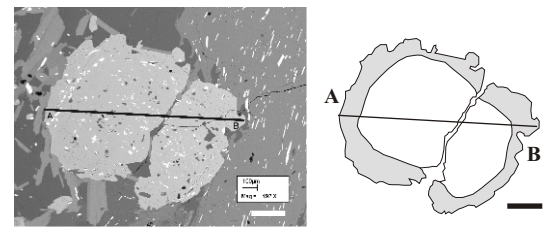
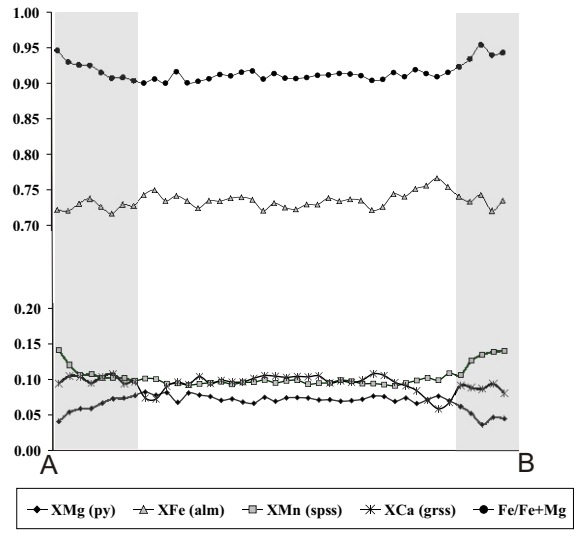
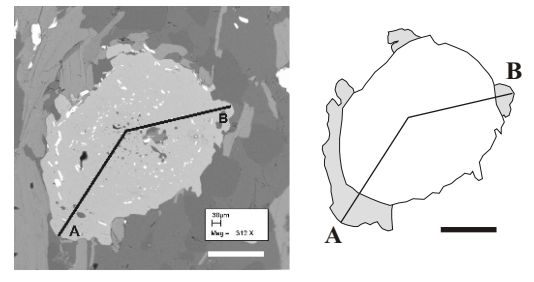


**Figure 6.3:** Major element zoning patterns of two garnets from sample 62601C. Traverses are plotted from A to B; scale bar is 0.2 mm long.

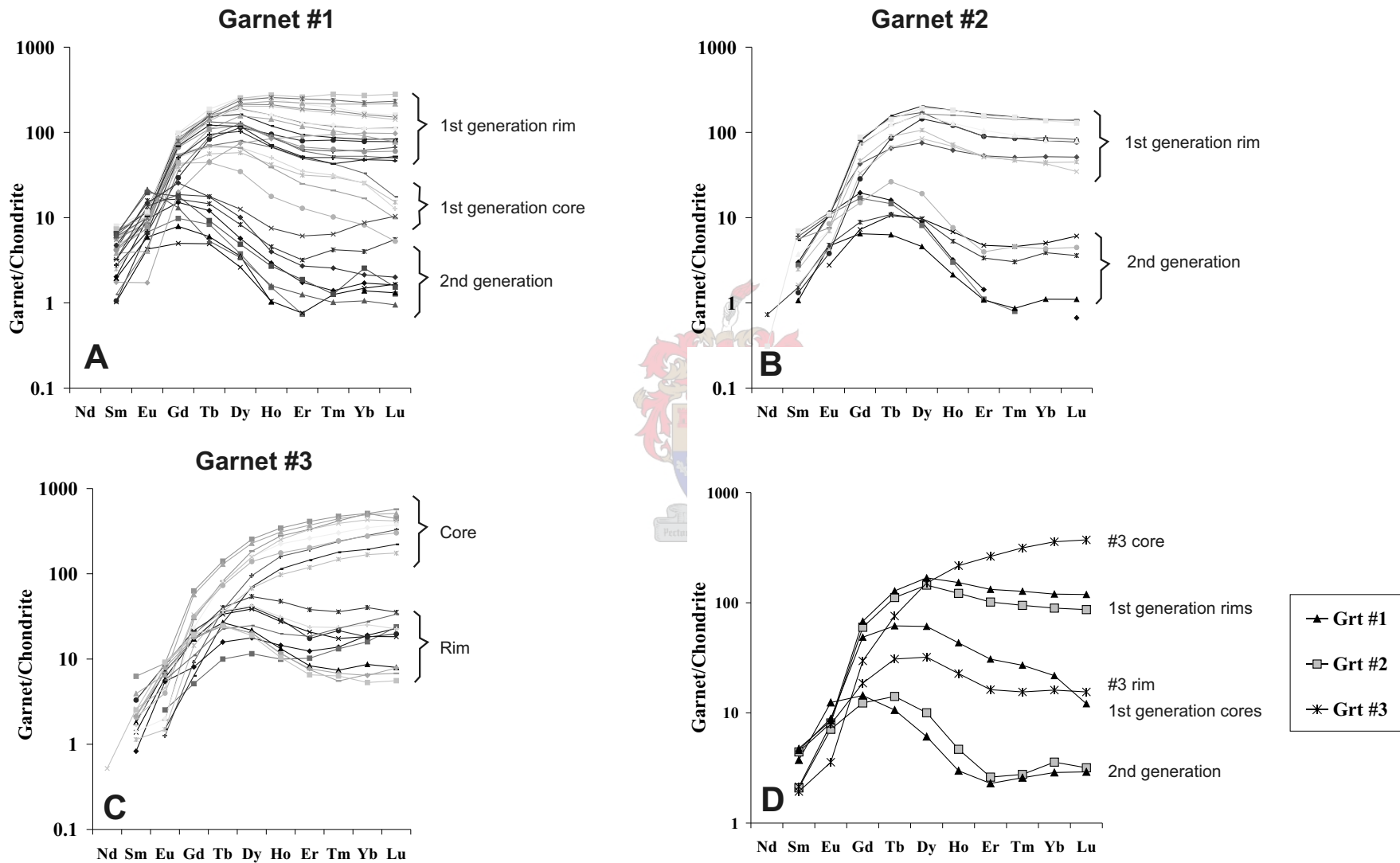


**Figure 6.4: (a-c):** Chondrite-normalized (Taylor and McLennan, 1985) REE profiles of three garnet grains from sample Tj 18. Note the different profiles produced by various garnet generations. **(d):** Comparison of REE in different garnet generations from sample Tj 18. Refer to Figure 6.2 for major-, trace- and rare earth element zoning profiles. Garnets are numbered as in Figure 6.2.

Chondrite-normalized (Taylor and McLennan, 1985) REE profiles reveal that there is a systematic variation in the concentration of the REEs between the various garnet generations (Fig. 6.4a, b and c). Garnet #1 and #2 have similar chondrite-normalized profiles (Fig. 6.4a, b and d), where the first-generation core displays a systematic depletion in Ho through Lu. Conversely, the first-generation rim has similar values of Ho through Lu and does not show any depletion. In turn, second-generation garnet shows a systematic depletion from Gd through Er, with a slight increase in the values of Tm, Yb and Lu. Garnet #3 displays petrographic, major-, trace- and REE zoning which indicates that it appears to have experienced three generations of garnet growth. The chondrite-normalized REE profiles from this garnet are not comparable to the profiles exhibited by garnet #1 and #2 (Fig. 6.4d). The core of garnet #3 shows a systematic enrichment in all the heavy REEs, while the rim exhibits a pattern similar to the rim pattern of garnet #1 and #2, but at significantly higher values (Fig. 6.4c and d).

The trace element and REE zoning profiles correlate well with the major element zoning profiles and confirm that the felsic schist experienced at least two episodes of garnet growth. However, the REE profiles indicate that the first episode may have consisted of two discrete growth events. Because these two events are not manifested in the major element profiles, it is likely that both events occurred under similar pressure-temperature conditions and are part of the same growth episode. The different REE concentrations and chondrite-normalized profiles could be the result of a change in the mineral assemblage as the destabilization of a phase rich in these elements might liberate them to be incorporated into garnet that is crystallizing at that time.

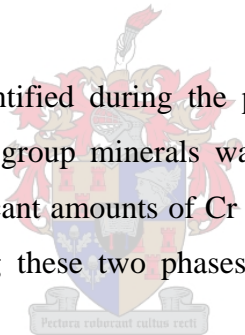
Significantly, none of the chondrite-normalized profiles displays an Eu anomaly and are typical profiles of garnet that crystallized under amphibolite-facies conditions (Schwandt et al., 1996; Villaseca et al., 2003). The profiles of first-generation rims have a similar shape to chondrite-normalized REE profiles recorded in garnet from staurolite-zone pelites (Schwandt et al., 1996). Likewise, second-generation garnet profiles have a shape most comparable to the rims of lower-grade garnet-zone pelites described during the same study.

### 6.3.2 *Staurolite*

Staurolite porphyroblasts are known to commonly exhibit chemical zonation (e.g. Spear, 1993), but no evidence of zonation is apparent in staurolite investigated during this study. Staurolite crystals have constant chemical compositions within a single grain and between different grains within the same sample. Staurolite also does not show any evidence of petrographic zonation, but most crystals have suffered plastic deformation subsequent to crystallization. It is likely that dynamic recrystallization during deformation destroyed any chemical zonation that might have been exhibited by these porphyroblasts. However, staurolite from different samples does contain variable amounts of Zn, V and Cr, possibly reflecting variations in bulk composition of the rocks.

### 6.3.3 *Aluminosilicates*

Kyanite and sillimanite were identified during the petrographic investigation and the presence of these aluminosilicate-group minerals was confirmed by mineral chemical analysis. Kyanite contains significant amounts of Cr (ca. 0.4 wt %), while very little Cr is present in sillimanite, allowing these two phases to be readily distinguished on a geochemical basis.



### 6.3.4 *Biotite*

Biotite primarily occurs in the matrix of felsic schists and has a homogeneous composition within a single sample. Biotite is also found as inclusions in garnet and these grains usually exhibit higher Mg-numbers than biotite found in the matrix. Matrix biotite has Mg-numbers between 55 and 67, compared with values of 60 to 74 from biotite inclusions. Both inclusion and matrix biotite have Ti concentrations that vary from 0,82 to 1,45 wt % TiO<sub>2</sub>. The Na content in biotite is below the limit of quantification (<0,5 wt % Na<sub>2</sub>O), while all grains contain 18 – 19 wt % Al<sub>2</sub>O<sub>3</sub>, corresponding to Al(VI) of 0,35 to 0,39 cations per formula unit.



### 6.3.5 Chlorite

The petrographic observation that two generations of chlorite are present in most felsic schist samples is confirmed by mineral chemistry. The two generations are intimately associated (Fig. 6.5), but have significantly different chemical compositions. First-generation chlorite is present in the matrix of all samples and has Mg-numbers that vary between 51 and 55. Conversely, second-generation chlorite does not occur in all samples and is present in variable amounts. Second-generation chlorite overprints first-generation chlorite (Fig. 6.5) and also occurs as a product of garnet and biotite breakdown. This generation of chlorite has Mg-numbers of 40 to 42, which is significantly lower than first-generation chlorite. Additionally, chlorite inclusions in garnet have Mg-numbers of 63 to 65.

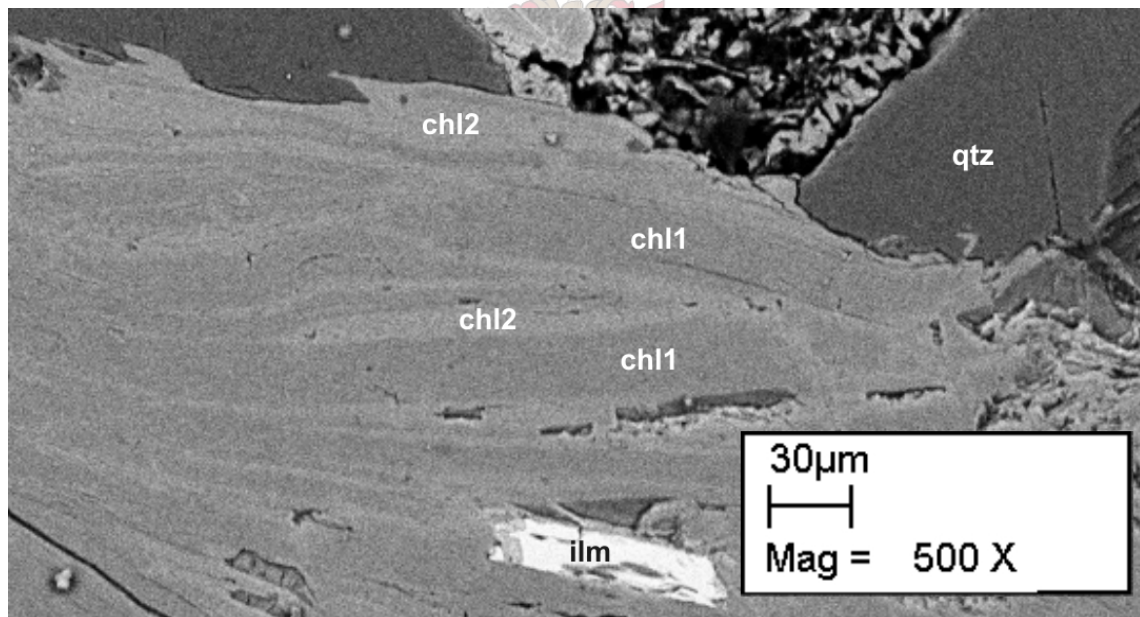


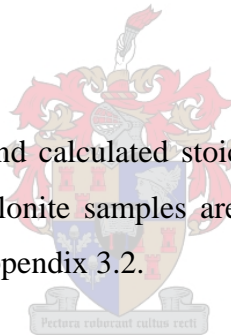
**Figure 6.5:** Backscatter electron image of two generations of chlorite that are typically present in felsic schist. Note the intimate association of the two generations and the replacement of first-generation chlorite (ch1, darker patches) by second-generation chlorite (ch2, lighter patches).

### 6.3.6 Plagioclase

Plagioclase is only present in the matrix of felsic schist samples and has a constant composition within a single sample. Plagioclase from most felsic schist samples has an anorthite content of 21 – 24 %, but certain grains in sample 62105F as well as plagioclase from sample Tj 18 have anorthite contents of 31 and 37 % respectively. Plagioclase does not display any chemical zoning but shows evidence of plastic deformation and dynamic recrystallization. It is likely that plagioclase underwent re-equilibration during deformation that destroyed any chemical zonation that might have been exhibited by these crystals. The An-rich grains preserved in certain samples are probably contained in low-strain lithons and escaped re-equilibration during deformation because of strain partitioning around these zones.

## 6.4 Amphibolite

The major element composition and calculated stoichiometry of minerals that occur in amphibolite and garnet-quartz mylonite samples are summarized in Table 6.2 and the complete dataset is presented in Appendix 3.2.



### 6.4.1 Garnet

Garnet in amphibolite is almandine-rich and consists of 51 – 63 % almandine, 1 – 5 % pyrope, 24 – 27 % grossular and 9 – 21 % spessartine. Garnet does not typically exhibit compositional variations (Fig. 6.6) and even garnet that displays petrographic zonation has a relatively constant major element composition (Fig. 6.6a, b and c). The slight chemical variation between garnet from different samples is most likely caused by differences in bulk-rock composition. However, garnet from sample 61406 (Fig. 6.6b) is enriched in Mn and depleted in Fe relative to garnet from other samples (Fig. 6.6a and c). Sample 61406 is spatially not associated with the other amphibolite samples and has been more adversely affected by retrogression than other amphibolites. In the case of sample 61406, the differences in garnet composition can probably be related to a difference in

**Table 6.2:** Major element content and structural formulae for representative mineral analyses from amphibolite and chlorite schist. Mineral stoichiometries are calculated by the number of oxygen-equivalent anions in the mineral formula.

Sample Mineral Generation	Tj 3 gamet peak	Tj3 hbl matrix	Tj3 epidote inclusion	Tj 3 epidote matrix	Tj 3 plag matrix	Tj 3 sphene matrix	Tj 3 chlorite retrograde	Sample Mineral Generation	62107 garnet peak	62107 garnet "core"	62107 hbl matrix	62107 epidote matrix
SiO <sub>2</sub>	36.85	41.87	40.10	40.28	60.83	32.54	30.97	SiO <sub>2</sub>	37.13	36.90	44.08	40.09
TiO <sub>2</sub>	0.15	0.71	0.16	0.19	0.00	37.13	0.00	TiO <sub>2</sub>	0.08	0.10	0.43	0.20
Al <sub>2</sub> O <sub>3</sub>	20.79	14.76	26.85	26.95	24.73	1.00	21.72	Al <sub>2</sub> O <sub>3</sub>	20.97	20.81	16.74	28.15
Cr <sub>2</sub> O <sub>3</sub>	0.00	0.00	0.06	0.03	0.00	0.00	0.00	Cr <sub>2</sub> O <sub>3</sub>	0.00	0.00	0.06	0.14
Fe <sub>2</sub> O <sub>3</sub>	0.00	0.00	8.83	8.66	0.00	0.00	0.88	Fe <sub>2</sub> O <sub>3</sub>	0.00	0.00	0.00	7.16
FeO	27.80	23.24	0.00	0.00	0.00	0.69	36.36	FeO	27.04	25.34	18.68	0.00
MnO	5.02	0.40	0.15	0.20	0.00	0.07	0.38	MnO	4.99	6.96	0.30	0.47
MgO	0.23	4.44	0.00	0.00	0.00	0.01	8.09	MgO	0.97	0.87	6.65	0.00
CaO	9.16	11.40	23.86	23.69	6.18	28.64	0.14	CaO	8.85	9.02	11.75	23.80
Na <sub>2</sub> O	0.00	2.13	0.00	0.00	8.14	0.00	1.20	Na <sub>2</sub> O	0.00	0.00	0.99	0.00
K <sub>2</sub> O	0.00	1.03	0.00	0.00	0.12	0.00	0.17	K <sub>2</sub> O	0.00	0.00	0.35	0.00
<b>Total</b>	100.00	99.98	100.00	100.01	100.00	100.09	99.91	<b>Total</b>	100.02	100.00	100.02	100.00
<b>Anions</b>	<b>12</b>	<b>23</b>	<b>13</b>	<b>13</b>	<b>8</b>	<b>5</b>	<b>14</b>	<b>Anions</b>	<b>12</b>	<b>12</b>	<b>23</b>	<b>13</b>
Si	3.00	Si 6.33 Al IV 1.67	Si 3.06 Al 2.42 Fe <sup>3+</sup> 0.51	3.07	Si 2.70 Al 1.30 Σ 4.00	Si 1.06 Al 1.00 Ca 1.00	Si IV 2.99 Al IV 1.01 Σ IV 4.00	Si 3.00	3.00	Si 6.42 Al IV 1.58	Si 3.05	Si 3.05
Al	1.99	Σ IV 8.00	Al 2.42 Fe <sup>3+</sup> 0.51	2.42	Σ 4.00	Ca 1.00	Σ IV 4.00	Al 2.00	1.99	Σ IV 8.00	Al 2.52 Fe <sup>3+</sup> 0.41	Al 2.52
Ti	0.01	Al M123 0.96	Cr 0.00	0.00	Ca 0.29	Ti 0.91	Al VI 1.45	Ti 0.01	0.01	Al M123 1.29	Cr 0.01	Cr 0.01
Cr	0.00	Cr 0.00	Mn 0.01	0.01	Na 0.70	Al 0.04	Ti 0.00	Cr 0.00	0.00	Cr 0.01	Mn 0.02	Mn 0.02
Fe <sup>3+</sup>	0.00	Ti 0.08	Σ 2.94	2.93	K 0.01	Fe <sup>2+</sup> 0.02	Cr 0.00	Fe <sup>3+</sup> 0.00	0.00	Ti 0.05	Σ 2.97	Σ 2.97
Fe <sup>2+</sup>	1.89	Mg 1.00	Σ 1.00	1.00	Σ 1.00	Mn 0.00	Fe <sup>3+</sup> 0.00	Fe <sup>2+</sup> 0.00	1.83	Mg 1.44	Σ 2.97	Σ 2.97
Mn	0.28	Fe M123 2.94	Ca 1.95	1.94	Σ cat 5.00	Mg 0.00	Fe <sup>2+</sup> 3.00	Mn 0.28	0.39	Fe M123 2.21	Ca 1.94	Ca 1.94
Mg	0.03	Mn M123 0.00	Σ cat 7.95	7.94	Σ cat 5.00	Σ 0.97	Mn 0.03	Mg 0.12	0.11	Mn M123 0.00	Σ cat 7.96	Σ cat 7.96
Ca	0.80	Σ M123 5.00	Σ cat 7.95	7.94	XAn 0.29	Σ cat 3.02	Mg 1.16	Ca 0.77	0.78	Σ M123 5.00	Σ cat 7.96	Σ cat 7.96
Σ cat	8.00	Fe M4 0.00 Mn M4 0.02	XPs 0.17	0.17	XAb 0.70	Na 0.22	Ca 0.01	Σ cat 7.99	8.00	Fe M4 0.06 Mn M4 0.03	XPs 0.14	XPs 0.14
XPy	0.01	Ca 1.85	Σ cat 7.95	7.94	XAn 0.29	Σ cat 3.02	Ca 0.01	XPy 0.04	0.04	Ca 1.83	Σ cat 7.96	Σ cat 7.96
XAlm	0.63	Na M4 0.14	Σ cat 7.95	7.94	XAn 0.29	Σ cat 3.02	Ca 0.01	XAlm 0.61	0.57	Na M4 0.08	Σ cat 7.96	Σ cat 7.96
XSpss	0.09	Σ M4 2.00	Σ cat 7.95	7.94	XAn 0.29	Σ cat 3.02	Ca 0.01	XSpss 0.09	0.13	Σ M4 2.00	Σ cat 7.96	Σ cat 7.96
XGrss	0.27	Σ cat 7.95	Σ cat 7.95	7.94	XAn 0.29	Σ cat 3.02	Ca 0.01	XGrss 0.26	0.26	Σ cat 7.96	Σ cat 7.96	Σ cat 7.96
Fe/Fe+Mg	0.99	A Na 0.49 A K 0.20 Σ A 0.69 Σ cat 15.69	Σ cat 7.95	7.94	XAn 0.29	Σ cat 3.02	Ca 0.01	Fe/Fe+Mg 0.94	0.94	A Na 0.20 A K 0.07 Σ A 0.27 Σ cat 15.27	Σ cat 7.96	Σ cat 7.96

**Note:** Fe<sup>3+</sup> is calculated using the formula of Droop (1987). XPy, XAlm, XSpss and XGrss as defined by Spear (1993). XAn = Ca/(Ca+Na), XAb = Na/(Ca+Na), XPs = Fe<sup>3+</sup>/(Fe<sup>3+</sup>+Al)

**Table 6.2:** continued

Sample Mineral Generation	62107 plag matrix	62107 sphene matrix	Sample Mineral Generation	61406 garnet peak	61406 garnet decomp	61406 zoisite inclusion	61406 amph incl	61406 hbl matrix	61406 plag peak	61406 plag decomp	61406 plag matrix	61406 sphene inclusion	61406 chlorite decomp	61406 chlorite post-tect						
SiO <sub>2</sub>	58.14	32.38	SiO <sub>2</sub>	37.01	36.74	40.35	50.61	47.62	60.67	62.71	62.20	31.64	31.92	31.57						
TiO <sub>2</sub>	0.00	35.06	TiO <sub>2</sub>	0.22	0.14	0.11	0.43	0.45	0.00	0.00	0.00	37.13	0.13	0.16						
Al <sub>2</sub> O <sub>3</sub>	26.65	2.68	Al <sub>2</sub> O <sub>3</sub>	20.88	21.19	30.96	8.99	13.59	24.77	23.49	23.85	1.58	24.87	25.24						
Cr <sub>2</sub> O <sub>3</sub>	0.00	0.00	Cr <sub>2</sub> O <sub>3</sub>	0.00	0.00	0.00	0.13	0.07	0.00	0.00	0.00	0.00	0.14	0.05						
Fe <sub>2</sub> O <sub>3</sub>	0.00	0.00	Fe <sub>2</sub> O <sub>3</sub>	0.00	0.00	3.67	0.00	0.00	0.00	0.00	0.00	0.00	0.00	0.00						
FeO	0.00	0.98	FeO	21.80	25.33	0.00	13.15	15.09	0.00	0.00	0.00	0.41	22.14	21.85						
MnO	0.00	0.28	MnO	10.97	9.92	0.52	1.39	0.67	0.00	0.00	0.00	0.26	0.39	0.39						
MgO	0.00	0.00	MgO	1.08	1.31	0.00	13.36	10.29	0.00	0.00	0.00	0.00	20.37	20.75						
CaO	8.16	28.91	CaO	8.04	5.37	24.39	11.60	11.04	6.37	4.59	4.91	29.17	0.00	0.00						
Na <sub>2</sub> O	6.98	0.00	Na <sub>2</sub> O	0.00	0.00	0.00	0.24	0.91	8.11	9.14	9.01	0.00	0.00	0.00						
K <sub>2</sub> O	0.08	0.00	K <sub>2</sub> O	0.00	0.00	0.00	0.14	0.28	0.07	0.08	0.05	0.00	0.04	0.02						
<b>Total</b>	<b>100.00</b>	<b>100.29</b>	<b>Total</b>	<b>100.00</b>	<b>100.00</b>	<b>100.00</b>	<b>100.00</b>	<b>99.99</b>	<b>99.99</b>	<b>100.00</b>	<b>100.00</b>	<b>100.17</b>	<b>100.01</b>	<b>100.02</b>						
<b>Anions</b>	<b>8</b>	<b>5</b>	<b>Anions</b>	<b>12</b>	<b>12</b>	<b>13</b>	<b>23</b>	<b>23</b>	<b>8</b>	<b>8</b>	<b>8</b>	<b>5</b>	<b>14</b>	<b>14</b>						
Si	2.60	Si	1.05	Si	3.01	3.00	Si	3.03	Si	7.16	6.79	Si	2.70	2.78	2.76	Si	1.03	Si IV	2.84	2.81
Al	1.40			Al	2.01	2.04	Al	2.74	Al IV	0.84	1.21	Al	1.30	1.23	1.25			Al IV	1.16	1.19
Σ	4.00	Ca	1.00			Fe <sup>3+</sup>	0.21	Σ IV	8.00	8.00	Σ	4.00	4.00	4.00	Ca	1.02	Σ IV	4.00	4.00	
Ca	0.39	Ti	0.99	Ti	0.01	0.01	Cr	0.00	Al M123	0.66	1.07	Ca	0.30	0.22	0.23	Ti	0.99	Al VI	1.45	1.45
Na	0.60	Al	0.10	Cr	0.00	0.00	Mn	0.03	Cr	0.01	0.01	Na	0.70	0.78	0.77	Al	0.06	Ti	0.01	0.01
K	0.00	Fe <sup>2+</sup>	0.03	Fe <sup>3+</sup>	0.00	0.00	Σ	2.98	Ti	0.05	0.05	K	0.00	0.00	0.00	Fe <sup>2+</sup>	0.01	Cr	0.01	0.00
Σ	1.00	Mn	0.01	Fe <sup>2+</sup>	1.49	1.73			Mg	2.82	2.19	Σ	1.01	1.01	1.01	Mn	0.01	Fe <sup>3+</sup>	0.00	0.00
		Mg	0.00	Mn	0.62	0.56	Ca	1.96	Fe M123	1.46	1.68					Mg	0.00	Fe <sup>2+</sup>	1.65	1.62
Σ cat	5.00	Σ	1.13	Mg	0.13	0.16			Mn M123	0.00	0.00	Σ cat	5.00	5.01	5.01	Σ	1.06	Mn	0.02	0.02
				Ca	0.70	0.47	Σ cat	7.98	Σ M123	5.00	5.00							Mg	2.70	2.75
XAn	0.39	Σ cat	3.18	Σ cat	7.97	7.97	XPs	0.07	Fe M4	0.10	0.11	XAn	0.30	0.22	0.23	Σ cat	3.11	Ca	0.00	0.00
XAb	0.61			XPy	0.04	0.05			Mn M4	0.14	0.07	XAb	0.69	0.78	0.77			Na	0.00	0.00
				XAlm	0.51	0.59			Ca	1.76	1.69							K	0.00	0.00
				XSpss	0.21	0.19			Na M4	0.01	0.13							Σ	5.84	5.86
				XGrss	0.24	0.16			Σ M4	2.00	2.00							Σ cat	9.84	9.86
				Fe/Fe+Mg	0.92	0.92			A Na	0.05	0.12									
									A K	0.02	0.05									
									Σ A	0.08	0.17									
									Σ cat	15.08	15.17									

**Note:** Fe<sup>3+</sup> is calculated using the formula of Droop (1987). XPy, XAlm, XSpss and XGrss as defined by Spear (1993). XAn = Ca/(Ca+Na), XAb = Na/(Ca+Na), XPs = Fe<sup>3+</sup>/(Fe<sup>3+</sup>+Al)

**Table 6.2:** continued

Sample Mineral Generation	62210 hbl matrix	62210 plag matrix	62210 sphene matrix	Sample Mineral Generation	Tj14 hbl matrix	Tj 14 epidote matrix	Tj 14 plag matrix	Tj 14 sphene matrix	Sample Mineral Generation	62105A garnet euh core	62105A garnet peak	62105A hbl matrix	62105A cumm matrix
SiO <sub>2</sub>	48.37	62.14	31.68	SiO <sub>2</sub>	54.34	40.34	61.92	32.44	SiO <sub>2</sub>	36.00	36.24	49.59	54.39
TiO <sub>2</sub>	0.75	0.00	37.78	TiO <sub>2</sub>	0.19	0.09	0.00	38.07	TiO <sub>2</sub>	0.07	0.15	0.32	0.05
Al <sub>2</sub> O <sub>3</sub>	9.88	23.89	1.00	Al <sub>2</sub> O <sub>3</sub>	4.56	27.80	23.99	0.48	Al <sub>2</sub> O <sub>3</sub>	20.47	20.85	7.55	0.23
Cr <sub>2</sub> O <sub>3</sub>	0.14	0.00	0.00	Cr <sub>2</sub> O <sub>3</sub>	0.00	0.04	0.00	0.00	Cr <sub>2</sub> O <sub>3</sub>	0.00	0.00	0.09	0.02
Fe <sub>2</sub> O <sub>3</sub>	0.00	0.00	0.00	Fe <sub>2</sub> O <sub>3</sub>	0.00	7.47	0.00	0.00	Fe <sub>2</sub> O <sub>3</sub>	0.00	0.00	0.00	0.00
FeO	17.49	0.00	0.72	FeO	11.18	0.00	0.00	0.28	FeO	27.22	31.62	21.33	32.42
MnO	0.43	0.00	0.02	MnO	0.24	0.03	0.00	0.08	MnO	11.02	3.51	0.30	0.94
MgO	9.90	0.00	0.05	MgO	15.65	0.00	0.00	0.02	MgO	0.21	0.67	8.70	11.41
CaO	11.86	4.95	28.76	CaO	12.75	24.27	5.42	28.63	CaO	5.02	6.98	11.67	0.98
Na <sub>2</sub> O	0.84	8.96	0.00	Na <sub>2</sub> O	0.85	0.00	8.54	0.00	Na <sub>2</sub> O	0.00	0.00	0.29	0.00
K <sub>2</sub> O	0.35	0.07	0.00	K <sub>2</sub> O	0.22	0.00	0.13	0.00	K <sub>2</sub> O	0.00	0.00	0.15	0.00
<b>Total</b>	<b>100.01</b>	<b>100.00</b>	<b>100.01</b>	<b>Total</b>	<b>100.00</b>	<b>100.02</b>	<b>100.00</b>	<b>100.00</b>	<b>Total</b>	<b>100.01</b>	<b>100.00</b>	<b>100.00</b>	<b>100.43</b>
<b>Anions</b>	<b>23</b>	<b>8</b>	<b>5</b>	<b>Anions</b>	<b>23</b>	<b>13</b>	<b>8</b>	<b>5</b>	<b>Anions</b>	<b>12</b>	<b>12</b>	<b>23</b>	<b>23</b>
Si	7.00	Si 2.75	Si 1.03	Si	7.60	Si 3.07	Si 2.75	Si 0.97	Si	2.99	2.96	Si 7.26	8.07
Al IV	1.00	Al 1.25		Al IV	0.40	Al 1.25	Al 1.25					Al IV 0.74	0.00
Σ IV	8.00	Σ 4.00	Ca 1.00	Σ IV	8.00	Al 2.49	Σ 4.00	Ca 0.97	Al	2.01	2.01	Σ IV 8.00	8.07
						Fe <sup>3+</sup> 0.43							
Al M123	0.69	Ca 0.24	Ti 0.98	Al M123	0.35	Cr 0.00	Ca 0.26	Ti 1.05	Ti	0.00	0.01	Al M123 0.57	0.04
Cr	0.02	Na 0.77	Al 0.04	Cr	0.00	Mn 0.00	Na 0.73	Al 0.02	Cr	0.00	0.00	Cr 0.01	0.00
Ti	0.08	K 0.00	Fe <sup>2+</sup> 0.02	Ti	0.02	Σ 2.92	K 0.01	Fe <sup>2+</sup> 0.01	Fe <sup>3+</sup>	0.00	0.00	Ti 0.04	0.01
Mg	2.13	Σ 1.01	Mn 0.00	Mg	3.26		Σ 1.00	Mn 0.00	Fe <sup>2+</sup>	1.89	2.16	Mg 1.90	2.52
Fe M123	2.08		Mg 0.00	Fe M123	1.31	Ca 1.98		Mg 0.00	Mn	0.63	0.20	Fe M123 2.49	2.43
Mn M123	0.00	Σ cat 5.01	Σ 1.04	Mn M123	0.02		Σ cat 5.00	Σ 1.08	Mg	0.03	0.08	Mn M123 0.00	0.00
Σ M123	5.00			Σ M123	4.96	Σ cat 7.96			Ca	0.45	0.61	Σ M123 5.00	5.00
		XAn 0.23	Σ cat 3.08				XAn 0.26	Σ cat 3.02					
Fe M4	0.04	XAb 0.76		Fe M4	0.00	XPs 0.15	XAb 0.73		Σ cat	8.00	8.03	Fe M4 0.13	1.59
Mn M4	0.04			Mn M4	0.00							Mn M4 0.03	0.10
Ca	1.84			Ca	1.91				XPy	0.01	0.03	Ca 1.83	0.16
Na M4	0.08			Na M4	0.09				XAlm	0.63	0.71	Na M4 0.01	0.00
Σ M4	2.00			Σ M4	2.00				XSpss	0.21	0.06	Σ M4 2.00	1.84
									XGrss	0.15	0.20		
A Na	0.15			A Na	0.14				Fe/Fe+Mg	0.99	0.96	A Na 0.07	0.00
A K	0.06			A K	0.04							A K 0.03	0.00
Σ A	0.22			Σ A	0.18							Σ A 0.10	0.00
Σ cat	15.22			Σ cat	15.14							Σ cat 15.10	14.91

**Note:** Fe<sup>3+</sup> is calculated using the formula of Droop (1987). XPy, XAlm, XSpss and XGrss as defined by Spear (1993). XAn = Ca/(Ca+Na), XAb = Na/(Ca+Na), XPs = Fe<sup>3+</sup>/(Fe<sup>3+</sup>+Al)

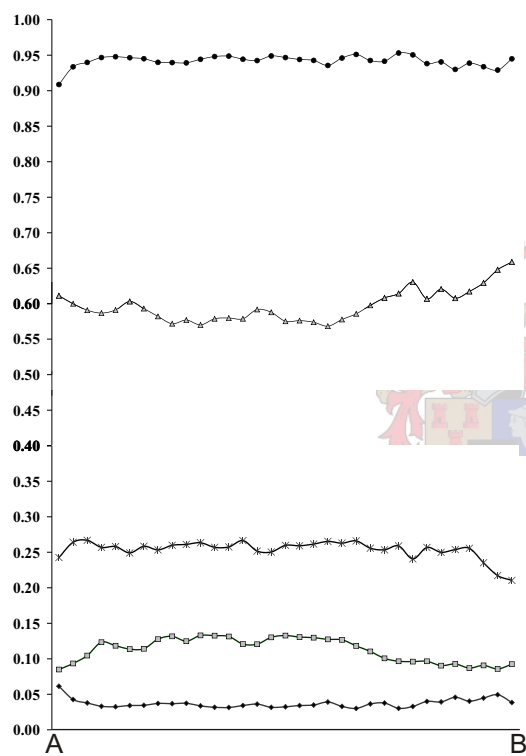
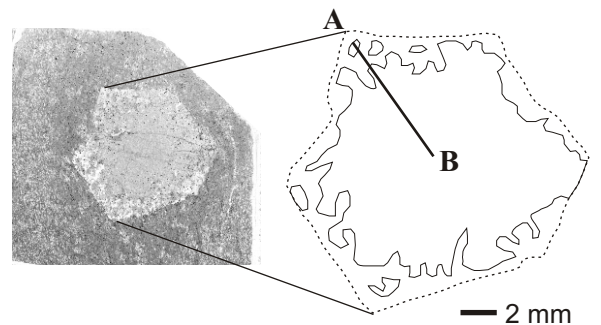
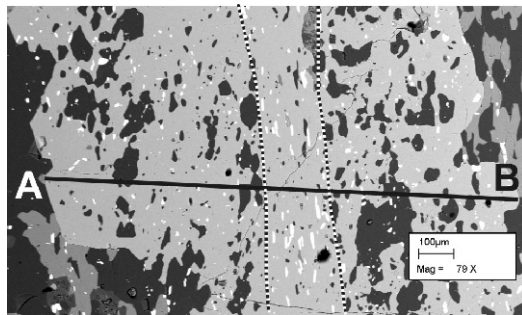


**Table 6.2:** continued

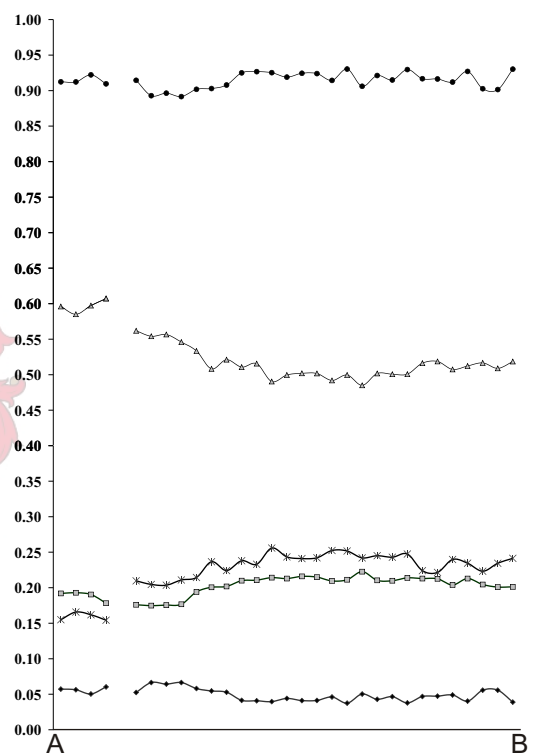
Sample	62105A	62105A	Sample	61610	61610	61610
Mineral	cumm	cumm	Mineral	garnet	chlorite	61610
Generation	rim incl	core incl	Generation		matrix	muscovite
SiO <sub>2</sub>	54.61	55.18	SiO <sub>2</sub>	35.96	27.09	49.46
TiO <sub>2</sub>	0.01	0.03	TiO <sub>2</sub>	0.16	0.11	0.23
Al <sub>2</sub> O <sub>3</sub>	0.25	0.00	Al <sub>2</sub> O <sub>3</sub>	20.34	24.54	33.96
Cr <sub>2</sub> O <sub>3</sub>	0.07	0.02	Cr <sub>2</sub> O <sub>3</sub>	0.00	0.03	0.00
Fe <sub>2</sub> O <sub>3</sub>	0.00	0.00	Fe <sub>2</sub> O <sub>3</sub>	0.00	0.00	0.00
FeO	31.65	30.89	FeO	24.76	41.29	3.98
MnO	0.93	2.23	MnO	14.29	0.77	0.00
MgO	12.24	11.62	MgO	0.00	6.10	0.00
CaO	0.76	0.70	CaO	4.71	0.00	0.00
Na <sub>2</sub> O	0.00	0.00	Na <sub>2</sub> O	0.00	0.00	1.38
K <sub>2</sub> O	0.00	0.02	K <sub>2</sub> O	0.00	0.08	11.07
<b>Total</b>	<b>100.51</b>	<b>100.68</b>	<b>Total</b>	<b>100.23</b>	<b>100.00</b>	<b>100.06</b>
<b>Anions</b>	<b>23</b>	<b>23</b>	<b>Anions</b>	<b>12</b>	<b>14</b>	<b>11</b>
Si	8.06	8.14	Si	3.00	Si IV 2.67	Si 3.18
Al IV	0.00	0.00			Al IV 1.33	Al IV 0.82
Σ IV	8.06	8.14	Al	2.00	Σ IV 4.00	Σ IV 4.00
Al M123	0.04	0.00	Ti	0.01	Al VI 1.52	Al VI 1.76
Cr	0.01	0.00	Cr	0.00	Ti 0.01	Ti 0.01
Ti	0.00	0.00	Fe <sup>3+</sup>	0.00	Cr 0.00	Fe <sup>2+</sup> 0.21
Mg	2.69	2.55	Fe <sup>2+</sup>	1.73	Fe <sup>3+</sup> 0.00	Σ VI 1.98
Fe M123	2.26	2.44	Mn	0.82	Fe <sup>2+</sup> 3.41	
Mn M123	0.00	0.00	Mg	0.00	Mn 0.05	Na 0.17
Σ M123	5.00	5.00	Ca	0.42	Mg 0.90	K 0.91
Fe M4	1.65	1.37			Ca 0.00	Σ 1.08
Mn M4	0.09	0.23	Σ cat	7.99	Na 0.00	
Ca	0.12	0.11			K 0.01	Σ cat 7.06
Na M4	0.00	0.00	XPy	0.00	Σ 5.90	
Σ M4	1.86	1.71	XAlm	0.58		XPa 0.16
A Na	0.00	0.00	XSpss	0.28	Σ cat 9.90	
A K	0.00	0.00	XGrss	0.14		
Σ A	0.00	0.00	Fe/Fe+Mg	1.00		
Σ cat	14.92	14.85				



**Note:** Fe<sup>3+</sup> is calculated using the formula of Droop (1987). XPy, XAlm, XSpss and XGrss as defined by Spear (1993). XAn = Ca/(Ca+Na), XAb = Na/(Ca+Na), XPs = Fe<sup>3+</sup>/(Fe<sup>3+</sup>+Al)



(A)



(B)

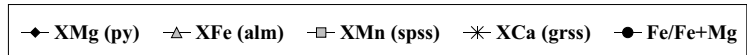


**Figure 6.6: (a and b):** Major element compositional variation in garnet from amphibolite. (a) is a garnet from sample 62107 and (b) is from sample 61406. All profiles are plotted from A to B.

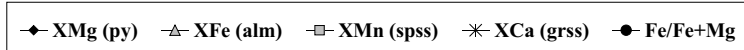
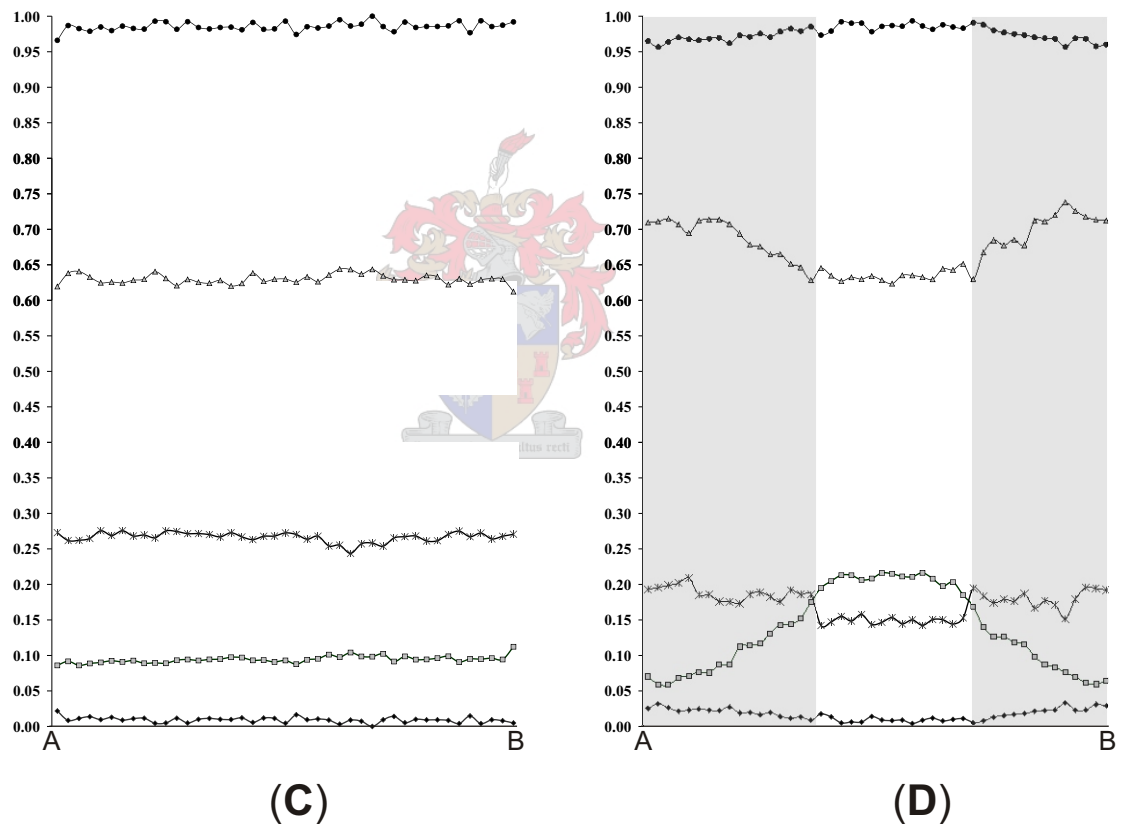
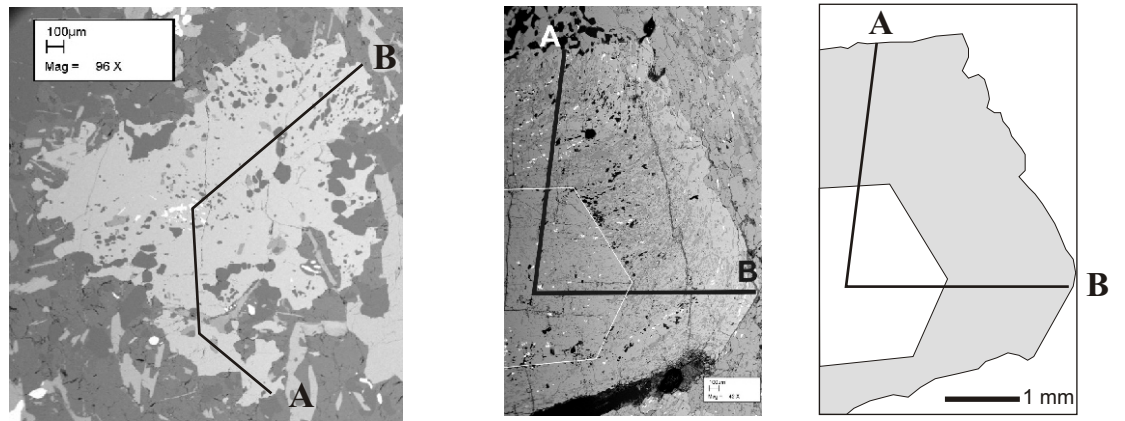


**Figure 6.6: (c and d):** Compositional variations in garnet from amphibolite and garnet-quartz-amphibole mylonite. **(c)** is a garnet from sample Tj 3 and **(d)** is a garnet from sample 62105A (garnet-quartz-amphibole mylonite). All traverses are plotted from A to B.

metamorphic grade. Petrography and mineral chemistry indicate that all amphibolite samples experienced only one episode of garnet growth. Garnet from the garnet-quartz mylonite (sample 62105A) shows petrographic and chemical evidence for two episodes of garnet growth (Fig. 6.6d). The first episode resulted in the euhedral core and is characterized by flat profiles of all the major elements. Second-generation garnet is more Ca-rich and displays a progressive enrichment in Fe and depletion in Mn towards the rim.

#### 6.4.2 *Amphibole*

Hornblende is present in all amphibolites and only the garnet-quartz mylonite (sample 62105A) contains cummingtonite in addition to hornblende. Hornblende does not exhibit chemical zonation and a single generation of hornblende is present in most samples. Sample 61406 is the only amphibolite that contains inclusions of hornblende in garnet. Hornblende inclusions in the garnets are characterized by lower Al, Fe and Na and elevated Mg concentrations relative to matrix hornblende. Hornblende grains from garnet-bearing amphibolite and garnet-free amphibolite have Mg-numbers between 25 and 55, while hornblende from epidote-amphibolite exhibits Mg-numbers of 70 – 75. Additionally, epidote-amphibolite hornblende contains less than 5 wt % Al<sub>2</sub>O<sub>3</sub>, compared to 14 – 17 wt % Al<sub>2</sub>O<sub>3</sub> in hornblende from other amphibolite samples.

#### 6.4.3 *Epidote*

Epidote is present in the matrix of certain amphibolite samples, while epidote and zoisite are also present as inclusions in garnet. No chemical zonation was found in these grains. Epidote has a relatively constant composition in all amphibolite samples and has a pistachite ( $\text{Fe}^{3+}/(\text{Fe}^{3+}+\text{Al})$ ) content of 14 – 17 %. No apparent compositional differences were found between epidote grains that are present as inclusions in garnet and grains that occur in the matrix of the sample.

#### 6.4.4 Plagioclase

Pervasively recrystallized plagioclase only occurs in the matrix of amphibolite and exhibits a constant chemical composition within individual samples. Plagioclase in these rocks consists of 30 – 39 % anorthite, but more albitic plagioclase ( $An_{22} - An_{24}$ ) are common in more retrogressed samples (e.g. 61406). Sample 61406 predominantly consists of plagioclase containing 23 % anorthite, but isolated zones within the matrix contain Ca-rich ( $An_{30}$ ) plagioclase. It is likely that the plagioclase in this sample was re-equilibrated and homogenized during retrogression and that the anorthite-rich grains represent unretrogressed, peak metamorphic plagioclase that escaped retrogression because of strain partitioning.





## **CHAPTER 7: ESTIMATION OF METAMORPHIC CONDITIONS**

### 7.1 Implications of garnet zoning profiles

The major-, trace- and REE zoning profiles of garnet from felsic schist indicates that these rocks experienced at least two episodes of garnet growth. The first episode is characterized by bell-shaped Mn profiles, a progressive increase in Fe towards the rim and relatively constant Ca and Mg concentrations. These characteristics are indicative of garnet that crystallized during prograde metamorphism in the amphibolite-facies (Spear, 1993). Additionally, this generation of garnet exhibits chondrite-normalized REE patterns that are considered to be characteristic of garnet crystallizing in the staurolite-zone of the amphibolite-facies (Schwandt et al., 1996).

The second episode of garnet growth formed the rims that are confined to the pressure shadow sites of garnet grains. This generation is characterized by an abrupt increase in Ca content and a simultaneous decrease in Fe concentration in the garnet. However, the behavior of Mg and Mn is not consistent between different samples as garnet from sample Tj 18 exhibits increasing Mg and decreasing Mn, while garnet from sample 62601C exhibits the opposite trends. Chondrite-normalized REE profiles of second-generation garnet in sample Tj 18 suggest that garnet growth occurred under retrograde metamorphic conditions, as the profiles are indicative of garnet that crystallized in the lower-grade garnet-zone (for metapelites) of the amphibolite-facies (Schwandt et al., 1996). Moreover, the enrichment in Ca as well as the two- to threefold increase of Cr and V in second-generation garnet might suggest that the growth of this generation involved the breakdown of Ca-rich plagioclase and a Cr-V rich phase such as staurolite. Plagioclase that exhibits peak metamorphic anorthite-rich compositions is only preserved in low-strain lithons and the matrix plagioclase has a relatively low anorthite content. This would suggest that large amounts of Ca (equivalent to ca. 7 % anorthite component in plagioclase) were liberated from plagioclase during retrogression and re-equilibration. Garnet that crystallized at that time would have incorporated the freely available Ca into its crystal structure, resulting in the precipitation of Ca-rich garnet. Similarly, staurolite

is the only mineral in these samples that contains appreciable amounts of Cr and V and the breakdown of staurolite could result in the precipitation of garnet enriched in these elements. This line of evidence strongly suggests that second-generation garnet crystallized via a reaction that involved the breakdown of Ca-rich plagioclase and Cr-V-rich staurolite under retrograde metamorphic conditions.

## 7.2 Peak metamorphic assemblages

### 7.2.1 *Clastic metasediments*

Garnet-bearing felsic schists (samples Tj 18, 62105F and 62601C) typically contain mineral assemblages that consist of the two generations of garnet discussed above, plastically deformed and recrystallized staurolite, two generations of chlorite, two generations of plagioclase, biotite, muscovite and quartz. In attempting to determine which of these minerals and mineral generations constitute the peak metamorphic assemblage, it is significant to note that muscovite is only present as a retrograde product and does not constitute part of the peak assemblage. Additionally, neither kyanite nor sillimanite occurs in these samples, indicating that the aluminosilicate-in reaction:



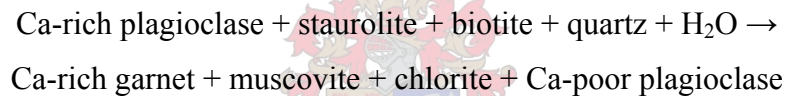
(Holland and Powell, 1998) did not occur due to a lack of prograde muscovite. The reaction that produced the peak metamorphic assemblage is believed to be reaction 2:



(Holland and Powell, 1998). Muscovite is the limiting reagent, implying that garnet and chlorite are in excess and that the peak assemblage consists of staurolite and biotite as well as garnet, chlorite, plagioclase and quartz.

Kyanite-bearing felsic schist (sample 62601D) consists of kyanite, sillimanite, staurolite, biotite, muscovite, plagioclase and quartz. Textures of staurolite reacting to form kyanite are present in this sample, while sillimanite is present as overgrowths on kyanite. Notably, this sample does not contain garnet or chlorite, but is intercalated with horizons that exhibit the garnet-bearing assemblage described above (sample 62601C). The reaction that produced the peak assemblage is considered to be reaction 1. Chlorite is the limiting reagent and consequently the peak assemblage in this sample consists of kyanite, biotite, staurolite, muscovite, plagioclase and quartz.

An episode of deformation and retrograde re-equilibration affected most of the minerals in the peak assemblages subsequent to their crystallization. In garnet-bearing samples, retrogression is believed to have occurred via a reaction similar to the reversal of reaction 2, but that also involved Ca-rich plagioclase, i.e.



as discussed above. Figure 7.1 indicates that this reaction did not reach completion and it is most likely that the reaction was restricted due to the limited availability of a H<sub>2</sub>O fluid phase. Additionally, plagioclase, staurolite, biotite, kyanite and quartz underwent pervasive recrystallization and re-equilibration during retrogression. The pervasive re-equilibration of plagioclase suggests that all of the peak metamorphic minerals must have re-equilibrated during retrogression and that the homogeneous composition currently exhibited by these minerals was most likely attained under retrograde, rather than peak metamorphic conditions. Re-equilibration of the metamorphic assemblage under retrograde conditions is most likely not perfect, but provides a good approximation of an equilibrium assemblage (Fig. 7.1). The mineral generations considered to provide the best estimate of an equilibrated, close-to-peak metamorphic assemblage in garnet-bearing samples are second-generation garnet, staurolite, low-anorthite plagioclase, biotite, first-generation chlorite and quartz (Table 7.1). First-generation chlorite is preferred over second-generation chlorite because second-generation chlorite occurs as a product of

biotite and garnet breakdown, indicating that it must have formed during later, low temperature retrogression.

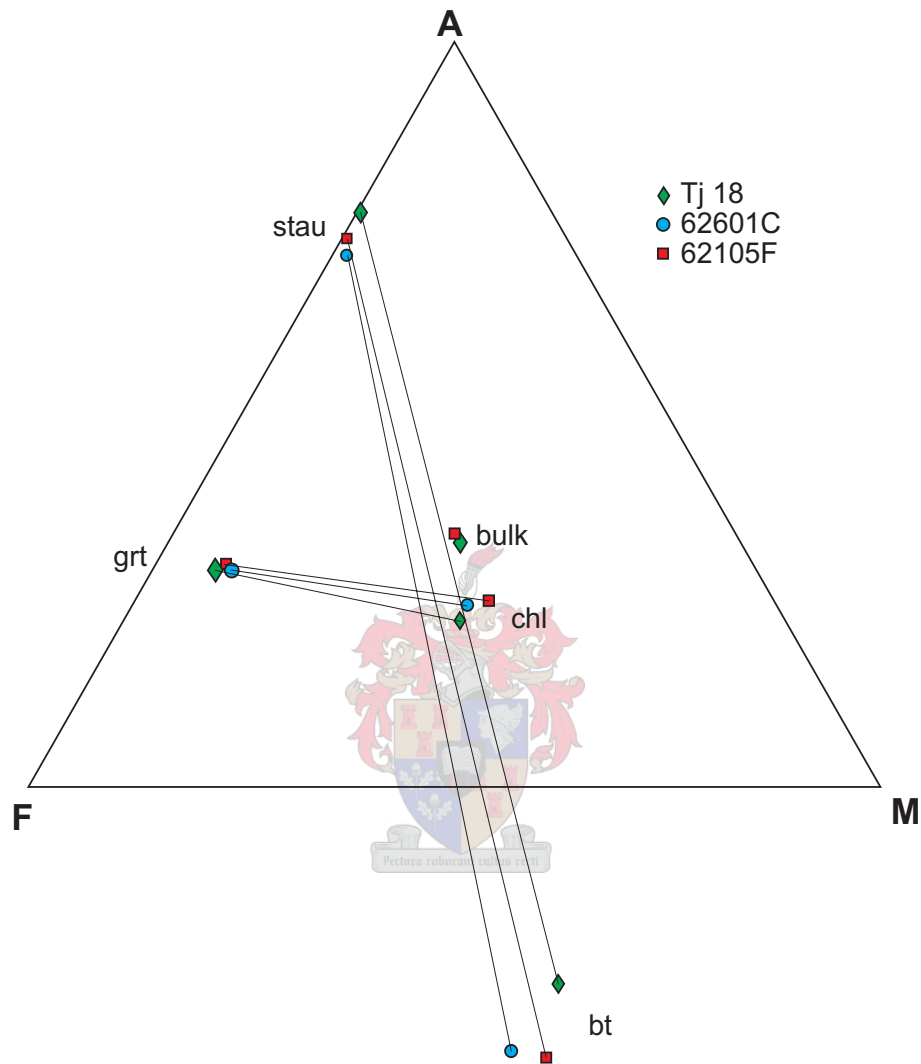


**Figure 7.1:** AFM diagram for metapelites, projected from muscovite, illustrating the equilibration of peak metamorphic assemblages in garnet-bearing felsic schist samples. The mineral pair tie-lines from different samples are roughly parallel; indicating very similar Fe-Mg distribution coefficients in the different samples. The grt-chl and stau-bt crossing tie-lines indicate that the retrograde reaction between these pairs did not reach completion because of the limited availability of a fluid phase. Note that the projection from muscovite cannot be strictly applied, as muscovite does not constitute part of the peak metamorphic assemblage in these samples.

**Table 7.1:** Summary of the different mineral generations present in clastic metasediments and amphibolite samples and which of these generations are considered to represent an equilibrium assemblage.

garnet-bearing metasediments (samples Tj 18, 62105F and 62601D)						
Paragenesis	grt	st	bt	chl	pl	
prograde	core					
peak	rim					An-rich
early retrograde	overgrowths	X	X	Mg-rich		Ab-rich
late retrograde				Fe-rich		
kyanite-bearing metasediments (sample 62601C)						
Paragenesis	ky	sil	st	bt	ms	pl
prograde						
peak	X					
early retrograde	X?	X	X	X	X	X
late retrograde						
garnet-bearing amphibolite (samples Tj 3 and 62107)						
Paragenesis	grt	hbl	ep	pl		
prograde	core?					
peak	rim	X	X	X?		
early retrograde				X?		
late retrograde						

### 7.2.2 Amphibolite

Amphibolite samples targeted for thermobarometric calculations contain a metamorphic assemblage that consists of garnet, hornblende, plagioclase, epidote and quartz. Plagioclase in amphibolite is pervasively recrystallized, although not to the same extent as in felsic schist samples. Garnet is not strongly zoned and does not display evidence of multiple garnet growth events. This would indicate that all garnet growth occurred during a single prograde garnet growth episode. Retrograde garnet growth did not occur in the amphibolite samples, as these rocks did not experience a retrograde reaction that produced garnet, such as the reaction that involves staurolite breakdown in felsic schist (reversal of reaction 1). Furthermore, only one generation of hornblende and one generation of epidote are present in amphibolite samples. The best estimate of an equilibrated, near-peak assemblage in amphibolite consists of the garnet rims, hornblende, epidote, plagioclase and quartz (Table 7.1).



## 7.3 Estimation of peak metamorphic conditions via THERMOCALC

### 7.3.1 Introduction

THERMOCALC (Powell and Holland, 1988; Holland and Powell, 1998) is a computer software program used for metamorphic petrological analysis. The program utilizes an experimentally-derived, internally consistent thermodynamic data set of mineral end-member properties to calculate the pressure-temperature coordinates of all reactions that occur between end-members in a specific mineral assemblage. THERMOCALC can be used to construct petrogenetic grids and pseudosections of multi-component systems as well as to estimate average metamorphic pressure-temperature conditions (e.g. Will et al., 1990, 1998; Tinkham et al., 2001; Hoschek, 2001). During this study, version 3.21 of THERMOCALC utilizing the thermodynamic data set of Holland and Powell (1998; with unpublished additions, 2002) was used in 'Average PT mode' to calculate the pressure-temperature conditions at which the metamorphic assemblages were equilibrated. To ensure that reactions are valid across the pressure-temperature interval investigated, the pressure and temperature was first calculated independently before the pressure-temperature conditions were calculated simultaneously. All calculations are performed assuming the presence of a pure water fluid phase. This is considered to be a reasonable approximation as no carbonate phases are present in any of the assemblages subjected to the calculations.

Mineral end-member activities used in the THERMOCALC calculations are determined with the program AX (Holland and Powell, 1998) that is provided with THERMOCALC. End-member activities are calculated at 7.5 kbar and 550 °C.

### 7.3.2 Results

Average pressure-temperature conditions are calculated for three garnet-bearing felsic schist samples (Tj 18, 62105F and 62601C) that contain the peak assemblage of garnet, staurolite, biotite, chlorite, plagioclase and quartz and one kyanite-bearing sample

(62601D) that contains the peak assemblage of kyanite, staurolite, biotite, muscovite, plagioclase and quartz. Calculations are also performed on two garnet-bearing amphibolite samples (Tj 3 and 62107) that contain the assemblage of garnet, epidote, hornblende, plagioclase and quartz. The pressure-temperature estimate produced by each sample is presented in Table 7.2 and Figure 7.2.

The result of all six samples plot within error of each other and only sample 62601D contains relatively large errors in the pressure-temperature estimate. Although the estimate from sample 62601D is in agreement with the estimates from other samples, it is disregarded because of the relatively large errors. The extremely small spread of pressure-temperature estimates, the relatively small errors in these estimates as well as the strong correlation between estimates from amphibolite and felsic schist strongly indicate that the central parts of the Tjakastad Schist Belt experienced peak metamorphism at pressures of  $7.4 \pm 1.0$  kbar and temperatures of  $560 \pm 20$  °C. The mineral assemblages used to generate these estimates are high-grade retrograde assemblages and consequently these estimates are considered to reflect the conditions experienced during high-grade retrogression and are most likely a conservative estimate of peak metamorphic pressures and temperatures.

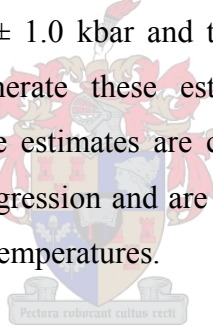


**Table 7.2:** THERMOCALC results of pressure-temperature conditions calculated from felsic schist and amphibolite

Sample	Assemblage	P (kbar)	s.d. (P)	T (°C)	s.d. (T)	corr	fit	N
62105F	grt-st-bi-chl-plag-qtz	7.9	1.1	556	19	0.152	1.35	7
62601C	grt-st-bi-chl-plag-qtz	7.7	0.9	563	14	0.125	0.90	7
Tj 18	grt-st-bi-chl-plag-qtz	7.2	1.0	569	18	0.290	1.16	7
62601D	ky-st-bi-ms-plag-qtz	8.0	4.3	548	115	0.402	2.30	4
62107	grt-hbl-plag-epi-qtz	7.0	1.6	556	59	0.952	1.57	7
Tj 3	grt-hbl-plag-epi-qtz	7.0	1.2	537	45	0.958	0.78	6

s.d. = standard deviation; N is the number of independent equilibria calculated for each assemblage

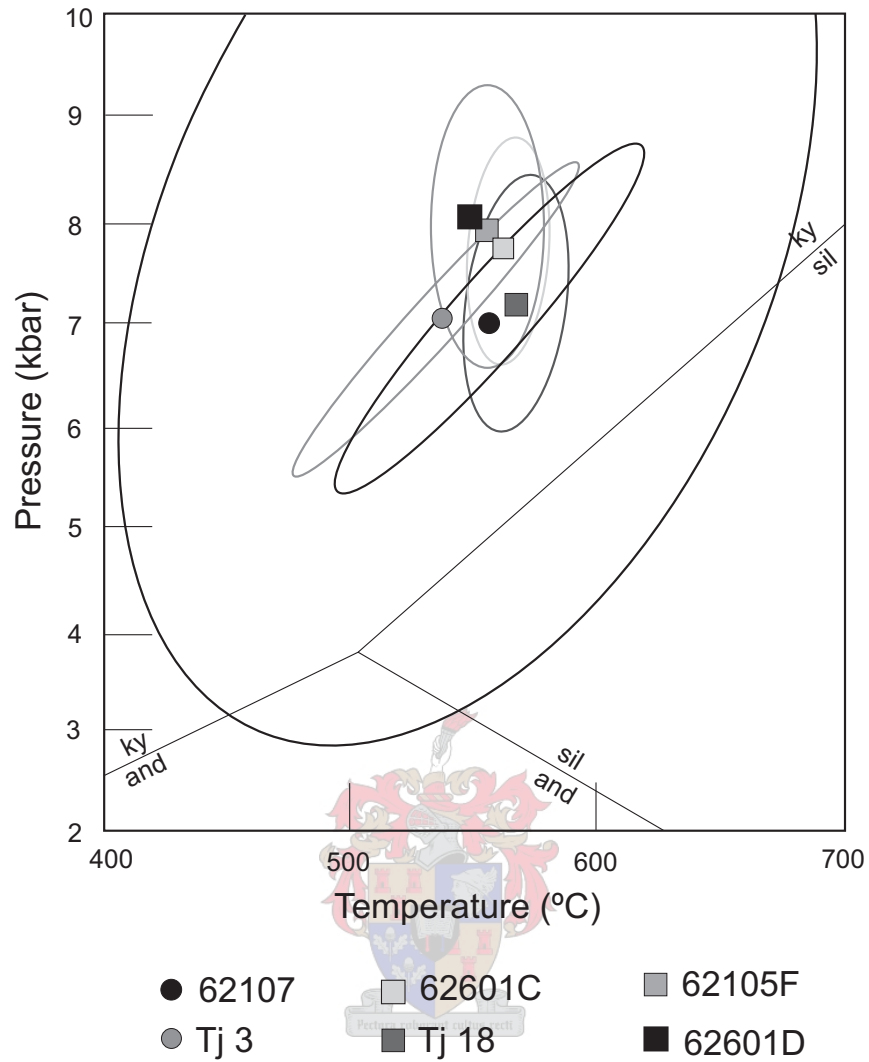


**Figure 7.2:** Plot of THERMOCALC pressure-temperature estimates from amphibolite samples (circles) and felsic schist samples (squares). Error ellipses are at one standard deviation. The aluminosilicate phase diagram is after Holdaway (1971).

An attempt was made to constrain the peak metamorphic conditions in felsic schist by using an assemblage consisting of biotite and chlorite inclusions in garnet, anorthite-rich plagioclase and first-generation garnet rims. This assemblage produced a poorly constrained estimate of  $8.3 \pm 2.9$  kbar and  $608 \pm 45$  °C (corr = 0.074, fit = 2.60, N = 5), which is in broad agreement with the better-constrained estimates from the high-grade retrograde assemblages.

## 7.4 Petrogenetic grids and pseudosections

Petrogenetic grids plot the stability fields of minerals as well as the reactions against which these fields terminate, in pressure-temperature space. Minerals and rocks are expressed as a series of chemical components and the most common chemical systems are  $K_2O$ - $FeO$ - $MgO$ - $Al_2O_3$ - $SiO_2$ - $H_2O$  (KFMASH; e.g. Spear and Cheney, 1989; Holland and Powell, 1998), which is an approximation of the chemistry of metapelites and  $Na_2O$ - $CaO$ - $FeO$ - $MgO$ - $Al_2O_3$ - $SiO_2$ - $H_2O$  (NCFMASH; e.g. Will et al., 1998), an approximation of the chemistry of metabasites. Pseudosections are sections through petrogenetic grids that show the mineral assemblage recorded in a specific bulk composition and can greatly simplify complex petrogenetic grids. The computer program Vertex (Connolly, 1990; Connolly and Petrini, 2002) was developed specifically for the calculation of pseudosections and was used to generate the pseudosections constructed during this study. Pseudosections were constructed following the method of Connolly and Petrini (2002) and using the thermodynamic dataset and mixing models of Holland and Powell (1998; with unpublished additions, 2002).



### 7.4.1 *Clastic metasediments*

The pressure-temperature position of reactions 1 and 2 that produced the peak assemblage in garnet- and kyanite-bearing felsic schists is presented on a petrogenetic grid for metapelites (Fig. 7.3; Holland and Powell, 1998). These reactions occur across a very narrow temperature band between ca. 580 and 600 °C at pressures greater than 6 kbar. Garnet- and kyanite-bearing assemblages are present in intercalated horizons of the same outcrop (samples 62601C and D), which indicates that these two assemblages can be metamorphic grade equivalents, as suggested by the petrogenetic grid. The origin of these two assemblages is most likely related to different bulk compositions, particularly variations in the concentration of Al, Ca, Fe and Mg, as demonstrated in Figure 7.4.

It should be noted that, strictly, garnet-bearing felsic schists can not be represented in KFMASH as muscovite is not part of the peak assemblage in these samples. The

KFMASH projection assumes that quartz, muscovite and water are present in excess in order to project these phases out and reduce the number of components in the chemical system. Therefore, the garnet-bearing samples have to be represented by a larger, more complex chemical system such as  $\text{Na}_2\text{O}-\text{CaO}-\text{K}_2\text{O}-\text{FeO}-\text{MgO}-\text{Al}_2\text{O}_3-\text{SiO}_2-\text{H}_2\text{O}$  (NCKFMASH).

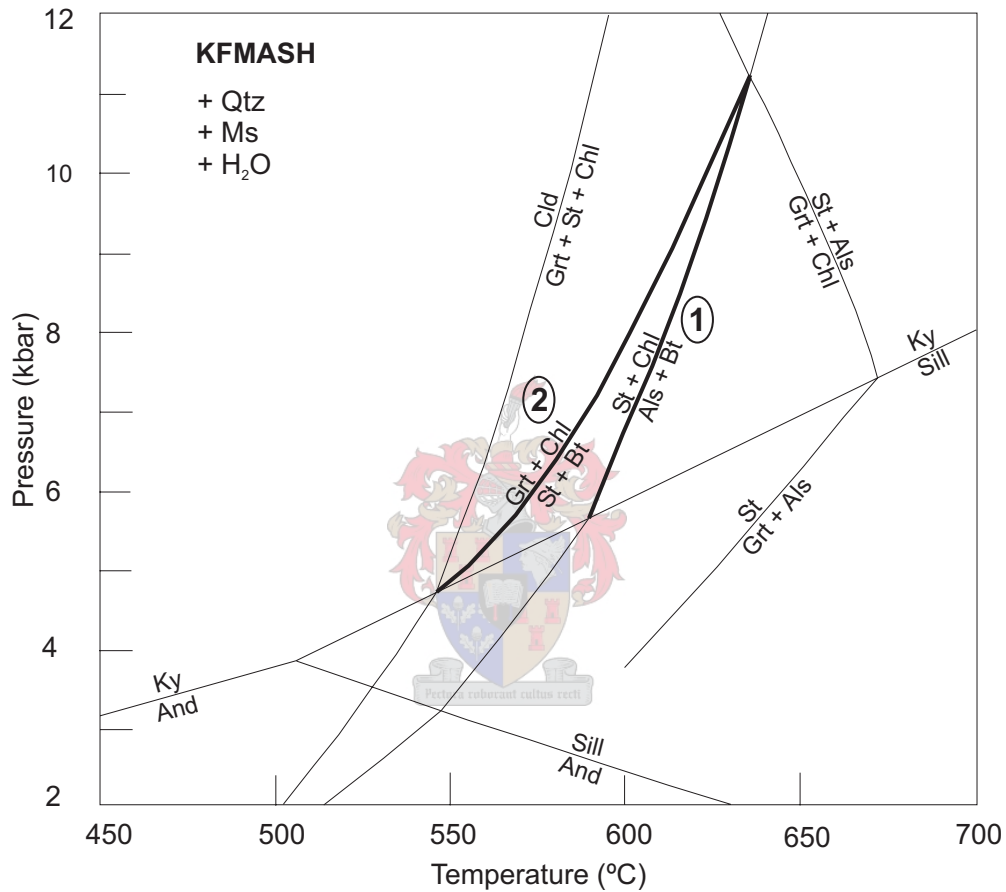


**Figure 7.3:** KFMASH petrogenetic grid showing the position of reaction (1) and (2) that formed the peak assemblages present in felsic schist samples (after Holland and Powell, 1998).

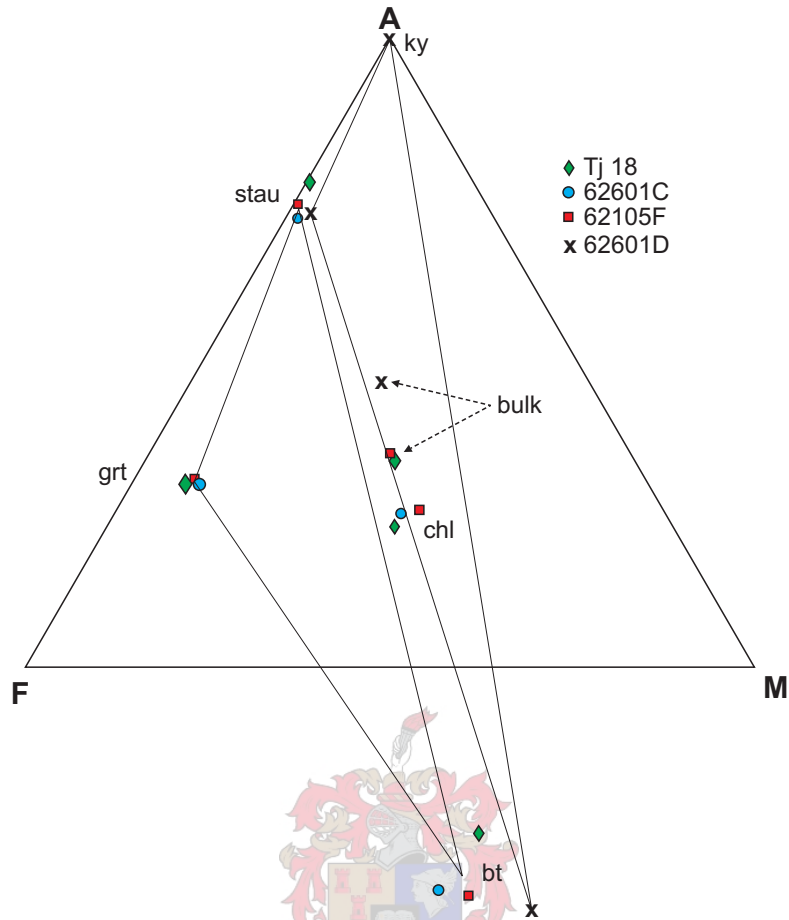


**Figure 7.4:** AFM diagram for metapelites, projected from muscovite, illustrating the bulk-rock and mineral compositional differences between felsic schist samples that contain the peak assemblage garnet-staurolite-biotite-chlorite (samples Tj 18, 62601C and 62105F) and kyanite-staurolite-biotite-muscovite (sample 62601D).

The bulk composition of samples Tj 18 and 62601D were used to calculate two NCKFMASH pseudosections (Figs. 7.5a and b). From these sections it is evident that the peak assemblage in garnet-bearing felsic schists is stable at pressures of 4 – 9 kbar and temperatures of 580 – 650 °C (Fig. 7.5a), while the peak assemblage in kyanite-bearing felsic schist is stable at pressures of 5.5 – 10 kbar and temperatures of 580 – 620 °C (Fig. 7.5b). These estimates confirm that the two assemblages are indeed grade equivalents and also correlate very well with average pressure-temperature estimates obtained from these samples.



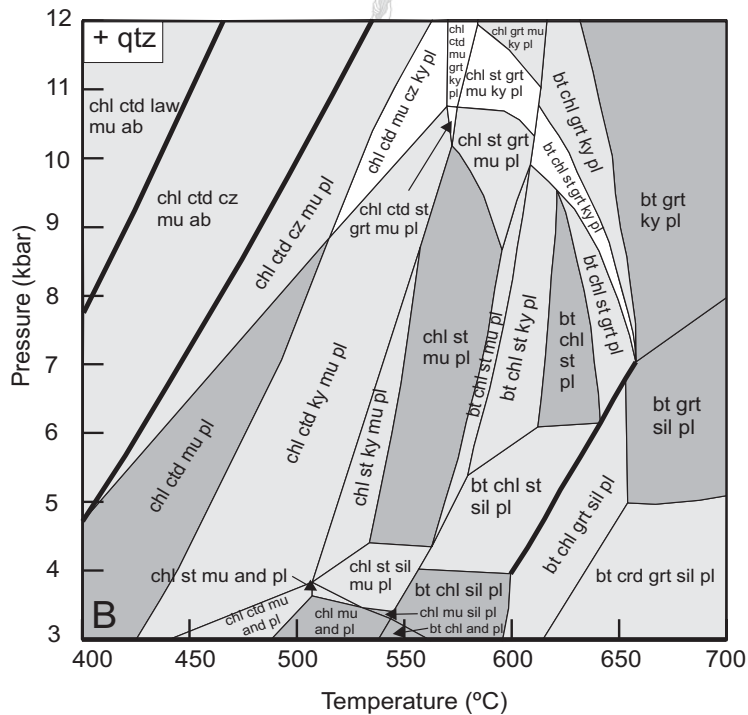
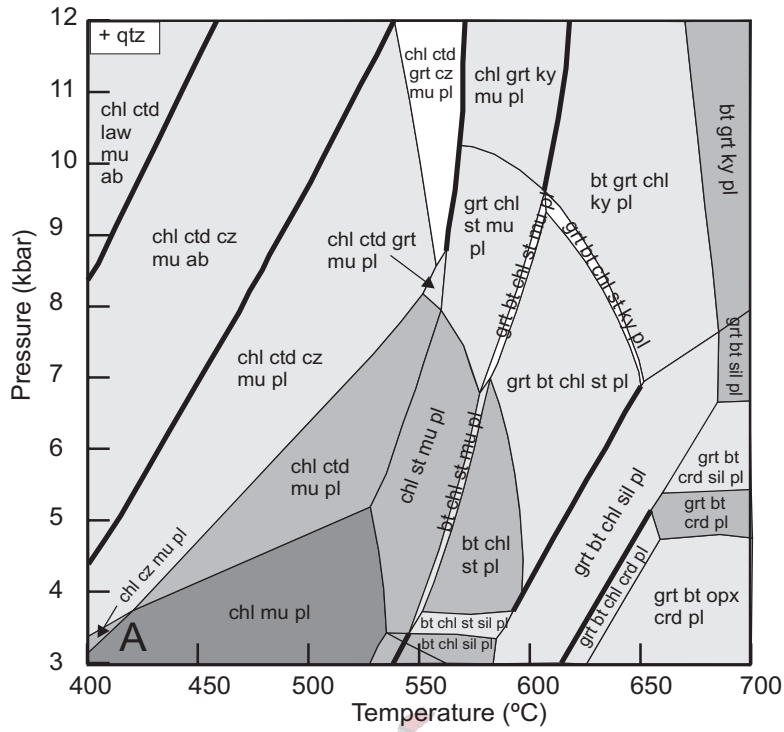


**Figure 7.5: (a):** NCKFMASH pseudosection calculated for sample Tj 18 indicating the stability field of the peak metamorphic assemblage garnet-staurolite-biotite-chlorite-plagioclase at 4 to 9 kbar and 580 to 650 °C in this sample. **(b):** NCKFMASH pseudosection calculated for sample 62601D indicating the stability field of the peak metamorphic assemblage kyanite-staurolite-biotite-chlorite-plagioclase at 5.5 to 10 kbar and 580 to 620 °C in this sample. Heavy lines on the diagrams indicate areas where one or more fields are too small to show.

#### 7.4.2 Amphibolite

The stability of garnet in amphibolite is strongly dependent on the bulk-rock composition, as shown in Chapter 5. In this study, garnet is only stable in amphibolite that contains more than 10 wt %  $\text{Al}_2\text{O}_3$ , less than 10 wt % CaO and has Mg-numbers lower than 50. These compositional parameters are similar to the material used in an experimental investigation (Poli, 1993), in which the garnet-in reaction occurred between 8 and 10 kbar at temperatures of 550 to 650 °C. These experiments were conducted in NCFMASH and did not account for the effect of Mn on garnet stability, but are in good agreement with the NCFASH petrogenetic grid calculated by Will et al. (1998).

#### 7.4.3 Correlation between THERMOCALC estimates and petrogenetic grids

The pressure-temperature position of the peak assemblages in felsic schist and amphibolite are in good agreement with the estimates produced by THERMOCALC and confirm that metamorphism in the Tjakastad Schist Belt occurred at ca. 7.4 kbar and 560 °C. However, temperature estimates from metapelite petrogenetic grids and pseudosections are consistently about 30 °C higher than THERMOCALC estimates for samples from the Tjakastad Schist Belt. This discrepancy is most likely a function of the re-equilibrated mineral compositions in samples of the Tjakastad Schist Belt. The THERMOCALC estimates are preferred over the petrogenetic grids because of the strong correlation between estimates from both felsic schist and amphibolite.

#### 7.5 Estimation of retrograde metamorphic conditions

All of the lithologies and samples investigated have been affected by retrogression to a greater or lesser extent. In kyanite-bearing felsic schist samples, retrogression is marked by sillimanite overgrowths on peak metamorphic kyanite (sample 62601D), and staurolite exhibits coronas of retrograde muscovite in most felsic schist samples. Additionally, garnet-bearing felsic schist (sample Tj 18) exhibits zones where garnet breakdown led to the formation of retrograde plagioclase, muscovite and chlorite (Fig. 7.6).

THERMOCALC estimates from the garnet breakdown assemblage (consisting of strongly retrograde garnet and associated plagioclase, chlorite, muscovite and quartz) in sample Tj 18 yield pressure-temperature conditions of  $3.8 \pm 1.3$  kbar and  $543 \pm 20$  °C (corr = 0.596; fit = 1.53; N = 5). Retrogression in amphibolite samples is marked by plagioclase-chlorite coronas that pseudomorph euhedral garnet (Fig. 3.5e) and pervasive chloritization in certain amphibolite samples (e.g. sample 61406). A THERMOCALC estimate from the garnet breakdown assemblage in sample 61406 (consisting of retrograde garnet and associated plagioclase, hornblende, chlorite and quartz) yields a pressure-temperature estimate of  $6.1 \pm 2.7$  kbar and  $569 \pm 42$  °C (corr = 0.186; fit = 2.81; N = 7).

These are the only quantitative pressure-temperature estimates of retrograde conditions that could be extracted from the samples investigated in this study. These estimates, as well as the implications of the retrograde mineral parageneses mentioned above will be discussed in Chapter 9, when the pressure-temperature-time path experienced by the Tjakastad Schist Belt is discussed.

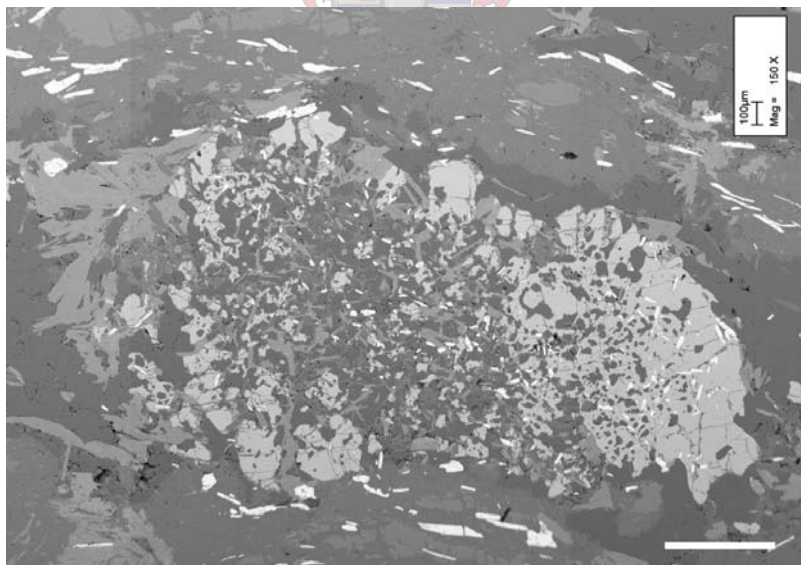


**Figure 7.6:** Backscatter electron image of a site of garnet breakdown in sample Tj 18 consisting of fine intergrowths of strongly retrograde garnet, plagioclase, muscovite, chlorite and quartz. Scale bar is 0,5 mm long.

## **CHAPTER 8: TIMING OF METAMORPHISM AND DEFORMATION**

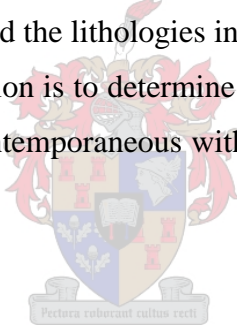
### 8.1 Introduction

A fundamental question that bears on almost any geological investigation concerns the timing of the events described. Radiometric dating of rocks and minerals provides the only means to constrain the absolute timing of geological events, particularly in terrains where index fossils and regionally correlateable lithological units are absent. Consequently, detailed geochronology has proven indispensable in unraveling the geological evolution of the Barberton terrain and a fairly extensive geochronological database exists for this terrain (refer to Figs. 2.1 and 2.2, as well as Poujol et al. (2003) and references therein for a review). Although the geological evolution of the Barberton granitoid-greenstone terrain spans ca. 490 Ma (De Ronde and De Wit, 1994), two main episodes of deformation, metamorphism and associated plutonism have been identified within the Barberton terrain (refer to Chapter 2; De Ronde and De Wit, 1994; Kamo and Davis, 1994; Lowe, 1999).

The first tectono-metamorphic and plutonic episode ( $D_1$ ) occurred at ca. 3.45 Ga and is characterized by metamorphism in the Komati Formation, which occurred between 3486 and 3425 Ma (Lopez-Martinez et al., 1992). During this episode, the Theespruit Formation was intruded by the early TTG suite and field relationships indicate that the Theespruit Pluton truncates amphibolite-facies fabrics and lithologies in the Theespruit Formation type locality (Viljoen and Viljoen, 1969b; De Wit et al., 1983). This suggests that the Theespruit Formation must have experienced high-grade metamorphism and deformation during  $D_1$  at 3.45 Ga (De Wit et al., 1983; 1987; Armstrong et al., 1990; De Ronde and De Wit, 1994).

The second tectono-metamorphic episode ( $D_2$ ) occurred at ca. 3.23 Ga and affected the whole of the greenstone belt (De Ronde and De Wit, 1994; Kamo and Davis, 1994; De Ronde and Kamo, 2000). Investigations into the metamorphic history of the

Schapenburg Schist Belt as well as greenstone xenoliths preserved in the granitoid-gneiss terrain to the south of the Barberton Greenstone Belt revealed that the equilibration of peak metamorphic assemblages occurred contemporaneous with D<sub>2</sub> at ca. 3230 Ma (Stevens et al., 2002; Dziggel et al., 2002; Kisters et al., 2003). Additionally, zircon and titanite from the Stolzburg Pluton has yielded ages of 3255, 3237 and 3201 Ma, while titanite from the Doornhoek Pluton has produced an age of 3215 Ma (Kamo and Davis, 1994). These ages are ca. 220 Ma younger than the reported crystallization ages of the early TTG plutons and are considered to reflect the timing of a metamorphic event that affected the southern Barberton granitoid-greenstone terrain at this time (Kamo and Davis, 1994). The occurrence of similar metamorphic ages across an extensive area of the southern Barberton terrain indicates that this terrain was affected by a widespread metamorphic (and deformational) event at ca. 3.23 Ga. The Theespruit Formation and the Tjakastad Schist Belt are spatially associated with this terrain, suggesting that this metamorphic event has also affected the lithologies in these areas. Consequently, the aim of this geochronological investigation is to determine whether peak metamorphism in the Theespruit Formation occurred contemporaneous with D<sub>1</sub> at ca. 3.45 Ga or D<sub>2</sub> at ca. 3.23 Ga.



## 8.2 Sample selection

Mineral phases suited to the dating of metamorphic and deformational events include zircon, monazite, titanite and apatite (e.g. Parrish, 1990; Sano et al., 1999; Frost et al., 2000; Carson et al., 2002). Zircon is not a common accessory phase in the lithologies investigated and is sporadically present as extremely small (<15 µm) grains in some felsic schist samples. Titanite is a common accessory mineral in amphibolite and felsic schist and is well suited to the dating of igneous and, particularly, metamorphic events (Frost et al., 2000).

The behavior of titanite in high-temperature metamorphic environments differs significantly from that of zircon. Zircon is the only Zr-bearing mineral in most rocks, thereby effectively limiting its reactivity during metamorphism to interaction with a Zr-

bearing fluid or the solution and re-precipitation of existing zircon (Frost et al., 2000). Consequently, zircon can easily preserve older crystallization ages and only thin rims might preserve the timing of the metamorphic event. In contrast, there are numerous phases that can contain Ca and Ti and consequently, titanite is highly reactive in high-temperature environments and readily precipitates new titanite during metamorphic events (Scott and St. Onge, 1995; Frost et al., 2000).

Titanite has a high closure temperature (ca. 650 °C for grains as small as 200 µm; Cherniak, 1993; Scott and St. Onge, 1995; Möller et al., 2000; Frost et al., 2000), which makes it suitable for dating metamorphic events in the amphibolite-facies. Titanite grains investigated during this study are small (30 – 70 µm) and, because the closure temperature is grain-size dependant, these grains probably have a closure temperature that is substantially lower than 650 °C. The closure temperature could potentially even be lower than the peak metamorphic temperature (ca. 560 °C) experienced by these samples (Scott and St. Onge, 1995; Frost et al., 2000).

As the objective of the geochronological investigation is to constrain the timing of metamorphism and deformation, samples that yielded metamorphic pressure-temperature estimates were preferred when selecting samples for geochronology. Consequently, a garnet-bearing amphibolite (sample Tj 3) and a garnet-staurolite-biotite felsic schist (sample Tj 18) were selected for this investigation (At the time of the investigation, sample Tj 3 was the only garnet-bearing amphibolite available).

### *8.2.1 Sample Tj 3*

Sample Tj 3 contains titanite that is present as inclusions in hornblende and also occurs in the matrix of the sample (Fig. 8.1a, b and c). Crystals are commonly diamond-shaped, yellow-brown translucent in colour and exhibit sub- to euhedral crystal faces. Grains are 30 – 70 µm in length and grains that are present as inclusions in hornblende are generally slightly smaller than grains found in the sample matrix. Titanite commonly contains a core inclusion of ilmenite, indicating that these grains nucleated on older ilmenite and



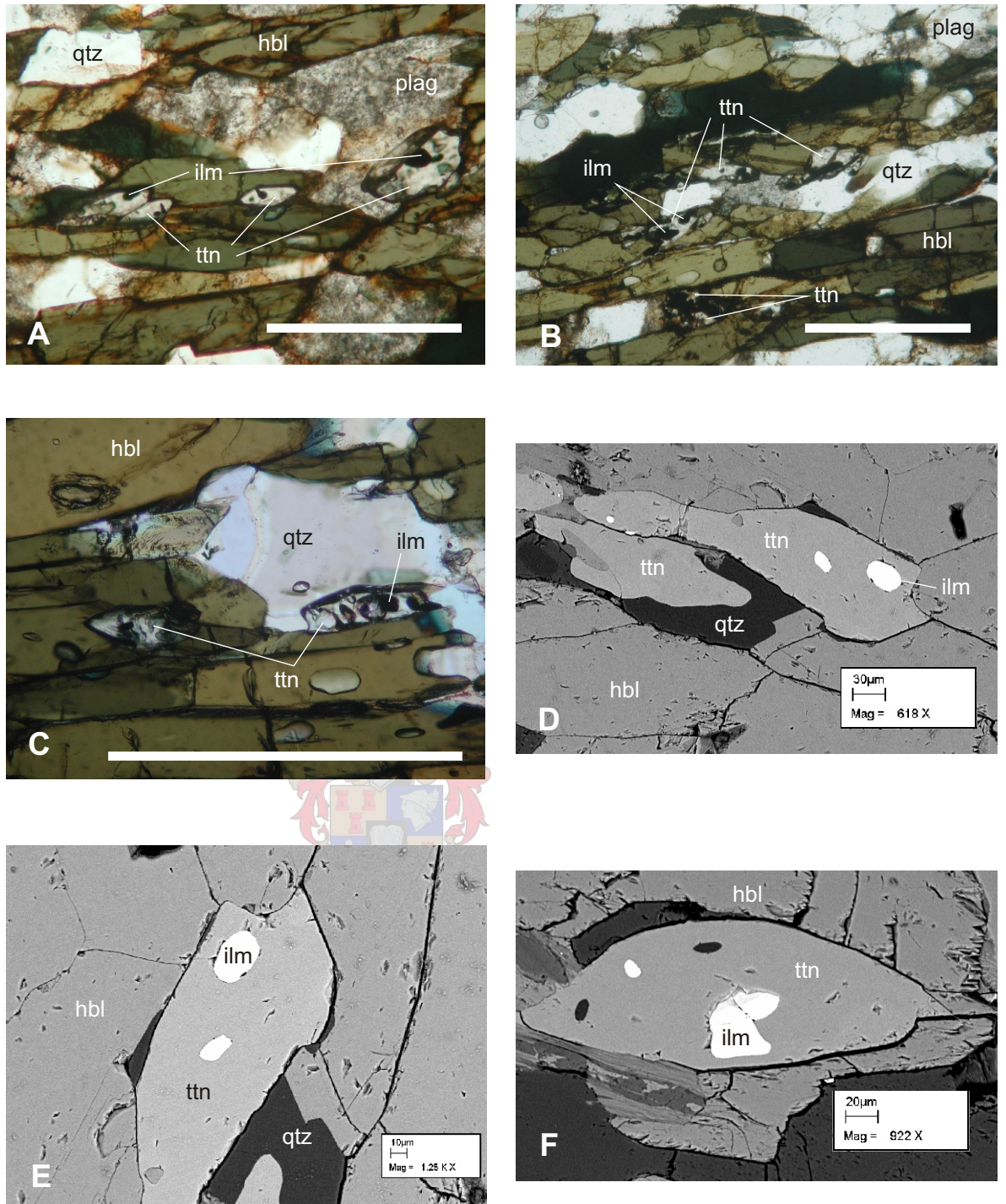
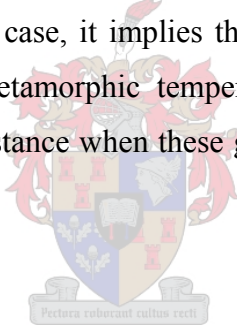


**Figure 8.1: (a-c):** Photomicrographs illustrating the occurrence and association of titanite (ttn) in sample Tj 3. Titanite is present as inclusions in hornblende (hbl) as well as in the matrix of the sample. Titanite grains are typically diamond-shaped and are aligned parallel to the fabric in this sample. Rounded inclusions of ilmenite (ilm) are common. All photographs are taken in plane-polarized light and the scale bar is 0.1 mm long. **(d-f):** Backscatter electron images of titanite from sample Tj 3 illustrating that titanite grains in this sample appear to be homogeneous and do not contain relic cores or display evidence of chemical zonation. Rounded grains of ilmenite and quartz are present as inclusions.

suggesting that they are likely of metamorphic origin (Fig. 8.1; Frost et al., 2000). Because titanite occurs as inclusions in peak metamorphic hornblende, these grains can potentially provide a maximum age constraint on the timing of metamorphism. All grains are aligned parallel to the predominant fabric in this sample, which is also the predominant fabric exhibited by most of the rocks in the study area ( $S_0/S_1$ ). Consequently, titanite can also place a maximum age constraint on the timing of deformation.

Titanite appears to be homogeneous and no evidence of zonation could be found by optical examination or backscatter electron imaging (Fig. 8.1d, e and f). Consequently, it is likely that grains formed during a single growth episode and it appears that this sample does not contain complex or inherited grains. The absence of multiple generations of titanite could be an indication that titanite has been reset and homogenized during the metamorphic event. If this is the case, it implies that the closure temperature of these grains is lower than the peak metamorphic temperature of ca. 560 °C and that the resulting age represents the last instance when these grains cooled to below their closure temperature.



### 8.2.2 *Sample Tj 18*

Sample Tj 18 contains two generations of titanite that are associated with rutile and ilmenite in small, complex grains (Fig. 8.2). Grains are euhedral and occur as slender, elongated prisms that are 100 – 150  $\mu\text{m}$  in length. Grains contain a 10 – 20  $\mu\text{m}$  subhedral core of rutile that is rimmed by a 5 – 20  $\mu\text{m}$  subhedral rim of first-generation titanite. First-generation titanite is in turn rimmed by a euhedral overgrowth of ilmenite that constitutes the bulk of the grain. Second-generation titanite occurs as thin ( $< 10 \mu\text{m}$ ), intermittently present anhedral rims on ilmenite and defines the outer rim of these complex grains.

A rim of ilmenite separates the two generations of titanite in these grains, indicating that the two generations have likely crystallized at different times during the sample history.

However, both generations of titanite are present in grains that are inclusions in garnet, indicating that the crystallization of both generations precedes the peak of metamorphism. Consequently, both generations of titanite can potentially constrain the maximum age of peak metamorphism. However, like titanite from sample Tj 3, the closure temperature of titanite in this sample could be lower than the peak metamorphic temperature, causing only the cooling age to be recorded.

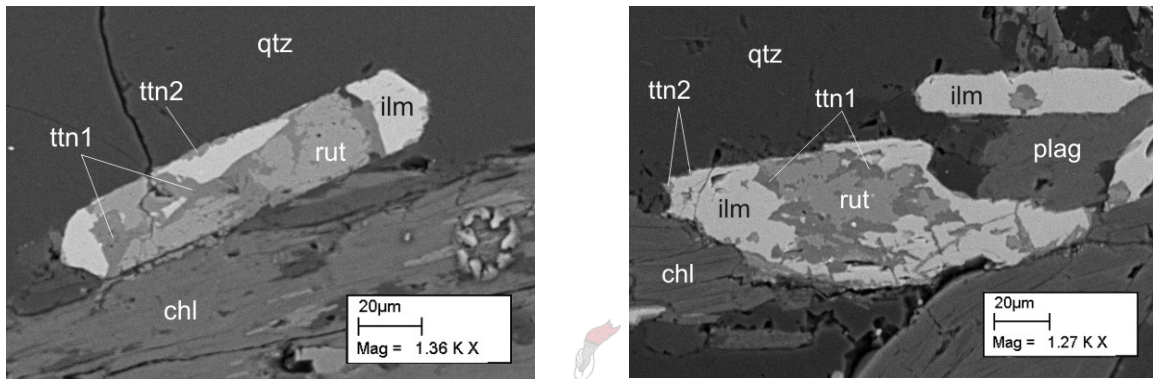


**Figure 8.2:** Backscatter electron images of complex rutile-titanite-ilmenite grains from sample Tj 18, consisting of an anhedral core of rutile (rut) overgrown by a first generation of titanite (ttn1), which is in turn overgrown by sub- to euhedral ilmenite (ilm) and a thin rim of second-generation titanite (ttn2).

### 8.3 Methodology

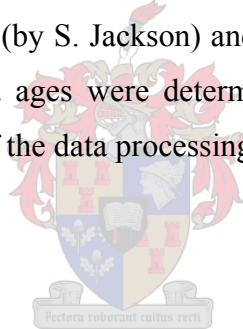
Most modern radiometric dating techniques utilize mineral grains and crystals that are obtained by crushing bulk samples and removing the crystals by mineral separation techniques. Because the minerals are examined and dated in isolation, the petrographic and paragenetic context of these minerals cannot be directly established. This introduces a potential ambiguity and uncertainty in the interpretation of the resulting age, particularly due to the possible presence of multiple mineral generations that cause mixed or inherited ages (Müller, 2003). The petrogenetic context of the mineral chosen for dating is particularly important when attempting to date a specific metamorphic or deformational event in a rock, rather than its age of crystallization.

In situ dating techniques allow minerals to be dated in thin section, allowing the mineral's petrographic and paragenetic context to be preserved. This allows the resulting age to be directly linked to petrography and removes much of the ambiguity in the interpretation of the age within the geological history of the sample (Müller, 2003). In situ techniques are very useful in constraining the timing of a specific metamorphic and deformational event because a single mineral generation – that is interpreted to have formed during, before or after the event/evolution of interest – can be analyzed. Consequently, the resulting age can be confidently interpreted to reflect the timing of the particular event, rather than the age of an earlier or subsequent geological event (Müller, 2003).

LA-ICP-MS is a relatively new in situ dating technique that has been successfully applied to a number of geological problems (e.g. Fryer et al., 1993; Machado and Gauthier, 1996; Košler et al., 2002; Tiepolo, 2003; Rawlings-Hinchey et al., 2003; Fonneland et al., 2004; Hodych et al., 2004). Early studies illustrated the potential as well as the pitfalls associated with U-Pb isotopic analysis by this technique (Feng et al., 1993; Fryer et al., 1993). Two of the biggest drawbacks of LA-ICP-MS are instrument mass bias and laser-induced elemental fractionation between isotopes of U and Pb that do not allow  $^{206}\text{Pb}/^{238}\text{U}$  and  $^{207}\text{Pb}/^{235}\text{U}$  ratios to be determined (Feng et al., 1993; Fryer et al., 1993; Hirata and Nesbitt, 1995; Machado and Gauthier, 1996). Consequently, early attempts at dating by LA-ICP-MS were restricted to the determination of relatively imprecise  $^{207}\text{Pb}/^{206}\text{Pb}$  ages. However, recent advancements, notably the introduction of nebulized tracer solutions that allow mass bias and elemental fractionation to be corrected, have greatly improved the technique (Horn et al., 2000; Košler et al., 2002). Currently, LA-ICP-MS can routinely produce U-Pb isotopic data with precision and accuracy comparable to SHRIMP (Horn et al., 2000; Košler et al., 2002). The use of a standard tracer solution also eliminates the need for calibration against a matrix-matched external standard (Horn et al., 2000; Košler et al., 2002). Because the technique utilizes time-resolved data acquisition, isotope concentrations and ratios can be monitored during ablation, ensuring that only a single, homogeneous mineral generation is analyzed (Horn et al., 2000).



The LA-ICP-MS instrument used during this study is located at the Memorial University of Newfoundland and a detailed description of the instrument as well as the analytical techniques used can be found in Košler et al. (2002). Analysis was performed on 100  $\mu\text{m}$ -thick petrographic thin sections and 40 x 40  $\mu\text{m}$  rastered ablation pits were used whenever possible. In cases where grain size was too small, or to avoid inclusions, smaller 20 x 20  $\mu\text{m}$  raster pits were used. Instrument stability was monitored by routinely analyzing an in-house titanite standard (LAC titanite; Pedersen et al., 1988).  $^{206}\text{Pb}$  and  $^{207}\text{Pb}$  isotopes were corrected for common Pb by measuring  $^{204}\text{Pb}$  (corrected for interference with  $^{204}\text{Hg}$ ) and calculating common Pb with the model of Stacey and Kramers (1975). Although titanite incorporates significant amounts of common Pb during crystallization (Frost et al., 2000), the amount of common Pb can be accurately estimated by measuring  $^{204}\text{Pb}$  and it is not usually necessary to measure the common Pb in associated phases, such as feldspars. Raw data was processed and reduced using the spreadsheet programs CONVERT (by S. Jackson) and LAMDATE (by J. Košler) before final U-Pb, Pb-Pb and Concordia ages were determined with the program Isoplot/Ex (Ludwig, 1999). Further details of the data processing techniques are presented in Košler et al. (2002).



#### 8.4 Results

An attempt was made to analyze first- and second-generation titanite from felsic schist (sample Tj 18), but the time-resolved acquisition signals indicated that it is impossible to avoid rutile and ilmenite inclusions in these complex grains, even when using small 20 x 20  $\mu\text{m}$  ablation pits. This sample did not yield any results.

Titanite from sample Tj 3 is low in U and consequently fairly large errors are associated with the isotopic measurements and these errors propagate through to relatively large uncertainties in the age determination. Time-resolved acquisition signals revealed that titanite present as inclusions in hornblende display fairly constant isotopic ratios during ablation and data acquisition. Conversely, grains found in the matrix of the sample show relatively large fluctuations in the isotopic ratios during acquisition. It is likely that

titanite in the sample matrix has been more adversely affected by retrogression and weathering than titanite found as inclusions in hornblende, as the hornblende could effectively shield these grains from retrogression. Consequently, only the reliable data obtained from titanite inclusions are presented in Table 8.1 and only this data were used in the final age determination.

**Table 8.1:** U-Pb isotopic data and calculated ages obtained from titanite in sample Tj 3

Spot	Isotopic ratios						Age calculations (Ma)		
	$\frac{^{207}\text{Pb}}{^{235}\text{U}}$	$\pm$	$\frac{^{206}\text{Pb}}{^{238}\text{U}}$	$\pm$	$\frac{^{207}\text{Pb}}{^{206}\text{Pb}}$	$\pm$	$\frac{^{207}\text{Pb}}{^{235}\text{U}}$	$\frac{^{206}\text{Pb}}{^{238}\text{U}}$	$\frac{^{207}\text{Pb}}{^{206}\text{Pb}}$
ttn 1	26.945	1.471	0.7687	0.0512	0.2542	0.0191	3381	3676	3211
ttn 2	21.052	2.036	0.5712	0.0690	0.2673	0.0353	3141	2913	3290
ttn 3	19.841	1.129	0.5317	0.0565	0.2706	0.0237	3084	2749	3310
ttn 4	24.491	0.751	0.7352	0.0259	0.2416	0.0073	3288	3553	3130
ttn 5	26.536	1.346	0.7878	0.0459	0.2443	0.0254	3367	3745	3148
ttn 6	24.019	1.689	0.6582	0.0861	0.2647	0.0171	3269	3260	3275
ttn 7	25.570	0.898	0.7666	0.0300	0.2419	0.0093	3330	3668	3133
ttn 8	21.063	1.042	0.5734	0.0377	0.2664	0.0188	3142	2922	3285
ttn 9	19.580	1.059	0.4706	0.0558	0.3018	0.0240	3071	2486	3479
ttn 10	21.781	1.098	0.5794	0.0491	0.2726	0.0148	3174	2946	3321
ttn 11	23.322	2.668	0.6658	0.0984	0.2541	0.0268	3240	3290	3210
ttn 12	23.437	1.399	0.7197	0.0332	0.2362	0.0160	3245	3495	3094

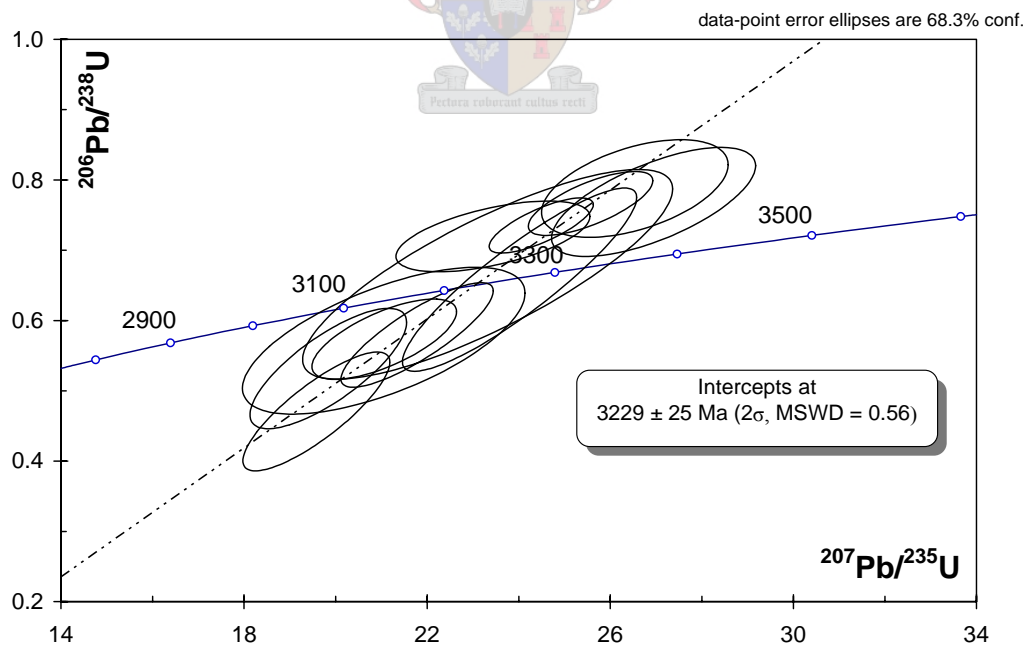


**Figure 8.3:** U-Pb Concordia diagram for titanite from sample Tj 3. Error ellipses are at one standard deviation.



Titanite from sample Tj 3 yields an upper Concordia intercept age of  $3229 \pm 25$  Ma (Fig. 8.3) and represents either the crystallization or cooling age of the titanite in this sample. If the age is interpreted as a crystallization age, the petrographic context indicates that the age provides a maximum estimate on the age of peak metamorphism and deformation. If it is interpreted as a cooling age, it constrains the timing of high-grade retrogression and consequently places a minimum estimate on the age of metamorphism and deformation. This age corresponds very well with other ages that constrain the timing of peak metamorphism in the southern Barberton terrain at ca. 3230 Ma (Kamo and Davis, 1994; Dziggel et al., 2002; Stevens et al., 2002; Kisters et al., 2003) and indicates that peak pressure-temperature conditions in the Tjakastad Schist Belt were attained during the second tectono-metamorphic episode ( $D_2$ ) that affected the Barberton terrain. The significant implication of this age is that peak metamorphism in the Theespruit Formation in the Tjakastad Schist Belt post-dates the intrusion of the Stolzburg and Theespruit Plutons into the Theespruit Formation during  $D_1$  by ca. 220 Ma.



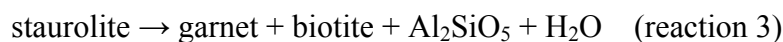
## **CHAPTER 9: DISCUSSION**

### 9.1 The pressure-temperature path

A detailed investigation of samples from the Tjakastad Schist Belt revealed that these lithologies only record evidence for a single prograde-retrograde regional metamorphic event. Almost all evidence of the early metamorphic history has been obliterated in the samples investigated and only the inclusion assemblages in garnet provide clues to the early, prograde metamorphic path. Zoisite and epidote are present as inclusions in garnet from amphibolite, while hornblende is only present in the matrix of these samples. This indicates that the prograde path involved initial burial and an increase in pressure, prior to heating to peak metamorphic temperatures (e.g. Apter and Liou, 1983; Spear, 1993).

Pressure-temperature estimates from peak metamorphic mineral assemblages in felsic schist and amphibolite constrain close-to-peak metamorphic conditions of  $7.4 \pm 1.0$  kbar and  $560 \pm 20$  °C, which is well within the stability field of kyanite. All samples were affected by a subsequent episode of retrogression that led to the re-equilibration of peak metamorphic minerals at lower grade conditions, as well as the generation of retrograde mineral assemblages.

Retrogression in amphibolite is characterized by the occurrence of plagioclase rims and coronas that pseudomorph after garnet and is indicative of decompression (e.g. Hoschek, 2001). Additionally, kyanite-bearing felsic schist exhibits overgrowths of sillimanite on peak metamorphic kyanite (sample 62601D). This sample also exhibits textures which indicate that kyanite formed via the breakdown of staurolite (reaction 1, Chapter 7), which is the aluminosilicate-in reaction in low-Al metapelites (Spear, 1993). Abundant staurolite is present in this sample, indicating that the staurolite-out reaction



(Holland and Powell, 1998) did not occur and that staurolite coexists with both kyanite and sillimanite. Figure 9.1 shows the pressure-temperature positions of reactions 1 and 3 as well as the fields of kyanite-staurolite and sillimanite-staurolite coexistence. The diagram illustrates that the kyanite-staurolite to sillimanite-staurolite transition cannot occur in response to a simple increase in temperature above pressures of ca. 7 kbar (Paths A and B in Fig. 9.1). Estimates from this study constrain a pressure of ca. 7.4 kbar, indicating that sillimanite in sample 62601D must have formed in response to decompression (Path C in Fig. 9.1), rather than an increase in temperature.

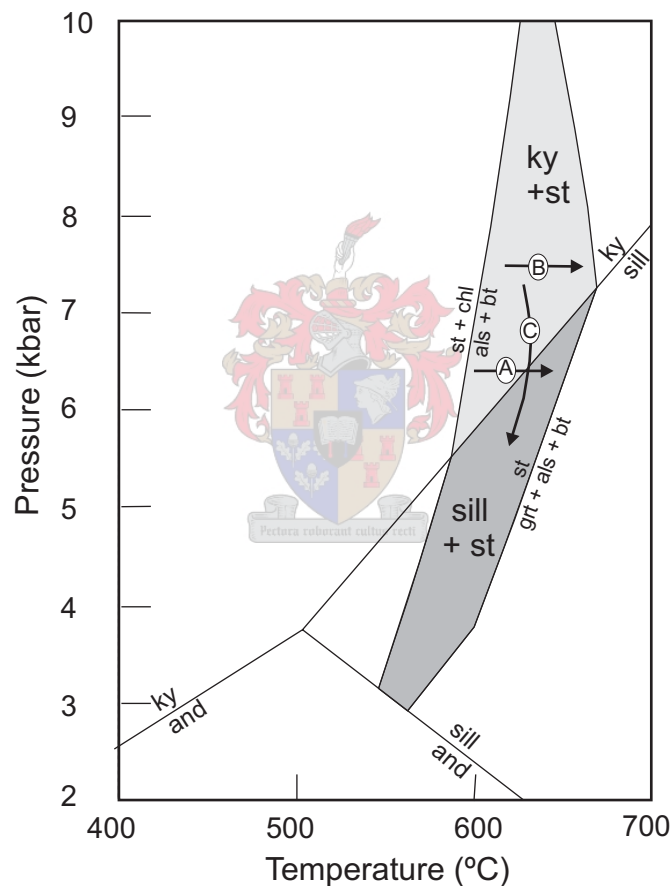


**Figure 9.1:** Pressure-temperature diagram showing the position of the aluminosilicate-in reaction in low-Al metapelites (left) and the staurolite-out reaction (right), as well as the stability fields of kyanite-staurolite (ky+st) and sillimanite-staurolite (sill+st) coexistence. Path (A) indicates the transition from ky-st coexistence to sill-st coexistence in response to increasing temperature below ca. 7 kbar. Path (B) illustrates that this transition cannot occur above ca. 7 kbar in response to increasing temperature, but must involve some component of decompression, as illustrated by path (C).

Further evidence of decompression during retrogression is presented by the pressure-temperature estimates from the retrograde assemblages in sample 61406 ( $6.1 \pm 2.7$  kbar and  $569 \pm 42$  °C; Fig. 9.2) and sample Tj 18 ( $3.8 \pm 1.3$  kbar and  $543 \pm 20$  °C; Fig. 9.2). Both these estimates are from zones of garnet breakdown that led to the formation of retrograde mineral assemblages and represent the likely pressure-temperature conditions under which garnet breakdown occurred in these samples during retrogression. Significantly, the temperature estimates from both samples are within error of peak temperature estimates, while pressure estimates are considerably lower than peak pressure estimates, indicating that the retrograde path involved close-to-isothermal decompression from ca. 7.4 kbar to less than 4 kbar prior to cooling (Fig. 9.2).

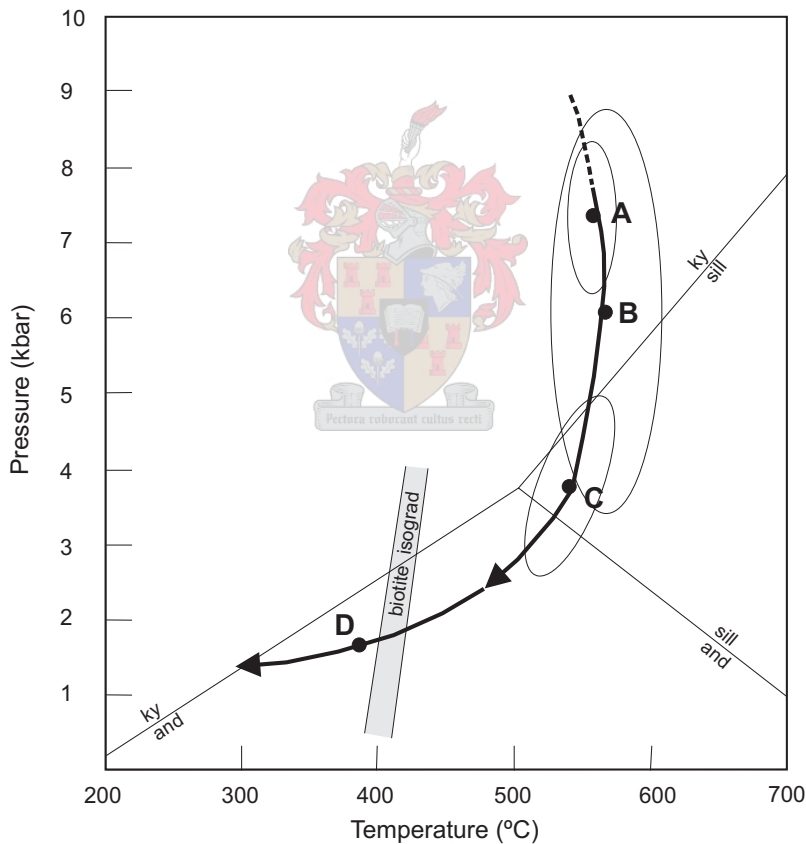


**Figure 9.2:** Proposed pressure-temperature path experienced by the lithologies of the Tjakastad Schist Belt. The path prior to attainment of peak metamorphic conditions is inferred. Peak metamorphic conditions are constrained by pressure-temperature estimates from felsic schist and amphibolite samples (point A). The retrograde path is constrained by point B, a pressure-temperature from the garnet breakdown assemblage in sample 61406; point C, a pressure-temperature estimate from the garnet breakdown assemblage in sample Tj 18; and point D, the retrograde mineral assemblage in sample 62105D.

The later part of the retrograde path is illustrated by sample 62105D (Fig. 9.2), which contains highly retrogressed relic crystals of staurolite and biotite in a matrix of chlorite, muscovite, albitic plagioclase and quartz. The presence of biotite and staurolite indicates that this sample was subjected to high-grade metamorphism, while the matrix of chlorite and muscovite indicates that retrogression must have continued into the greenschist-facies to below the biotite isograd in muscovite- and chlorite-bearing rocks (ca. 420 °C; Ferry, 1984).

In summary, these observations indicate that the metamorphic event described in the lithologies of the Tjakastad Schist Belt likely followed a clockwise pressure-temperature path that involved early burial followed by an increase in temperature to peak metamorphic conditions. Retrogression was via a path that involved initial close-to-isothermal decompression of some 4 kbar prior to cooling into the greenschist-facies (Fig. 9.2).

## 9.2 Comparative styles of metamorphism

Assuming a maximum crustal density of ca. 2.9 g/cm<sup>3</sup> (the density of greenschist-facies komatiite; Cloete, 1999), peak pressure estimates of 7.4 kbar imply that the rocks of the Tjakastad Schist Belt were buried to a depth of at least 25 km. Assuming a granitic crustal density of ca. 2.7 g/cm<sup>3</sup> constrains the maximum depth of burial to ca. 27 km. Given that peak temperature estimates have been constrained at 560 °C, these estimates indicate that the Tjakastad Schist Belt experienced an apparent geothermal gradient of 20 – 22 °C/km during burial (Fig. 9.3). Radiometric dating of titanite related to this event indicates that it occurred contemporaneously with high-grade metamorphism in the southern TTG terrain at ca. 3230 Ma (Kamo and Davis, 1994; Dziggel et al., 2002; Stevens et al., 2002). Pressure-temperature estimates from greenstone xenoliths preserved in the southern granitoid-gneiss terrain constrain peak metamorphic conditions at 8 – 11 kbar and 650 – 700 °C (Fig. 9.3; Dziggel et al., 2002). Although the pressure-temperature estimates from the Tjakastad Schist Belt are slightly lower, both localities

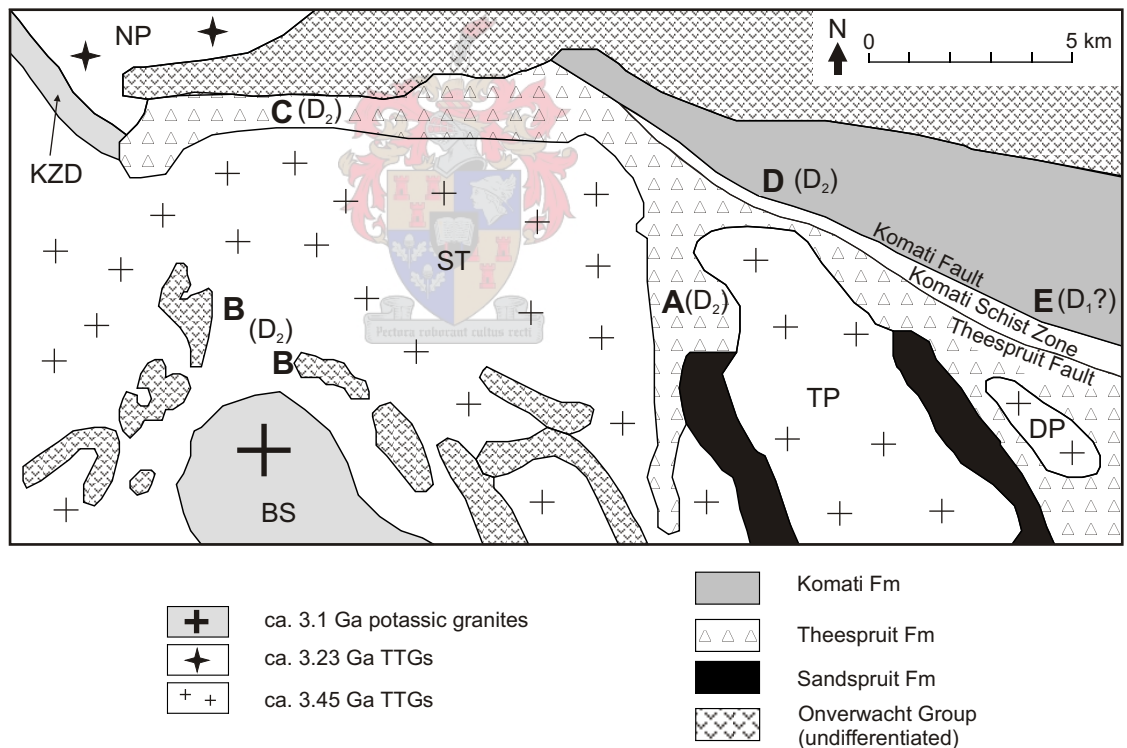
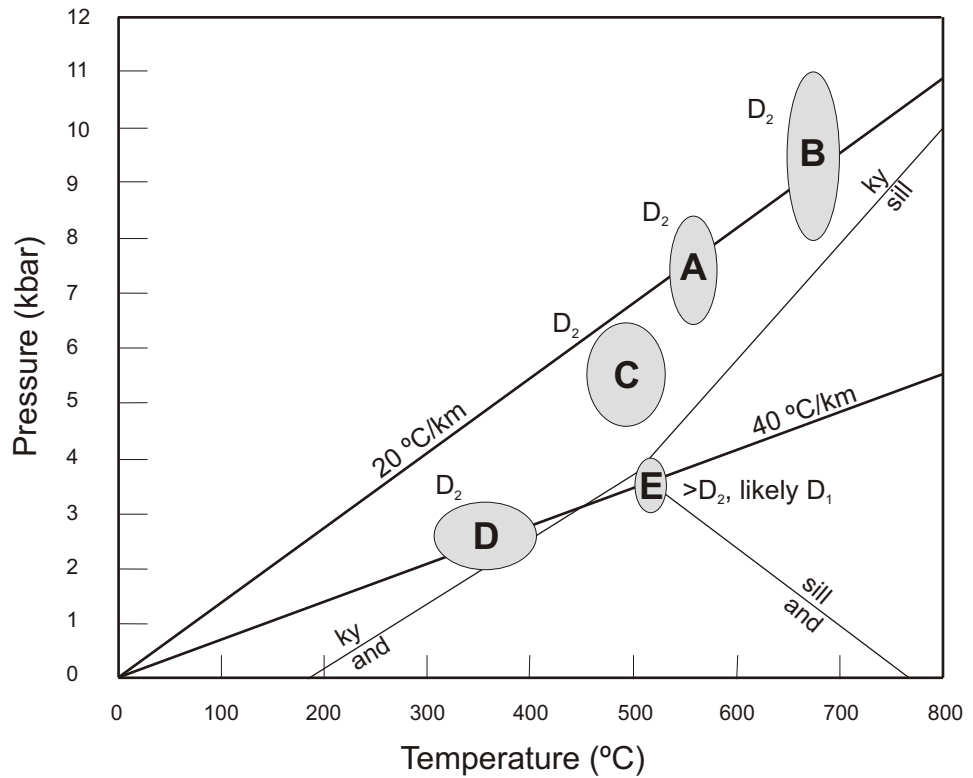


**Figure 9.3:** Pressure-temperature diagram and map summarizing the available metamorphic pressure-temperature data for the southern part of the Barberton terrain. Peak pressure-temperature estimates from the Tjakastad Schist Belt (point A), greenstone xenoliths in the southern gneiss terrain (point B; Dziggel et al., 2002) and the Stolzburg Schist Belt (point C; Kisters et al., 2003) were attained during  $D_2$  at 3.23 Ga and record similar apparent geothermal gradients. Point D represents P-T conditions in the Komati Formation during  $D_2$  (Cloete, 1999), while point E indicates peak metamorphic conditions in the Komati Formation that were attained prior to  $D_2$  (Cloete, 1999); likely during  $D_1$  at 3.45 Ga (Lopez-Martinez et al., 1992). Note the contrasting styles of metamorphism in the Theespruit Formation and gneiss terrain compared to the Komati Formation. Also note the location of the Komati Schist Zone and the Komati Fault on the boundary between the high-grade and low-grade terrains. NP = Nelshoogte Pluton, KZD = Kees Zyn Doorns Syenite, ST = Stolzburg Pluton, TP = Theespruit Pluton, DP = Doornhoek Pluton, BS = Boesmanskop Syenite.



are characterized by the same style of high-pressure, moderate-temperature regional metamorphism and exhibit very similar apparent geothermal gradients. This indicates that the rocks at these two localities most probably experienced similar burial paths (Fig. 9.3). Dziggel et al. (2002) estimated that the greenstone xenoliths were buried to a minimum depth of ca. 30 km, which is ca. 5 km more than the rocks from the Tjakastad Schist Belt. Currently these two localities are ca. 11 km apart (Fig. 9.3), indicating that, in its present orientation and erosion level, the granitoid-gneiss terrain exposed in this area is likely to be a relatively intact oblique crustal section without significant structural or metamorphic breaks.

In contrast, peak pressure-temperature conditions of metamorphism in the Komati and Hooggenoeg Formations within the greenstone belt were constrained at 3 – 4 kbar and 520 °C in a static (burial) environment (Fig. 9.3), as the rocks investigated do not exhibit penetrative fabrics and preserve protolith structures and textures (Cloete, 1999). These estimates indicate that the Komati and Hooggenoeg Formations were never buried to depths greater than 15 km, corresponding to the approximate apparent thickness of the upper Onverwacht, Fig Tree and Moodies Groups that overlie these formations (Viljoen and Viljoen, 1969a; Cloete, 1999). Consequently, Cloete (1999) proposed that metamorphism in the Komati Formation was caused by burial due to the deposition of the upper formations of the Barberton Supergroup (refer to Chapter 2, Fig. 2.2) and that peak metamorphic conditions were attained subsequent to Moodies Group deposition at ca. 3225 Ma. However,  $^{40}\text{Ar}/^{39}\text{Ar}$  amphibole ages from the Komati Formation constrain the timing of peak metamorphism to between 3425 and 3486 Ma, i.e. contemporaneous with  $D_1$  (Lopez-Martinez et al., 1992). This age represents the last time that the temperature in these rocks passed below the closure temperature of Ar in amphibole (ca. 500 °C; e.g. Von Blanckenburg et al., 1989; Dahl, 1996) and consequently has to reflect the timing of peak metamorphic temperature conditions in the Komati Formation.

North of the Theespruit Pluton, Cloete (1999) identified a zone where  $D_1$ -related peak metamorphism in the Komati Formation is overprinted by a retrograde, regional metamorphic event that is likely related to the  $D_2$  deformational event (Cloete, 1999). A

pressure-temperature estimate of  $2.6 \pm 0.6$  kbar and  $360 \pm 50$  °C (Sample MC120, Cloete, 1999) constrains the likely conditions of metamorphism in the Komati Formation during  $D_2$  at ca. 3230 Ma (Fig. 9.3). This locality is less than 4 km from the central parts of the Tjakastad Schist Belt and implies that a structural and metamorphic break equivalent to a crustal column of ca. 18 km existed between these two localities at that time (Fig. 9.3).

Although the Tjakastad Schist Belt appears, at least geographically, to be an extension and continuation of the Barberton Greenstone Belt, this study has shown that the geological evolution experienced by the Theespruit Formation in the Tjakastad Schist Belt differs significantly from that experienced by the other formations of the Onverwacht Group. Conversely, it has been shown that the Tjakastad Schist Belt experienced a geological history very similar to that proposed for the high-grade granitoid-gneiss terrain south of the greenstone belt. This implies that the Theespruit Formation has a close affinity to the southern granitoid-gneiss terrain – rather than the greenstone belt – and supports the proposal of previous workers that the Theespruit Formation is largely allochthonous with respect to the rest of the greenstone belt (e.g. De Wit et al., 1983, 1987, 1992; Armstrong et al., 1990; De Ronde and De Wit, 1994; Lowe et al., 1999). This also implies that the Theespruit Formation and southern granitoid-gneiss terrain must have been effectively decoupled from the bulk of the Barberton Greenstone Belt until at least after the  $D_2$  collisional and high-grade metamorphic event. The observation that both the Theespruit and Hooggenoeg Formations were affected by the ca. 3.45 Ga felsic magmatic event does not necessarily support the supposition that these two formations were spatially associated by ca. 3.45 Ga (refer to section 9.7).

### 9.3 The timing of deformation relative to metamorphism

The peak metamorphic mineral assemblages recorded in the Tjakastad Schist Belt are clearly pre-tectonic and all of the minerals have been affected by deformation subsequent to their crystallization. Deformation is marked by pervasive plastic deformation and boudinage of peak metamorphic plagioclase, staurolite and kyanite. Garnet porphyroblasts are also part of this assemblage but, because of garnet competency, were

not extensively affected by deformation. Retrograde garnet growth is confined to the pressure shadow sites of certain grains, suggesting that retrograde growth occurred during deformation. All of the peak metamorphic minerals display a grain-shape preferred orientation parallel to the pervasive  $S_0/S_1$  fabric exhibited in these rocks. Additionally, minerals that crystallized during retrogression, including muscovite and second-generation chlorite, are aligned parallel to the same fabric as the peak metamorphic minerals. The sum of this evidence indicates that the main deformational and fabric-forming event occurred during retrogression subsequent to the attainment of peak metamorphic conditions.

S-C' fabrics are intermittently developed in the  $S_1$  fabric, while the  $L_1$  mineral stretching lineation associated with  $S_1$  is orientated perpendicular to the intersection of the S and C' planes. S-C' fabrics are thought to principally form in stretching shear zones and in an extensional regime (e.g. Platt and Vissers, 1980; Passchier and Trouw, 1996). This, combined with the orientation of the stretching lineation, indicates that the  $S_0/S_1$  and  $L_1$  fabrics most likely formed in an extensional shear zone.

The combination of (1) isothermal decompression during retrogression, (2) pervasive deformation during retrogression and (3) the occurrence of (1) and (2) during extensional shearing indicates that the  $S_2/L_2$  fabric described in the Tjakastad Schist Belt and to the north and east of the Theespruit Pluton is an exhumation fabric that formed during the exhumation of the high-grade rocks subsequent to peak metamorphism.

#### 9.4 Kinematics of exhumation

Similar exhumation fabrics are documented in the Stolzberg Schist Belt, to the west of the current study area (Kisters et al., 2003). However, the fabric in the Stolzberg Schist Belt trends east-west and is deflected through  $90^\circ$  around the Stolzberg Pluton to achieve the north-south trend exhibited in the Tjakastad Schist Belt. Similarly, the fabric rotates through  $30 - 45^\circ$  around the Theespruit Pluton to achieve the northwest-southeast trend exhibited to the east of the Theespruit Pluton. Kisters et al. (2003) identified the presence

of an upright, isoclinal, shallow easterly-plunging synform in the Stolzburg Schist Belt that rotated the originally subhorizontal exhumation fabrics to their current subvertical orientation. The fabrics in the Tjakastad Schist Belt and east of the Theespruit Pluton are a continuation of fabrics in the Stolzburg Schist Belt but have been rotated and re-orientated subsequent to their formation (refer to section 9.6). However, because these fabrics are continuous, it may be valid to assume that they originally had a subparallel orientation.

When the fabrics in the Tjakastad Schist Belt and the Theespruit Formation to the east of the Theespruit Pluton are rotated to an east-west orientation and then ‘unfolded’ to the subhorizontal (Fig. 9.4), the mineral stretching lineation in these rocks has a northeast-southwest orientation and kinematic indicators define a top-to-the-northeast sense of movement similar to that in the Stolzburg Schist Belt (Kisters et al., 2003). In the Tjakastad Schist Belt, this sense of movement corresponds to the northeast displacement of the Theespruit Pluton relative to the Stolzburg Pluton. East of the Theespruit Pluton, this sense of movement indicates the northeast displacement of the greenstone belt relative to the Theespruit Pluton (Fig. 9.5).

The occurrence of similar exhumation fabrics and kinematics in large areas of the Theespruit Formation along the southern margin of the Barberton Greenstone Belt indicates that these fabrics represent part of a large-scale extensional shear zone along which the high-grade southern granitoid-gneiss terrain, including the Theespruit Formation, was exhumed and juxtaposed against the low-grade bulk of the Barberton Greenstone Belt (Kisters et al., 2003).

Previous workers (De Wit, 1982; De Wit et al., 1983, 1987, 1992; Armstrong et al., 1990; De Ronde and De Wit, 1994) have proposed that the Theespruit Formation and granitoid-gneiss terrain represents a basement onto which the Onverwacht Group and other formations of the greenstone belt were tectonically emplaced by thrusting during  $D_1$  at 3.45 Ga. This argument is based primarily on the age relationship between the Theespruit and Komati Formations, as the Theespruit Formation has yielded ages that are

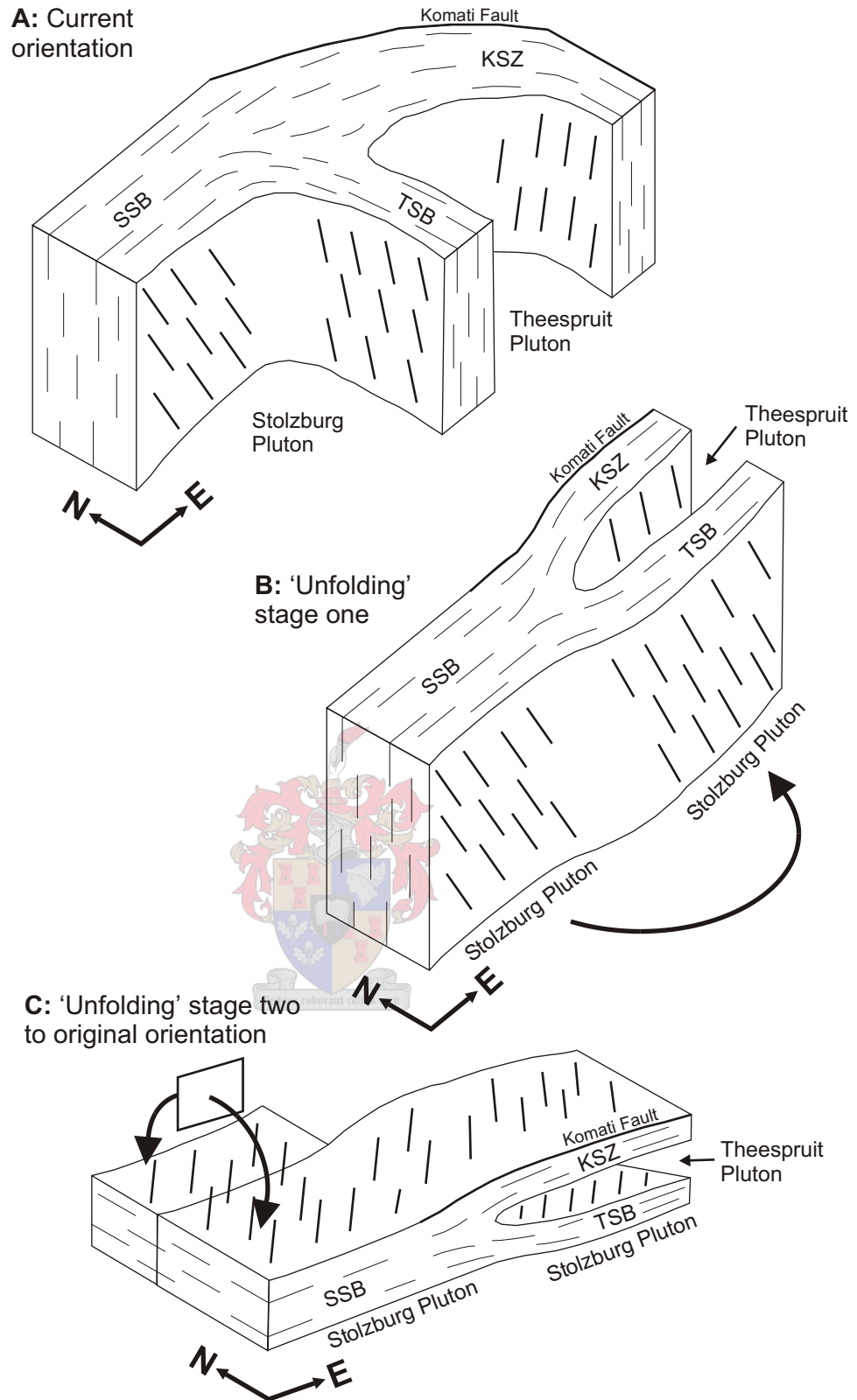


**Figure 9.4:** A series of sketches illustrating the rotation and unfolding of subvertical fabrics in the Theespruit Formation to their original subhorizontal orientation. **(a):** The current orientation of foliations (thin lines) and lineations (heavy lines) in the Stolzberg Schist Belt (SSB), Tjakastad Schist Belt (TSB) and Komati Schist Zone (KSZ). **(b):** The horizontal rotation of the TSB and KSZ from their respective N-S and NW-SE orientations into an E-W trend parallel to the SSB. **(c):** The vertical unfolding of fabrics around the axis of an upright isoclinal fold in the SSB (Kisters et al., 2003) into a subhorizontal orientation. In their original orientation, lineations in the Theespruit Formation have a horizontal, NE-SW orientation. Note that only the Theespruit Formation is shown and that the Stolzberg and Theespruit Plutons have been removed for clarity. Also refer to section 9.6 and Figure 9.7.

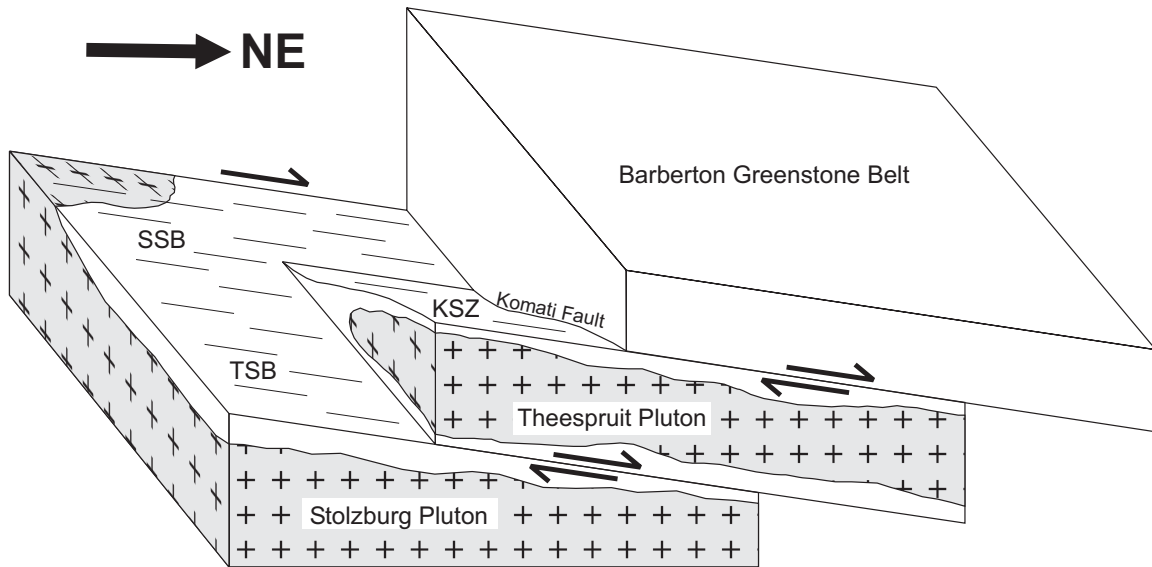


**Figure 9.5:** Sketch illustrating the top-to-the-northeast sense of displacement indicated by shear sense indicators in the Stolzburg Schist Belt (SSB; Kisters et al., 2003), the Tjakastad Schist Belt (TSB) and the Komati Schist Zone (KSZ). Note the position of the Komati Fault at the top of the KSZ, where it forms the boundary between the highly deformed rocks of the KSZ and the overlying Komati Formation.

younger than the overlying Komati Formation (Armstrong et al., 1990). The occurrence of similar 3.45 Ga felsic rocks in the Theespruit and Hooggenoeg Formations is proposed to indicate that these formations were spatially associated during  $D_1$  and that thrusting and emplacement of the Onverwacht Group onto the granitoid-gneiss basement must have occurred during  $D_1$  (De Wit et al., 1987; Armstrong et al., 1990; De Ronde and De Wit, 1994).

However, the detailed metamorphic and structural data presented in this study and other recent works (Dziggel et al., 2002; Kisters et al., 2003) are new aspects that were not considered in the model proposed by previous workers. These new aspects are: (1) peak metamorphism in the Theespruit Formation and granitoid-gneiss terrain occurred during  $D_2$ , indicating that the Onverwacht Group must have been decoupled from the granitoid-gneiss terrain at least until  $D_2$ ; (2) the bulk of deformation in the Theespruit Formation occurred during the exhumation of the high-grade terrain subsequent to peak metamorphism and (3) kinematic indicators in these rocks indicate a top-to-the-northeast



(i.e. normal) sense of movement, opposite to that expected during thrusting. These new aspects are incompatible with the model proposed by previous workers and favor the re-interpretation of the Theespruit Formation and granitoid-gneiss terrain as a tectonically exhumed terrain that has been underplated with respect to the Onverwacht Group and the rest of the greenstone belt during D<sub>2</sub>.

To the north and east of the Theespruit Pluton, the extensional shear zone corresponds to the highly deformed rocks of the Komati Schist Zone (e.g. Viljoen and Viljoen, 1969a,b; Williams and Furnell, 1979; De Wit et al., 1983). The Komati Schist Zone is bounded at its base by the Theespruit Fault and against the Komati Formation by the Komati Fault (Fig. 9.3; Viljoen and Viljoen, 1969a,b; Williams and Furnell, 1979; De Wit et al., 1983, 1987, 1992; De Ronde and De Wit, 1994; Lowe et al., 1999; Dann, 2000). Although the Komati Schist Zone and the Komati and Theespruit Faults could initially have been active as thrust faults during the burial of the southern terrain, the results of this study indicate that the bulk of deformation accommodated by these structures is the result of extension and normal faulting during D<sub>2</sub> at ca. 3.23 Ga, rather than compression and thrusting during D<sub>1</sub> at 3.45 Ga (De Wit et al., 1983, 1987, 1992; Armstrong et al., 1990; De Ronde and De Wit, 1994) or D<sub>2</sub> (Lowe et al., 1999).



## 9.5 Regional context and a model for the exhumation of the southern terrain

The D<sub>2</sub> accretionary and collisional episode is characterized by northwest-southeast-directed shortening and ultimately resulted in the amalgamation of the northern and southern Barberton terrains along the Saddleback-Inyoka Fault (De Ronde and De Wit, 1994; Kamo and Davis, 1994; Lowe, 1994, 1999; De Ronde and Kamo, 2000). Deposition and deformation of the Moodies Group occurred during D<sub>2</sub>, as the onset of sedimentation is constrained at 3224 ± 6 Ma (Tegtmeyer and Kröner, 1987) and Moodies strata are affected by D<sub>2</sub> shortening and folding (Heubeck and Lowe, 1994a,b; De Ronde and Kamo, 2000). The Moodies Group consists predominantly of coarse-clastic terrestrial sediments but recent studies have revealed that the succession also contains interbedded basaltic flows and airfall tuffs (Heubeck and Lowe, 1994a). The presence of

basaltic flows as well as syndepositional normal faults and the unconformable relationship between Moodies strata and underlying rocks led these workers to propose that the Moodies Group was deposited in a series of isolated, fault-bounded intramontane basins in an extensional setting (Heubeck and Lowe, 1994a,b), rather than a foreland basin as proposed by Jackson et al. (1987).

Consequently, the formation of Moodies basins as well as the exhumation of the southern high-grade terrain occurred via extension in a tectonic regime dominated by overall compression and crustal thickening. The occurrence of (1) extension in an overall compressional tectonic regime combined with (2) the occurrence of constrictional, largely coaxial ( $L \gg S$ ) fabrics in the high-grade mylonites that are (3) overprinted by non-coaxial (S-L) fabrics in the retrograde mylonites and (4) the sharp metamorphic gradient between the Theespruit rocks and the overlying formations all indicate that the highly deformed rocks of the Theespruit Formation represent an extensional detachment related to the extensional collapse of the  $D_2$  orogen (e.g. Dewey, 1988; Platt and Vissers, 1989; Andersen and Osmundsen, 1994; Krabbendam and Dewey, 1998; Kisters et al., 2003).

During collision and orogeny, the crust is laterally shortened and vertically thickened by folding and thrusting. The thickening of the crust can lead to gravitational instability which, during the ensuing thermal equilibration, may cause the thickened crust to collapse and be extruded at right angles to the regional shortening direction (e.g. Dewey, 1988). In the mid- to lower crust, extrusion occurs by means of ductile flow and, because the crust is confined in two directions (i.e. laterally in the direction of convergence and vertically because of crustal stacking and loading), extrusion results in the formation of pervasive constrictional coaxial fabrics similar to those described in the high-grade lithologies of the Theespruit Formation and the southern gneiss terrain (Fig. 9.6). In contrast, extension in the brittle upper crust is accommodated by normal faulting and the formation of small, fault-bounded intramontane basins (Dewey, 1988), such as has been proposed for the Moodies Group (Heubeck and Lowe, 1994a,b). During lateral extension, the crust is thinned and high-grade, deep-crustal rocks are progressively

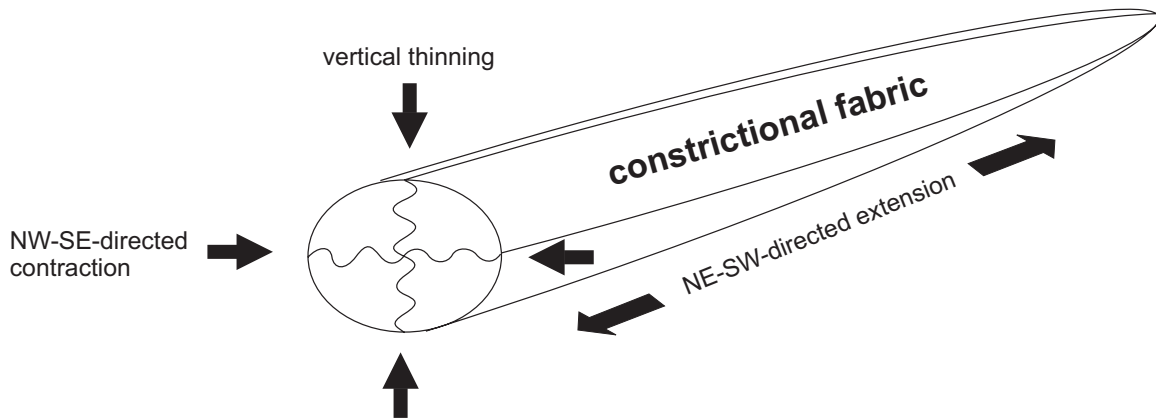


**Figure 9.6:** Sketch illustrating that the development of the highly constrictional fabrics present in the Lower Plate rocks must have formed during northeast-southwest-directed extension accompanied by shortening in two directions, i.e. vertical thinning and continued northwest-southeast-directed contraction. If there was no continued lateral contraction, these fabrics would record flattening-type strains, rather than constrictional strains.

exhumed and brought closer to the surface. During this process, normal faults that were initiated in the upper crust can cut into the deep-crustal rocks, causing the high-grade coaxial mylonites in these rocks to be overprinted by non-coaxial retrograde mylonites (Dewey, 1988). This overprinting relationship of coaxial and non-coaxial fabrics has been documented in the Theespruit Formation during this study (refer to Chapter 4) and by Kisters et al. (2003). Because high-grade rocks are exhumed along the extensional detachment and juxtaposed against low-grade rocks, continued extensional orogenic collapse can lead to the formation of metamorphic core complexes (e.g. Davis, 1980; Davis, 1987; Davis and Lister, 1988; Lister and Davis, 1989; Granillo and Calmus, 2003).

In this scenario, the southern gneiss terrain and high-grade greenstone lithologies, including the Theespruit Formation, correspond to the Lower Plate rocks that are found below the detachment and have been tectonically exhumed from deep crustal levels. Similarly, the bulk of the Barberton Greenstone Belt, including the Komati and Hoogenoeg Formations, represent the low-grade rocks of the Upper Plate that have

effectively ‘floated’ above the detachment and were not subjected to high-grade metamorphism.

## 9.6 The rotation and re-orientation of fabrics

The highly constrictional ( $L \gg S$ ) fabrics that are ubiquitous of the Lower Plate rocks indicate that northeast-southwest-directed extension was accompanied by vertical thinning and continued northwest-southeast-directed contraction (Fig. 9.6). The extensional detachment in the Stolzburg Schist Belt – Komati Schist Zone is also folded by the  $D_2$  Onverwacht Anticline. Moreover, Moodies strata that were deposited during the extensional collapse have been shortened and are folded by prominent  $D_2$  structures (Heubeck and Lowe, 1994a, b; De Ronde and De Wit, 1994). The shortening and folding of  $D_2$  extensional features by  $D_2$  upright folds strongly suggests that northeast-southwest-directed extension and the exhumation of the high-grade terrain occurred during continued northwest-southeast-directed shortening. This continued shortening resulted in the formation of the prominent upright isoclinal folds present in the Barberton Greenstone Belt and it is proposed that progressive shortening is also responsible for the rotation of the Tjakastad Schist Belt to its current right-angle orientation relative to the Stolzburg Schist Belt.

The high-temperature mylonitic fabrics in the Tjakastad Schist Belt are not overprinted by low-temperature cataclasites. In contrast, the Komati Schist Zone is characterized by more pervasive retrogression and the development of cataclasites and other lower-grade fabrics. This suggests that shearing in the Tjakastad Schist Belt was confined to the early, deep-crustal stages of exhumation and that deformation was progressively partitioned into the Komati Schist Zone during the later stages of exhumation. The cessation of deformation in the Tjakastad Schist Belt could indicate that it became misorientated relative to the top-to-the-northeast material transport direction. The misorientation and lock-up of extensional detachments has been documented in other terrains, such as the Western Gneiss Region of Norway (Krabbendam and Dewey, 1998). This terrain consists of a high-grade Lower Plate displaying highly constrictional fabrics

and an allochthonous, low-grade Upper Plate that contains a series of molasse-type basins. The molasse basins formed in response to mid- and lower-crustal extension and the basins are folded perpendicular to the extension direction (Krabbendam and Dewey, 1998). The Lower Plate is separated from the Upper Plate by the Middle Plate that consists of a series of bifurcating extensional detachment faults and low-strain zones. Some of the early extensional detachments in the Middle Plate have been shortened and folded perpendicular to the extension direction, rendering them misorientated to accommodate further shearing. This caused the early detachments to ‘lock up’ and shearing to be partitioned into new, favourably orientated detachments (Krabbendam and Dewey, 1998). If this model is applied to the Barberton terrain, the Tjakastad Schist Belt could represent part of an early detachment that became misorientated during progressive exhumation. The Theespruit Pluton and low-strain greenstones that occur between the Tjakastad Schist Belt and the Komati Schist Zone could represent part of an allochthonous Middle Plate (Figs. 9.5 and 9.7; refer to section 9.8).

The exhumation fabrics described in the Theespruit Formation as well as many of the D<sub>2</sub> fabrics and structures in the Barberton Greenstone Belt formed in an originally subhorizontal orientation and were then rotated and steepened to their current subvertical orientation (e.g. Lowe, 1999). The 3215 Ma Dalmein Pluton truncates subvertical D<sub>2</sub> structures, indicating that the steepening of fabrics must have been a continuum of D<sub>2</sub> deformation, rather than re-orientation during a later episode of deformation. Much of the steepening of fabrics as well as the right-angle orientation of the Tjakastad Schist Belt relative to the Stolzburg Schist Belt can be explained by continued shortening during extension (see above). However, the extensional detachment itself is orientated perpendicular to the shortening direction, meaning that the steepening of the extensional detachment to a subvertical orientation cannot be accomplished by this mechanism.

Folding, warping and local steepening of the extensional detachment in the direction of extension is a common feature of metamorphic core complexes (e.g. Lister and Davis, 1989) and is caused by isostatic rebound related to the tectonic denudation of the upper crust as well as local granite magma input into the middle crust (Lister and Davis, 1989).

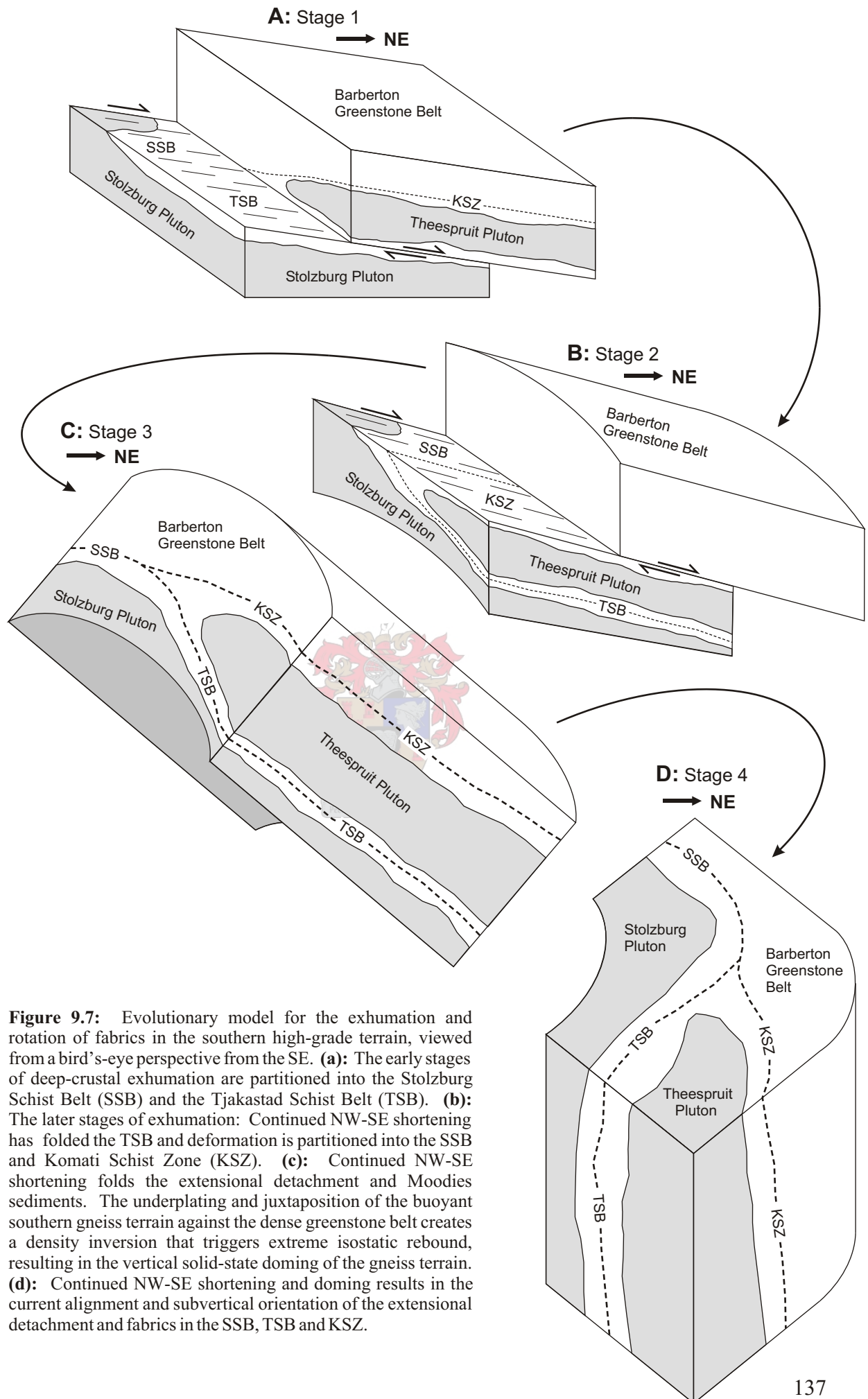
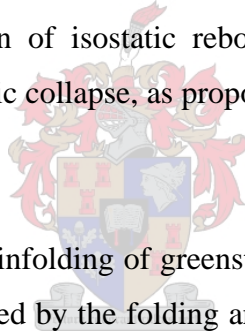


**Figure 9.7:** Evolutionary model for the exhumation and rotation of fabrics in the southern high-grade terrain, viewed from a bird's-eye perspective from the SE. **(a):** The early stages of deep-crustal exhumation are partitioned into the Stolzberg Schist Belt (SSB) and the Tjakastad Schist Belt (TSB). **(b):** The later stages of exhumation: Continued NW-SE shortening has folded the TSB and deformation is partitioned into the SSB and Komati Schist Zone (KSZ). **(c):** Continued NW-SE shortening folds the extensional detachment and Moodies sediments. The underplating and juxtaposition of the buoyant southern gneiss terrain against the dense greenstone belt creates a density inversion that triggers extreme isostatic rebound, resulting in the vertical solid-state doming of the gneiss terrain. **(d):** Continued NW-SE shortening and doming results in the current alignment and subvertical orientation of the extensional detachment and fabrics in the SSB, TSB and KSZ.



The steepening through almost 90° of the extensional detachment in the Theespruit Formation is more extreme than steepening observed in modern core complexes. However, a feature that is largely unique to the Archaean is the density inversion caused by dense mafic-ultramafic supracrustal greenstones that overly buoyant granitoid basement (e.g. Marshak et al, 1992, 1997; Marshak, 1999). It should be noted that, in the southern Barberton terrain, the density inversion post-dates the emplacement of the TTGs by ca. 220 Ma and occurred in response to terrain accretion and high-grade metamorphism, rather than TTG plutonism. It is possible that the density inversion drove an extreme case of isostatic rebound whereby the originally subhorizontal exhumation fabrics were rotated to the subvertical and the dense greenstone material was tightly infolded between the zones of buoyant basement. In this sense, the steepening of fabrics as well as the arcuate dome-and-keel outcrop pattern of many granitoid-greenstone terrains can be explained by the late-stage solid-state doming of lower-crustal granitoid-gneisses driven by a combination of isostatic rebound and density inversion during crustal extension related to orogenic collapse, as proposed by Marshak et al. (1992, 1997) and Marshak (1999).



The steepening of fabrics and the infolding of greenstone material between the granitoid domes must have been accompanied by the folding and tightening of existing structures, as indicated by the presence of a late, upright isoclinal synform in the Stolzburg Schist Belt (Kisters et al., 2003). The steepening and tightening must have involved some apparently reverse sense of displacement of the Upper Plate greenstones relative to the Lower Plate rocks (Fig. 9.8). A prominent silicified chlorite schist unit that occurs close to the base of the Komati Schist Zone north of the Theespruit Pluton (refer to Chapter 4, Fig. 4.11) displays well-developed shear fabrics that point to a north side (greenstone) up – south side (granitoid) down sense of displacement. This unit, and other similar units, indicate that sections of the Komati Schist Zone must have been re-activated under lower greenschist-facies conditions and experienced an apparent reverse sense of displacement. The occurrence of apparently reverse displacement under low-grade metamorphic conditions is consistent with the style of deformation expected during the late-stage steepening of fabrics.

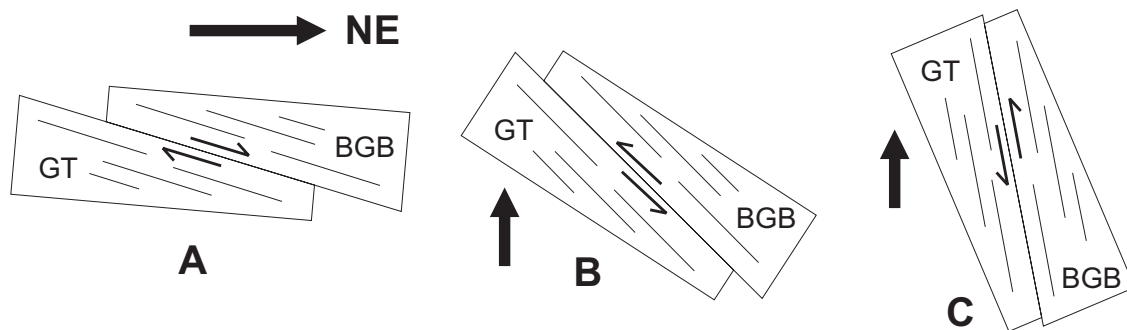


**Figure 9.8:** Series of schematic sketches illustrating the apparent reverse sense of shear that must have been associated with the steepening of the extensional detachment. **(a):** The subhorizontal orientation and normal sense of movement along the extensional detachment during the exhumation and underplating of the high-grade gneiss terrain (GT) to the greenstone belt (BGB). **(b and c):** Buoyant doming of the gneiss terrain (solid arrow) leads to the steepening of fabrics with an associated reverse sense of displacement along the extensional detachment.

In summary, the right-angle orientation of the Tjakastad Schist Belt relative to the Stolzburg Schist Belt and Komati Schist Zone as well as folding in the Moodies Group can be explained by continued shortening during extension, while the steepening of the extensional detachment can be explained by a special case of isostatic rebound accentuated by the density inversion unique to the Archaean. These mechanisms are two end-members that combined and operated simultaneously to achieve the current fabric orientation and dome-and-keel outcrop pattern exhibited by the granitoids and greenstones along the southern margin of the Barberton Greenstone Belt (Fig. 9.7).

### 9.7 The significance of felsic rocks in the Theespruit Formation

An interesting and quite unintentional result of this study concerns the origin of the felsic rocks that are ubiquitous of the Theespruit Formation and are, along with felsic units in the Hooggenoeg Formation, the only occurrence of these rocks in the Onverwacht Group. An investigation of these rocks by De Wit et al. (1987) and Armstrong et al. (1990) revealed that the felsic volcanics have chemical compositions and ages similar to the TTGs that intrude and surround the Barberton Greenstone Belt. On this basis, it was proposed that the felsic rocks in the Onverwacht Group are extrusive equivalents of the ca. 3.45 Ga TTG suite. Whereas the correlation of the Hooggenoeg Formation to the

TTG suite was made on the basis of geochemical and geochronological data (De Wit et al., 1987), the Theespruit Formation rocks were only correlated on the basis of a ca. 3.45 Ga depositional age of a volcanoclastic unit in this formation (Armstrong et al., 1990). Thus far, no geochemical data has been presented to support the correlation of the Theespruit Formation felsic volcanics to the Hooggenoeg Formation and the ca. 3.45 Ga TTG suite.

The geochemical and petrographic analysis of felsic volcanics during this study has revealed that these rocks have chemical compositions that are, apart from their REE profiles, largely indistinguishable from the felsic rocks in the Hooggenoeg Formation and the early TTG plutonic suite (refer to Chapter 5). However, the REE profiles of the Theespruit Formation rocks differ significantly from those of the Hooggenoeg Formation as well as the ca. 3.45 Ga TTG plutons. The Theespruit rocks are not depleted in heavy REEs and display pronounced negative Eu anomalies, whereas the Hooggenoeg rocks and TTGs are depleted in heavy REEs and do not exhibit Eu anomalies (refer to Chapter 5). These differences cast significant doubt on the correlation of the Theespruit Formation felsic volcanics with felsic rocks in the Hooggenoeg Formation as well as to the early TTG plutonic suite. On these grounds it is suggested that, contrary to the proposal of previous workers (De Wit et al., 1987; Armstrong et al., 1990), the Theespruit and Hooggenoeg Formations do not appear to be stratigraphic equivalents; nor are the felsic rocks in the Theespruit Formation derived from the ca. 3.45 Ga TTG plutons that intrude this formation.

The Doornhoek and Steynsdorp Plutons and phases of the Ngwane Gneiss are the only felsic rocks that have REE profiles similar to those of the felsic volcanics in the Theespruit Formation (refer to Chapter 5; Hunter et al., 1984; Kröner and Tegtmeier, 1994; Yerron, 2003). Apart from the Doornhoek Pluton, which has a crystallization age of  $3448 \pm 4$  Ma (Kamo and Davis, 1994), both the Steynsdorp Pluton and Ngwane Gneiss are more than 50 Ma older than the ca. 3.45 Ga early TTG suite. The Steynsdorp Pluton has a crystallization age of  $3509 \pm 4$  Ma (Kröner et al., 1996), while different phases of the Ngwane Gneiss have yielded crystallization ages of  $3521 \pm 23$  Ma and  $3490 \pm 3$  Ma

(Kröner and Tegtmeier, 1994). The crystallization age of the felsic volcanics described in this study has not been determined, but the geochemical similarities between these rocks and the older, pre-3.5 Ga plutons and gneisses suggests that they might be genetically related and could form part of the same felsic magmatic event. Consequently, one might speculate that the felsic volcanics in the Theespruit Formation are volcanic equivalents of the older, pre-3.5 Ga gneisses, rather than the ca. 3.45 Ga TTG suite.

The ca. 3.45 Ga depositional age of the volcanoclastic unit mentioned above is, to date, the only age obtained from the Theespruit Formation that is similar to that of the Hooggenoeg Formation and the ca. 3.45 Ga TTG suite. Interestingly, the agglomerate unit that yielded this age is not typical of the agglomerate found in the Theespruit Formation as it is the only unit that contains a polymict clast assemblage. This unit contains clasts of felsic volcanics, banded and white chert, amphibolite and banded gneiss (refer to Chapter 3, Fig. 3.2b and c; De Wit et al., 1983), while all other agglomerate units investigated during this study are monomict and only contain clasts of felsic volcanic rocks (refer to Chapter 3, Fig. 3.2a). Consequently, it is possible that this unit – and its age – might not be representative of felsic rocks in the Theespruit Formation and that most of the felsic rocks conceivably belong to an older, pre-3.5 Ga age group similar to the Theespruit Formation in the Steynsdorp Anticline (Kröner et al., 1996). If this is the case, it would support the supposition that the bulk of the Theespruit Formation is older than the Komati Formation and that the Theespruit Formation only contains localized and isolated lenses of younger material (refer to section 9.8; Lowe and Byerly, 1999).

This study has also identified the presence of clastic sedimentary horizons in the Theespruit Formation. The sediments are intercalated and closely associated with felsic volcanic and volcanoclastic rocks and have a geochemical signature typical of many Archaean sediments; i.e. extreme enrichment in the transition trace elements (McLennan and Taylor, 1984; Toulkeridis et al., 1999; Dziggel et al., 2002). However, the REE pattern of these sediments is distinctive and indicates that they are derived almost exclusively from mafic volcanic sources, without significant input from a felsic igneous

source (McLennan and Taylor, 1984). These sediments appear to be more primitive than, for example, Fig Tree sediments that were derived from a mixed granite-greenstone source (Toulkeridis et al., 1999). The apparent lack of a felsic component in these sediments could indicate that they were derived from a confined hinterland that did not contain any of the granitoids present in the Barberton terrain at the time. Alternatively, one may speculate that these sediments were derived prior to the presence of a significant granitoid component in the Barberton terrain. Gneissose fragments preserved in Theespruit Formation indicate the existence of a granitoid basement as early as 3538 Ma (Armstrong et al., 1990; Kamo and Davis, 1994). This might suggest that these sediments could have been derived and deposited prior to ca. 3.54 Ga. The close association of these sediments with felsic volcanics could indicate that they were deposited contemporaneously, as has been proposed for the chert units that are commonly associated with the felsic volcanic units (Viljoen and Viljoen, 1969b). If the felsic volcanics of the Theespruit Formation in the Tjakastad Schist Belt can indeed be correlated with those of the Steynsdorp Anticline, these rocks can potentially be as old as 3.54 Ga, which would support the apparent antiquity and primitive nature of the sediments. However, considering the current lack of constraints on the depositional or crystallization age of these rocks as well as the intense tectonization of the Theespruit Formation, the interpretation of their geochemical signature as a reflection of their age remains circumstantial and highly speculative (refer to section 9.8).

The Theespruit and Hooggenoeg Formations both experienced geochemically similar felsic magmatism at ca. 3.45 Ga as the Theespruit Formation was intruded by the Stolzburg and Theespruit Plutons and felsic rocks were erupted in the Hooggenoeg Formation (De Wit et al., 1987; Armstrong et al., 1990; Kamo and Davis, 1994). This might suggest that the Theespruit and Hooggenoeg Formations were already juxtaposed and spatially associated during this event (De Wit et al., 1987; Armstrong et al., 1990). However, ca. 3.45 Ga felsic magmatic activity has a relatively homogeneous geochemical signature, as reflected by the composition of the various TTGs in the Barberton terrain (Anhaeusser and Robb, 1983b; Robb and Anhaeusser, 1983; Yerron, 2003). Moreover, this magmatic event has not only been documented in the Barberton terrain but has also

been reported from other parts of the Kaapvaal Craton, such as the Vredefort Dome (Hart et al., 1981; 1999). This indicates that ca. 3.45 Ga felsic magmatism was not localized but occurred on a craton-wide scale, suggesting that this event cannot be unequivocally used to infer the timing of juxtaposition of the Theespruit Formation and the Onverwacht Group.

## 9.8 The significance of the Theespruit Formation as a basal mélangé

The mélangé-like nature of the Theespruit Formation has been documented by previous workers (De Wit et al., 1983; Lowe et al., 1999) and has also been highlighted by this study (refer to Chapter 4). The results of this study favour the re-interpretation of the Theespruit Formation as part of an allochthonous, underplated high-grade terrain that was tectonically exhumed during the main D<sub>2</sub> collisional event. Consequently, the Theespruit Formation mélangé was only assembled and emplaced in its current location at ca. 3.23 Ga. This implies that any lithological unit older than ca. 3.23 Ga could potentially have been sampled and incorporated into the mélangé, suggesting that the Theespruit Formation could conceivably contain litho-tectonic units as young as the Fig Tree Group (Byerly et al., 1996). The (apparently) inconsistent crystallization and depositional ages that have been reported from the Theespruit Formation (Armstrong et al., 1990; Kröner et al., 1996) supports the proposal that the Theespruit Formation consists of litho-tectonic units of variable age that were sampled from a variety of sources and localities.

Notably, all of the peak metamorphic estimates from rocks in the Tjakastad Schist Belt constrain the same pressure-temperature conditions of metamorphism (refer to Chapter 7), suggesting that all of the rocks in the belt were sampled from a similar crustal depth. Considering that it is likely that the Theespruit Formation was only assembled during the exhumation of these rocks, it is surprising that the Theespruit Formation apparently does not contain lithologies that record different peak metamorphic conditions to suggest sampling from a variety of localities and crustal depths. However, most of the rocks do not have chemical compositions suited to the generation of pressure-temperature sensitive mineral assemblages and it is only the rare clastic sediments that exhibit mineral



assemblages able to constrain relatively detailed metamorphic pressure-temperature paths. The isolated and sporadic occurrence of the sediments makes it impossible to achieve the resolution required to identify subtle differences in peak metamorphic conditions that might indicate sampling at different crustal depths. Alternatively, the extremely small spread in pressure-temperature estimates from the Tjakastad Schist Belt could be explained by the re-equilibration of the peak assemblages during deformation. Because re-equilibration was driven by the continued dynamic recrystallization of the assemblage, the termination of deformation would effectively close the system to further diffusion, causing the pressure-temperature conditions at that point to be accurately recorded. The characteristic mylonitic fabrics of the Tjakastad Schist Belt are not overprinted by low-temperature brittle- or brittle-ductile fabrics, suggesting that deformation must have ceased at relatively high temperatures when exhumation was partitioned into the Komati Schist Zone (refer to section 9.6). It is possible that the pressure-temperature estimates from all samples reflect the conditions at which deformation in the Tjakastad Schist Belt stopped, rather than the crustal depth from which each sample was incorporated into the mélangé.

Kinematic indicators in the Tjakastad Schist Belt indicate that the Stolzburg Pluton was uplifted relative to the Theespruit Pluton during exhumation (Fig. 9.5). Although the amount of relative movement between the two plutons is not constrained, this might indicate that the Theespruit Pluton was incorporated into the mélangé at a shallower crustal depth than the Stolzburg Pluton and could form part of an allochthonous Middle Plate, as suggested in section 9.6. This supposition is supported by the metamorphic grade of lithologies east of the Theespruit Pluton, which generally exhibit greenschist-facies grades and only contain isolated occurrences of amphibolite-facies lithologies. However, the occurrence of greenschist-facies lithologies does not necessarily reflect lower peak metamorphic conditions in these rocks, but could simply be the result of the more intense and pervasive retrogression of these rocks relative to rocks of the Tjakastad Schist Belt.

## 9.9 The preservation of D<sub>1</sub> metamorphism and deformation

This study, along with the work of Dziggel et al. (2002) and Kisters et al. (2003) has shown that peak metamorphism in the southern granitoid-greenstone terrain occurred during D<sub>2</sub> at ca. 3.23 Ga and that the deformation exhibited by the Theespruit Formation occurred during the exhumation of this terrain subsequent to peak metamorphism. However, most of the evolutionary models of the Barberton Greenstone Belt describe an earlier D<sub>1</sub> event that particularly affected the Theespruit Formation (e.g. De Ronde and De Wit, 1994; Lowe et al., 1999). Evidence of this event is provided by amphibolite-facies lithologies that are truncated by the Theespruit Pluton in the type locality of the Theespruit Formation (Viljoen and Viljoen, 1969b; De Wit et al., 1983). During this study, a similar truncation of lithologies was documented in the eastern part of the Tjakastad Schist Belt and intrusive breccias of TTG into amphibolite are also preserved in a number of localities around the Stolzburg and Theespruit Plutons (refer to Chapter 3, Fig. 3.6b; Kisters and Anhaeusser, 1995b). The metamorphism and fabrics exhibited by the truncated rocks is indistinguishable from the metamorphism and fabrics that occur in the bulk of the Theespruit Formation and that have been dated to have formed during D<sub>2</sub>. The identification of an (apparently) older metamorphic and deformational event in these rocks could not be resolved as it would require extensive and extremely detailed geochronological work that falls outside the scope of this study. However, it is conceivable that D<sub>1</sub> fabrics and features could be preserved in low-strain domains that escaped D<sub>2</sub> deformation by strain partitioning. The voluminous felsic schist in the Theespruit Formation provides a significant competency contrast relative to massive amphibolite and crystalline granitic plutons that would allow deformation to be partitioned into the less competent felsic units. The occurrence of apparently D<sub>1</sub> metamorphism in the truncated rocks cannot be easily explained as no preserved evidence of poly-metamorphism was found during this study. Garnet porphyroblasts in felsic schist only record D<sub>2</sub> prograde and retrograde metamorphism, which might suggest that D<sub>1</sub> metamorphism had a greenschist-facies peak that did not allow garnet growth. Alternatively, all evidence of D<sub>1</sub> peak metamorphism could have been destroyed by a retrograde event that selectively affected the felsic schist, thereby only preserving D<sub>1</sub>

metamorphism in the truncated and brecciated amphibolite. However, considering that D<sub>2</sub> metamorphism is the peak metamorphic event manifested across an extensive area of the southern granitoid-greenstone terrain, it is unlikely that parts of this terrain could have escaped this blanket high-grade event to preserve pre-D<sub>2</sub> peak metamorphic assemblages.



## **CHAPTER 10: CONCLUSIONS**

### 10.1 Conclusions

The main conclusions of this study are:

(1) The Theespruit Formation experienced high-pressure low-temperature regional metamorphism very similar to metamorphism documented for the southern granitoid-gneiss terrain (Dziggel et al., 2002). Peak metamorphism in both localities occurred during the main  $D_2$  collisional event in the Barberton Greenstone Belt at ca. 3.23 Ga. Peak pressure-temperature estimates from the Komati Formation (Cloete, 1999) indicate that a metamorphic break equivalent to a crustal column of ca. 18 km existed between the Theespruit and Komati Formations during  $D_2$ .

(2) The juxtaposition of the southern high-grade granitoid-gneiss terrain, including the Theespruit Formation, against the low-grade bulk of the greenstone belt was achieved by extensional detachment faulting in the Theespruit Formation that led to core complex formation (Kisters et al., 2003). Extension occurred in response to  $D_2$  compression, similar to the extensional collapse documented in modern orogenic environments such as the Himalaya and the Norwegian Caledonides (Dewey, 1988; Krabbendam and Dewey, 1998). The location of the extensional detachment corresponds, in part, to the Komati Schist Zone and the Komati Fault, indicating that these structures are  $D_2$  normal faults, rather than  $D_1$  thrusts as suggested by previous workers (e.g. De Wit et al., 1983; De Ronde and De Wit, 1994).

(3) The felsic volcanic rocks that are characteristic of the Theespruit Formation are geochemically distinct from felsic volcanics in the Hooggenoeg Formation and the ca. 3.45 Ga TTG suite that intrudes the Theespruit Formation. This casts doubt on the proposal of previous workers (e.g. De Wit et al., 1987; Armstrong et al., 1990) that felsic rocks in the Theespruit and Hooggenoeg Formations are extrusive equivalents of the ca. 3.45 Ga TTG suite and that the Theespruit and Hooggenoeg Formations are stratigraphic

equivalents. Geochemically, felsic rocks of the Theespruit Formation have a close affinity to earlier, pre-3.5 Ga TTGs, such as the Steynsdorp Pluton, and are most likely to be extrusive equivalents of these plutons.

(4) The Theespruit Formation contains rare aluminous clastic sediments that are associated with the felsic volcanic rocks and were derived from a source consisting almost exclusively of mafic igneous rocks. These sediments appear to be more primitive than younger Fig Tree Group sediments that were derived from a mixed granite-greenstone source. The primitive nature of these sediments could suggest that they were derived prior to the presence of a significant granitoid component in the Barberton terrain.

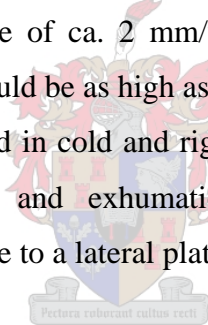
(5) The results of this study favor the re-interpretation of the Theespruit Formation as an allochthonous basal mélange that forms part of a tectonically exhumed and underplated high-grade terrain. The Theespruit Formation was only fully assembled and emplaced in its current location during D<sub>2</sub> and consists of a series of litho-tectonic units of variable origin and age (Armstrong et al., 1990; Kröner et al., 1996), some of which can conceivably be as young as the Fig Tree Group.



## 10.2 Implications for Archaean crustal evolution

This study, in conjunction with the work of Dziggel et al. (2002) and Kisters et al. (2003) indicates that many of the processes of Archaean crustal evolution as exhibited in the Theespruit Formation of the Barberton Greenstone Belt can be explained within a slightly modified plate tectonic framework. Peak metamorphic pressure-temperature estimates from the Theespruit Formation indicate that these lithologies were buried to depths of 25 – 30 km and experienced extremely low apparent geothermal gradients of ca. 20 °C/km. The high-pressure low-temperature style of metamorphism is confirmed by the presence of kyanite in samples with appropriate bulk composition.

The low apparent geothermal gradients recorded during these studies are intermediate to the apparent geothermal gradients reported from modern continental orogenic environments (Barrovian metamorphism) and subduction zones (Sanbagawan metamorphism) (e.g. Spear, 1993) and have never before been documented from a Mid-Archaean metamorphic terrain. The preservation of such low apparent geothermal gradients are at odds with the widely established models of elevated heat production, heat flow and a generally hotter and weaker crustal environment in the Archaean (e.g. Marshak, 1999; Chardon et al., 2002; Sandiford and McLaren, 2002) and suggests that these rocks were exhumed rapidly and did not reach thermal equilibrium. It has recently been recognized that the D<sub>2</sub> collisional event was extremely short-lived and could have spanned as little as ca. 3 Ma (De Ronde and Kamo, 2000), while the post-tectonic Dalmejn Pluton constrains the exhumation of the high-grade rocks to have occurred within ca. 15 Ma. Considering the depths of burial, these time constraints suggest a minimum average exhumation rate of ca. 2 mm/year for the rocks of the high-grade terrain and a maximum rate that could be as high as ca. 10 mm/year. The depths of burial of this terrain can only be achieved in cold and rigid crustal environments which, along with the rapid rates of burial and exhumation, strongly suggest that tectono-metamorphism occurred in response to a lateral plate tectonic process.



Diamonds with crystallization ages of 3.2 to 3.3 Ga (Richardson et al., 1984; Shirey et al., 2003) are cited as evidence for the formation and presence of a lithospheric mantle keel below the Kaapvaal Craton as early as the Mid-Archaean. The presence of a stable, depleted lithospheric mantle provides the high-pressure low-temperature conditions required for diamond stability and growth. The style of metamorphism exhibited in the southern Barberton terrain provides tectonic evidence that further supports the presence of a lithospheric mantle by 3.23 Ga, as the high-pressure low-temperature metamorphic conditions documented in these rocks are unlikely to have been achieved or preserved without the presence of an insulating lithospheric mantle.

In conclusion, the results of this study suggest that the ca. 3.23 Ga amalgamation of the Barberton granitoid-greenstone terrain occurred by rapid, lateral plate-tectonic processes



that involved crustal blocks with a thermal structure and rheology similar to the present day. This study also provides tectonic evidence that the first episode of cratonization and the establishment of an insulating lithospheric mantle below the Kaapvaal Craton had already occurred by ca. 3.23 Ga.



## **REFERENCES**

Andersen, T.B. and Osmundsen, P.T. (1994) Deep crustal fabrics and a model for the extensional collapse of the southwest Norwegian Caledonides, *Journal of Structural Geology*, 16, 1191 - 1203

Anhaeusser, C.R. (1973) The evolution of the Precambrian crust of southern Africa, *Philosophical Transactions, Royal Society, London, A 2731*, 359 – 388

Anhaeusser, C.R. (1984) Structural elements of Archaean granite-greenstone terranes as exemplified by the Barberton Mountain Land, southern Africa. In: *Precambrian Tectonics Illustrated* (edited by Kröner, A. and Greiling, R.), Stuttgart, 418pp

Anhaeusser, C.R. (2001) The anatomy of an extrusive-intrusive Archaean mafic-ultramafic sequence: the Nelshoogte Schist Belt and Stolzburg Layered Ultramafic Complex, Barberton Greenstone Belt, South Africa, *South African Journal of Geology*, 104, 167 – 204

Anhaeusser, C.R. and Robb, L.J. (1983a) Geological and geochemical characteristics of the Heerenveen and Mpuluzi Batholiths south of the Barberton Greenstone Belt and preliminary thoughts on their petrogenesis, *Special Publication, Geological Society of South Africa*, 9, 131 – 152

Anhaeusser, C.R. and Robb, L.J. (1983b) Chemical analyses of granitoid rocks from the Barberton Mountain Land, *Special Publication, Geological Society of South Africa*, 9, 189 – 219

Anhaeusser, C.R., Robb, L.J. and Viljoen, M.J. (1981) Provisional geological map of the Barberton Greenstone Belt and surrounding granitic terrane, Eastern Transvaal and Swaziland, *Geological Society of South Africa*, scale 1:250 000

Apted, M.J. and Liou, J.G. (1983) Phase relations among greenschist, epidote-amphibolite and amphibolite in a basaltic system, *American Journal of Science*, 283-A, 328 - 354

Armstrong, R.A., Compston, W., De Wit, M.J. and Williams, I.S. (1990) The stratigraphy of the Barberton Greenstone Belt revisited: a single zircon ion microprobe study, *Earth and Planetary Science Letters*, 101, 90 - 106

Belcher, R.W. and Kisters, A.F.M. (in review) Syntectonic emplacement and deformation of the Heerenveen batholith: Conjectures on the structural setting of the 3.1 Ga granite magmatism in the Barberton granite-greenstone terrain, South Africa, submitted to the *Geological Society of America Special Publication*

Berthé, D., Choukroune, P. and Jegouza, P. (1979) Orthogneiss, mylonite and noncoaxial deformation of granites: the example of the South American shear zone, *Journal of Structural Geology*, 1, 31 – 42

Brooks, C. and Hart, S.R. (1974) On the significance of komatiite, *Geology*, 2, 107 - 110

Byerly, G.R., Kröner, A., Lowe, D.R., Todt, W. and Walsh, M.M. (1996) Prolonged magmatism and time constraints for sediment deposition in the early Archaean Barberton greenstone belt: evidence from the Upper Onverwacht and Fig Tree Groups, *Precambrian Research*, 78, 125 - 138

Carson, C.J., Ague, J.J. and Coath, C.D. (2002) U-Pb geochronology from Tonagh Island, East Antarctica: implications for the timing of ultra-high temperature metamorphism of the Napier Complex, *Precambrian Research*, 116, 237 - 263

Chardon, D., Peucat, J.J., Jayananda, M., Choukroune, P., Fanning, C.M., (2002) Archaean granite-greenstone tectonics at Kolar, (South India): Interplay of diapirism and bulk inhomogeneous contraction during juvenile magmatic accretion. *Tectonics*, 21, 700-717.

Chaussidon, M. and Appel, P.W.U. (1997) Boron isotopic composition of tourmalines from the 3.8-Ga-old Isua supracrustals, West Greenland: implications on the  $\delta^{11}\text{B}$  value of early Archaean seawater, *Chemical Geology*, 136, 171 - 180

Cherniak, D.J. (1993) Lead diffusion in titanite and preliminary results on the effects of radiation damage on Pb transport, *Chemical Geology*, 110, 177 - 194

Chopin, C. (1984) Coesite and pure pyrope in high-grade blueschists of the western Alps: a first record and some consequences, *Contributions to Mineralogy and Petrology*, 86, 107 - 118

Cloete, M. (1991) An overview of the metamorphism in the Barberton Greenstone Belt. In: Two cratons and an orogen (edited by Ashwal, L.D.) Excursion guidebook and review articles for a field workshop through selected Archaean terranes of Swaziland, South Africa and Zimbabwe, IGCP Project 280, Department of Geology, University of the Witwatersrand, Johannesburg, 84 - 98

Cloete, M. (1999) Aspects of volcanism and metamorphism of the Onverwacht Group lavas in the southwestern portion of the Barberton Greenstone Belt, *Memoirs of the Geological Survey of South Africa*, 84, 232pp

Condie, K.C. (1994) Greenstones through time. In: *Archaean Crustal Evolution* (edited by Condie, K.C.), Elsevier, Amsterdam, 85 - 120

Connolly, J.A.D. (1990) Multivariable phase diagrams: an algorithm based on generalized thermodynamics, *American Journal of Science*, 290, 666 – 718

Connolly, J.A.D. and Petrini, K. (2002) An automated strategy for calculation of phase diagram sections and retrieval of rock properties as a function of physical conditions, *Journal of Metamorphic Geology*, 20, 697 - 708

Dahl, P.S. (1996) The effects of composition on retentivity of argon and oxygen in hornblende and related amphiboles: A field-tested empirical model, *Geochimica et Cosmochimica Acta*, 60, 3687 - 3700

Dann, J.C. (2000) The 3.5 Ga Komati Formation, Barberton Greenstone Belt, South Africa: part I: new maps and magmatic architecture, *South African Journal of Geology*, 103, 47 – 68

Davies, G.F. (1992) On the emergence of plate tectonics, *Geology*, 20, 963 – 966

Davies, G.F. (1995) Punctuated evolution of the earth, *Earth and Planetary Science Letters*, 136, 363 – 379

Davis, G.A. (1980) Structural characteristics of metamorphic core complexes, southern Arizona, *Geological Society of America Memoir*, 153, 35 - 77

Davis, G.A. and Lister, G.S. (1988) Detachment faulting in continental extension: perspectives from the southwestern US Cordillera, *Geological Society of America Special Paper*, 218, 133 - 159

Davis, G.H. (1987) A shear-zone model for the structural evolution of metamorphic core complexes in southeastern Arizona. In: *Continental Extensional Tectonics* (edited by Coward, M.P., Dewey, J.F. and Hancock, P.L.), *Geological Society of London Special Publication*, 28, 247 - 266

De Ronde, C.E.J. and De Wit, M.J. (1994) The tectonic history of the Barberton greenstone belt, South Africa: 490 million years of Archaean crustal evolution, *Tectonics*, 13, 983 – 1005

De Ronde, C.E.J. and Kamo, S.L. (2000) An Archaean arc-arc collisional event: a short-lived (ca 3 Myr) episode, Weltevreden area, Barberton Greenstone Belt, South Africa, *Journal of African Earth Sciences*, 30, 219 - 248

De Ronde, C.E.J., Kamo, S.L., Davis, D.W., De Wit, M.J. and Spooner, E.T.C. (1991) Field, geochemical and U-Pb isotopic constraints from hypabyssal felsic intrusions within the Barberton Greenstone Belt, South Africa: Implications for tectonics and the timing of gold mineralization, *Precambrian Research*, 49, 261 – 280

Dewey, J.F. (1988) Extensional collapse of orogens, *Tectonics*, 7, 1123 - 1139

De Wit, M.J. (1982) Gliding and overthrust nappe tectonics in the Barberton greenstone belt, *Journal of Structural Geology*, 4, 117 – 136

De Wit, M.J. (1998) On Archaean granites, greenstones, cratons and tectonics: does the evidence demand a verdict?, *Precambrian Research*, 91, 181 - 226

De Wit, M.J., Fripp, R.E.P. and Stanistreet, I.G. (1983) Tectonic and stratigraphic implications of new field observations along the southern part of the Barberton greenstone belt, *Special Publication, Geological Society of South Africa*, 9, 21 – 29

De Wit, M.J., Armstrong, R.A., Hart, R.J. and Wilson, A.H. (1987) Felsic igneous rocks within the 3.3 to 3.5 Ga Barberton greenstone belt: high-level equivalents of the surrounding tonalite trondhjemite terrain, emplaced during thrusting, *Tectonics*, 6, 529 – 549



De Wit, M.J., Roering, C., Hart, R.J., Armstrong, R.A., De Ronde, C.E.J., Green, R.W.E., Tredoux, M., Peberdy, E. and Hart, R.A. (1992) Formation of an Archaean continent, *Nature*, 357, 553 - 562

Droop, G.T.R. (1987) A general equation for estimating  $\text{Fe}^{3+}$  concentrations in ferromagnesian silicates and oxides from microprobe analysis, using stoichiometric data, *Mineralogical Magazine*, 51, 431 - 435

Dziggel, A., Stevens, G., Poujol, M., Anhaeusser, C.R. and Armstrong, R.A. (2002) Metamorphism of the granite-greenstone terrane south of the Barberton greenstone belt, South Africa: an insight into the tectono-thermal evolution of the 'lower' portions of the Onverwacht Group, *Precambrian Research*, 114, 221 – 247

Ernst, W.G. (1973) Blueschist metamorphism and P-T regimes in active subduction zones, *Tectonophysics*, 17, 255 - 272

Ernst, W.G. (1975) Systematics of large-scale tectonics and age progressions in Alpine and circum-Pacific blueschist belts, *Tectonophysics*, 26, 229 – 246

Ernst, W.G. (1988) Tectonic history of subduction zones inferred from retrograde blueschist P-T paths, *Geology*, 16, 1081 - 1084

Feng, R., Machado, N. and Ludden, J. (1993) Lead geochronology of zircon by laser probe-inductively coupled plasma mass spectrometry (LP-ICPMS), *Geochimica et Cosmochimica Acta*, 57, 3479 - 3786

Ferry, J.M. (1984) A biotite isograd in south-central Maine, USA: mineral reactions, fluid transfer and heat transfer, *Journal of Petrology*, 25, 871 - 893

Flinn, D. (1962) On folding during three-dimensional progressive deformation, *Geological Society of London Quarterly Journal*, 118, 385 - 433

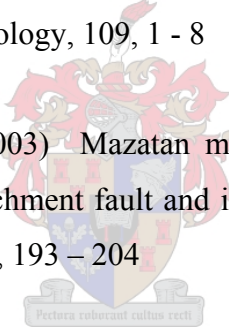
Fonneland, H.C., Trond, L., Martinsen, O.J., Pedersen, R.B. and Košler, J. (2004) Detrital zircon ages: a key to understanding the deposition of deep marine sandstones in the Norwegian Sea, *Sedimentary Geology*, 164, 147 - 159

Fripp R.E.P., Van Nierop, D.A., Callow, M.J., Lilly, P.A. and Du Plessis, L.U. (1980) Deformation in part of the Archaean Kaapvaal craton, South Africa, *Precambrian Research*, 13, 241 - 251

Frost, B.R., Chamberlain, K.R. and Schumacher, J.C. (2000) Sphene (titanite): phase relations and role as a geochronometer, *Chemical Geology*, 172, 131 - 148

Fryer, B.J., Jackson, S.E. and Longerich, H.P. (1993) The application of laser ablation microprobe - inductively coupled plasma - mass spectrometry (LAM-ICP-MS) to in situ U-Pb geochronology, *Chemical Geology*, 109, 1 - 8

Granillo R.V. and Calmus, T. (2003) Mazatan metamorphic core complex (Sonora, Mexico): structures along the detachment fault and its exhumation evolution, *Journal of South American Earth Sciences*, 16, 193 – 204



Hall, A.L. (1918) The geology of the Barberton gold mining district, *Memoir Geological Survey of South Africa*, 9, 347pp

Hamilton, W.B. (1998) Archaean magmatism and deformation were not products of plate tectonics, *Precambrian Research*, 91, 143 - 179

Harriss, R.C. (1969) Boron regulation in the oceans, *Nature*, 223, 290 - 291

Hart, R.J., Welke, H.J. and Nicolaysen, L.O. (1981) Geochronology of the deep profile through Archaean basement at Vredefort, with implications for early crustal evolution, *Journal of Geophysical Research*, 86, 10663 - 10680

Hart, R.J., Moser, D. and Andreoli, M.A.G. (1999) Archaean age for the granulite facies metamorphism near the centre of the Vredefort structure, South Africa, *Geology*, 27, 1091 - 1094

Heubeck, C. and Lowe D.R. (1994a) Depositional and tectonic setting of the Archaean Moodies Group, Barberton Greenstone Belt, South Africa, *Precambrian Research*, 68, 257 - 290

Heubeck, C. and Lowe, D.R. (1994b) Late syndepositional deformation and detachment tectonics in the Barberton Greenstone Belt, South Africa, *Tectonics*, 13, 1514 - 1536

Hirata, T. and Nesbitt, R.W. (1995) U-Pb isotope geochronology of zircon: evaluation of the laser probe-inductively coupled plasma mass spectrometry technique, *Geochimica et Cosmochimica Acta*, 59, 2491 - 2500

Hodych, J.P., Cox, R.A. and Košler, J. (2004) An equatorial Laurentia at 550 Ma confirmed by Grenvillian inherited zircons dated by LAM ICP-MS in the Skinner Cove volcanics of western Newfoundland: implications for inertial interchange true polar wander, *Precambrian Research*, 129, 93 – 113

Holdaway, M.J. (1971) Stability of andalusite and the aluminum phase diagram, *American Journal of Science*, 271, 97 - 131

Holland, T.J.B. and Powell, R. (1998) An internally consistent thermodynamic data set for phases of petrological interest, *Journal of Metamorphic Geology*, 16, 309 - 343

Horn, I., Hinton, R.W., Jackson, S.E. and Longerich, H.P. (1997) Ultra-trace element analysis of NIST SRM 616 using laser ablation microprobe – inductively coupled plasma – mass spectrometry (LAM-ICP-MS): a comparison with secondary ion mass spectrometry (SIMS), *Geostandards Newsletter*, 21, 191 - 203

Horn, I., Rudnick, R.L. and McDonough, W.F. (2000) Precise elemental and isotope ratio determination by simultaneous solution nebulization and laser ablation-ICP-MS: application to U-Pb geochronology, *Chemical Geology*, 164, 281 - 301

Hoschek, G. (2001) Thermobarometry of metasediments and metabasites from the eclogite zone of the Hohe Tauern, Eastern Alps, Austria, *Lithos*, 59, 127 - 150

Hubbard, M.S. (1989) Thermobarometric constraints on the thermal history of the Main Central Thrust Zone and Tibetan Slab, eastern Nepal Himalaya, *Journal of Metamorphic Geology*, 1, 19 - 30

Hunter, D.R., Barker, F. and Millard, H.T. (1984) Geochemical investigations of Archaean bimodal and Dwalile metamorphic suites, Ancient Gneiss Complex, Swaziland, *Precambrian Research*, 24, 131 - 155

Ishikawa, T. and Nakamura, E. (1993) Boron isotope systematics of marine sediments, *Earth and Planetary Science Letters*, 117, 567 - 580

Jackson, M.P.A. and Robertson, D.I. (1983) Regional implications of Early-Precambrian strains in the Onverwacht Group adjacent to the Lochiel Granite, north-west Swaziland, *Special Publication, Geological Society of South Africa*, 9, 45 – 62

Jackson, M.P.A., Eriksson, K.A. and Harris, C.W. (1987) Early Archaean foredeep sedimentation related to crustal shortening: a reinterpretation of the Barberton Sequence, southern Africa, *Tectonophysics*, 136, 197 - 221

Kamo, S.L. and Davis, D.W. (1994) Reassessment of of Archaean crustal development in the Barberton Mountain Land, South Africa, based on U-Pb dating, *Tectonics*, 13, 167 – 192

Kisters, A.F.M. and Anhaeusser, C.R. (1995a) The structural significance of the Steynsdorp pluton and anticline within the tectono-magmatic framework of the Barberton Mountain Land, South African Journal of Geology, 98, 43 - 51

Kisters, A.F.M. and Anhaeusser, C.R. (1995b) Emplacement features of Archaean TTG plutons along the southern margin of the Barberton Greenstone Belt, South Africa, Precambrian Research, 75, 1 – 15

Kisters, A.F.M., Stevens, G., Dziggel, A. and Armstrong, R.A. (2003) Extensional detachment faulting and core-complex formation in the southern Barberton granite-greenstone terrain, South Africa: evidence for a 3.2 Ga orogenic collapse, Precambrian Research, 127, 355 - 378

Košler, J., Frönneland, H., Sylvester, P., Tubrett, M. and Pedersen, R-B. (2002) U-Pb dating of detrital zircons for sediment provenance studies – a comparison of laser ablation ICPMS and SIMS techniques, Chemical Geology, 182, 605 - 618

Krabbendam, M. and Dewey, J.F. (1998) Exhumation of UHP rocks by transtension in the Western Gneiss Region, Scandinavian Caledonides. In: Continental Transpressional and Transtensional Tectonics (edited by Holdsworth, R.E., Strachan, R.A. and Dewey, J.F.), Geological Society, London, Special Publications, 135, 159 - 181

Kretz, R. (1983) Symbols for rock-forming minerals, American Mineralogist, 68, 277 - 279

Kröner, A., Byerly, G.R. and Lowe, D.R. (1991) Chronology of early Archaean granite-greenstone evolution in the Barberton Mountain land, South Africa, based on precise dating by single zircon evaporation, Earth and Planetary Science Letters, 103, 41 -54

Kröner, A., Hegner, E., Byerly, G.R. and Lowe, D.R. (1992) Possible terrane identification in the early Archaean Barberton Greenstone Belt, South Africa, using single zircon geochronology, *Eos (Transactions, American Geophysical Union)*, 73, 6 - 16

Kröner, A. and Tegtmeier, A.R. (1994) Gneiss-greenstone relationships in the Ancient Gneiss Complex of southwestern Swaziland, southern Africa, and implications for early crustal evolution, *Precambrian Research*, 67, 109 - 139

Kröner, A., Hegner, E., Wendt, J.I. and Byerly, G.R. (1996) The oldest part of the Barberton granitoid-greenstone terrain, South Africa, evidence for crust formation between 3.5 and 3.7 Ga, *Precambrian Research*, 78, 105 - 124

Kusky, T.M. and Polat, A. (1999) Growth of granite-greenstone terranes at convergent margins, and stabilization of Archaean cratons, *Tectonophysics*, 305, 43 – 73

Lister, G.S. and Davis, G.A. (1989) The origin of metamorphic core complexes and detachment faults formed during Tertiary continental extension in the northern Colorado River region, U.S.A., *Journal of Structural Geology*, 11, 65 – 94

Lopez-Martinez, M., York, D. and Hanes, J.A. (1992) A  $^{40}\text{Ar}/^{39}\text{Ar}$  geochronological study of komatiites and komatiitic basalts from the lower Onverwacht volcanics: Barberton Mountain Land, South Africa, *Precambrian Research*, 57, 91 - 119

Lowe, D.R. (1994) Accretionary history of the Archaean Barberton Greenstone Belt (3.55 – 3.22 Ga), southern Africa, *Geology*, 22, 1099 - 1102

Lowe, D.R. (1999) Geologic evolution of the Barberton Greenstone Belt and vicinity. In: *Geologic Evolution of the Barberton Greenstone Belt, South Africa* (edited by Lowe, D.R. and Byerly, G.R.), Special Paper of the Geological Society of America, 329, 287 - 312



Lowe, D.R. and Byerly, G.R. (1999) Stratigraphy of the west-central part of the Barberton Greenstone Belt, South Africa. In: Geologic Evolution of the Barberton Greenstone Belt, South Africa (edited by Lowe, D.R. and Byerly, G.R.), Special Paper of the Geological Society of America, 329, 1 - 36

Lowe, D.R., Byerly, G.R., Ransom, B.L. and Nocita, B.R. (1985) Stratigraphic and sedimentological evidence bearing on structural repetition in Early Archaean rocks of the Barberton Greenstone Belt, South Africa, *Precambrian Research*, 27, 165 - 186

Lowe, D.R., Byerly, G.R. and Heubeck, C. (1999) Structural divisions and development of the west-central part of the Barberton Greenstone Belt. In: Geologic Evolution of the Barberton Greenstone Belt, South Africa (edited by Lowe, D.R. and Byerly, G.R.), Special Paper of the Geological Society of America, 329, 37 - 82

Ludwig, K.R. (1999) Isoplot/Ex v. 2.6. Berkeley Geochronological Center Special Publication no. 1a

Machado, N. and Gauthier, G. (1996) Determination of  $^{207}\text{Pb}/^{206}\text{Pb}$  ages on zircon and monazite by laser-ablation ICPMS and application to a study of sedimentary provenance and metamorphism in southeastern Brazil, *Geochimica et Cosmochimica Acta*, 60, 5063 - 5073

Marshak, S. (1999) Deformation style way back when: thoughts on the contrasts between Archaean/Paleoproterozoic and contemporary orogens, *Journal of Structural Geology*, 21, 1175 - 1182

Marshak, S., Alkmin, F.F and Jordt-Evangelista, H. (1992) Proterozoic crustal extension and the generation of dome-and-keel structure in an Archaean granite-greenstone terrane, *Nature*, 357, 491 - 493

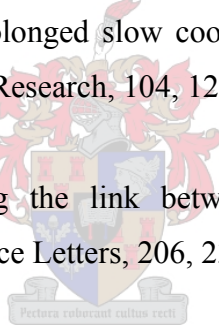
Marshak, S., Tinkham, D., Alkmin, F.F., Brueckner, H. and Bornhorst, T. (1997) Dome-and-keel provinces formed during Paleoproterozoic orogenic collapse – core complexes, diapirs, or neither? Examples from the Quadrilatero Ferrifero and the Penokean orogen, *Geology*, 25, 415 - 418

McLennan, S.M. and Taylor, S.R. (1984) Archaean sedimentary rocks and their relation to the composition of the Archaean continental crust. In: *Archaean Geochemistry – The origin and evolution of the Archaean continental crust* (edited by Kröner, A., Hanson, G.N. and Goodwin, A.M.). Springer, 286pp

Miyashiro, A. (1961) Evolution of metamorphic belts, *Journal of Petrology*, 2, 277 - 311

Möller, A., Mezger, K., and Schenk, V. (2000) U-Pb dating of metamorphic minerals: Pan-African metamorphism and prolonged slow cooling of high pressure granulites in Tanzania, East Africa, *Precambrian Research*, 104, 123 - 146

Müller, W. (2003) Strengthening the link between geochronology, textures and petrology, *Earth and Planetary Science Letters*, 206, 237 - 251



Parrish, R.R. (1990) U-Pb dating of monazite and its application to geological problems, *Canadian Journal of Earth Sciences*, 27, 1431 - 1450

Passchier, C.W. and Trouw, R.A.J. (1996) *Microtectonics*, Springer-Verlag, Berlin.

Pearce, N.J.G., Perkins, W.T., Westgate, J.A., Gorton, M.P., Jackson, S.E., Neal, C.R., and Cherney, S.P. (1996) A compilation of new and published major and trace element data for NIST SRM 610 and NIST SRM 612 glass reference material, *Geostandards Newsletter*, 21, 115 - 144

Pedersen, R-B., Dunning, G and Robins, B. (1988) U-Pb ages of nepheline syenite pegmatites from the Seiland Province, N. Norway, p 3 – 8. In: The Caledonide Geology of Scandinavia (edited by Gayer, R.A.), Graham and Trotman, 381pp

Platt, J.P. and Vissers, R.L.M. (1980) Extensional structures in anisotropic rocks, *Journal of Structural Geology*, 2, 397 - 410

Platt, J.P. and Vissers, R.L.M. (1989) Extensional collapse of thickened lithosphere: a working hypothesis for the Alboran Sea and Gibraltar Arc, *Geology*, 17, 540 - 543

Poli, S. (1993) The amphibolite-eclogite transformation: an experimental study on basalt, *American Journal of Science*, 293, 1061 - 1107

Poujol, M., Robb, L.J., Anhaeusser, C.R. and Gericke, B. (2003) A review of the geochronological constraints on the evolution of the Kaapvaal Craton, South Africa, *Precambrian Research*, 127, 181 - 213

Powell, R. and Holland, T.J.B. (1988) An internally consistent dataset with uncertainties and correlations; 3, Applications to geobarometry, worked examples and a computer program, *Journal of Metamorphic Geology*, 6, 173 - 204

Ramsay, J.G. (1963) Structural investigations in the Barberton Mountain Land, eastern Transvaal, *Transactions of the Geological Society of South Africa*, 66, 353 - 398

Rawlings-Hinchey, A.M., Sylvester, P.J., Myers, J.S., Dunning, G.R. and Košler, J. (2003) Paleoproterozoic crustal genesis: calc-alkaline magmatism of the Torngat Orogen, Voisey's Bay area, Labrador, *Precambrian Research*, 125, 55 - 85

Richardson, S.H., Gurney, J.J., Erlank, A.J. and Harris, J.W. (1984) Origin of diamonds in old enriched mantle, *Nature*, 310, 198 - 202

Ridley, J.R., Vearncombe, J.R. and Jelsma, H.A. (1997) Relations between greenstone belts and associated granitoids. In: Greenstone Belts (edited by De Wit, M.J. and Ashwal, L.D.), Oxford University Press, 376 - 397

Robb, L.J. (1983) Geological and geochemical characteristics of late granite plutons in the Barberton region and Swaziland with an emphasis on the Dalmein Pluton – a review, Special Publication, Geological Society of South Africa, 9, 117 - 130

Robb, L.J. and Anhaeusser, C.R. (1983) Chemical and petrogenetic characteristics of Archaean tonalite-trondhjemite gneiss plutons in the Barberton Mountain Land, Special Publication, Geological Society of South Africa, 9, 103 – 116

Robb, L.J., Anhaeusser, C.R. and Van Nierop, D.A. (1983) The recognition of the Nelspruit Batholith north of the Barberton Greenstone Belt and its significance in terms of Archaean crustal evolution, Special Publication, Geological Society of South Africa, 9, 117 – 130

SACS (South African Committee for Stratigraphy) (1980) Stratigraphy of South Africa, Part 1 (Compiled by Kent, L.E.) Lithostratigraphy of the Republic of South Africa, South West Africa/Namibia and the Republics of Bophutatswana, Transkei and Venda: Handbook of the Geological Survey of South Africa, 8, 690pp

Sandiford, M. and McLaren, S., (2002) Tectonic feedback and the ordering of heat producing elements within the continental lithosphere, Earth and Planetary Science Letters, 204, 133-150.

Sano, Y., Oyama, T., Terada, K. and Hidaka, H. (1999) Ion microprobe U-Pb dating of apatite, Chemical Geology, 153, 249 - 258

Schwandt, C.S., Papike, J.J. and Shearer, C.K. (1996) Trace element zoning in pelitic garnet of the Black Hills, South Dakota, American Mineralogist, 81, 1195 - 1207

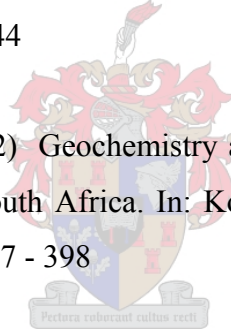
Scott, D.J. and St. Onge, M.R. (1995) Constraints on Pb closure temperature in titanite based on rocks from the Ungava Orogen, Canada: implications for U-Pb geochronology and P-T-t path determinations, *Geology*, 23, 1123 - 1126

Shirey, S.B., Harris, J.W., Richardson, S.H., Fouch, M., James, D.E., Cartigny, P., Deines, P., and Viljoen, F. (2003) Regional patterns in the paragenesis and age of inclusions in diamond, diamond composition, and the lithospheric seismic structure of Southern Africa, *Lithos*, 71, 243 - 258

Simpson, C. and Schmid, S.M. (1983) An evaluation of criteria to deduce the sense of movement in sheared rocks, *Geological Society of America Bulletin*, 94, 1281 - 1288

Smith, D.C. (1984) Coesite in clinopyroxene in the Caledonides and its implication for geodynamics, *Nature*, 310, 641 - 644

Smith, H.S. and Erlank, A.J. (1982) Geochemistry and petrogenesis of komatiites from the Barberton Greenstone Belt, South Africa. In: *Komatiite* (edited by Arndt, N.T. and Nisbet, E.G.), Allen and Unwin, 347 - 398



Spear, F.S. (1993) Metamorphic phase equilibria and pressure-temperature-time paths, *Mineralogical Society of America Monograph*, Washington D.C, 799pp

Spear, F.S. and Cheney, J.T. (1989) A petrogenetic grid for pelite schists in the system  $\text{SiO}_2 - \text{Al}_2\text{O}_3 - \text{FeO} - \text{MgO} - \text{K}_2\text{O} - \text{H}_2\text{O}$ , *Contributions to Mineralogy and Petrology*, 101, 149 - 164

Stacey, J.S. and Kramers, J.D. (1975) Approximation of terrestrial lead isotope evolution by a two stage model, *Earth and Planetary Science Letters*, 26, 207 - 221

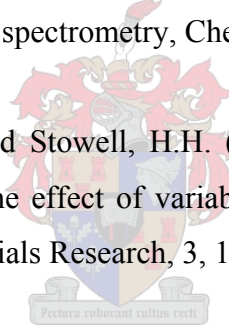
Stevens, G., Droop, G.T.R., Armstrong, R.A. and Anhaeusser, C.R. (2002) Amphibolite facies metamorphism in the Schapenburg schist belt: A record of the mid-crustal response to ~ 3.23 Ga terrane accretion in the Barberton greenstone belt, South African Journal of Geology, 105, 271 - 284

Taylor, S.R. and McLennan, S.M. (1985) The continental crust: its composition and evolution, Blackwell, 312pp

Tegtmeyer A.R. and Kröner A. (1987) U-Pb zircon ages bearing on the nature of early Archaean greenstone belt evolution, Barberton Mountain Land, Southern Africa, Precambrian Research, 36, 1 - 20

Tiepolo, M. (2003) In situ Pb geochronology of zircon with laser ablation – inductively coupled plasma – sector field mass spectrometry, Chemical Geology, 199, 159 - 177

Tinkham, D.K., Zuluaga, C.A. and Stowell, H.H. (2001) Metapelite phase equilibria modelling in MnNCKFMASH: The effect of variable Al<sub>2</sub>O<sub>3</sub> and MgO/(MgO+FeO) on mineral stability, Geological Materials Research, 3, 1 - 42



Toulkeridis, T., Clauer, N., Kröner, A., Reimer, T.O. and Todt, W. (1999) Characterization, provenance and tectonic setting of Fig Tree greywackes from the Archaean Barberton Greenstone Belt, South Africa, Sedimentary Geology, 124, 113 - 129

Viljoen, M.J. and Viljoen, R.P. (1969a) An introduction to the geology of the Barberton granite-greenstone terrain, Special Publication, Geological Society of South Africa, 2, 9 - 28

Viljoen, M.J. and Viljoen, R.P. (1969b) The geology and geochemistry of the lower ultramafic unit of the Onverwacht Group and a proposed new class of igneous rocks, Special Publication, Geological Society of South Africa, 2, 55 - 86



Viljoen, R.P. and Viljoen, M.J. (1969c) The geological and geochemical significance of the upper formations of the Onverwacht Group, Special Publication, Geological Society of South Africa, 2, 113 - 152

Viljoen, M.J., Viljoen, R.P. and Pearton, T.N. (1982) The nature and distribution of Archaean komatiite volcanics in South Africa. In: Komatiite (edited by Arndt, N.T. and Nisbet, E.G.), Allen and Unwin, 53 - 79

Villaseca, C., Martin Romera, C., De La Rosa, J. and Barbero, L. (2003) Residence and redistribution of REE, Y, Zr, Th and U during granulite-facies metamorphism: behaviour of accessory and major phases in peraluminous granulites of central Spain, *Chemical Geology*, 200, 293 - 323

Visser, D.J.L. (1956) The geology of the Barberton area, Geological Survey of South Africa Special Publication, 15, 253pp

Von Blanckenburg, F., Villa, I.M., Baur, H., Morteani, G. and Steiger, R.H. (1989) Time calibration of a PT path from the Western Tauern Window, Eastern Alps: the problem of closure temperatures, *Contributions to Mineralogy and Petrology*, 101, 1 - 11

Westraat, J.D., Kisters, A.F.M., Poujol, M. and Stevens, G. (2005) Transcurrent shearing, granite sheeting and the incremental construction of the tabular 3.1 Ga Mpuluzi Batholith, Barberton granite-greenstone terrain, South Africa, *Journal of the Geological Society: London* (in press)

Wilkins, C. (1997) Regional and contact metamorphism. In: *Greenstone Belts* (edited by De Wit, M.J. and Ashwal, L.D.), Oxford University Press, 126 - 163

Will, T.M., Powell, R. and Holland, T.J.B. (1990) A calculated petrogenetic grid for ultramafic rocks at low pressures in the system CaO-FeO-MgO-Al<sub>2</sub>O<sub>3</sub>-SiO<sub>2</sub>-CO<sub>2</sub>-H<sub>2</sub>O, *Contributions to Mineralogy and Petrology*, 105, 347 - 358

Will, T., Okrusch, M., Schmädicke, E. and Chen, G. (1998) Phase relations in the greenschist-blueschist-amphibolite-eclogite facies in the system Na<sub>2</sub>O-CaO-FeO-MgO-Al<sub>2</sub>O<sub>3</sub>-SiO<sub>2</sub>-H<sub>2</sub>O (NCFMASH), with application to metamorphic rocks from Samos, Greece, *Contributions to Mineralogy and Petrology*, 132, 85 - 102

Williams, D.A.C. and Furnell, R.G. (1979) Reassessment of part of the Barberton type area, South Africa, *Precambrian Research*, 9, 325 - 347

Xie, X., Byerly, G.R. and Ferrell, R.E. (1997) I1b trioctahedral chlorite from the Barberton Greenstone Belt: crystal structure and rock composition constraints with implications to geothermometry, *Contributions to Mineralogy and Petrology*, 126, 275 – 291

Yearron, L.M. (2003) Archaean granite petrogenesis and implications for the evolution of the Barberton Mountain Land, South Africa, Ph.D thesis, Kingston University, 315pp



## **APPENDICES**

### **Appendix 1**

Geological map of the Tjakastad Schist Belt and surrounding areas of the Barberton Greenstone Belt, South Africa

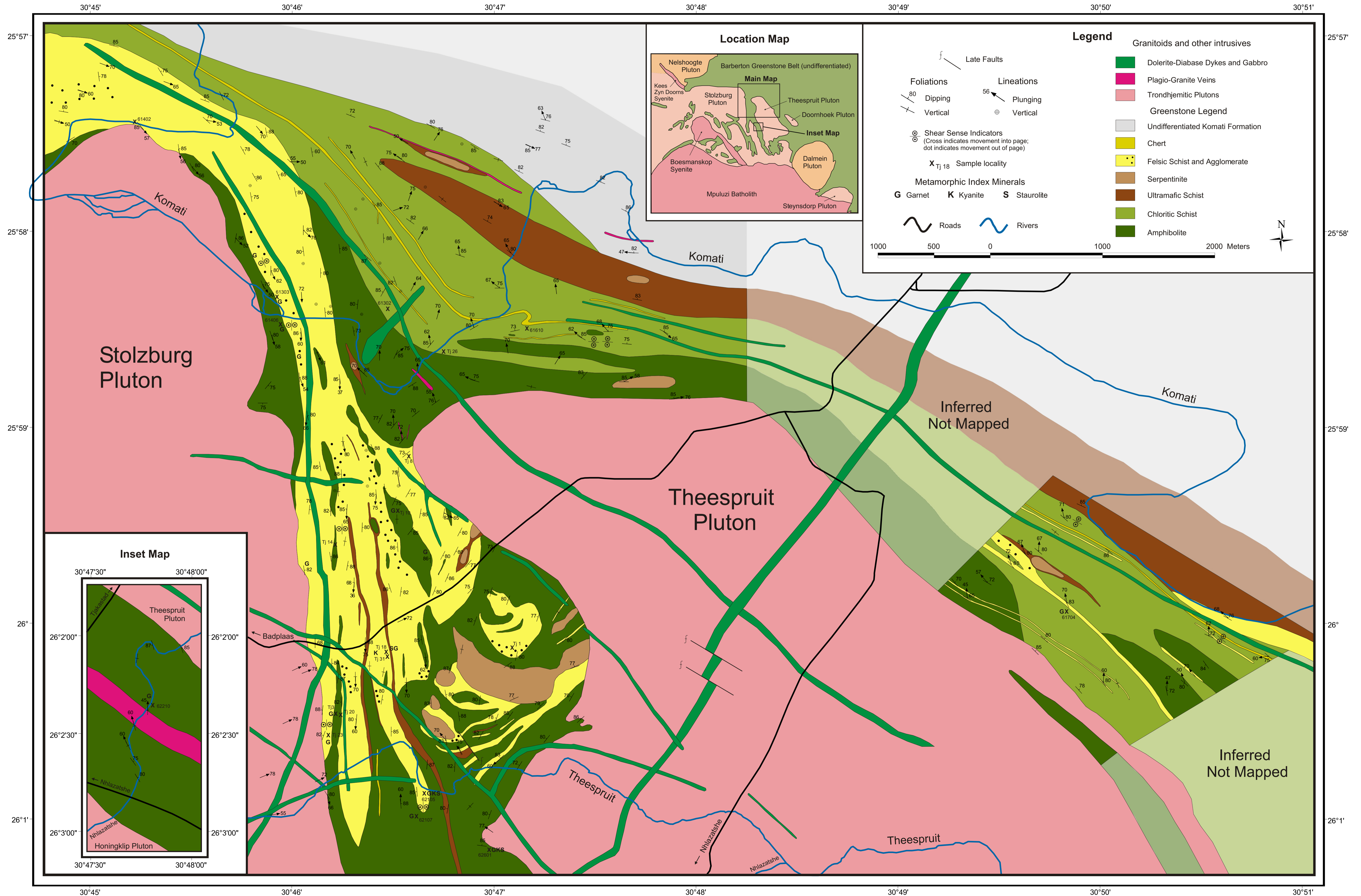




# Geological Map of the Tjakastad Schist Belt and Surrounding Areas of the Barberton Greenstone Belt, South Africa

By Johann F.A. Diener, Department of Geology, University of Stellenbosch

2001 - 2003



**Appendix 2.1a:** Comparison of actual published major element concentrations of geological standards and measured values as determined by XRF analysis  
All major element concentrations reported as wt % oxide.

Element	CSE <sup>a</sup>	K <sup>b</sup>	SiO <sub>2</sub>			JG-1			JB-1			BHVO-1			NIM-N		
			actual	measured	% Dev	actual	measured	% Dev	actual	measured	% Dev	actual	measured	% Dev	actual	measured	% Dev
SiO <sub>2</sub>	0.035	0.020	100.00	99.67	-0.33	72.30	72.77	0.65	52.17	52.35	0.34	49.94	49.69	-0.50	52.64	52.70	0.10
TiO <sub>2</sub>	0.006	0.093	0.00	0.00	-	0.26	0.24	-8.46	1.34	1.28	-4.55	2.71	2.73	0.55	0.20	0.18	-10.50
Al <sub>2</sub> O <sub>3</sub>	0.016	0.140	0.00	0.02	-	14.20	14.23	0.20	14.53	14.56	0.17	13.80	13.67	-0.96	16.50	16.59	0.52
Fe <sub>2</sub> O <sub>3</sub>	0.007	0.027	0.00	0.00	-	2.14	2.12	-0.84	8.97	8.94	-0.30	12.23	12.39	1.28	8.91	9.07	1.84
MnO	0.002	0.041	0.00	0.00	-	0.06	0.06	-6.35	0.16	0.16	-1.88	0.17	0.18	5.95	0.18	0.19	2.78
MgO	0.003	0.052	0.00	0.00	-	0.74	0.75	1.62	7.73	7.61	-1.50	7.23	7.04	-2.64	7.50	7.35	-1.95
CaO	0.020	0.101	0.00	0.00	-	2.18	0.56	-74.22	9.29	9.30	0.08	11.40	11.43	0.22	11.50	11.53	0.22
Na <sub>2</sub> O	0.007	0.165	0.00	0.00	-	3.39	3.35	-1.18	2.79	2.79	-0.14	2.26	2.16	-4.42	2.46	2.46	-0.16
K <sub>2</sub> O	0.014	0.086	0.00	0.00	-	3.97	3.94	-0.76	1.43	1.35	-5.80	0.52	0.48	-7.31	0.25	0.20	-19.20
P <sub>2</sub> O <sub>5</sub>	0.002	0.044	0.00	0.00	-	0.10	0.10	-2.06	0.26	0.26	-0.38	0.27	0.26	-4.03	0.03	0.00	-100.00
H <sub>2</sub> O- LOI			0.00	0.25	-	0.48	0.39	-19.17	1.02	0.93	-8.43	0.16	0.27	70.00	0.33	0.41	23.03
Total			100.00	100.10		99.82	99.00		99.69	100.50		100.69	99.90		100.50	100.60	

a: CSE = Counting Statistical Error

b: K = fit of regression line, must approach 0

**Appendix 2.1b:** Comparison of actual published trace element concentrations of geological standards and measured values as determined by XRF analysis  
All trace element concentrations reported as ppm.

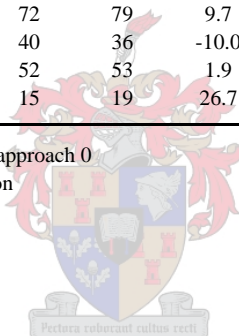
Element	K <sup>a</sup>	LLD <sup>b</sup> (ppm)	Nim-G			Agv-1		
			actual	measured	% Dev	actual	measured	% Dev
V	0.00263	8	2*	1*	-	121	112	-7.4
Cr	0.00131	8	12	9	-25.0	10	4	-60.0
Co	0.00011	1	n/d	n/d	-	n/d	n/d	-
Ni	0.00032	9	8*	1*	-	15	9	-40.0
Cu	0.05002	1	12	14	16.7	59	65	10.2
Zn	0.00182	8	50	49	-2.0	86	87	1.2
Ga	0.00079	3	27	30	11.1	21	21	0.0
Rb	0.00128	5	320	293	-8.4	67	62	-7.5
Sr	0.00179	4	10	9	-10.0	660	682	3.3
Y	0.00281	5	145	138	-4.8	19	23	21.1
Zr	0.00234	4	300	288	-4.0	230	242	5.2
Nb	0.00065	5	53	56	5.7	16	17	6.3
Ba	0.04647	20	120	108	-10.0	1226	1187	-3.2
La	0.00464	5	109	134	22.9	38	46	21.1
Ce	0.00951	5	195	222	13.8	67	62	-7.5
Nd	0.0023	5	72	79	9.7	33	30	-9.1
Pb	0.00185	7	40	36	-10.0	33	35	6.1
Th	0.0006	11	52	53	1.9	6*	7*	-
U	0.00093	6	15	19	26.7	2*	1*	-

a: K = fit of regression line, must approach 0

b: LLD = Lower Limit of Detection

n/d = not determined

\* = below detection limits





**Appendix 2.2:** Comparison of actual published major element concentrations of mineral standards and measured values as determined by electron microprobe EDS analysis

plagioclase				garnet				biotite				chlorite				hornblende			
	actual	measured	% Dev		actual	measured	% Dev		actual*	measured	% Dev		actual*	measured	% Dev		actual	measured	% Dev
SiO <sub>2</sub>	54.21	53.07	-2.1	SiO <sub>2</sub>	39.19	39.43	0.6	SiO <sub>2</sub>	40.38	40.80	1.0	SiO <sub>2</sub>	34.84	36.74	5.2	SiO <sub>2</sub>	40.37	42.21	4.4
TiO <sub>2</sub>	0.07	0.00	n/d	TiO <sub>2</sub>	0.00	0.00	n/d	TiO <sub>2</sub>	1.85	1.61	-14.6	TiO <sub>2</sub>	0.00	0.00	n/d	TiO <sub>2</sub>	4.72	4.99	5.4
Al <sub>2</sub> O <sub>3</sub>	28.53	29.93	4.7	Al <sub>2</sub> O <sub>3</sub>	22.05	22.15	0.5	Al <sub>2</sub> O <sub>3</sub>	15.78	15.42	-2.3	Al <sub>2</sub> O <sub>3</sub>	20.97	21.77	3.7	Al <sub>2</sub> O <sub>3</sub>	14.90	14.15	-5.3
Cr <sub>2</sub> O <sub>3</sub>	0.00	0.00	n/d	Cr <sub>2</sub> O <sub>3</sub>	0.00	0.00	n/d	Cr <sub>2</sub> O <sub>3</sub>	0.00	0.00	n/d	Cr <sub>2</sub> O <sub>3</sub>	1.14	1.25	9.1	Cr <sub>2</sub> O <sub>3</sub>	0.00	0.00	n/d
FeO	0.37	0.00	n/d	FeO	23.27	23.41	0.6	FeO	11.18	11.76	4.9	FeO	3.84	4.11	6.6	FeO	11.25	11.96	5.9
MnO	0.00	0.00	n/d	MnO	0.59	0.34	-73.5	MnO	0.04	0.21	80.1	MnO	0.00	0.00	n/d	MnO	0.09	0.00	-
MgO	0.13	0.00	n/d	MgO	10.70	10.74	0.4	MgO	20.36	20.07	-1.4	MgO	38.86	36.06	-7.8	MgO	12.80	12.16	-5.3
CaO	11.80	12.01	1.7	CaO	4.20	3.95	-6.3	CaO	0.10	0.00	n/d	CaO	0.03	0.00	-	CaO	10.30	10.22	-0.8
Na <sub>2</sub> O	4.35	4.53	4.0	Na <sub>2</sub> O	0.00	0.00	n/d	Na <sub>2</sub> O	0.00	0.00	n/d	Na <sub>2</sub> O	0.00	0.00	n/d	Na <sub>2</sub> O	2.60	1.86	-39.3
K <sub>2</sub> O	0.41	0.47	12.8	K <sub>2</sub> O	0.00	0.00	n/d	K <sub>2</sub> O	10.33	11.46	9.8	K <sub>2</sub> O	0.00	0.00	n/d	K <sub>2</sub> O	2.05	2.35	12.9
Total	99.87	100.01		Total	100.00	100.02		Total	100.02	101.33		Total	99.67	99.93		Total	99.08	99.90	
<b>Anions</b>	<b>8</b>	<b>8</b>		<b>Anions</b>	<b>12</b>	<b>12</b>		<b>Anions</b>	<b>11</b>	<b>11</b>		<b>Anions</b>	<b>14</b>	<b>14</b>		<b>Anions</b>	<b>23</b>	<b>23</b>	
Si	2.46	2.40		Si	2.98	2.99		Si IV	2.81	2.83		Si IV	2.88	3.01		Si	5.89	6.09	
Al	1.52	1.60						Al IV	1.19	1.17		Al IV	1.11	0.99		Ti	0.52	0.54	
Σ	3.98	4.00		Al	1.98	1.98		Σ IV	4.00	4.00		Σ IV	4.00	4.00		Al	2.56	2.41	
				Fe	1.48	1.49		Al VI	0.11	0.09		Al VI	0.93	1.12		Fe	1.37	1.44	
Ca	0.57	0.58		Mn	0.03	0.02		Ti	0.10	0.08		Cr	0.07	0.08		Mn	0.01	0.00	
Na	0.38	0.40		Mg	1.21	1.22		Fe	0.65	0.68		Fe	0.27	0.28		Mg	2.78	2.62	
K	0.02	0.03		Ca	0.34	0.32		Mn	0.00	0.01		Mg	4.79	4.41		Ca	1.61	1.58	
Σ	0.98	1.01		Σ cat	8.03	8.02		Mg	2.11	2.08		Σ	6.06	5.89		Na	0.74	0.52	
Σ cat	4.98	5.01						Σ	2.97	2.94						K	0.38	0.43	
XAn	0.60	0.59		XPy	0.40	0.40		K	0.92	1.01		Σ cat	10.06	9.89		Σ cat	15.87	15.64	
XAb	0.40	0.41		XAlm	0.48	0.49						Mg#	94.75	93.99		Mg#	66.97	64.44	
				XSpss	0.01	0.01		Σ cat	7.89	7.96									
				XGrss	0.11	0.11		Mg#	76.44	75.25									
				Fe/Fe+Mg	0.55	0.55													

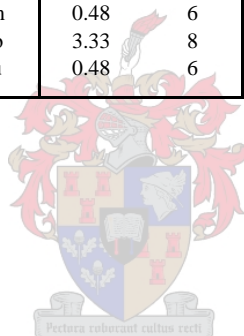
**Note:** XPy, XAlm, XSpss and XGrss as defined by Spear (1993). XAn = Ca/(Ca+Na), XAb = Na/(Ca+Na), Mg# = 100 x Mg/(Mg+Fe)

\* Recalculated as water-free equivalent

n/d = not determined

**Appendix 2.3:** Results of LA-ICP-MS analysis of reference material USGS BCR2-G obtained during this study compared to the long-term average of the instrument

	This study n = 15		Long-term average n = 231	
	ppm	% RSD	ppm	% RSD
Sc	33.49	4	34.75	12
V	417.11	2	400.08	8
Cr	16.19	21	16.90	20
Co	36.56	3	35.42	9
La	24.27	4	24.39	10
Ce	50.90	3	51.01	9
Pr	6.32	4	6.40	10
Nd	27.27	4	27.48	10
Sm	6.21	4	6.20	11
Eu	1.84	4	1.85	10
Gd	6.21	5	6.03	11
Tb	0.92	6	0.93	13
Dy	6.08	6	5.92	12
Ho	1.19	6	1.19	13
Er	3.27	3	3.30	13
Tm	0.48	6	0.48	14
Yb	3.33	8	3.23	13
Lu	0.48	6	0.48	14



**Appendix 3.1:** Major element content and structural formulae for garnet from felsic schist

Sample Analysis	62601C grt1	62601C grt2	62601C grt3	62601C grt7	62601C grt8	62601C grt9	62601C grt10	62601C grt11	62601C grt12	62601C grt14	62601C grt15	62601C grt16	62601C grt17	62601C grt18	62601C grt19	62601C grt20	62601C grt21	62601C grt22
SiO <sub>2</sub>	36.16	36.45	36.53	36.84	35.99	36.70	36.39	35.85	36.57	36.08	36.49	36.43	35.77	36.06	36.05	35.64	35.65	35.82
TiO <sub>2</sub>	0.91	0.49	0.47	0.00	0.71	0.29	0.41	1.74	0.10	1.52	0.31	0.60	2.30	1.77	1.89	2.93	2.03	2.47
Al <sub>2</sub> O <sub>3</sub>	20.22	20.09	20.20	20.43	20.29	20.48	20.55	19.97	20.19	20.05	20.40	20.43	19.98	19.61	19.89	19.69	19.94	19.91
FeO	31.34	32.06	31.48	32.47	32.27	32.66	32.79	32.00	32.65	31.99	32.24	31.73	31.84	31.87	31.64	31.16	31.77	31.37
MnO	5.87	5.56	5.52	4.89	4.90	4.96	4.94	5.07	4.92	4.84	4.65	5.01	5.06	5.41	5.13	5.06	5.07	5.06
MgO	1.94	1.79	1.90	2.46	2.27	2.49	2.56	2.44	2.42	2.35	2.49	2.53	1.99	1.86	2.31	2.47	2.53	2.30
CaO	3.55	3.56	3.89	3.26	3.57	2.43	2.35	2.93	3.15	3.17	3.41	3.27	3.07	3.42	3.09	3.04	3.02	3.07
Total	99.99	100.00	99.99	100.35	100.00	100.01	99.99	100.00	100.00	100.00	99.99	100.00	100.01	100.00	100.00	99.99	100.01	100.00
Si	2.96	2.99	2.99	3.00	2.95	2.99	2.97	2.93	2.99	2.95	2.98	2.97	2.93	2.96	2.95	2.91	2.92	2.92
Al	1.95	1.94	1.95	1.96	1.96	1.97	1.98	1.93	1.95	1.93	1.96	1.96	1.93	1.90	1.92	1.89	1.92	1.92
Ti	0.06	0.03	0.03	0.00	0.04	0.02	0.03	0.11	0.01	0.09	0.02	0.04	0.14	0.11	0.12	0.18	0.12	0.15
Fe <sup>2+</sup>	2.15	2.20	2.15	2.21	2.21	2.23	2.24	2.19	2.23	2.19	2.20	2.16	2.18	2.19	2.16	2.13	2.17	2.14
Mn	0.33	0.32	0.31	0.27	0.28	0.28	0.28	0.29	0.28	0.27	0.26	0.28	0.29	0.31	0.29	0.29	0.29	0.29
Mg	0.24	0.22	0.23	0.30	0.28	0.30	0.31	0.30	0.30	0.29	0.30	0.31	0.24	0.23	0.28	0.30	0.31	0.28
Ca	0.31	0.31	0.34	0.28	0.31	0.21	0.21	0.26	0.28	0.28	0.30	0.29	0.27	0.30	0.27	0.27	0.26	0.27
Σ cat	8.00	8.01	8.01	8.02	8.03	8.00	8.01	8.00	8.03	7.99	8.02	8.01	7.97	7.98	7.98	7.96	8.00	7.97
XPy	0.08	0.07	0.08	0.10	0.09	0.10	0.10	0.10	0.10	0.09	0.10	0.10	0.08	0.08	0.09	0.10	0.10	0.09
XAlm	0.71	0.72	0.71	0.72	0.72	0.74	0.74	0.72	0.72	0.72	0.72	0.71	0.73	0.72	0.72	0.71	0.72	0.72
XSpss	0.11	0.10	0.10	0.09	0.09	0.09	0.09	0.09	0.09	0.09	0.09	0.09	0.10	0.10	0.10	0.10	0.09	0.10
XGrss	0.10	0.10	0.11	0.09	0.10	0.07	0.07	0.08	0.09	0.09	0.10	0.09	0.09	0.10	0.09	0.09	0.09	0.09
Fe/Fe+Mg	0.90	0.91	0.90	0.88	0.89	0.88	0.88	0.88	0.88	0.88	0.88	0.88	0.90	0.91	0.88	0.88	0.88	0.88

**Note:** XPy, XAlm, XSpss and XGrss as defined by Spear (1993)

**Appendix 3.1:** Major element content and structural formulae for garnet from felsic schist

Sample Analysis	62601C grt23	62601C grt24	62601C grt25	62601C grt26	62601C grt27	62601C grt28	62601C grt29	62601C grt30	62601C grt31	62601C grt32	62601C grt33	62601C grt34	62601C grt35	62601C grt36	62601C grt38	62601C grt39	62601C grt40	62601C grt41
SiO <sub>2</sub>	36.33	35.91	31.96	36.52	36.42	36.20	36.39	36.55	36.12	36.93	36.56	36.59	36.48	36.76	38.34	36.05	34.26	35.69
TiO <sub>2</sub>	0.68	2.16	11.36	1.31	0.69	1.24	0.90	0.20	0.95	0.00	0.78	0.00	1.27	0.26	0.62	1.11	4.84	2.48
Al <sub>2</sub> O <sub>3</sub>	20.16	19.80	17.75	19.92	20.16	20.11	20.25	20.49	20.68	20.61	20.53	20.61	20.09	20.35	19.64	20.23	19.26	19.92
FeO	32.02	31.68	29.37	31.69	32.15	31.68	31.44	31.97	31.33	31.39	31.00	32.21	31.72	32.26	31.47	31.36	31.05	30.88
MnO	5.09	4.94	4.77	5.03	5.19	5.20	5.29	5.19	5.24	5.26	5.35	5.23	5.05	5.29	5.06	5.06	4.88	5.09
MgO	2.52	2.53	2.05	2.46	2.48	2.51	2.49	2.67	2.69	2.70	2.69	2.53	2.65	2.60	2.46	2.19	2.04	1.98
CaO	3.20	2.97	2.74	3.08	2.91	3.07	3.25	2.95	2.98	3.20	3.09	2.95	2.74	2.47	2.42	4.00	3.67	3.97
Total	100.00	99.99	100.00	100.01	100.00	100.01	100.01	100.02	99.99	100.09	100.00	100.12	100.00	99.99	100.01	100.00	100.00	100.01
Si	2.97	2.93	2.62	2.98	2.98	2.96	2.97	2.98	2.94	3.00	2.97	2.98	2.97	3.00	3.10	2.95	2.81	2.92
Al	1.94	1.91	1.72	1.91	1.94	1.94	1.95	1.97	1.99	1.97	1.97	1.98	1.93	1.96	1.87	1.95	1.86	1.92
Ti	0.04	0.13	0.70	0.08	0.04	0.08	0.06	0.01	0.06	0.00	0.05	0.00	0.08	0.02	0.04	0.07	0.30	0.15
Fe <sup>2+</sup>	2.19	2.16	2.02	2.16	2.20	2.16	2.15	2.18	2.14	2.13	2.11	2.20	2.16	2.20	2.13	2.14	2.13	2.11
Mn	0.29	0.28	0.27	0.28	0.29	0.29	0.30	0.29	0.30	0.30	0.30	0.29	0.28	0.30	0.28	0.29	0.28	0.29
Mg	0.31	0.31	0.25	0.30	0.30	0.31	0.30	0.32	0.33	0.33	0.33	0.31	0.32	0.32	0.30	0.27	0.25	0.24
Ca	0.28	0.26	0.24	0.27	0.25	0.27	0.28	0.26	0.26	0.28	0.27	0.26	0.24	0.22	0.21	0.35	0.32	0.35
Σ cat	8.02	7.98	7.82	7.98	8.01	8.00	8.00	8.02	8.01	8.01	7.99	8.02	7.99	8.01	7.93	8.01	7.96	7.97
XPy	0.10	0.10	0.09	0.10	0.10	0.10	0.10	0.11	0.11	0.11	0.11	0.10	0.11	0.10	0.10	0.09	0.08	0.08
XAlm	0.71	0.72	0.73	0.72	0.72	0.71	0.71	0.71	0.71	0.70	0.70	0.72	0.72	0.73	0.73	0.70	0.72	0.71
XSpss	0.09	0.09	0.10	0.09	0.10	0.10	0.10	0.10	0.10	0.10	0.10	0.10	0.09	0.10	0.10	0.09	0.09	0.10
XGrss	0.09	0.09	0.09	0.09	0.08	0.09	0.09	0.08	0.09	0.09	0.09	0.08	0.08	0.07	0.07	0.11	0.11	0.12
Fe/Fe+Mg	0.88	0.88	0.89	0.88	0.88	0.88	0.88	0.87	0.87	0.87	0.87	0.88	0.87	0.87	0.88	0.89	0.90	0.90

**Note:** XPy, XAlm, XSpss and XGrss as defined by Spear (1993)

**Appendix 3.1:** Major element content and structural formulae for garnet from felsic schist

Sample Analysis	62601C grt42	62601C grt43	62601C grt44	62601C grt2.1	62601C grt2.3	62601C grt2.4	62601C grt2.5	62601C grt2.7	62601C grt2.9	62601C grt2.10	62601C grt2.11	62601C grt2.12	62601C grt2.13	62601C grt2.15	62601C grt2.16	62601C grt2.17	62601C grt2.18	62601C grt2.19
SiO <sub>2</sub>	35.69	36.92	36.63	36.34	36.36	36.41	36.58	36.65	36.45	36.77	36.30	36.13	36.42	35.74	36.01	35.81	36.25	35.76
TiO <sub>2</sub>	1.89	0.00	0.14	0.44	0.27	0.00	0.00	0.00	0.23	0.42	0.96	0.94	0.65	1.28	1.23	1.14	0.88	1.59
Al <sub>2</sub> O <sub>3</sub>	19.62	20.28	20.29	20.01	20.18	20.22	20.08	20.59	20.36	20.29	20.25	19.86	20.13	19.78	19.54	19.64	19.77	19.40
FeO	31.39	31.54	31.25	31.32	32.15	32.68	32.20	31.95	32.58	32.48	32.03	32.68	32.28	32.53	32.50	32.85	32.61	32.58
MnO	4.95	5.13	6.74	7.46	5.70	5.77	5.50	5.43	5.38	5.27	4.96	5.04	4.90	5.12	5.18	5.01	5.12	5.15
MgO	1.90	1.92	1.50	1.23	1.78	1.82	2.05	2.22	2.48	2.32	2.44	2.05	2.44	2.31	2.14	2.21	2.06	2.02
CaO	4.56	4.86	3.45	3.20	3.56	3.29	3.61	3.23	2.53	2.45	3.06	3.31	3.18	3.24	3.40	3.34	3.32	3.50
Total	100.00	100.65	100.00	100.00	100.00	100.19	100.02	100.07	100.01	100.00	100.00	100.01	100.00	100.00	100.00	100.00	100.01	100.00
Si	2.93	3.00	3.01	3.00	2.99	2.99	3.00	2.99	2.98	3.00	2.96	2.97	2.98	2.94	2.96	2.95	2.97	2.94
Al	1.90	1.94	1.97	1.95	1.95	1.96	1.94	1.98	1.96	1.95	1.95	1.92	1.94	1.92	1.89	1.90	1.91	1.88
Ti	0.12	0.00	0.01	0.03	0.02	0.00	0.00	0.00	0.01	0.03	0.06	0.06	0.04	0.08	0.08	0.07	0.05	0.10
Fe <sup>2+</sup>	2.15	2.14	2.15	2.16	2.21	2.24	2.21	2.18	2.23	2.22	2.19	2.24	2.21	2.24	2.23	2.26	2.24	2.24
Mn	0.28	0.29	0.38	0.43	0.32	0.33	0.31	0.31	0.30	0.30	0.28	0.29	0.28	0.29	0.29	0.28	0.29	0.29
Mg	0.23	0.23	0.18	0.15	0.22	0.22	0.25	0.27	0.30	0.28	0.30	0.25	0.30	0.28	0.26	0.27	0.25	0.25
Ca	0.40	0.42	0.30	0.28	0.31	0.29	0.32	0.28	0.22	0.21	0.27	0.29	0.28	0.29	0.30	0.29	0.29	0.31
Σ cat	8.01	8.03	8.00	8.00	8.02	8.03	8.03	8.02	8.02	7.99	8.00	8.02	8.01	8.03	8.02	8.03	8.01	8.02
XPy	0.08	0.08	0.06	0.05	0.07	0.07	0.08	0.09	0.10	0.09	0.10	0.08	0.10	0.09	0.08	0.09	0.08	0.08
XAlm	0.70	0.69	0.71	0.72	0.72	0.73	0.72	0.72	0.73	0.74	0.72	0.73	0.72	0.72	0.72	0.73	0.73	0.73
XSpss	0.09	0.09	0.13	0.14	0.11	0.11	0.10	0.10	0.10	0.10	0.09	0.09	0.09	0.09	0.10	0.09	0.09	0.09
XGrss	0.13	0.14	0.10	0.09	0.10	0.09	0.10	0.09	0.07	0.07	0.09	0.09	0.09	0.09	0.10	0.09	0.10	0.10
Fe/Fe+Mg	0.90	0.90	0.92	0.93	0.91	0.91	0.90	0.89	0.88	0.89	0.88	0.90	0.88	0.89	0.89	0.89	0.90	0.90

**Note:** XPy, XAlm, XSpss and XGrss as defined by Spear (1993)

**Appendix 3.1:** Major element content and structural formulae for garnet from felsic schist

Sample Analysis	62601C grt2.20	62601C grt2.22	62601C grt2.23	62601C grt2.24	62601C grt2.25	62601C grt2.26	62601C grt2.27	62601C grt2.28	62601C grt2.30	62601C grt2.31	62601C grt2.32	62601C grt2.33	62601C grt2.34	62601C grt2.36	62601C grt2.37	62601C grt2.38	62601C grt2.39	62601C grt2.41
SiO <sub>2</sub>	36.17	37.22	36.02	36.74	36.53	34.28	36.83	35.99	35.97	36.27	35.51	36.40	36.96	37.16	36.21	35.75	36.00	35.96
TiO <sub>2</sub>	1.27	1.04	1.34	2.12	0.76	5.50	0.92	0.93	1.29	1.01	1.90	0.20	0.00	0.00	0.65	1.07	0.67	0.67
Al <sub>2</sub> O <sub>3</sub>	19.88	19.24	19.98	19.16	19.49	18.63	19.08	19.52	20.01	19.90	19.96	20.36	20.55	20.45	20.33	20.10	19.76	19.82
FeO	31.57	31.61	31.64	31.45	32.34	31.45	32.41	32.83	31.72	31.97	32.50	32.63	33.25	33.33	32.73	32.44	32.21	31.55
MnO	5.26	5.17	5.24	4.87	5.09	4.92	5.29	5.26	5.01	4.94	4.82	5.05	5.27	5.20	5.71	5.62	6.74	7.37
MgO	2.25	2.21	2.23	2.19	2.17	2.09	2.10	2.15	2.31	2.29	2.07	2.23	2.01	2.28	2.08	1.88	1.58	1.41
CaO	3.60	3.50	3.56	3.47	3.63	3.12	3.37	3.32	3.69	3.62	3.25	3.13	2.90	1.99	2.29	3.13	3.03	3.21
Total	100.00	99.99	100.01	100.00	100.01	99.99	100.00	100.00	100.00	100.00	100.01	100.00	100.94	100.41	100.00	99.99	99.99	99.99
Si	2.96	3.04	2.95	3.00	3.00	2.82	3.02	2.96	2.94	2.97	2.91	2.98	3.00	3.02	2.97	2.94	2.98	2.98
Al	1.92	1.85	1.93	1.84	1.88	1.81	1.85	1.89	1.93	1.92	1.93	1.97	1.97	1.96	1.97	1.95	1.93	1.93
Ti	0.08	0.06	0.08	0.13	0.05	0.34	0.06	0.06	0.08	0.06	0.12	0.01	0.00	0.00	0.04	0.07	0.04	0.04
Fe <sup>2+</sup>	2.16	2.16	2.17	2.14	2.22	2.16	2.22	2.26	2.17	2.19	2.23	2.23	2.26	2.27	2.25	2.23	2.23	2.18
Mn	0.30	0.29	0.30	0.27	0.29	0.28	0.30	0.30	0.28	0.28	0.27	0.29	0.30	0.29	0.32	0.32	0.39	0.42
Mg	0.27	0.27	0.27	0.27	0.27	0.26	0.26	0.26	0.28	0.28	0.25	0.27	0.24	0.28	0.25	0.23	0.19	0.17
Ca	0.32	0.31	0.31	0.30	0.32	0.27	0.30	0.29	0.32	0.32	0.29	0.27	0.25	0.17	0.20	0.28	0.27	0.28
Σ cat	8.00	7.97	8.01	7.95	8.02	7.94	8.00	8.03	8.01	8.01	8.00	8.02	8.02	8.00	8.00	8.02	8.02	8.02
XPy	0.09	0.09	0.09	0.09	0.09	0.09	0.08	0.08	0.09	0.09	0.08	0.09	0.08	0.09	0.08	0.08	0.06	0.06
XAlm	0.71	0.71	0.71	0.72	0.72	0.73	0.72	0.73	0.71	0.71	0.73	0.73	0.74	0.75	0.74	0.73	0.72	0.71
XSpss	0.10	0.10	0.10	0.09	0.09	0.09	0.10	0.10	0.09	0.09	0.09	0.09	0.10	0.10	0.11	0.10	0.13	0.14
XGrss	0.10	0.10	0.10	0.10	0.10	0.09	0.10	0.09	0.11	0.10	0.09	0.09	0.08	0.06	0.07	0.09	0.09	0.09
Fe/Fe+Mg	0.89	0.89	0.89	0.89	0.89	0.89	0.90	0.90	0.89	0.89	0.90	0.89	0.90	0.89	0.90	0.91	0.92	0.93

**Note:** XPy, XAlm, XSpss and XGrss as defined by Spear (1993)



**Appendix 3.1:** Major element content and structural formulae for garnet from felsic schist

Sample Analysis	62601C	62105F	62105F	62105F	62105F	62105F	62105F	Tj 18	Tj 18	Tj 18	Tj 18	Tj 18	Tj 18	Tj 18	Tj 18	Tj 18	Tj 18
	grt2.42	grt sb2	grtsb3	grt3a	grt3d	grt3f	grtsb1a	grtpeak1	grtpeak2	grtpeak3	grtrim1	grtrim2	grtrim3	grtcore1	grtcore2	grtcore3	grtcore4
SiO <sub>2</sub>	35.72	36.73	36.35	36.77	36.86	36.74	36.75	37.59	37.37	37.36	37.16	37.35	37.11	36.92	37.36	37.06	36.79
TiO <sub>2</sub>	0.55	0.47	1.74	0.00	0.29	1.24	0.66	0.09	0.03	0.13	0.13	0.12	0.03	-0.10	-0.04	0.02	0.06
Al <sub>2</sub> O <sub>3</sub>	19.86	20.46	20.38	20.67	20.84	20.35	20.83	20.92	21.03	20.87	21.06	20.87	20.88	20.80	20.76	20.86	20.74
FeO	32.27	30.01	29.38	30.22	31.16	31.70	31.01	32.33	33.02	32.52	32.23	32.21	31.39	31.38	28.90	31.52	31.38
MnO	7.46	6.30	6.09	6.58	5.56	5.40	4.94	2.46	2.24	2.43	4.29	5.26	6.72	7.22	5.98	6.83	7.35
MgO	1.37	2.17	2.56	1.71	2.07	2.11	2.34	2.29	2.00	2.06	2.07	1.99	1.68	1.74	1.47	1.65	1.63
CaO	2.76	3.87	3.50	4.31	3.23	2.46	3.47	4.32	4.31	4.63	3.06	2.20	2.19	2.04	5.57	2.05	2.06
Total	99.99	100.01	100.00	100.26	100.01	100.00	100.00	67.67	66.98	67.48	67.77	67.79	68.61	68.62	71.10	68.47	68.63
Si	2.97	2.99	2.95	3.00	3.00	2.99	2.98	3.03	3.01	3.01	3.01	3.03	3.03	3.02	3.03	3.03	3.02
Al	1.94	1.97	1.95	1.99	2.00	1.95	1.99	1.99	2.00	1.99	2.01	2.00	2.01	2.01	1.99	2.01	2.01
Ti	0.03	0.03	0.11	0.00	0.02	0.08	0.04	0.01	0.00	0.01	0.01	0.01	0.00	-0.01	0.00	0.00	0.00
Fe <sup>2+</sup>	2.24	2.05	2.00	2.06	2.12	2.16	2.10	2.18	2.23	2.19	2.18	2.19	2.14	2.15	1.96	2.16	2.15
Mn	0.43	0.36	0.34	0.37	0.31	0.30	0.28	0.14	0.12	0.14	0.24	0.30	0.38	0.41	0.34	0.39	0.42
Mg	0.17	0.26	0.31	0.21	0.25	0.26	0.28	0.27	0.24	0.25	0.25	0.24	0.20	0.21	0.18	0.20	0.20
Ca	0.25	0.34	0.30	0.38	0.28	0.21	0.30	0.37	0.37	0.40	0.27	0.19	0.19	0.18	0.48	0.18	0.18
Σ cat	8.03	7.99	7.96	8.01	7.98	7.96	7.98	7.98	7.98	7.99	7.97	7.96	7.96	7.98	7.98	7.96	7.98
XPy	0.05	0.09	0.10	0.07	0.08	0.09	0.10	0.09	0.08	0.08	0.09	0.08	0.07	0.07	0.06	0.07	0.07
XAlm	0.73	0.68	0.68	0.68	0.71	0.74	0.71	0.74	0.75	0.74	0.74	0.75	0.73	0.73	0.66	0.74	0.73
XSpss	0.14	0.12	0.12	0.12	0.11	0.10	0.09	0.05	0.04	0.05	0.08	0.10	0.13	0.14	0.11	0.13	0.14
XGrss	0.08	0.11	0.10	0.12	0.09	0.07	0.10	0.13	0.13	0.13	0.09	0.07	0.07	0.06	0.16	0.06	0.06
Fe/Fe+Mg	0.93	0.89	0.87	0.91	0.89	0.89	0.88	0.89	0.90	0.90	0.90	0.90	0.91	0.91	0.92	0.91	0.92

**Note:** XPy, XAlm, XSpss and XGrss as defined by Spear (1993)

**Appendix 3.1:** Major element content and structural formulae for garnet from felsic schist

Sample Analysis	Tj 18 LA grt 1.1	Tj 18 LA grt 1.2	Tj 18 LA grt 1.3	Tj 18 LA grt 1.4	Tj 18 la grt 1.5	Tj 18 la grt 1.6	Tj 18 la grt 1.7	Tj 18 la grt 1.9	Tj 18 la grt 1.8	Tj 18 la grt 1.10	Tj 18 la grt 1.11	Tj 18 la grt 1.12	Tj 18 la grt 1.13	Tj 18 la grt 1.14	Tj 18 la grt 1.15	Tj 18 la grt 1.16	Tj 18 la grt 1.17	Tj 18 la grt 1.18
SiO <sub>2</sub>	38.42	36.37	36.62	36.07	36.64	37.19	35.75	35.46	35.52	35.46	35.69	35.11	35.89	35.64	35.52	35.12	35.51	35.42
TiO <sub>2</sub>	0.00	0.00	0.00	0.00	0.00	0.00	0.00	0.00	0.00	0.00	0.00	0.00	0.00	0.00	0.00	0.00	0.00	0.00
Al <sub>2</sub> O <sub>3</sub>	17.62	18.38	18.58	18.66	18.51	18.44	18.14	18.07	18.19	18.09	18.01	17.70	17.98	17.96	18.01	17.92	18.15	18.14
FeO	35.37	36.75	35.50	35.49	34.86	34.26	37.49	36.52	36.70	35.73	35.82	36.60	35.70	35.60	35.30	35.56	34.96	34.98
MnO	1.11	1.10	1.20	1.53	2.52	3.42	4.75	6.29	5.83	7.43	7.32	7.24	7.27	7.48	7.81	8.06	7.95	8.34
MgO	1.72	1.49	1.39	1.31	1.21	1.19	1.40	1.34	1.42	1.11	1.15	1.14	0.88	0.99	1.24	1.13	1.21	1.00
CaO	5.76	5.91	6.70	6.94	6.26	5.50	2.46	2.32	2.33	2.18	2.01	2.21	2.30	2.40	2.35	2.21	2.22	2.11
Total	100.00	100.00	99.99	100.00	100.00	100.00	99.99	100.00	99.99	100.00	100.00	100.00	100.02	100.07	100.23	100.00	100.00	99.99
Si	3.13	3.00	3.01	2.98	3.02	3.06	3.00	2.99	2.99	3.00	3.01	2.98	3.03	3.01	3.00	2.98	3.00	3.00
Al	1.69	1.79	1.80	1.82	1.80	1.79	1.80	1.80	1.81	1.80	1.79	1.77	1.79	1.79	1.79	1.79	1.81	1.81
Ti	0.00	0.00	0.00	0.00	0.00	0.00	0.00	0.00	0.00	0.00	0.00	0.00	0.00	0.00	0.00	0.00	0.00	0.00
Fe <sup>2+</sup>	2.41	2.54	2.44	2.45	2.41	2.36	2.63	2.58	2.58	2.53	2.53	2.60	2.52	2.52	2.49	2.53	2.47	2.48
Mn	0.06	0.06	0.07	0.09	0.14	0.19	0.28	0.37	0.34	0.43	0.43	0.43	0.42	0.44	0.46	0.47	0.46	0.49
Mg	0.21	0.18	0.17	0.16	0.15	0.15	0.18	0.17	0.18	0.14	0.14	0.14	0.11	0.12	0.16	0.14	0.15	0.13
Ca	0.50	0.52	0.59	0.61	0.55	0.49	0.22	0.21	0.21	0.20	0.18	0.20	0.21	0.22	0.21	0.20	0.20	0.19
Σ cat	8.02	8.10	8.09	8.11	8.08	8.04	8.10	8.11	8.11	8.10	8.09	8.13	8.08	8.09	8.11	8.12	8.10	8.09
XPy	0.07	0.06	0.05	0.05	0.05	0.05	0.05	0.05	0.05	0.04	0.04	0.04	0.03	0.04	0.05	0.04	0.05	0.04
XAlm	0.76	0.77	0.75	0.74	0.74	0.74	0.80	0.78	0.78	0.77	0.77	0.77	0.77	0.76	0.75	0.76	0.75	0.75
XSpss	0.02	0.02	0.02	0.03	0.04	0.06	0.08	0.11	0.10	0.13	0.13	0.13	0.13	0.13	0.14	0.14	0.14	0.15
XGrss	0.16	0.16	0.18	0.19	0.17	0.15	0.07	0.06	0.06	0.06	0.06	0.06	0.06	0.07	0.06	0.06	0.06	0.06
Fe/Fe+Mg	0.92	0.93	0.93	0.94	0.94	0.94	0.94	0.94	0.94	0.95	0.95	0.95	0.96	0.95	0.94	0.95	0.94	0.95

**Note:** XPy, XAlm, XSpss and XGrss as defined by Spear (1993)

**Appendix 3.1:** Major element content and structural formulae for garnet from felsic schist

Sample Analysis	Tj 18 la grt 1.19	Tj 18 la grt 1.20	Tj 18 la grt 1.21	Tj 18 la grt 1.22	Tj 18 la grt 1.23	Tj 18 la grt 1.24	Tj 18 la grt 1.25	Tj 18 la grt 1.26	Tj 18 la grt 1.27	Tj 18 la grt 1.28	Tj 18 la grt 1.29	Tj 18 la grt 1.30	Tj 18 la grt 1.31	Tj 18 la grt 1.32	Tj 18 la grt 1.33	Tj 18 la grt 1.34	Tj 18 la grt 2.1	Tj 18 la grt 2.2
SiO <sub>2</sub>	35.25	35.44	35.30	36.06	35.49	35.71	33.74	35.67	37.26	36.01	38.78	36.30	36.50	35.98	36.07	36.40	37.40	36.93
TiO <sub>2</sub>	0.00	0.00	0.00	0.00	0.00	0.00	0.00	0.00	0.00	0.00	0.00	0.00	0.00	0.00	0.00	0.00	0.00	0.00
Al <sub>2</sub> O <sub>3</sub>	17.91	17.92	18.43	18.09	17.96	17.90	16.98	18.14	18.87	17.94	17.67	18.23	17.29	18.08	18.38	17.96	18.39	18.39
FeO	35.16	35.09	34.75	34.39	35.18	35.91	39.57	36.79	35.10	36.63	32.48	34.60	36.35	37.13	36.78	36.82	35.64	36.26
MnO	8.32	8.16	8.08	7.99	7.76	6.66	5.81	5.42	5.12	4.23	3.23	2.46	3.69	2.93	2.78	2.26	1.06	1.09
MgO	1.13	1.16	1.27	0.98	1.21	1.28	1.31	1.63	1.45	1.37	2.38	1.17	1.38	1.48	1.77	1.26	1.68	1.53
CaO	2.22	2.23	2.17	2.49	2.40	2.54	2.59	2.34	2.20	3.81	5.47	7.24	4.78	4.40	4.22	5.29	5.84	5.80
Total	99.99	100.00	100.00	100.00	100.00	100.00	100.00	99.99	100.00	99.99	100.01	100.00	99.99	100.00	100.00	99.99	100.01	100.00
Si	2.99	3.00	2.98	3.04	3.00	3.01	2.91	3.00	3.08	3.01	3.15	3.00	3.05	3.00	3.00	3.02	3.06	3.04
Al	1.79	1.79	1.84	1.80	1.79	1.78	1.72	1.80	1.84	1.77	1.69	1.78	1.70	1.78	1.80	1.76	1.77	1.78
Ti	0.00	0.00	0.00	0.00	0.00	0.00	0.00	0.00	0.00	0.00	0.00	0.00	0.00	0.00	0.00	0.00	0.00	0.00
Fe <sup>2+</sup>	2.50	2.49	2.45	2.42	2.49	2.53	2.85	2.58	2.42	2.56	2.21	2.40	2.54	2.59	2.55	2.56	2.44	2.49
Mn	0.49	0.48	0.47	0.46	0.45	0.39	0.35	0.31	0.29	0.24	0.18	0.14	0.21	0.17	0.16	0.13	0.06	0.06
Mg	0.14	0.15	0.16	0.12	0.15	0.16	0.17	0.20	0.18	0.17	0.29	0.14	0.17	0.18	0.22	0.16	0.20	0.19
Ca	0.20	0.20	0.20	0.22	0.22	0.23	0.24	0.21	0.19	0.34	0.48	0.64	0.43	0.39	0.38	0.47	0.51	0.51
Σ cat	8.11	8.10	8.10	8.07	8.10	8.10	8.23	8.11	8.00	8.10	8.00	8.11	8.10	8.11	8.10	8.10	8.05	8.07
XPy	0.04	0.04	0.05	0.04	0.05	0.05	0.05	0.06	0.06	0.05	0.09	0.04	0.05	0.06	0.07	0.05	0.06	0.06
XAlm	0.75	0.75	0.75	0.75	0.75	0.76	0.79	0.78	0.78	0.77	0.70	0.72	0.76	0.78	0.77	0.77	0.76	0.77
XSpss	0.15	0.14	0.14	0.14	0.14	0.12	0.10	0.09	0.09	0.07	0.06	0.04	0.06	0.05	0.05	0.04	0.02	0.02
XGrss	0.06	0.06	0.06	0.07	0.07	0.07	0.07	0.06	0.06	0.10	0.15	0.19	0.13	0.12	0.11	0.14	0.16	0.16
Fe/Fe+Mg	0.95	0.94	0.94	0.95	0.94	0.94	0.94	0.93	0.93	0.94	0.88	0.94	0.94	0.93	0.92	0.94	0.92	0.93

**Note:** XPy, XAlm, XSpss and XGrss as defined by Spear (1993)

**Appendix 3.1:** Major element content and structural formulae for garnet from felsic schist

Sample Analysis	Tj 18 la grt 2.3	Tj 18 la grt 2.4	Tj 18 la grt 2.5	Tj 18 la grt 2.6	Tj 18 la grt 2.7	Tj 18 la grt 2.8	Tj 18 la grt 2.9	Tj 18 la grt 2.10	Tj 18 la grt 2.11	Tj 18 la grt 2.12	Tj 18 la grt 2.13	Tj 18 la grt 2.14	Tj 18 la grt 2.15	Tj 18 la grt 2.16a	Tj 18 grt 2.11t	Tj 18 la grt 3.1	Tj 18 la grt 3.2	Tj 18 la grt 3.3
SiO <sub>2</sub>	36.51	36.55	36.12	36.41	35.56	35.84	35.57	36.16	36.06	37.49	35.56	35.91	35.55	36.22	35.96	38.81	35.89	35.88
TiO <sub>2</sub>	0.00	0.00	0.00	0.00	0.00	0.00	0.00	0.00	0.00	0.00	0.00	0.00	0.00	0.00	0.00	0.00	0.00	0.00
Al <sub>2</sub> O <sub>3</sub>	18.37	18.31	18.32	17.43	18.22	18.12	18.05	17.86	17.84	16.74	17.93	18.06	18.19	18.38	18.11	16.37	18.15	17.88
FeO	35.51	34.71	36.15	37.10	35.32	34.13	35.16	35.49	35.33	34.87	36.50	36.24	36.19	35.75	35.83	36.19	36.86	37.14
MnO	1.51	2.33	3.66	5.35	7.29	8.45	7.74	6.61	6.20	7.13	6.04	5.80	6.03	4.47	6.28	1.37	2.17	2.41
MgO	1.32	1.13	1.42	1.20	1.37	1.35	1.66	1.40	1.64	1.47	1.73	1.76	1.76	1.69	1.79	1.32	1.30	1.22
CaO	6.77	6.98	4.32	2.52	2.24	2.11	1.82	2.49	2.93	2.30	2.24	2.23	2.28	3.49	2.03	5.94	5.63	5.47
Total	99.99	100.01	99.99	100.01	100.00	100.00	100.00	100.01	100.00	100.00	100.00	100.00	100.00	100.00	100.00	100.00	100.00	100.00
Si	3.01	3.02	3.01	3.06	3.00	3.02	3.00	3.04	3.02	3.14	2.99	3.01	2.99	3.01	3.02	3.19	2.99	2.99
Al	1.79	1.78	1.80	1.73	1.81	1.80	1.80	1.77	1.76	1.65	1.78	1.79	1.80	1.80	1.79	1.58	1.78	1.76
Ti	0.00	0.00	0.00	0.00	0.00	0.00	0.00	0.00	0.00	0.00	0.00	0.00	0.00	0.00	0.00	0.00	0.00	0.00
Fe <sup>2+</sup>	2.45	2.40	2.52	2.61	2.49	2.41	2.48	2.49	2.48	2.44	2.57	2.54	2.54	2.49	2.51	2.49	2.57	2.59
Mn	0.09	0.13	0.21	0.31	0.42	0.49	0.45	0.38	0.36	0.41	0.35	0.34	0.35	0.26	0.36	0.08	0.12	0.14
Mg	0.16	0.14	0.18	0.15	0.17	0.17	0.21	0.18	0.20	0.18	0.22	0.22	0.22	0.21	0.22	0.16	0.16	0.15
Ca	0.60	0.62	0.39	0.23	0.20	0.19	0.16	0.22	0.26	0.21	0.20	0.20	0.21	0.31	0.18	0.52	0.50	0.49
Σ cat	8.09	8.09	8.09	8.08	8.10	8.08	8.10	8.08	8.09	8.04	8.12	8.10	8.11	8.08	8.09	8.02	8.12	8.13
XPy	0.05	0.04	0.05	0.05	0.05	0.05	0.06	0.05	0.06	0.06	0.06	0.07	0.07	0.06	0.07	0.05	0.05	0.04
XAlm	0.74	0.73	0.77	0.79	0.76	0.74	0.75	0.76	0.75	0.75	0.77	0.77	0.77	0.76	0.77	0.77	0.76	0.77
XSpss	0.03	0.04	0.06	0.09	0.13	0.15	0.14	0.12	0.11	0.13	0.11	0.10	0.11	0.08	0.11	0.02	0.04	0.04
XGrss	0.18	0.19	0.12	0.07	0.06	0.06	0.05	0.07	0.08	0.06	0.06	0.06	0.06	0.10	0.06	0.16	0.15	0.15
Fe/Fe+Mg	0.94	0.95	0.93	0.95	0.94	0.93	0.92	0.93	0.92	0.93	0.92	0.92	0.92	0.92	0.92	0.94	0.94	0.94

**Note:** XPy, XAlm, XSpss and XGrss as defined by Spear (1993)

**Appendix 3.1:** Major element content and structural formulae for garnet from felsic schist

Sample Analysis	Tj 18 la grt 3.4	Tj 18 la grt 3.5	Tj 18 la grt 3.6	Tj 18 la grt 3.7	Tj 18 la grt 3.8	Tj 18 la grt 3.9	Tj 18 la grt 3.10	Tj 18 la grt 3.11	Tj 18 la grt 3.12	Tj 18 la grt 3.13	Tj 18 la grt 3.15	Tj 18 la grt 3.16	Tj 18 la grt 3.17	Tj 18 la grt 3.18	Tj 18 la grt 3.19	Tj 18 la grt 3.20
SiO <sub>2</sub>	35.87	35.91	35.90	35.93	34.13	35.39	36.21	38.19	39.48	35.72	35.67	35.97	36.11	36.30	36.69	36.48
TiO <sub>2</sub>	0.00	0.00	0.00	0.00	0.00	0.00	0.00	0.00	0.00	0.00	0.00	0.00	0.00	0.00	0.00	0.00
Al <sub>2</sub> O <sub>3</sub>	18.39	17.97	18.31	18.00	17.40	17.97	15.77	17.16	15.55	17.58	18.03	18.03	17.97	18.21	18.51	18.30
FeO	36.53	36.48	35.86	35.84	37.87	35.34	36.78	34.05	34.75	36.43	36.56	35.62	36.64	36.54	36.44	36.83
MnO	3.85	4.40	4.42	6.42	7.04	7.58	7.56	6.88	6.48	6.64	6.21	4.75	3.63	1.89	0.92	0.92
MgO	1.12	1.27	1.39	1.28	1.17	1.35	0.95	1.15	1.30	0.86	1.47	1.51	1.42	1.67	1.95	1.81
CaO	4.25	3.96	4.12	2.52	2.39	2.38	2.72	2.57	2.45	2.77	2.06	4.12	4.23	5.39	5.50	5.66
Total	100.01	99.99	100.00	99.99	100.00	100.01	99.99	100.00	100.01	100.00	100.00	100.00	100.00	100.00	100.01	100.00
Si	3.00	3.01	3.00	3.02	2.93	2.99	3.09	3.17	3.28	3.02	3.00	3.01	3.01	3.01	3.02	3.01
Al	1.81	1.77	1.80	1.78	1.76	1.79	1.59	1.68	1.52	1.75	1.79	1.78	1.77	1.78	1.79	1.78
Ti	0.00	0.00	0.00	0.00	0.00	0.00	0.00	0.00	0.00	0.00	0.00	0.00	0.00	0.00	0.00	0.00
Fe <sup>2+</sup>	2.55	2.56	2.50	2.52	2.72	2.50	2.62	2.37	2.41	2.58	2.57	2.49	2.56	2.53	2.50	2.54
Mn	0.22	0.25	0.26	0.37	0.42	0.44	0.45	0.40	0.37	0.39	0.36	0.27	0.21	0.11	0.05	0.05
Mg	0.14	0.16	0.17	0.16	0.15	0.17	0.12	0.14	0.16	0.11	0.18	0.19	0.18	0.21	0.24	0.22
Ca	0.38	0.36	0.37	0.23	0.22	0.22	0.25	0.23	0.22	0.25	0.19	0.37	0.38	0.48	0.48	0.50
Σ cat	8.10	8.11	8.10	8.09	8.19	8.11	8.12	7.99	7.96	8.10	8.10	8.10	8.10	8.11	8.09	8.10
XPy	0.04	0.05	0.05	0.05	0.04	0.05	0.04	0.05	0.05	0.03	0.06	0.06	0.05	0.06	0.07	0.07
XAlm	0.77	0.77	0.76	0.77	0.78	0.75	0.76	0.76	0.76	0.78	0.78	0.75	0.77	0.76	0.76	0.77
XSpss	0.07	0.08	0.08	0.11	0.12	0.13	0.13	0.13	0.12	0.12	0.11	0.08	0.06	0.03	0.02	0.02
XGrss	0.12	0.11	0.11	0.07	0.06	0.06	0.07	0.07	0.07	0.08	0.06	0.11	0.11	0.14	0.15	0.15
Fe/Fe+Mg	0.95	0.94	0.94	0.94	0.95	0.94	0.96	0.94	0.94	0.96	0.93	0.93	0.94	0.92	0.91	0.92

**Note:** XPy, XAlm, XSpss and XGrss as defined by Spear (1993)

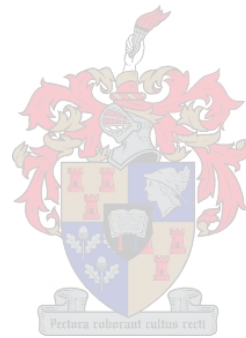
**Appendix 3.1:** Major element content and structural formulae for staurolite from felsic schist

Sample Analysis	62601C stau1	62601C stau1b	62601C stau2a	62601C stau5	62601D stau1	62601D stau2	62601D stau3	62105F stau1	62105F stau2	62105F stau3	62105D stau1	62105D stau2	62105D stau3	Tj 18 stau1	Tj 18 stau1b
SiO <sub>2</sub>	29.29	29.04	29.58	28.63	29.41	29.50	29.13	29.53	29.24	29.36	29.54	29.95	30.04	30.04	29.88
TiO <sub>2</sub>	0.52	0.61	0.64	0.74	0.66	0.74	0.64	0.63	0.56	0.54	0.24	0.25	0.25	0.64	0.60
Al <sub>2</sub> O <sub>3</sub>	54.64	54.66	54.52	54.60	54.90	54.91	55.09	55.36	55.31	55.06	56.60	56.40	56.41	55.98	56.41
Cr <sub>2</sub> O <sub>3</sub>	0.07	0.13	0.09	0.12	0.13	0.08	0.22	0.15	0.22	0.36	0.00	0.00	0.00	0.40	0.39
V <sub>2</sub> O <sub>5</sub>	0.35	0.08	0.20	0.17	0.13	0.13	0.09	0.31	0.16	0.25	0.00	0.00	0.04	0.16	0.24
ZnO	0.04	0.22	0.00	0.18	0.29	0.00	0.05	1.21	0.19	0.21	2.20	3.35	2.19	1.28	0.85
Fe <sub>2</sub> O <sub>3</sub>	0.00	0.00	0.00	0.00	0.00	0.00	0.00	0.00	0.00	0.00	0.00	0.00	0.00	0.00	0.00
FeO	14.12	14.51	14.17	14.71	13.72	13.80	14.07	12.29	13.72	13.41	10.80	10.05	10.31	11.53	11.35
MnO	0.40	0.33	0.39	0.26	0.34	0.31	0.11	0.52	0.61	0.45	0.48	0.36	0.48	0.49	0.45
MgO	0.57	0.42	0.42	0.59	0.41	0.56	0.60	0.00	0.00	0.35	0.19	0.00	0.31	0.00	0.00
CaO	0.00	0.00	0.00	0.00	0.00	0.00	0.00	0.00	0.00	0.00	0.00	0.00	0.00	0.00	0.00
Na <sub>2</sub> O	0.00	0.00	0.00	0.00	0.00	0.00	0.00	0.00	0.00	0.00	0.00	0.00	0.00	0.00	0.00
K <sub>2</sub> O	0.00	0.00	0.00	0.00	0.00	0.00	0.00	0.00	0.00	0.00	0.00	0.00	0.00	0.00	0.00
Total	99.54	99.57	99.72	99.53	99.44	99.82	99.64	98.33	99.44	99.17	97.85	97.01	97.80	98.68	98.69
Si	3.97	3.95	4.01	3.90	3.98	3.99	3.95	3.99	3.96	3.97	3.98	4.03	4.03	4.02	4.00
Al	8.74	8.77	8.71	8.77	8.77	8.75	8.80	8.82	8.84	8.79	8.99	8.94	8.93	8.84	8.91
Fe <sup>2+</sup>	1.60	1.65	1.61	1.68	1.55	1.56	1.59	1.39	1.56	1.52	1.22	1.13	1.16	1.29	1.27
Mg	0.12	0.09	0.08	0.12	0.08	0.11	0.12	0.00	0.00	0.07	0.04	0.00	0.06	0.00	0.00
Zn	0.00	0.02	0.00	0.02	0.03	0.00	0.00	0.12	0.02	0.02	0.22	0.33	0.22	0.13	0.08
Mn	0.04	0.03	0.04	0.02	0.03	0.03	0.01	0.05	0.06	0.04	0.04	0.03	0.04	0.05	0.04
V	0.03	0.01	0.02	0.02	0.01	0.01	0.01	0.03	0.01	0.02	0.00	0.00	0.00	0.01	0.02
Cr	0.01	0.01	0.01	0.01	0.01	0.01	0.02	0.02	0.02	0.04	0.00	0.00	0.00	0.04	0.04
Ti	0.05	0.06	0.07	0.08	0.07	0.08	0.07	0.06	0.06	0.05	0.02	0.03	0.03	0.06	0.06
Σ	1.85	1.87	1.82	1.94	1.79	1.80	1.83	1.67	1.73	1.77	1.54	1.52	1.51	1.58	1.52
Σ cat	14.56	14.59	14.54	14.61	14.54	14.54	14.57	14.48	14.53	14.53	14.50	14.48	14.47	14.45	14.43



**Appendix 3.1:** Major element content and structural formulae for staurolite from felsic schist

Sample mineral	Tj 18 stau1c	Tj 18 stau2a	Tj 18 stau2b	Tj 18 stau2c
SiO <sub>2</sub>	29.94	29.23	29.15	29.56
TiO <sub>2</sub>	0.67	0.64	0.56	0.62
Al <sub>2</sub> O <sub>3</sub>	55.96	56.12	55.99	56.42
Cr <sub>2</sub> O <sub>3</sub>	0.28	0.35	0.30	0.38
V <sub>2</sub> O <sub>5</sub>	0.45	0.18	0.39	0.27
ZnO	0.82	0.73	0.60	2.52
Fe <sub>2</sub> O <sub>3</sub>	0.00	0.00	0.00	0.00
FeO	11.60	12.14	12.35	10.35
MnO	0.52	0.34	0.35	0.34
MgO	0.00	0.27	0.32	0.00
CaO	0.00	0.00	0.00	0.00
Na <sub>2</sub> O	0.00	0.00	0.00	0.00
K <sub>2</sub> O	0.00	0.00	0.00	0.00
<b>Total</b>	<b>98.69</b>	<b>98.74</b>	<b>98.72</b>	<b>97.29</b>
Si	4.01	3.94	3.93	3.97
Al	8.84	8.91	8.90	8.92
Fe <sup>2+</sup>	1.30	1.37	1.39	1.16
Mg	0.00	0.05	0.06	0.00
Zn	0.08	0.07	0.06	0.25
Mn	0.05	0.03	0.03	0.03
V	0.04	0.02	0.03	0.02
Cr	0.03	0.04	0.03	0.04
Ti	0.07	0.06	0.06	0.06
Σ	1.57	1.64	1.67	1.57
Σ cat	14.42	14.50	14.50	14.46



**Appendix 3.1: Major element content and structural formulae for biotite from felsic schist**

Sample Analysis	Tj 18 bt1	Tj 18 bt1b	Tj 18 bt1c	Tj 18 bt i1	Tj 18 bt i2	62601C bt1a	62601C bt1c	62601C bt2a	62601C bt2b	62601C bt5a	62601C bt5b	62601C bt i1	62601C bt i2	62601D bt1b	62601D bt2	62601D bt3
SiO <sub>2</sub>	40.13	38.18	36.70	38.20	38.40	39.65	39.57	39.29	39.42	40.92	39.01	40.42	40.13	40.52	40.12	40.88
TiO <sub>2</sub>	0.53	1.49	1.30	1.00	1.16	1.34	1.27	1.23	1.29	1.47	1.57	1.04	1.25	1.32	1.49	1.38
Al <sub>2</sub> O <sub>3</sub>	18.22	15.32	15.55	15.76	15.30	18.14	18.01	18.03	18.37	18.32	18.17	18.75	18.84	18.08	18.49	18.35
Cr <sub>2</sub> O <sub>3</sub>	0.00	0.00	0.00	0.00	0.00	0.21	0.16	0.10	0.09	0.10	0.08	0.06	0.13	0.28	0.45	0.25
FeO	20.83	21.39	25.48	20.72	21.51	18.06	17.99	18.27	18.93	17.44	19.00	13.37	15.17	15.00	14.73	14.49
MnO	0.00	0.00	0.00	0.00	0.00	0.10	0.27	0.15	0.04	0.10	0.16	0.14	0.15	0.22	0.00	0.13
MgO	12.55	13.27	12.66	12.77	13.35	12.60	12.55	12.97	12.00	11.95	12.64	16.18	14.42	14.51	14.48	14.89
Na <sub>2</sub> O	0.60	0.00	0.00	0.00	0.00	0.00	0.00	0.00	0.00	0.00	0.00	0.00	0.00	0.00	0.00	0.00
K <sub>2</sub> O	7.13	10.42	8.62	10.56	10.34	10.05	10.58	10.44	10.36	10.12	10.02	10.33	10.64	10.44	10.68	10.46
Total	99.99	100.07	100.31	99.01	100.06	100.15	100.40	100.48	100.50	100.42	100.65	100.29	100.73	100.37	100.44	100.83
Si IV	2.86	2.80	2.72	2.82	2.81	2.83	2.83	2.81	2.82	2.89	2.79	2.82	2.82	2.85	2.82	2.85
Al IV	1.14	1.20	1.28	1.18	1.19	1.17	1.17	1.19	1.18	1.11	1.21	1.18	1.18	1.15	1.18	1.15
Σ IV	4.00	4.00	4.00	4.00	4.00	4.00	4.00	4.00	4.00	4.00	4.00	4.00	4.00	4.00	4.00	4.00
Al VI	0.39	0.12	0.08	0.20	0.14	0.36	0.35	0.33	0.37	0.42	0.32	0.36	0.38	0.35	0.35	0.36
Ti	0.03	0.08	0.07	0.06	0.06	0.07	0.07	0.07	0.07	0.08	0.08	0.05	0.07	0.07	0.08	0.07
Cr	0.00	0.00	0.00	0.00	0.00	0.01	0.01	0.01	0.01	0.01	0.00	0.00	0.01	0.02	0.03	0.01
Fe <sup>2+</sup>	1.24	1.31	1.58	1.28	1.32	1.08	1.08	1.09	1.13	1.03	1.14	0.78	0.89	0.88	0.87	0.85
Mn	0.00	0.00	0.00	0.00	0.00	0.00	0.01	0.01	0.00	0.00	0.01	0.01	0.01	0.01	0.00	0.01
Mg	1.33	1.45	1.40	1.41	1.46	1.34	1.34	1.38	1.28	1.26	1.35	1.68	1.51	1.52	1.52	1.55
Σ	2.99	2.97	3.12	2.94	2.98	2.87	2.85	2.88	2.86	2.80	2.90	2.89	2.86	2.85	2.84	2.85
K + Na	0.73	0.97	0.81	1.00	0.97	0.92	0.97	0.95	0.95	0.91	0.91	0.92	0.95	0.94	0.96	0.93
Σ cat	7.72	7.94	7.94	7.93	7.94	7.78	7.82	7.84	7.81	7.72	7.82	7.81	7.81	7.79	7.80	7.78
Mg#	51.78	52.51	46.96	52.34	52.52	55.42	55.42	55.85	53.04	54.98	54.24	68.32	62.88	63.29	63.66	64.68

Note: Mg# = 100 x Mg/(Mg+Fe)

**Appendix 3.1: Major element content and structural formulae for biotite from felsic schist**

Sample Analysis	62601D bt4	62105F bt i1	62105F bt i2	62105F bt4	62105F bt6	62601D bt1	62601D bt2	62601D bt3	62601D bt4	Tj 23 bt2	Tj 23 bt3	Tj 23 bt4	Tj 23 bt5	Tj 23 bt6	Tj 23 bt7	Tj 23 bt8
SiO <sub>2</sub>	40.53	41.49	40.94	40.22	39.75	40.31	40.75	41.13	40.79	41.39	41.23	41.13	42.47	41.71	45.23	46.35
TiO <sub>2</sub>	1.39	0.98	1.10	1.24	1.17	1.43	1.36	1.30	1.69	0.95	0.80	0.78	0.61	0.89	0.03	0.00
Al <sub>2</sub> O <sub>3</sub>	18.26	18.23	18.73	18.15	18.28	19.09	18.78	19.21	18.93	18.01	18.49	18.20	18.20	17.93	16.97	14.66
Cr <sub>2</sub> O <sub>3</sub>	0.31	0.06	0.07	0.21	0.21	0.02	0.00	0.01	0.00	0.00	0.00	0.00	0.00	0.00	0.00	0.00
FeO	15.04	11.30	11.48	16.67	17.87	14.07	14.23	13.76	14.47	12.97	13.11	13.41	12.78	13.02	8.10	9.43
MnO	0.16	0.12	0.35	0.22	0.28	0.27	0.08	0.08	0.05	0.00	0.00	0.00	0.00	0.00	0.00	0.00
MgO	14.76	18.03	17.51	13.51	13.00	14.76	15.17	15.38	14.82	15.56	15.26	15.55	15.47	15.63	16.51	18.38
Na <sub>2</sub> O	0.00	0.00	0.00	0.00	0.00	0.00	0.00	0.00	0.00	0.34	0.30	0.37	0.23	0.28	2.18	0.22
K <sub>2</sub> O	10.48	10.12	10.18	10.54	10.19	10.54	10.31	9.95	10.07	10.78	10.81	10.55	10.24	10.54	10.98	10.97
Total	100.93	100.33	100.36	100.76	100.75	100.49	100.68	100.82	100.82	100.00	100.00	99.99	100.00	100.00	100.00	100.01
Si IV	2.84	2.86	2.83	2.84	2.82	2.82	2.84	2.84	2.84	2.89	2.88	2.88	2.95	2.91	3.09	3.16
Al IV	1.16	1.14	1.17	1.16	1.18	1.18	1.16	1.16	1.16	1.11	1.12	1.12	1.05	1.09	0.91	0.84
Σ IV	4.00	4.00	4.00	4.00	4.00	4.00	4.00	4.00	4.00	4.00	4.00	4.00	4.00	4.00	4.00	4.00
Al VI	0.34	0.34	0.36	0.36	0.35	0.39	0.38	0.41	0.39	0.38	0.41	0.38	0.44	0.39	0.46	0.34
Ti	0.07	0.05	0.06	0.07	0.06	0.08	0.07	0.07	0.09	0.05	0.04	0.04	0.03	0.05	0.00	0.00
Cr	0.02	0.00	0.00	0.01	0.01	0.00	0.00	0.00	0.00	0.00	0.00	0.00	0.00	0.00	0.00	0.00
Fe <sup>2+</sup>	0.88	0.65	0.66	0.99	1.06	0.82	0.83	0.80	0.84	0.76	0.77	0.79	0.74	0.76	0.46	0.54
Mn	0.01	0.01	0.02	0.01	0.01	0.01	0.00	0.00	0.00	0.00	0.00	0.00	0.00	0.00	0.00	0.00
Mg	1.54	1.85	1.80	1.42	1.38	1.54	1.58	1.59	1.54	1.62	1.59	1.62	1.60	1.63	1.68	1.87
Σ	2.86	2.90	2.90	2.85	2.88	2.85	2.86	2.86	2.85	2.81	2.81	2.83	2.81	2.82	2.60	2.75
K + Na	0.94	0.89	0.90	0.95	0.92	0.94	0.92	0.88	0.89	1.01	1.01	0.99	0.94	0.98	1.25	0.98
Σ cat	7.80	7.79	7.80	7.80	7.80	7.79	7.78	7.74	7.75	7.82	7.81	7.82	7.75	7.79	7.85	7.74
Mg#	63.62	73.98	73.10	59.09	56.45	65.15	65.51	66.58	64.60	68.13	67.47	67.39	68.33	68.14	78.41	77.65

Note: Mg# = 100 x Mg/(Mg+Fe)

**Appendix 3.1: Major element content and structural formulae for chlorite from felsic schist**

Sample Analysis	62601C chl2a	62601C chl2b	62601C chl4	62601C chl4b	62601C chl i3	62601C chl i3b	62601C chl i4	62105F chl1	62105F chl2	62105F chl3	62105F chl4	62105F chl6	62105F chl i1	62105D chl p1	62105D chl p2
SiO <sub>2</sub>	31.49	29.59	29.82	30.28	30.31	33.00	30.78	30.64	32.41	31.44	29.88	30.12	31.26	30.71	30.31
TiO <sub>2</sub>	0.13	0.09	0.04	0.11	0.03	0.08	0.47	0.06	0.06	0.45	0.10	0.17	0.12	0.00	0.06
Al <sub>2</sub> O <sub>3</sub>	26.05	25.92	26.79	25.26	27.04	25.67	26.27	26.34	24.87	26.18	27.09	26.74	27.19	26.99	27.42
Cr <sub>2</sub> O <sub>3</sub>	0.10	0.17	0.19	0.11	0.04	0.08	0.21	0.14	0.14	0.09	0.10	0.16	0.05	0.00	0.00
FeO	25.94	27.75	26.52	27.00	21.45	20.93	20.72	24.31	25.05	24.21	25.86	25.09	20.31	22.16	22.16
MnO	0.26	0.30	0.16	0.19	0.24	0.21	0.16	0.25	0.28	0.33	0.34	0.23	0.35	0.16	0.34
MgO	15.82	16.16	16.34	16.96	20.75	19.89	21.34	18.29	16.97	17.25	16.60	17.55	20.77	20.08	19.78
K <sub>2</sub> O	0.21	0.03	0.15	0.08	0.14	0.15	0.06	0.00	0.21	0.05	0.04	0.00	0.00	0.00	0.00
Total	100.00	100.01	100.01	99.99	100.00	100.01	100.01	100.03	99.99	100.00	100.01	100.06	100.05	100.10	100.07
Si IV	2.85	2.71	2.71	2.76	2.69	2.91	2.72	2.75	2.92	2.82	2.71	2.72	2.75	2.73	2.70
Al IV	1.15	1.29	1.29	1.24	1.31	1.09	1.28	1.25	1.08	1.18	1.29	1.28	1.25	1.27	1.30
Σ IV	4.00	4.00	4.00	4.00	4.00	4.00	4.00	4.00	4.00	4.00	4.00	4.00	4.00	4.00	4.00
Al VI	1.62	1.51	1.58	1.48	1.52	1.57	1.46	1.54	1.55	1.59	1.60	1.56	1.57	1.55	1.57
Ti	0.01	0.01	0.00	0.01	0.00	0.01	0.03	0.00	0.00	0.03	0.01	0.01	0.01	0.00	0.00
Cr	0.01	0.01	0.01	0.01	0.00	0.01	0.01	0.01	0.01	0.01	0.01	0.01	0.01	0.00	0.00
Fe <sup>2+</sup>	1.96	2.13	2.02	2.06	1.59	1.54	1.53	1.83	1.88	1.82	1.96	1.89	1.50	1.65	1.65
Mn	0.02	0.02	0.01	0.01	0.01	0.01	0.01	0.02	0.02	0.02	0.02	0.01	0.02	0.01	0.02
Mg	2.13	2.21	2.21	2.30	2.75	2.61	2.81	2.45	2.28	2.30	2.24	2.36	2.73	2.66	2.62
Ca	0.00	0.00	0.00	0.00	0.00	0.00	0.00	0.00	0.00	0.00	0.00	0.00	0.00	0.00	0.00
Na	0.00	0.00	0.00	0.00	0.00	0.00	0.00	0.00	0.00	0.00	0.00	0.00	0.00	0.00	0.00
K	0.02	0.00	0.02	0.01	0.02	0.02	0.01	0.00	0.02	0.01	0.00	0.00	0.00	0.00	0.00
Σ	5.77	5.88	5.85	5.88	5.90	5.76	5.87	5.84	5.77	5.77	5.84	5.85	5.83	5.86	5.86
Σ cat	9.77	9.88	9.85	9.88	9.90	9.76	9.87	9.84	9.77	9.77	9.84	9.85	9.83	9.86	9.86
Mg#	52.08	50.93	52.33	52.82	63.29	62.87	64.73	57.28	54.69	55.94	53.36	55.49	64.57	61.76	61.40

Note: Mg# = 100 x Mg/(Mg+Fe)

**Appendix 3.1: Major element content and structural formulae for chlorite from felsic schist**

Sample Analysis	62105D chl p3	62105D chl m1	62105D chl m2	62105D chl m3	62105D chl m4	62105D chl m5	62105D chl m6	62105D chl m7	Tj 18 chl10	Tj 18 chl12a	Tj 18 chl12b	Tj 18 chl12c	Tj 18 chl12d	Tj 18 chl13a	Tj 18 chl13b
SiO <sub>2</sub>	30.66	30.51	30.91	30.34	31.11	33.01	34.70	34.58	30.37	29.52	29.86	29.66	30.06	31.23	30.79
TiO <sub>2</sub>	0.13	0.05	0.09	0.07	0.06	0.05	0.13	0.00	0.02	0.03	0.01	0.00	0.00	0.00	0.02
Al <sub>2</sub> O <sub>3</sub>	27.37	26.71	27.39	27.20	27.28	27.67	27.72	26.73	25.76	25.11	25.31	25.45	22.62	23.28	25.50
Cr <sub>2</sub> O <sub>3</sub>	0.04	0.04	0.00	0.00	0.01	0.04	0.08	0.00							
FeO	21.57	22.32	21.42	22.06	21.21	19.89	18.31	18.98	28.28	27.49	28.13	26.79	32.73	33.21	28.76
MnO	0.29	0.26	0.32	0.31	0.30	0.29	0.21	0.17	0.31	0.53	0.36	0.34	0.32	0.51	0.36
MgO	19.97	19.78	19.87	19.99	19.92	18.47	17.47	17.92	15.94	15.99	15.96	16.17	12.03	12.10	16.74
K <sub>2</sub> O	0.00	0.34	0.02	0.05	0.12	0.59	1.38	1.68	0.00	1.34	0.36	1.59	2.24	0.00	0.00
Total	100.03	100.01	100.02	100.02	100.01	100.01	100.00	100.06	100.68	100.01	99.99	100.00	100.00	100.33	102.17
Si IV	2.72	2.72	2.74	2.70	2.75	2.89	3.02	3.02	2.76	2.73	2.75	2.73	2.86	2.92	2.76
Al IV	1.28	1.28	1.26	1.30	1.25	1.11	0.98	0.98	1.24	1.27	1.25	1.27	1.14	1.08	1.24
Σ IV	4.00	4.00	4.00	4.00	4.00	4.00	4.00	4.00	4.00	4.00	4.00	4.00	4.00	4.00	4.00
Al VI	1.58	1.53	1.59	1.55	1.60	1.75	1.86	1.78	1.52	1.46	1.49	1.49	1.40	1.48	1.46
Ti	0.01	0.00	0.01	0.00	0.00	0.00	0.01	0.00	0.00	0.00	0.00	0.00	0.00	0.00	0.00
Cr	0.00	0.00	0.00	0.00	0.00	0.00	0.01	0.00	0.00	0.00	0.00	0.00	0.00	0.00	0.00
Fe <sup>2+</sup>	1.60	1.67	1.59	1.64	1.57	1.46	1.33	1.39	2.15	2.12	2.16	2.06	2.61	2.60	2.16
Mn	0.02	0.02	0.02	0.02	0.02	0.02	0.01	0.01	0.02	0.03	0.02	0.02	0.02	0.03	0.02
Mg	2.64	2.63	2.62	2.65	2.63	2.41	2.26	2.33	2.16	2.20	2.19	2.22	1.71	1.69	2.24
Ca	0.00	0.00	0.00	0.00	0.00	0.00	0.00	0.00	0.00	0.00	0.00	0.00	0.00	0.00	0.00
Na	0.00	0.00	0.00	0.00	0.00	0.00	0.00	0.00	0.00	0.00	0.00	0.00	0.00	0.00	0.00
K	0.00	0.04	0.00	0.01	0.01	0.07	0.15	0.19	0.00	0.16	0.04	0.19	0.27	0.00	0.00
Σ	5.84	5.89	5.83	5.87	5.83	5.71	5.63	5.69	5.86	5.98	5.90	5.98	6.01	5.80	5.89
Σ cat	9.84	9.89	9.83	9.87	9.83	9.71	9.63	9.69	9.86	9.98	9.90	9.98	10.01	9.80	9.89
Mg#	62.26	61.23	62.31	61.76	62.60	62.33	62.97	62.72	50.11	50.90	50.27	51.82	39.58	39.37	50.91

Note: Mg# = 100 x Mg/(Mg+Fe)

**Appendix 3.1: Major element content and structural formulae for chlorite from felsic schist**

Sample Analysis	Tj 18 chl13c	Tj 18 chl13d	Tj 18 chl14a	Tj 18 chl14c	Tj 18 chl15b	Tj 18 chl1 gi	Tj 18 chl2 gi	Tj 18 chl3 gi	Tj 18 chl4 gi	Tj 8 chl1	Tj 8 chl2	Tj 8 chl3	Tj 8 chl4	Tj 8 chl5
SiO <sub>2</sub>	30.88	30.04	29.93	30.32	30.42	32.12	30.31	29.68	29.06	33.35	30.52	32.87	33.97	33.81
TiO <sub>2</sub>	0.00	0.00	0.03	0.06	0.01	0.03	0.02	0.11	0.13	0.07	6.05	0.09	0.05	0.01
Al <sub>2</sub> O <sub>3</sub>	20.60	24.09	25.13	23.68	25.29	26.28	26.28	26.59	26.16	27.55	26.21	28.15	26.31	28.69
Cr <sub>2</sub> O <sub>3</sub>														
FeO	32.00	31.18	28.26	31.64	28.04	23.48	28.24	27.87	28.88	13.30	12.67	13.03	13.83	11.58
MnO	0.30	0.29	0.39	0.55	0.38	0.24	0.36	0.21	0.24	0.01	0.03	0.05	-0.09	0.07
MgO	12.96	14.48	15.76	12.81	16.56	17.87	14.81	15.56	15.50	25.62	24.46	25.71	25.60	25.86
K <sub>2</sub> O	3.27	0.00	0.48	0.94	0.00	-0.02	-0.02	-0.02	-0.03	0.11	0.05	0.09	0.34	-0.02
Total	100.01	100.08	99.98	100.00	100.70	100.00	100.00	100.00	100.00	100.01	99.99	99.99	100.01	100.00
Si IV	2.95	2.79	2.76	2.85	2.77	2.86	2.77	2.71	2.68	2.83	2.61	2.79	2.89	2.84
Al IV	1.05	1.21	1.24	1.15	1.23	1.14	1.23	1.29	1.32	1.17	1.39	1.21	1.11	1.16
Σ IV	4.00	4.00	4.00	4.00	4.00	4.00	4.00	4.00	4.00	4.00	4.00	4.00	4.00	4.00
Al VI	1.27	1.43	1.48	1.47	1.48	1.62	1.61	1.58	1.52	1.59	1.26	1.61	1.53	1.68
Ti	0.00	0.00	0.00	0.00	0.00	0.00	0.00	0.01	0.01	0.00	0.39	0.01	0.00	0.00
Cr	0.00	0.00	0.00	0.00	0.00	0.00	0.00	0.00	0.00	0.00	0.00	0.00	0.00	0.00
Fe <sup>2+</sup>	2.56	2.43	2.18	2.48	2.13	1.75	2.16	2.13	2.22	0.94	0.91	0.92	0.98	0.81
Mn	0.02	0.02	0.02	0.04	0.02	0.01	0.02	0.01	0.02	0.00	0.00	0.00	-0.01	0.00
Mg	1.85	2.01	2.16	1.79	2.24	2.37	2.02	2.12	2.13	3.24	3.12	3.25	3.25	3.24
Ca	0.00	0.00	0.00	0.00	0.00	0.00	0.00	0.00	0.00	0.00	0.00	0.00	0.00	0.00
Na	0.00	0.00	0.00	0.00	0.00	0.00	0.00	0.00	0.00	0.00	0.00	0.00	0.00	0.00
K	0.40	0.00	0.06	0.11	0.00	0.00	0.00	0.00	0.00	0.01	0.01	0.01	0.04	0.00
Σ	6.09	5.89	5.91	5.90	5.88	5.76	5.81	5.85	5.90	5.79	5.68	5.80	5.80	5.74
Σ cat	10.09	9.89	9.91	9.90	9.88	9.76	9.81	9.85	9.90	9.79	9.68	9.80	9.80	9.74
Mg#	41.92	45.28	49.84	41.91	51.28	57.56	48.31	49.87	48.89	77.44	77.48	77.86	76.74	79.92

Note: Mg# = 100 x Mg/(Mg+Fe)



**Appendix 3.1: Major element content and structural formulae for plagioclase from felsic schist**

Sample Analysis	Tj 18 plag rim	Tj 18 plag2	Tj 18 plag3	Tj 18 plag4	Tj 18 plag2a	Tj 18 plag2b	Tj 18 plag1 grt4	Tj 18 plag2 grt4	Tj 18 plag2 grt5	Tj 18 plag3 grt5	Tj 18 plag4 grt5	62601C plag1a	62601C plag1b	62601C plag2a	62601C plag3a
SiO <sub>2</sub>	59.12	58.21	58.86	58.79	58.64	60.22	33.20	32.64	59.42	58.27	58.00	63.10	61.77	63.16	62.78
TiO <sub>2</sub>	0.00	0.00	0.00	0.00	0.00	0.00	0.00	0.00	0.00	0.00		0.00	0.00	0.00	0.00
Al <sub>2</sub> O <sub>3</sub>	25.97	26.51	26.16	26.07	26.21	25.16	53.33	53.20	25.68	26.44	26.51	23.33	23.78	23.12	23.39
FeO	0.00	0.00	0.00	0.00	0.00	0.00	0.00	0.00	0.00	0.00	0.00	0.00	0.00	0.00	0.00
CaO	7.20	8.10	7.62	8.02	8.00	6.94	12.71	13.24	7.52	8.31	8.48	4.40	5.29	4.12	4.56
Na <sub>2</sub> O	7.65	7.09	7.21	7.07	7.03	7.57	0.64	0.67	7.29	6.87	6.88	9.10	9.05	9.54	9.17
K <sub>2</sub> O	0.06	0.10	0.15	0.05	0.12	0.11	0.12	0.25	0.09	0.10	0.13	0.07	0.11	0.07	0.10
Total	100.00	100.01	100.00	100.00	100.00	100.00	100.00	100.00	100.00	99.99	100.00	100.00	100.00	100.01	100.00
Si	2.64	2.60	2.63	2.63	2.62	2.68	1.52	1.50	2.65	2.61	2.60	2.79	2.74	2.79	2.78
Al	1.37	1.40	1.38	1.37	1.38	1.32	2.87	2.88	1.35	1.39	1.40	1.22	1.25	1.21	1.22
Σ	4.00	4.00	4.00	4.00	4.00	4.00	4.39	4.38	4.00	4.00	4.00	4.00	3.99	4.00	4.00
Ca	0.34	0.39	0.36	0.38	0.38	0.33	0.62	0.65	0.36	0.40	0.41	0.21	0.25	0.20	0.22
Na	0.66	0.61	0.62	0.61	0.61	0.65	0.06	0.06	0.63	0.60	0.60	0.78	0.78	0.82	0.79
K	0.00	0.01	0.01	0.00	0.01	0.01	0.01	0.01	0.01	0.01	0.01	0.00	0.01	0.00	0.01
Σ	1.01	1.01	1.00	1.00	1.00	0.99	0.69	0.73	0.99	1.00	1.01	0.99	1.04	1.02	1.01
Σ cat	5.01	5.01	5.00	5.00	5.00	4.99	5.08	5.10	4.99	5.00	5.01	5.00	5.03	5.02	5.01
XAn	0.34	0.39	0.37	0.39	0.39	0.34	0.92	0.92	0.36	0.40	0.41	0.21	0.24	0.19	0.22
XAb	0.66	0.61	0.63	0.61	0.61	0.66	0.08	0.08	0.64	0.60	0.59	0.79	0.76	0.81	0.78

Note: XAn = Ca/(Ca+Na); XAb = Na/(Ca+Na)

**Appendix 3.1: Major element content and structural formulae for plagioclase from felsic schist**

Sample Analysis	62601C plag3b	62601D plag1	62601D plag2	62601D plag m1	62601D plag m2	62601D plag m3	62105F plag1	62105F plag2	62105F plag3	62105F plag4	62105F plag5	62105F plag6	62105D plag1	62105D plag2	62105D plag3
SiO <sub>2</sub>	62.76	62.59	62.62	61.27	61.10	62.22	59.94	61.66	61.88	61.48	63.07	62.11	64.18	65.07	67.63
TiO <sub>2</sub>	0.00	0.00	0.00	0.00	0.00	0.00	0.00	0.00	0.00	0.00	0.00	0.00	0.00	0.00	0.00
Al <sub>2</sub> O <sub>3</sub>	23.45	23.54	23.63	24.52	24.53	24.08	25.52	24.12	24.22	24.37	23.21	24.02	22.42	21.78	19.93
FeO	0.00	0.00	0.00	0.00	0.00	0.00	0.00	0.00	0.00	0.00	0.00	0.00	0.00	0.00	0.00
CaO	4.56	4.87	4.80	5.80	5.97	4.81	6.56	5.41	5.15	5.42	4.90	4.92	3.40	2.65	0.79
Na <sub>2</sub> O	9.19	8.91	9.00	8.32	8.34	8.83	7.88	8.77	8.74	8.65	8.74	8.88	9.92	10.46	11.58
K <sub>2</sub> O	0.05	0.09	0.00	0.10	0.05	0.06	0.10	0.04	0.02	0.08	0.08	0.08	0.09	0.04	0.07
Total	100.01	100.00	100.05	100.01	99.99	100.00	100.00	100.00	100.01	100.00	100.00	100.01	100.01	100.00	100.00
Si	2.78	2.77	2.77	2.72	2.71	2.75	2.67	2.74	2.74	2.73	2.79	2.75	2.83	2.87	2.96
Al	1.22	1.23	1.23	1.28	1.28	1.26	1.34	1.26	1.26	1.27	1.21	1.25	1.17	1.13	1.03
Σ	4.00	4.00	4.00	4.00	4.00	4.01	4.01	4.00	4.01	4.00	4.00	4.01	4.00	4.00	3.99
Ca	0.22	0.23	0.23	0.28	0.28	0.23	0.31	0.26	0.24	0.26	0.23	0.23	0.16	0.13	0.04
Na	0.79	0.76	0.77	0.72	0.72	0.76	0.68	0.75	0.75	0.74	0.75	0.76	0.85	0.89	0.98
K	0.00	0.01	0.00	0.01	0.00	0.00	0.01	0.00	0.00	0.00	0.00	0.00	0.01	0.00	0.00
Σ	1.01	1.00	1.00	1.00	1.01	0.99	1.00	1.01	1.00	1.01	0.99	1.00	1.01	1.02	1.02
Σ cat	5.01	5.00	5.00	5.00	5.00	5.00	5.01	5.01	5.00	5.01	4.98	5.01	5.01	5.02	5.02
XAn	0.22	0.23	0.23	0.28	0.28	0.23	0.32	0.25	0.25	0.26	0.24	0.23	0.16	0.12	0.04
XAb	0.78	0.77	0.77	0.72	0.72	0.77	0.68	0.75	0.75	0.74	0.76	0.77	0.84	0.88	0.96

Note: XAn = Ca/(Ca+Na); XAb = Na/(Ca+Na)

**Appendix 3.1: Major element content and structural formulae for plagioclase from felsic schist**

Sample Analysis	62105D plag4	62105D plag5	62105D plag6	Tj 23 plag1	Tj 23 plag2	Tj 23 plag3	Tj 23 plag4	Tj 23 plag5	Tj 23 plag6	Tj 23 plag7	Tj 23 plag8
SiO <sub>2</sub>	68.15	67.49	65.57	65.27	65.80	65.55	65.62	65.73	65.12	69.09	65.47
TiO <sub>2</sub>	0.00	0.00	0.00	0.00	0.00	0.00	0.00	0.00	0.00	0.00	0.00
Al <sub>2</sub> O <sub>3</sub>	19.70	20.22	21.45	21.78	21.41	21.63	21.46	21.50	21.74	18.87	21.60
FeO	0.00	0.00	0.00	0.00	0.00	0.00	0.00	0.00	0.00	0.00	0.00
CaO	0.42	0.99	2.58	2.76	2.56	2.69	2.50	2.78	2.92	0.08	2.74
Na <sub>2</sub> O	11.75	11.31	10.39	10.15	10.16	10.02	10.36	9.96	10.16	11.92	10.08
K <sub>2</sub> O	0.00	0.00	0.01	0.04	0.07	0.11	0.06	0.04	0.06	0.03	0.12
Total	100.02	100.01	100.00	100.00	100.00	100.00	100.00	100.01	100.00	99.99	100.01
Si	2.98	2.95	2.88	2.87	2.89	2.88	2.89	2.89	2.87	3.02	2.88
Al	1.02	1.04	1.11	1.13	1.11	1.12	1.11	1.11	1.13	0.97	1.12
Σ	3.99	4.00	4.00	4.00	4.00	4.00	4.00	4.00	4.00	3.99	4.00
Ca	0.02	0.05	0.12	0.13	0.12	0.13	0.12	0.13	0.14	0.00	0.13
Na	1.00	0.96	0.89	0.87	0.87	0.85	0.88	0.85	0.87	1.01	0.86
K	0.00	0.00	0.00	0.00	0.00	0.01	0.00	0.00	0.00	0.00	0.01
Σ	1.02	1.01	1.01	1.00	0.99	0.99	1.00	0.98	1.01	1.01	1.00
Σ cat	5.01	5.00	5.00	5.00	4.99	4.99	5.00	4.98	5.00	5.00	4.99
XAn	0.02	0.05	0.12	0.13	0.12	0.13	0.12	0.13	0.14	0.00	0.13
XAb	0.98	0.95	0.88	0.87	0.88	0.87	0.88	0.87	0.86	1.00	0.87

Note: XAn = Ca/(Ca+Na); XAb = Na/(Ca+Na)

**Appendix 3.1: Major element content and structural formulae for muscovite from felsic schist**

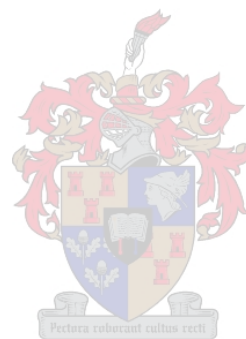
Sample Analysis	Tj 18 ms1	Tj 18 ms2	62601D ms1	62601D ms2	62601D ms4	62601D ms5	62601D ms6	62105D ms1	62105D ms2	62105D ms3	62105D ms4	Tj 23 ms1	Tj 23 ms2	Tj 23 ms3	Tj 23 ms4
SiO <sub>2</sub>	51.36	50.38	49.65	51.42	50.02	49.74	49.95	49.01	48.77	49.09	49.23	50.84	51.26	50.64	50.57
TiO <sub>2</sub>	0.27	0.26	0.06	0.28	0.38	0.36	0.14	0.45	0.41	0.48	0.39	0.34	0.22	0.31	0.35
Al <sub>2</sub> O <sub>3</sub>	30.04	34.34	38.44	35.46	35.90	36.56	36.74	38.16	38.28	38.21	36.81	34.05	33.67	35.10	35.29
FeO	3.30	2.03	0.61	0.77	1.18	0.79	0.63	0.63	0.57	0.54	1.22	1.32	1.32	1.26	1.16
MgO	2.41	0.75	0.00	0.00	0.00	0.00	0.00	0.00	0.00	0.00	0.00	1.25	1.31	0.45	0.54
Na <sub>2</sub> O	0.60	1.45	1.53	3.26	1.36	2.25	2.08	2.44	3.52	3.82	3.48	1.31	1.23	1.39	1.28
K <sub>2</sub> O	12.02	10.79	10.10	9.07	10.82	10.22	10.55	9.53	8.91	8.26	8.56	10.90	11.01	10.86	10.82
Total	100.00	100.00	100.39	100.26	99.66	99.92	100.09	100.22	100.46	100.40	99.69	100.01	100.02	100.01	100.01
Si	3.36	3.24	3.11	3.22	3.17	3.14	3.15	3.08	3.06	3.07	3.11	3.24	3.27	3.22	3.22
Al IV	0.64	0.76	0.89	0.78	0.83	0.86	0.85	0.92	0.94	0.93	0.89	0.76	0.73	0.78	0.78
Σ IV	4.00	4.00	4.00	4.00	4.00	4.00	4.00	4.00	4.00	4.00	4.00	4.00	4.00	4.00	4.00
Al VI	1.68	1.84	1.94	1.84	1.86	1.87	1.88	1.90	1.89	1.89	1.86	1.80	1.80	1.86	1.86
Ti	0.01	0.01	0.00	0.01	0.02	0.02	0.01	0.02	0.02	0.02	0.02	0.02	0.01	0.01	0.02
Fe <sup>2+</sup>	0.00	0.00	0.03	0.04	0.06	0.04	0.03	0.03	0.03	0.03	0.06	0.00	0.00	0.00	0.00
Mg	0.24	0.07	0.00	0.00	0.00	0.00	0.00	0.00	0.00	0.00	0.00	0.12	0.12	0.04	0.05
Σ VI	1.93	1.92	1.98	1.89	1.94	1.93	1.92	1.96	1.94	1.94	1.94	1.94	1.93	1.92	1.93
Na	0.08	0.18	0.19	0.40	0.17	0.28	0.25	0.30	0.43	0.46	0.43	0.16	0.15	0.17	0.16
K	1.00	0.88	0.81	0.73	0.88	0.82	0.85	0.76	0.71	0.66	0.69	0.89	0.90	0.88	0.88
Σ	1.08	1.06	0.99	1.12	1.04	1.10	1.10	1.06	1.14	1.12	1.12	1.05	1.05	1.05	1.04
Σ cat	7.01	6.98	6.97	7.02	6.99	7.03	7.03	7.02	7.08	7.06	7.06	6.99	6.98	6.97	6.96
XPa	0.07	0.17	0.19	0.35	0.16	0.25	0.23	0.28	0.38	0.41	0.38	0.15	0.15	0.16	0.15

**Note:** XPa = Na/(Na+K)

**Appendix 3.1: Major element content and structural formulae for muscovite from felsic schist**

Sample Analysis	Tj 23 ms5	Tj 8 ms1	Tj 8 ms2	Tj 8 ms3	Tj 8 ms4	Tj 8 ms6
SiO <sub>2</sub>	50.20	49.98	49.29	51.07	50.17	50.27
TiO <sub>2</sub>	0.32	0.33	0.65	0.59	0.62	0.44
Al <sub>2</sub> O <sub>3</sub>	34.95	36.78	38.23	36.06	37.51	37.32
FeO	1.50	0.67	0.49	1.21	0.42	0.45
MgO	0.66	0.30	0.00	0.10	0.00	0.10
Na <sub>2</sub> O	1.35	2.46	2.45	1.70	2.77	2.83
K <sub>2</sub> O	11.02	9.49	9.15	9.27	8.66	8.59
Total	100.00	100.01	100.26	100.00	100.15	100.00
Si	3.21	3.15	3.09	3.22	3.14	3.15
Al IV	0.79	0.85	0.91	0.78	0.86	0.85
Σ IV	4.00	4.00	4.00	4.00	4.00	4.00
Al VI	1.85	1.89	1.92	1.90	1.91	1.91
Ti	0.02	0.02	0.03	0.03	0.03	0.02
Fe <sup>2+</sup>	0.00	0.00	0.00	0.00	0.00	0.00
Mg	0.06	0.03	0.00	0.01	0.00	0.01
Σ VI	1.92	1.93	1.95	1.94	1.93	1.94
Na	0.17	0.30	0.30	0.21	0.34	0.34
K	0.90	0.76	0.73	0.75	0.69	0.69
Σ	1.07	1.06	1.03	0.95	1.03	1.03
Σ cat	6.99	7.00	6.98	6.89	6.96	6.97
XPa	0.16	0.28	0.29	0.22	0.33	0.33

**Note:** XPa = Na/(Na+K)



**Appendix 3.2: Major element content and structural formulae for garnet from mafic rocks**

Sample Analysis	Tj 3 grt1	Tj 3 grt2	Tj 3 grt3	Tj 3 grt4	Tj 3 grt5	Tj 3 grt6	Tj 3 grt7	Tj 3 grt8	Tj 3 grt9	Tj 3 grt10	Tj 3 grt11	Tj 3 grt12	Tj 3 grt13	Tj 3 grt14	Tj 3 grt15	Tj 3 grt16
SiO <sub>2</sub>	37.00	36.89	36.90	36.92	36.52	36.88	36.74	37.15	36.52	37.42	37.06	36.51	36.83	36.68	36.85	36.82
TiO <sub>2</sub>	0.10	0.16	0.15	0.14	0.16	0.02	0.04	0.11	0.13	0.04	0.15	0.20	0.03	0.12	0.14	0.12
Al <sub>2</sub> O <sub>3</sub>	20.95	20.70	20.81	20.72	20.86	20.88	20.81	20.91	20.80	20.79	20.93	20.79	21.05	20.86	20.92	20.91
FeO	27.39	28.14	28.25	27.99	27.79	27.68	27.74	27.50	28.08	27.89	27.62	27.64	27.66	27.71	27.50	27.67
MnO	4.60	4.89	4.59	4.75	4.85	4.95	4.89	4.91	4.80	4.72	4.71	5.02	5.01	4.98	5.03	5.06
MgO	0.54	0.21	0.28	0.34	0.24	0.32	0.22	0.27	0.29	0.11	0.12	0.29	0.12	0.25	0.28	0.25
CaO	9.42	9.01	9.02	9.14	9.57	9.28	9.55	9.16	9.38	9.03	9.41	9.54	9.31	9.39	9.29	9.18
Total	100.00	100.00	100.00	100.00	99.99	100.01	99.99	100.01	100.00	100.00	100.00	99.99	100.01	99.99	100.01	100.01
Si	3.00	3.00	3.00	3.00	2.97	3.00	2.99	3.01	2.98	3.03	3.01	2.97	2.99	2.98	2.99	2.99
Al	2.00	1.99	1.99	1.98	2.00	2.00	2.00	2.00	2.00	1.99	2.00	2.00	2.02	2.00	2.00	2.00
Ti	0.01	0.01	0.01	0.01	0.01	0.00	0.00	0.01	0.01	0.00	0.01	0.01	0.00	0.01	0.01	0.01
Fe <sup>2+</sup>	1.86	1.91	1.92	1.90	1.89	1.88	1.89	1.86	1.91	1.89	1.87	1.88	1.88	1.89	1.87	1.88
Mn	0.26	0.27	0.26	0.27	0.27	0.28	0.28	0.28	0.27	0.26	0.26	0.28	0.28	0.28	0.28	0.28
Mg	0.07	0.03	0.03	0.04	0.03	0.04	0.03	0.03	0.04	0.01	0.01	0.04	0.01	0.03	0.03	0.03
Ca	0.82	0.79	0.79	0.80	0.83	0.81	0.83	0.80	0.82	0.78	0.82	0.83	0.81	0.82	0.81	0.80
Σ cat	8.00	8.00	8.00	8.00	8.02	8.00	8.01	7.98	8.02	7.97	7.98	8.02	8.00	8.01	8.00	8.00
XPy	0.02	0.01	0.01	0.01	0.01	0.01	0.01	0.01	0.01	0.00	0.00	0.01	0.00	0.01	0.01	0.01
XAlm	0.62	0.64	0.64	0.63	0.62	0.63	0.62	0.63	0.63	0.64	0.63	0.62	0.63	0.63	0.62	0.63
XSpss	0.09	0.09	0.09	0.09	0.09	0.09	0.09	0.09	0.09	0.09	0.09	0.09	0.09	0.09	0.09	0.09
XGrss	0.27	0.26	0.26	0.26	0.28	0.27	0.28	0.27	0.27	0.27	0.28	0.27	0.27	0.27	0.27	0.27
Fe/Fe+Mg	0.97	0.99	0.98	0.98	0.98	0.98	0.99	0.98	0.98	0.99	0.99	0.98	0.99	0.98	0.98	0.98

**Note:** XPy, XAlm, XSpss and XGrss as defined by Spear (1993)



**Appendix 3.2: Major element content and structural formulae for garnet from mafic rocks**

Sample Analysis	Tj 3 grt17	Tj 3 grt18	Tj 3 grt19	Tj 3 grt20	Tj 3 grt21	Tj 3 grt22	Tj 3 grt23	Tj 3 grt24	Tj 3 grt25	Tj 3 grt26	Tj 3 grt27	Tj 3 grt28	Tj 3 grt29	Tj 3 grt30	Tj 3 grt31	Tj 3 grt32
SiO <sub>2</sub>	36.88	36.77	36.59	36.77	36.80	36.89	36.45	38.25	36.78	36.87	36.92	36.78	36.80	36.99	36.71	36.73
TiO <sub>2</sub>	0.15	0.16	0.13	0.37	0.08	0.36	0.39	0.15	0.25	0.11	0.11	0.20	0.13	0.18	0.26	0.08
Al <sub>2</sub> O <sub>3</sub>	20.78	20.80	20.76	20.93	21.07	20.62	20.87	20.36	20.93	20.88	20.53	20.80	20.70	20.51	20.86	20.74
FeO	27.36	27.58	28.29	27.51	27.71	27.72	27.80	27.25	27.52	27.85	28.38	28.15	28.09	28.26	27.83	27.97
MnO	5.20	5.19	4.99	4.96	4.84	4.95	4.71	4.89	5.07	5.36	5.20	5.51	5.26	5.22	5.43	4.92
MgO	0.24	0.30	0.14	0.29	0.28	0.11	0.41	0.23	0.26	0.22	0.08	0.22	0.18	0.00	0.23	0.35
CaO	9.39	9.21	9.10	9.17	9.21	9.36	9.37	8.86	9.19	8.69	8.78	8.32	8.85	8.85	8.69	9.21
Total	100.00	100.01	100.00	100.00	99.99	100.01	100.00	99.99	100.00	99.98	100.00	99.98	100.01	100.01	100.01	100.00
Si	3.00	2.99	2.98	2.99	2.99	3.00	2.96	3.09	2.99	3.00	3.01	3.00	3.00	3.01	2.99	2.99
Al	1.99	1.99	2.00	2.00	2.02	1.98	2.00	1.94	2.00	2.00	1.97	2.00	1.99	1.97	2.00	1.99
Ti	0.01	0.01	0.01	0.02	0.00	0.02	0.02	0.01	0.02	0.01	0.01	0.01	0.01	0.01	0.02	0.00
Fe <sup>2+</sup>	1.86	1.88	1.93	1.87	1.88	1.89	1.89	1.84	1.87	1.90	1.94	1.92	1.91	1.93	1.90	1.90
Mn	0.29	0.29	0.28	0.28	0.27	0.28	0.26	0.27	0.28	0.30	0.29	0.31	0.30	0.29	0.31	0.28
Mg	0.03	0.04	0.02	0.04	0.03	0.01	0.05	0.03	0.03	0.03	0.01	0.03	0.02	0.00	0.03	0.04
Ca	0.82	0.80	0.80	0.80	0.80	0.82	0.82	0.77	0.80	0.76	0.77	0.73	0.77	0.77	0.76	0.80
Σ cat	8.00	8.00	8.01	7.99	8.00	7.99	8.01	7.94	7.99	7.99	8.00	7.99	8.00	7.99	7.99	8.01
XPy	0.01	0.01	0.01	0.01	0.01	0.00	0.02	0.01	0.01	0.01	0.00	0.01	0.01	0.00	0.01	0.01
XAlm	0.62	0.62	0.64	0.63	0.63	0.63	0.63	0.63	0.63	0.64	0.64	0.64	0.64	0.64	0.63	0.63
XSpss	0.10	0.10	0.09	0.09	0.09	0.09	0.09	0.09	0.10	0.10	0.10	0.10	0.10	0.10	0.10	0.09
XGrss	0.27	0.27	0.26	0.27	0.27	0.27	0.27	0.26	0.27	0.25	0.26	0.24	0.26	0.26	0.25	0.27
Fe/Fe+Mg	0.98	0.98	0.99	0.98	0.98	0.99	0.97	0.99	0.98	0.99	1.00	0.99	0.99	1.00	0.99	0.98

**Note:** XPy, XAlm, XSpss and XGrss as defined by Spear (1993)

**Appendix 3.2: Major element content and structural formulae for garnet from mafic rocks**

Sample Analysis	Tj 3 grt33	Tj 3 grt34	Tj 3 grt35	Tj 3 grt36	Tj 3 grt37	Tj 3 grt38	Tj 3 grt39	Tj 3 grt40	Tj 3 grt41	Tj 3 grt42	Tj 3 grt43	61406 grt1	61406 grt2	61406 grt3	61406 grt4
SiO <sub>2</sub>	36.85	36.87	36.75	36.84	36.87	37.01	36.56	36.98	36.98	36.74	37.10	37.09	37.09	37.02	37.08
TiO <sub>2</sub>	0.16	0.14	0.07	0.11	0.04	0.16	0.09	0.11	0.07	0.05	0.19	0.16	0.18	0.19	0.19
Al <sub>2</sub> O <sub>3</sub>	20.70	20.74	20.83	20.76	20.95	20.56	20.68	20.87	20.72	20.85	20.72	20.86	20.96	20.61	20.89
FeO	27.71	27.72	28.07	27.92	27.37	27.84	27.84	27.59	27.79	27.87	26.72	22.34	22.00	22.48	21.97
MnO	5.26	5.03	5.05	5.13	5.26	4.85	5.14	5.03	5.13	5.05	5.93	10.49	10.51	10.77	11.05
MgO	0.13	0.25	0.23	0.23	0.21	0.10	0.37	0.10	0.23	0.20	0.12	0.94	1.35	1.36	0.97
CaO	9.19	9.24	9.01	9.00	9.29	9.48	9.32	9.32	9.08	9.25	9.22	8.12	7.91	7.58	7.85
Total	100.00	99.99	100.01	99.99	99.99	100.00	100.00	100.00	100.00	100.01	100.00	100.00	100.00	100.01	100.00
Si	3.00	3.00	2.99	3.00	3.00	3.01	2.98	3.00	3.01	2.99	3.02	3.02	3.01	3.02	3.02
Al	1.99	1.99	2.00	1.99	2.01	1.97	1.99	2.00	1.99	2.00	1.99	2.00	2.01	1.98	2.01
Ti	0.01	0.01	0.00	0.01	0.00	0.01	0.01	0.01	0.00	0.00	0.01	0.01	0.01	0.01	0.01
Fe <sup>2+</sup>	1.89	1.89	1.91	1.90	1.86	1.89	1.90	1.87	1.89	1.90	1.82	1.52	1.50	1.53	1.50
Mn	0.30	0.28	0.28	0.29	0.30	0.27	0.29	0.28	0.29	0.28	0.33	0.59	0.59	0.61	0.62
Mg	0.02	0.03	0.03	0.03	0.03	0.01	0.04	0.01	0.03	0.02	0.01	0.11	0.16	0.17	0.12
Ca	0.80	0.81	0.79	0.78	0.81	0.83	0.81	0.81	0.79	0.81	0.80	0.71	0.69	0.66	0.69
Σ cat	8.00	8.00	8.00	8.00	8.00	7.99	8.02	7.99	8.00	8.01	7.98	7.97	7.97	7.98	7.96
XPy	0.01	0.01	0.01	0.01	0.01	0.00	0.01	0.00	0.01	0.01	0.00	0.04	0.06	0.06	0.04
XAlm	0.63	0.63	0.64	0.63	0.62	0.63	0.62	0.63	0.63	0.63	0.61	0.52	0.51	0.52	0.51
XSpss	0.10	0.09	0.09	0.10	0.10	0.09	0.10	0.09	0.10	0.09	0.11	0.20	0.20	0.20	0.21
XGrss	0.27	0.27	0.26	0.26	0.27	0.27	0.27	0.27	0.26	0.27	0.27	0.24	0.23	0.22	0.23
Fe/Fe+Mg	0.99	0.98	0.99	0.99	0.99	0.99	0.98	0.99	0.99	0.99	0.99	0.93	0.90	0.90	0.93

**Note:** XPy, XAlm, XSpss and XGrss as defined by Spear (1993)

**Appendix 3.2: Major element content and structural formulae for garnet from mafic rocks**

Sample Analysis	61406 grt5	61406 grt6	61406 grt7	61406 grt8	61406 grt9	61406 grt10	61406 grt11	61406 grt12	61406 grt13	61406 grt14	61406 grt15	61406 grt16	61406 grt17	61406 grt18	61406 grt19	61406 grt20
SiO <sub>2</sub>	37.00	36.77	37.01	37.01	37.15	37.04	37.16	36.97	37.12	36.91	37.10	36.81	37.08	37.06	36.97	36.73
TiO <sub>2</sub>	0.19	0.17	0.20	0.23	0.18	0.29	0.23	0.28	0.26	0.42	0.24	0.28	0.25	0.20	0.15	0.10
Al <sub>2</sub> O <sub>3</sub>	20.82	21.16	20.92	21.06	20.71	21.12	20.96	20.62	20.68	21.01	20.75	20.86	20.73	20.97	20.94	21.02
FeO	21.99	22.28	22.17	21.44	21.65	21.46	20.80	21.64	21.30	21.45	21.59	21.62	21.17	22.08	21.99	22.64
MnO	10.69	11.05	11.06	11.08	10.98	10.89	11.55	11.07	10.98	11.12	11.24	11.15	11.19	10.92	10.94	10.61
MgO	1.19	1.14	1.13	0.91	1.13	1.03	1.21	0.91	1.12	0.99	0.99	1.07	0.96	0.98	1.00	1.29
CaO	8.11	7.43	7.51	8.27	8.20	8.18	8.10	8.51	8.53	8.08	8.09	8.22	8.62	7.79	8.00	7.60
Total	99.99	100.00	100.00	100.00	100.00	100.01	100.01	100.00	99.99	99.98	100.00	100.01	100.00	100.00	99.99	99.99
Si	3.01	3.00	3.02	3.01	3.03	3.01	3.02	3.02	3.02	3.01	3.02	3.00	3.02	3.02	3.01	3.00
Al	2.00	2.03	2.01	2.02	1.99	2.02	2.01	1.98	1.98	2.02	1.99	2.01	1.99	2.01	2.01	2.02
Ti	0.01	0.01	0.01	0.01	0.01	0.02	0.01	0.02	0.02	0.03	0.01	0.02	0.02	0.01	0.01	0.01
Fe <sup>2+</sup>	1.50	1.52	1.51	1.46	1.47	1.46	1.41	1.48	1.45	1.46	1.47	1.47	1.44	1.50	1.50	1.54
Mn	0.60	0.62	0.62	0.62	0.62	0.61	0.65	0.62	0.62	0.63	0.63	0.63	0.63	0.61	0.62	0.60
Mg	0.14	0.14	0.14	0.11	0.14	0.12	0.15	0.11	0.14	0.12	0.12	0.13	0.12	0.12	0.12	0.16
Ca	0.71	0.65	0.66	0.72	0.72	0.71	0.71	0.74	0.74	0.71	0.71	0.72	0.75	0.68	0.70	0.66
Σ cat	7.98	7.97	7.97	7.96	7.97	7.96	7.96	7.97	7.97	7.96	7.96	7.98	7.97	7.96	7.97	7.99
XPy	0.05	0.05	0.05	0.04	0.05	0.04	0.05	0.04	0.05	0.04	0.04	0.04	0.04	0.04	0.04	0.05
XAlm	0.51	0.52	0.52	0.50	0.50	0.50	0.49	0.50	0.49	0.50	0.50	0.50	0.49	0.52	0.51	0.52
XSpss	0.20	0.21	0.21	0.21	0.21	0.21	0.22	0.21	0.21	0.21	0.22	0.21	0.21	0.21	0.21	0.20
XGrss	0.24	0.22	0.22	0.25	0.24	0.25	0.24	0.25	0.25	0.24	0.24	0.24	0.26	0.23	0.24	0.22
Fe/Fe+Mg	0.91	0.92	0.92	0.93	0.91	0.92	0.91	0.93	0.91	0.92	0.92	0.92	0.93	0.93	0.93	0.91

**Note:** XPy, XAlm, XSpss and XGrss as defined by Spear (1993)

**Appendix 3.2: Major element content and structural formulae for garnet from mafic rocks**

Sample Analysis	61406 grt21	61406 grt22	61406 grt23	61406 grt24	61406 grt25	61406 grt26	61406 gb grt1	61406 gb grt2	61406 gb grt3	61406 gb grt4	62105A grt8	62105A grt9	62105A grt13	62105A grt14	62105A grt15
SiO <sub>2</sub>	36.71	36.76	36.69	37.06	36.93	37.15	36.70	36.76	36.77	37.34	36.06	36.07	36.03	36.50	36.28
TiO <sub>2</sub>	0.25	0.16	0.13	0.24	0.19	0.15	0.09	0.19	0.14	0.17	0.08	0.21	0.11	0.11	0.00
Al <sub>2</sub> O <sub>3</sub>	21.13	20.90	21.12	21.06	20.82	21.01	21.35	21.18	21.04	21.25	20.75	20.47	20.52	20.34	20.58
FeO	22.05	23.24	23.88	24.04	24.21	24.20	25.43	25.01	25.56	25.63	31.49	30.06	29.33	27.38	28.16
MnO	10.53	10.23	9.35	9.17	9.24	9.17	9.91	9.98	9.86	9.10	5.30	6.25	7.48	8.90	9.67
MgO	1.33	1.42	1.63	1.56	1.63	1.27	1.37	1.35	1.21	1.43	0.55	0.47	0.21	0.15	0.27
CaO	8.01	7.29	7.20	6.86	6.98	7.05	5.16	5.53	5.41	5.08	5.77	6.48	6.32	6.62	5.16
Total	100.01	100.00	100.00	99.99	100.00	100.00	100.01	100.00	99.99	100.00	100.00	100.01	100.00	100.00	100.12
Si	2.99	3.00	2.98	3.01	3.00	3.02	3.00	3.00	3.01	3.03	2.97	2.97	2.98	3.01	3.00
Al	2.03	2.01	2.03	2.02	2.00	2.01	2.06	2.04	2.03	2.03	2.01	1.99	2.00	1.98	2.01
Ti	0.02	0.01	0.01	0.01	0.01	0.01	0.01	0.01	0.01	0.01	0.00	0.01	0.01	0.01	0.00
Fe <sup>2+</sup>	1.50	1.58	1.62	1.63	1.65	1.64	1.74	1.71	1.75	1.74	2.17	2.07	2.03	1.89	1.95
Mn	0.59	0.58	0.53	0.51	0.52	0.51	0.56	0.56	0.56	0.51	0.30	0.36	0.43	0.51	0.55
Mg	0.16	0.17	0.20	0.19	0.20	0.15	0.17	0.16	0.15	0.17	0.07	0.06	0.03	0.02	0.03
Ca	0.70	0.64	0.63	0.60	0.61	0.61	0.45	0.48	0.47	0.44	0.51	0.57	0.56	0.59	0.46
Σ cat	7.98	7.99	7.99	7.97	7.99	7.97	7.97	7.97	7.97	7.94	8.02	8.02	8.02	7.99	8.00
XPy	0.05	0.06	0.07	0.06	0.07	0.05	0.06	0.06	0.05	0.06	0.02	0.02	0.01	0.01	0.01
XAlm	0.51	0.53	0.55	0.56	0.55	0.56	0.60	0.59	0.60	0.61	0.71	0.68	0.67	0.63	0.65
XSpss	0.20	0.19	0.18	0.18	0.17	0.18	0.19	0.19	0.19	0.18	0.10	0.12	0.14	0.17	0.18
XGrss	0.24	0.21	0.21	0.20	0.20	0.21	0.15	0.17	0.16	0.15	0.17	0.19	0.18	0.20	0.15
Fe/Fe+Mg	0.90	0.90	0.89	0.90	0.89	0.91	0.91	0.91	0.92	0.91	0.97	0.97	0.99	0.99	0.98

**Note:** XPy, XAlm, XSpss and XGrss as defined by Spear (1993)

**Appendix 3.2: Major element content and structural formulae for garnet from mafic rocks**

Sample Analysis	62105A grt16	62105A grt17	62105A grt18	62105A grt19	62105A grt20	62105A grt21	62105A grt22	62105A grt23	62105A grt24	62105A grt25	62105A grt26	62105A grt27	62105A grt28	62105A grt29	62105A grt30	62105A grt31
SiO <sub>2</sub>	36.05	36.09	35.67	36.15	36.07	35.75	35.98	36.09	36.39	36.02	35.92	36.03	35.96	35.80	36.02	36.11
TiO <sub>2</sub>	0.00	0.00	0.08	0.04	0.11	0.12	0.14	0.05	0.06	0.04	0.10	0.03	0.00	0.13	0.03	0.17
Al <sub>2</sub> O <sub>3</sub>	20.51	20.44	20.44	20.69	20.39	20.40	20.68	20.39	20.29	20.27	20.70	20.43	20.45	20.47	20.51	20.46
FeO	27.76	27.86	27.43	27.00	27.32	27.53	26.72	27.06	27.27	27.34	27.12	27.06	27.58	28.08	27.51	28.39
MnO	10.62	10.34	10.97	11.17	10.97	11.08	11.15	11.26	10.84	10.84	11.05	11.12	10.76	10.26	9.32	8.13
MgO	0.24	0.19	0.29	0.21	0.10	0.22	0.20	0.22	0.34	0.15	0.15	0.12	0.33	0.43	0.24	0.35
CaO	4.86	5.07	5.12	4.74	5.04	4.89	5.13	4.93	4.82	5.34	4.97	5.22	4.99	4.83	6.37	6.39
Total	100.04	99.99	100.00	100.00	100.00	99.99	100.00	100.00	100.01	100.00	100.01	100.01	100.07	100.00	100.00	100.00
Si	2.99	3.00	2.97	3.00	3.00	2.98	2.99	3.00	3.02	3.00	2.98	3.00	2.99	2.98	2.98	2.98
Al	2.01	2.00	2.01	2.02	2.00	2.00	2.02	2.00	1.98	1.99	2.03	2.00	2.00	2.01	2.00	1.99
Ti	0.00	0.00	0.01	0.00	0.01	0.01	0.01	0.00	0.00	0.00	0.01	0.00	0.00	0.01	0.00	0.01
Fe <sup>2+</sup>	1.93	1.94	1.91	1.87	1.90	1.92	1.85	1.88	1.89	1.90	1.88	1.88	1.92	1.95	1.90	1.96
Mn	0.61	0.59	0.63	0.64	0.63	0.64	0.64	0.65	0.62	0.62	0.63	0.64	0.62	0.59	0.53	0.46
Mg	0.03	0.02	0.04	0.03	0.01	0.03	0.02	0.03	0.04	0.02	0.02	0.01	0.04	0.05	0.03	0.04
Ca	0.43	0.45	0.46	0.42	0.45	0.44	0.46	0.44	0.43	0.48	0.44	0.47	0.44	0.43	0.56	0.57
Σ cat	8.00	8.00	8.02	7.99	8.00	8.01	7.99	8.00	7.99	8.01	8.00	8.00	8.01	8.01	8.02	8.01
XPy	0.01	0.01	0.01	0.01	0.00	0.01	0.01	0.01	0.01	0.01	0.01	0.00	0.01	0.02	0.01	0.01
XAlm	0.64	0.64	0.63	0.63	0.64	0.64	0.62	0.63	0.63	0.63	0.63	0.63	0.63	0.65	0.63	0.65
XSpss	0.20	0.20	0.21	0.22	0.21	0.21	0.21	0.22	0.21	0.21	0.21	0.21	0.20	0.19	0.18	0.15
XGrss	0.14	0.15	0.15	0.14	0.15	0.14	0.15	0.15	0.14	0.16	0.15	0.15	0.15	0.14	0.19	0.19
Fe/Fe+Mg	0.98	0.99	0.98	0.99	0.99	0.99	0.99	0.99	0.98	0.99	0.99	0.99	0.98	0.97	0.98	0.98

**Note:** XPy, XAlm, XSpss and XGrss as defined by Spear (1993)

**Appendix 3.2: Major element content and structural formulae for garnet from mafic rocks**

Sample Analysis	62105A grt32	62105A grt33	62105A grt34	62105A grt35	62105A grt36	62105A grt37	62105A grt38	62105A grt39	62105A grt40	62105A grt43	62105A grt47	62107 grt2	62107 grt3	62107 grt4	62107 grt5
SiO <sub>2</sub>	36.19	36.12	36.09	36.34	35.93	35.98	38.93	35.99	36.18	36.22	36.60	36.95	37.07	37.16	37.05
TiO <sub>2</sub>	0.17	0.09	0.15	0.22	0.11	0.14	0.13	0.20	0.04	0.12	0.15	0.19	0.05	0.10	0.02
Al <sub>2</sub> O <sub>3</sub>	20.55	20.51	20.27	20.57	20.31	20.62	17.86	20.65	20.41	20.68	20.60	21.15	20.93	20.99	21.04
FeO	28.54	29.20	29.54	29.70	30.37	30.72	31.29	31.54	31.90	31.13	31.48	28.48	27.86	27.28	26.97
MnO	7.67	7.65	7.09	6.25	6.22	6.05	4.89	4.77	4.74	3.93	3.82	4.56	4.86	4.65	4.98
MgO	0.30	0.37	0.51	0.43	0.52	0.49	1.52	0.71	0.57	0.60	0.65	1.22	1.11	1.00	1.14
CaO	6.58	6.05	6.36	6.50	6.53	6.00	5.38	6.14	6.16	7.33	6.71	7.45	8.13	8.82	8.79
Total	100.00	99.99	100.01	100.01	99.99	100.00	100.00	100.00	100.00	100.01	100.01	100.00	100.01	100.00	99.99
Si	2.98	2.98	2.98	2.98	2.97	2.96	3.17	2.96	2.98	2.96	2.99	2.99	3.00	3.00	2.99
Al	2.00	2.00	1.97	1.99	1.98	2.00	1.72	2.00	1.98	1.99	1.98	2.02	2.00	2.00	2.01
Ti	0.01	0.01	0.01	0.01	0.01	0.01	0.01	0.01	0.00	0.01	0.01	0.01	0.00	0.01	0.00
Fe <sup>2+</sup>	1.97	2.02	2.04	2.04	2.10	2.12	2.13	2.17	2.19	2.13	2.15	1.93	1.89	1.84	1.82
Mn	0.44	0.44	0.40	0.35	0.35	0.34	0.28	0.27	0.27	0.22	0.22	0.25	0.27	0.26	0.28
Mg	0.04	0.05	0.06	0.05	0.06	0.06	0.18	0.09	0.07	0.07	0.08	0.15	0.13	0.12	0.14
Ca	0.58	0.54	0.56	0.57	0.58	0.53	0.47	0.54	0.54	0.64	0.59	0.65	0.71	0.76	0.76
Σ cat	8.01	8.02	8.03	8.01	8.04	8.03	7.96	8.03	8.03	8.03	8.01	7.99	8.00	7.99	8.00
XPy	0.01	0.02	0.02	0.02	0.02	0.02	0.06	0.03	0.02	0.02	0.03	0.05	0.04	0.04	0.05
XAlm	0.65	0.66	0.66	0.68	0.68	0.69	0.70	0.71	0.71	0.69	0.71	0.65	0.63	0.62	0.61
XSpss	0.14	0.14	0.13	0.12	0.11	0.11	0.09	0.09	0.09	0.07	0.07	0.09	0.09	0.09	0.09
XGrss	0.19	0.18	0.18	0.19	0.19	0.17	0.15	0.18	0.18	0.21	0.19	0.22	0.24	0.26	0.25
Fe/Fe+Mg	0.98	0.98	0.97	0.97	0.97	0.97	0.92	0.96	0.97	0.97	0.96	0.93	0.93	0.94	0.93

**Note:** XPy, XAlm, XSpss and XGrss as defined by Spear (1993)



**Appendix 3.2: Major element content and structural formulae for garnet from mafic rocks**

Sample Analysis	62107 grt7	62107 grt9	62107 grt11	62107 grt12	62107 grt13	62107 grt14	62107 grt15	62107 grt16	62107 grt17	62107 grt18	62107 grt20	62107 grt22	62107 grt23	62107 grt24	62107 grt25	62107 grt30	62107 grt31
SiO <sub>2</sub>	37.29	37.02	37.07	37.29	37.18	37.05	36.68	36.96	36.92	36.95	37.14	37.06	37.06	36.83	36.98	36.94	37.09
TiO <sub>2</sub>	0.00	0.21	0.17	0.21	0.14	0.04	0.07	0.13	0.15	0.17	0.08	0.16	0.18	0.18	0.20	0.04	0.15
Al <sub>2</sub> O <sub>3</sub>	21.04	20.79	20.87	20.80	20.93	20.87	20.88	20.63	20.87	20.79	21.07	20.84	20.83	20.72	20.74	20.81	20.85
FeO	26.77	27.14	26.32	25.61	25.26	25.11	25.47	25.49	25.28	25.81	25.35	25.35	25.01	25.60	25.20	25.93	26.15
MnO	5.15	5.16	5.88	6.25	6.70	6.81	6.97	6.99	7.06	6.92	6.40	7.03	7.06	6.70	7.02	6.60	5.60
MgO	0.99	0.75	0.90	0.74	0.81	0.97	0.87	0.85	0.80	0.78	0.84	0.78	0.83	0.93	0.91	0.82	0.94
CaO	8.84	8.93	8.79	9.08	8.97	9.15	9.06	8.95	8.91	8.58	9.11	8.79	9.02	9.04	8.94	8.86	9.22
Total	100.08	100.00	100.00	99.98	99.99	100.00	100.00	100.00	99.99	100.00	99.99	100.01	99.99	100.00	99.99	100.00	100.00
Si	3.01	3.00	3.00	3.02	3.01	3.00	2.98	3.00	3.00	3.00	3.01	3.01	3.01	2.99	3.00	3.00	3.00
Al	2.00	1.99	1.99	1.98	2.00	1.99	2.00	1.98	2.00	1.99	2.01	1.99	1.99	1.98	1.99	1.99	1.99
Ti	0.00	0.01	0.01	0.01	0.01	0.00	0.00	0.01	0.01	0.01	0.00	0.01	0.01	0.01	0.01	0.00	0.01
Fe <sup>2+</sup>	1.81	1.84	1.78	1.73	1.71	1.70	1.73	1.73	1.72	1.75	1.72	1.72	1.70	1.74	1.71	1.76	1.77
Mn	0.29	0.29	0.33	0.35	0.38	0.38	0.39	0.39	0.40	0.39	0.36	0.39	0.40	0.38	0.39	0.37	0.31
Mg	0.12	0.09	0.11	0.09	0.10	0.12	0.11	0.10	0.10	0.09	0.10	0.09	0.10	0.11	0.11	0.10	0.11
Ca	0.76	0.78	0.76	0.79	0.78	0.79	0.79	0.78	0.78	0.75	0.79	0.76	0.78	0.79	0.78	0.77	0.80
Σ cat	7.99	7.99	7.99	7.98	7.98	8.00	8.01	8.00	7.99	7.99	7.98	7.99	7.99	8.00	7.99	8.00	8.00
XPy	0.04	0.03	0.04	0.03	0.03	0.04	0.03	0.03	0.03	0.03	0.03	0.03	0.03	0.04	0.04	0.03	0.04
XAlm	0.61	0.61	0.60	0.59	0.58	0.57	0.57	0.58	0.58	0.59	0.58	0.58	0.57	0.58	0.57	0.59	0.59
XSpss	0.10	0.10	0.11	0.12	0.13	0.13	0.13	0.13	0.13	0.13	0.12	0.13	0.13	0.12	0.13	0.12	0.10
XGrss	0.26	0.26	0.26	0.27	0.26	0.27	0.26	0.26	0.26	0.25	0.27	0.26	0.26	0.26	0.26	0.26	0.27
Fe/Fe+Mg	0.94	0.95	0.94	0.95	0.95	0.94	0.94	0.94	0.95	0.95	0.94	0.95	0.94	0.94	0.94	0.95	0.94

**Note:** XPy, XAlm, XSpss and XGrss as defined by Spear (1993)

**Appendix 3.2: Major element content and structural formulae for amphibole from mafic rocks**

Sample Analysis	Tj 3 hbl1	Tj 3 hbl2	Tj 3 hbl3	Tj 3 hbl4	62107 hbl1	62107 hbl2	62107 hbl3	61406 amph i1	61406 amph i2	61406 amph gb1	61406 amph m1	61406 amph m3	62210 hbl1	62210 hbl2	62210 hbl3
SiO <sub>2</sub>	41.73	41.95	41.94	42.79	44.30	44.29	43.66	51.08	50.13	49.55	47.72	47.51	49.76	46.85	48.95
TiO <sub>2</sub>	0.72	0.76	0.64	0.66	0.48	0.34	0.46	0.55	0.30	0.37	0.48	0.42	0.61	0.79	0.76
Al <sub>2</sub> O <sub>3</sub>	14.66	14.96	14.66	14.50	16.41	16.88	16.94	9.70	8.27	11.93	13.45	13.73	8.16	11.31	9.60
Cr <sub>2</sub> O <sub>3</sub>	0.00	0.00	0.00	0.00	0.05	0.00	0.12	0.14	0.11	0.14	0.07	0.06	0.18	0.15	0.06
FeO	23.54	22.94	23.24	22.81	18.51	18.67	18.87	12.15	14.14	13.75	15.03	15.15	17.40	17.86	17.14
MnO	0.46	0.41	0.34	0.27	0.42	0.22	0.25	0.80	1.98	0.51	0.66	0.68	0.49	0.41	0.46
MgO	4.34	4.35	4.62	4.58	6.82	6.49	6.63	13.30	13.41	11.06	10.47	10.11	10.58	9.13	10.21
CaO	11.42	11.47	11.30	11.31	11.69	11.86	11.70	11.67	11.52	11.74	10.90	11.18	11.96	11.94	11.74
Na <sub>2</sub> O	2.08	2.05	2.27	2.01	1.03	0.93	1.00	0.45	0.02	0.75	0.92	0.89	0.59	1.11	0.77
K <sub>2</sub> O	1.03	1.10	0.97	1.07	0.30	0.37	0.38	0.15	0.12	0.20	0.29	0.26	0.28	0.44	0.32
Total	99.98	99.99	99.98	100.00	100.01	100.05	100.01	99.99	100.00	100.00	99.99	99.99	100.01	99.99	100.01
Si	6.32	6.33	6.34	6.43	6.45	6.44	6.37	7.17	7.16	7.01	6.80	6.78	7.18	6.82	7.06
Al IV	1.68	1.67	1.66	1.57	1.55	1.56	1.63	0.83	0.84	0.99	1.20	1.22	0.82	1.18	0.94
Σ IV	8.00	8.00	8.00	8.00	8.00	8.00	8.00	8.00	8.00	8.00	8.00	8.00	8.00	8.00	8.00
Al M123	0.94	0.99	0.95	1.00	1.26	1.33	1.28	0.77	0.55	0.99	1.06	1.09	0.57	0.76	0.69
Cr	0.00	0.00	0.00	0.00	0.01	0.00	0.01	0.02	0.01	0.02	0.01	0.01	0.02	0.02	0.01
Ti	0.08	0.09	0.07	0.07	0.05	0.04	0.05	0.06	0.03	0.04	0.05	0.05	0.07	0.09	0.08
Mg	0.98	0.98	1.04	1.03	1.48	1.41	1.44	2.78	2.85	2.33	2.22	2.15	2.28	1.98	2.19
Fe M123	2.98	2.89	2.94	2.87	2.20	2.23	2.21	1.37	1.55	1.62	1.66	1.71	2.06	2.16	2.03
Mn M123	0.02	0.04	0.00	0.03	0.00	0.00	0.00	0.00	0.00	0.00	0.00	0.00	0.00	0.00	0.00
Σ M123	5.00	4.99	5.00	4.99	5.00	5.00	5.00	5.00	5.00	5.00	5.00	5.00	5.00	5.00	5.00
Fe M4	0.00	0.00	0.00	0.00	0.05	0.04	0.09	0.06	0.14	0.00	0.13	0.10	0.04	0.02	0.04
Mn M4	0.03	0.00	0.03	0.00	0.04	0.02	0.03	0.08	0.20	0.05	0.06	0.07	0.05	0.04	0.05
Ca	1.85	1.85	1.83	1.82	1.82	1.85	1.83	1.75	1.76	1.78	1.66	1.71	1.85	1.86	1.81
Na M4	0.12	0.15	0.14	0.18	0.08	0.09	0.06	0.11	0.00	0.17	0.14	0.13	0.06	0.08	0.10
Σ M4	2.00	2.00	2.00	2.00	2.00	2.00	2.00	2.00	2.09	2.00	2.00	2.00	2.00	2.00	2.00
A Na	0.49	0.45	0.53	0.41	0.21	0.18	0.22	0.01	0.01	0.04	0.12	0.12	0.10	0.23	0.12
A K	0.20	0.21	0.19	0.21	0.06	0.07	0.07	0.03	0.02	0.04	0.05	0.05	0.05	0.08	0.06
Σ A	0.69	0.67	0.71	0.61	0.26	0.24	0.30	0.04	0.03	0.07	0.17	0.17	0.15	0.31	0.18
Σ cat	15.69	15.66	15.71	15.61	15.26	15.24	15.30	15.04	15.12	15.07	15.17	15.17	15.15	15.31	15.18
Mg#	24.73	25.26	26.16	26.35	39.63	38.25	38.50	66.11	62.83	58.90	55.38	54.32	52.00	47.67	51.49

Note: Mg# = 100 x Mg/(Mg+Fe)

**Appendix 3.2: Major element content and structural formulae for amphibole from mafic rocks**

Sample Analysis	62210 hbl4	62105A cumm m1	62105A cumm m2	62105A cumm m4	62105A cumm m5	62105A hbl m1	62105A hbl m2	62105A hbl m3	62105A cumm ri1	62105A cumm ri2	62105A cumm ci1	62105A cumm ci3	62105A cumm ci4	Tj 14 hbl1	Tj 14 hbl2
SiO <sub>2</sub>	47.93	54.54	53.84	54.58	54.59	49.83	49.37	49.56	55.17	54.05	55.78	54.86	54.89	53.78	53.24
TiO <sub>2</sub>	0.82	0.00	0.05	0.08	0.07	0.36	0.34	0.27	0.01	0.01	0.02	0.00	0.06	0.13	0.16
Al <sub>2</sub> O <sub>3</sub>	10.46	0.02	0.77	0.00	0.13	7.18	7.65	7.83	0.00	0.49	0.00	0.00	0.00	5.49	5.71
Cr <sub>2</sub> O <sub>3</sub>	0.17	0.03	0.03	0.00	0.00	0.01	0.19	0.08	0.04	0.10	0.01	0.03	0.01	0.00	0.00
FeO	17.57	32.95	31.90	32.72	32.09	21.35	21.30	21.33	31.23	32.07	30.22	31.34	31.12	11.14	11.72
MnO	0.35	1.05	0.89	0.98	0.85	0.27	0.35	0.29	1.01	0.85	2.14	2.07	2.48	0.26	0.18
MgO	9.67	11.22	11.15	11.73	11.55	8.85	8.65	8.59	12.36	12.11	11.73	11.64	11.48	15.51	15.05
CaO	11.79	0.50	1.71	0.53	1.18	11.83	11.65	11.54	0.71	0.80	0.78	0.67	0.64	12.45	12.74
Na <sub>2</sub> O	0.90	0.00	0.00	0.00	0.00	0.16	0.31	0.40	0.00	0.00	0.00	0.00	0.00	0.97	0.93
K <sub>2</sub> O	0.35	0.00	0.00	0.00	0.00	0.16	0.17	0.12	0.00	0.00	0.01	0.06	0.00	0.27	0.27
Total	100.01	100.31	100.34	100.62	100.46	100.00	99.98	100.01	100.53	100.48	100.69	100.67	100.68	100.00	100.00
Si	6.94	8.11	7.99	8.08	8.08	7.30	7.24	7.25	8.11	8.00	8.19	8.11	8.12	7.52	7.47
Al IV	1.06	0.00	0.01	0.00	0.00	0.70	0.76	0.75	0.00	0.00	0.00	0.00	0.00	0.48	0.53
Σ IV	8.00	8.11	8.00	8.08	8.08	8.00	8.00	8.00	8.11	8.00	8.19	8.11	8.12	8.00	8.00
Al M123	0.72	0.00	0.13	0.00	0.02	0.54	0.56	0.61	0.00	0.08	0.00	0.00	0.00	0.42	0.42
Cr	0.02	0.00	0.00	0.00	0.00	0.00	0.02	0.01	0.00	0.01	0.00	0.00	0.00	0.00	0.00
Ti	0.09	0.00	0.01	0.01	0.01	0.04	0.04	0.03	0.00	0.00	0.00	0.00	0.01	0.01	0.02
Mg	2.09	2.49	2.47	2.59	2.55	1.93	1.89	1.87	2.71	2.67	2.57	2.57	2.53	3.23	3.15
Fe M123	2.08	2.51	2.39	2.40	2.42	2.49	2.49	2.48	2.29	2.23	2.43	2.43	2.46	1.30	1.38
Mn M123	0.00	0.00	0.00	0.00	0.00	0.00	0.00	0.00	0.00	0.00	0.00	0.00	0.00	0.03	0.02
Σ M123	5.00	5.00	5.00	5.00	5.00	5.00	5.00	5.00	5.00	5.00	5.00	5.00	5.00	5.00	4.97
Fe M4	0.05	1.59	1.57	1.65	1.55	0.12	0.12	0.13	1.56	1.74	1.28	1.45	1.39	0.00	0.00
Mn M4	0.04	0.11	0.09	0.10	0.09	0.03	0.04	0.03	0.10	0.09	0.22	0.21	0.25	0.00	0.00
Ca	1.83	0.08	0.27	0.08	0.19	1.86	1.83	1.81	0.11	0.13	0.12	0.11	0.10	1.86	1.92
Na M4	0.09	0.00	0.00	0.00	0.00	0.00	0.01	0.03	0.00	0.00	0.00	0.00	0.00	0.14	0.08
Σ M4	2.00	1.78	1.93	1.83	1.82	2.01	2.00	2.00	1.77	1.95	1.62	1.76	1.75	2.00	2.00
A Na	0.16	0.00	0.00	0.00	0.00	0.05	0.08	0.08	0.00	0.00	0.00	0.00	0.00	0.13	0.17
A K	0.06	0.00	0.00	0.00	0.00	0.03	0.03	0.02	0.00	0.00	0.00	0.01	0.00	0.05	0.05
Σ A	0.23	0.00	0.00	0.00	0.00	0.08	0.11	0.10	0.00	0.00	0.00	0.01	0.00	0.18	0.22
Σ cat	15.23	14.89	14.93	14.91	14.90	15.08	15.11	15.10	14.88	14.95	14.81	14.89	14.87	15.17	15.19
Mg#	49.51	37.76	38.38	38.98	39.08	42.48	41.98	41.78	41.36	40.22	40.89	39.83	39.66	71.27	69.59

**Note:** Mg# = 100 x Mg/(Mg+Fe)

**Appendix 3.2: Major element content and structural formulae for amphibole from mafic rocks**

Sample Analysis	Tj 14 hbl3	Tj 14 hbl5	Tj 14 hbl7	Tj 14 hbl8	Tj 14 hbl9
SiO <sub>2</sub>	54.88	54.39	54.16	55.65	54.30
TiO <sub>2</sub>	0.19	0.42	0.17	0.13	0.16
Al <sub>2</sub> O <sub>3</sub>	3.94	4.34	4.63	3.44	4.39
Cr <sub>2</sub> O <sub>3</sub>	0.00	0.00	0.00	0.00	0.00
FeO	11.00	10.93	11.51	10.69	11.26
MnO	0.31	0.25	0.14	0.27	0.30
MgO	16.00	15.72	15.56	16.28	15.45
CaO	12.66	12.87	12.85	12.75	12.96
Na <sub>2</sub> O	0.86	0.88	0.72	0.59	1.00
K <sub>2</sub> O	0.16	0.20	0.26	0.20	0.18
Total	100.00	100.00	100.00	100.00	100.00
Si	7.66	7.60	7.58	7.74	7.60
Al IV	0.34	0.40	0.42	0.26	0.40
Σ IV	8.00	8.00	8.00	8.00	8.00
Al M123	0.31	0.32	0.35	0.31	0.33
Cr	0.00	0.00	0.00	0.00	0.00
Ti	0.02	0.04	0.02	0.01	0.02
Mg	3.33	3.27	3.25	3.38	3.22
Fe M123	1.28	1.28	1.35	1.24	1.32
Mn M123	0.03	0.02	0.01	0.03	0.03
Σ M123	4.97	4.93	4.97	4.96	4.92
Fe M4	0.00	0.00	0.00	0.00	0.00
Mn M4	0.00	0.00	0.00	0.00	0.00
Ca	1.89	1.93	1.93	1.90	1.94
Na M4	0.11	0.07	0.07	0.10	0.06
Σ M4	2.00	2.00	2.00	2.00	2.00
A Na	0.13	0.17	0.12	0.06	0.22
A K	0.03	0.04	0.05	0.04	0.03
Σ A	0.15	0.20	0.17	0.10	0.25
Σ cat	15.13	15.14	15.14	15.06	15.17
Mg#	72.16	71.93	70.67	73.07	70.97

**Note:** Mg# = 100 x Mg/(Mg+Fe)



**Appendix 3.2: Major element content and structural formulae for epidote from mafic rocks**

Sample Analysis	Tj 3 epi1 grti	Tj 3 epi2 grti	Tj 3 epi1	Tj 3 epi2	Tj 3 epi3	Tj 3 epi4	Tj 3 epi5	Tj 14 epi1	Tj 14 epi2	Tj 14 epi3	Tj 14 epi4	61406 zoil	62107 epi1	62107 epi2	62107 epi3
SiO <sub>2</sub>	39.92	40.28	40.21	40.72	39.96	40.33	40.17	40.23	40.66	39.98	40.47	40.35	40.31	40.07	39.88
TiO <sub>2</sub>	0.12	0.19	0.21	0.18	0.16	0.31	0.10	0.12	0.11	0.12	0.00	0.11	0.13	0.24	0.22
Al <sub>2</sub> O <sub>3</sub>	26.07	27.63	26.68	27.14	26.72	26.84	27.36	27.77	28.18	27.13	28.10	30.96	28.02	28.34	28.10
Cr <sub>2</sub> O <sub>3</sub>	0.06	0.06	0.05	0.02	0.00	0.02	0.06	0.00	0.13	0.00	0.03	0.00	0.06	0.29	0.06
Fe <sub>2</sub> O <sub>3</sub>	9.72	7.93	8.80	8.23	9.18	8.82	8.29	7.57	6.97	8.47	6.85	3.67	7.01	7.12	7.36
MnO	0.04	0.25	0.20	0.03	0.17	0.32	0.29	0.03	0.00	0.07	0.03	0.52	0.47	0.52	0.42
MgO	0.00	0.00	0.00	0.00	0.00	0.00	0.00	0.00	0.00	0.00	0.00	0.00	0.00	0.00	0.00
CaO	24.06	23.66	23.86	23.67	23.83	23.36	23.74	24.30	23.94	24.26	24.57	24.39	24.01	23.42	23.96
Total	99.99	100.00	100.01	99.99	100.02	100.00	100.01	100.02	99.99	100.03	100.05	100.00	100.01	100.00	100.00
Si	3.06	3.07	3.07	3.10	3.06	3.08	3.06	3.06	3.08	3.05	3.07	3.03	3.06	3.05	3.04
Al	2.36	2.48	2.40	2.43	2.41	2.41	2.46	2.49	2.52	2.44	2.51	2.74	2.51	2.54	2.52
Fe <sup>3+</sup>	0.56	0.45	0.51	0.47	0.53	0.51	0.48	0.43	0.40	0.49	0.39	0.21	0.40	0.41	0.42
Ti	0.01	0.01	0.01	0.01	0.01	0.02	0.01	0.01	0.01	0.01	0.00	0.01	0.01	0.01	0.01
Cr	0.00	0.00	0.00	0.00	0.00	0.00	0.00	0.00	0.01	0.00	0.00	0.00	0.00	0.02	0.00
Mn	0.00	0.01	0.01	0.00	0.01	0.02	0.02	0.00	0.00	0.00	0.00	0.03	0.02	0.03	0.02
Σ	2.92	2.95	2.92	2.91	2.95	2.94	2.95	2.92	2.92	2.93	2.91	2.98	2.94	2.99	2.97
Ca	1.98	1.93	1.95	1.93	1.95	1.91	1.94	1.98	1.94	1.98	2.00	1.96	1.96	1.91	1.96
Σ cat	7.96	7.94	7.95	7.93	7.96	7.93	7.96	7.96	7.95	7.97	7.98	7.98	7.96	7.94	7.96
XP <sub>s</sub>	0.19	0.15	0.17	0.16	0.18	0.17	0.16	0.15	0.14	0.17	0.13	0.07	0.14	0.14	0.14

Note: XP<sub>s</sub> = Fe<sup>3+</sup>/(Fe<sup>3+</sup>+Al)

**Appendix 3.2: Major element content and structural formulae for plagioclase from mafic rocks**

Sample Analysis	Tj 3 plag1	Tj 3 plag2	Tj 3 plag3	Tj 3 plag4	Tj 3 gb plag1	Tj 3 gb plag2	Tj 3 gb plag3	62107 plag1	62107 plag2	62107 plag3	62107 plag4	61406 plag gb1	61406 plag gb2	61406 plag gb4	61406 plag gb5
SiO <sub>2</sub>	61.57	61.21	61.04	60.51	61.38	60.32	59.79	57.84	58.50	58.67	57.56	62.87	62.95	62.73	62.28
TiO <sub>2</sub>	0.00	0.00	0.00	0.00		0.00	0.00	0.00	0.00	0.00	0.00	0.00	0.00	0.00	0.00
Al <sub>2</sub> O <sub>3</sub>	24.10	24.52	24.67	24.91	24.45	25.02	25.45	26.71	26.56	26.26	27.07	23.36	23.38	23.53	23.69
FeO	0.00	0.00	0.00	0.00	0.00	0.00	0.00	0.00	0.00	0.00	0.00	0.00	0.00	0.00	0.00
CaO	5.72	5.95	6.20	6.22	5.75	6.48	6.92	8.39	8.06	7.73	8.44	4.43	4.45	4.52	4.94
Na <sub>2</sub> O	8.45	8.19	8.00	8.24	8.33	8.11	7.68	6.94	6.83	7.28	6.87	9.25	9.12	9.18	9.01
K <sub>2</sub> O	0.16	0.13	0.09	0.13	0.08	0.07	0.15	0.13	0.05	0.06	0.06	0.09	0.09	0.05	0.08
Total	100.00	100.00	100.00	100.01	99.99	100.00	99.99	100.01	100.00	100.00	100.00	100.00	99.99	100.01	100.00
Si	2.73	2.72	2.71	2.69	2.72	2.68	2.66	2.59	2.61	2.62	2.58	2.78	2.78	2.77	2.76
Al	1.26	1.28	1.29	1.31	1.28	1.31	1.34	1.41	1.40	1.38	1.43	1.22	1.22	1.23	1.24
Σ	4.00	4.00	4.00	4.00	4.00	4.00	4.00	4.00	4.01	4.00	4.00	4.00	4.00	4.00	4.00
Ca	0.27	0.28	0.29	0.30	0.27	0.31	0.33	0.40	0.39	0.37	0.40	0.21	0.21	0.21	0.23
Na	0.73	0.71	0.69	0.71	0.72	0.70	0.66	0.60	0.59	0.63	0.60	0.79	0.78	0.79	0.77
K	0.01	0.01	0.01	0.01	0.00	0.00	0.01	0.01	0.00	0.00	0.00	0.01	0.01	0.00	0.00
Σ	1.01	1.00	0.99	1.01	0.99	1.01	1.00	1.01	0.98	1.00	1.00	1.01	1.00	1.00	1.01
Σ cat	5.00	5.00	4.99	5.01	5.00	5.01	5.00	5.01	4.99	5.01	5.01	5.01	5.00	5.01	5.01
XAn	0.27	0.29	0.30	0.29	0.28	0.31	0.33	0.40	0.39	0.37	0.40	0.21	0.21	0.21	0.23
XAb	0.73	0.71	0.70	0.71	0.72	0.69	0.67	0.60	0.61	0.63	0.60	0.79	0.79	0.79	0.77

Note: XAn = Ca/(Ca+Na); XAb = Na/(Ca+Na)

**Appendix 3.2: Major element content and structural formulae for plagioclase from mafic rocks**

Sample Analysis	61406 plag m1	61406 plag m2	61406 plag m3	62210 plag1	62210 plag2	62210 plag3	62210 plag4	Tj 14 plag1	Tj 14 plag2	Tj 14 plag3	Tj 14 plag4	Tj 14 plag5	Tj 14 plag6	Tj 14 plag7	Tj 14 plag8	Tj 14 plag9
SiO <sub>2</sub>	60.67	61.67	62.72	61.54	62.63	62.92	61.46	62.37	67.90	67.55	68.42	61.88	61.86	66.72	68.70	61.56
TiO <sub>2</sub>	0.00	0.00	0.00	0.00	0.00	0.00	0.00	0.00	0.00	0.00	0.00	0.00	0.00	0.00	0.00	0.00
Al <sub>2</sub> O <sub>3</sub>	24.77	24.26	23.44	24.27	23.54	23.35	24.38	23.49	19.94	19.83	19.46	24.06	24.15	20.76	19.33	24.25
FeO	0.00	0.00	0.00	0.00	0.00	0.00	0.00	0.00	0.00	0.00	0.00	0.00	0.00	0.00	0.00	0.00
CaO	6.37	5.29	4.52	5.29	4.63	4.54	5.34	5.24	0.39	0.86	0.40	5.26	5.57	1.69	0.45	5.61
Na <sub>2</sub> O	8.11	8.73	9.28	8.84	9.13	9.13	8.73	8.79	11.23	11.69	11.65	8.63	8.28	10.74	11.48	8.47
K <sub>2</sub> O	0.07	0.06	0.03	0.06	0.07	0.06	0.10	0.11	0.54	0.07	0.07	0.17	0.14	0.08	0.05	0.10
Total	99.99	100.01	99.99	100.00	100.00	100.00	100.01	100.00	100.00	100.00	100.00	100.00	100.00	99.99	100.01	99.99
Si	2.70	2.73	2.78	2.73	2.77	2.78	2.73	2.76	2.97	2.96	2.99	2.74	2.74	2.93	3.00	2.73
Al	1.30	1.27	1.22	1.27	1.23	1.22	1.28	1.23	1.03	1.02	1.00	1.26	1.26	1.07	0.99	1.27
Σ	4.00	4.00	4.00	4.00	4.00	4.00	4.00	3.99	4.00	3.99	3.99	4.00	4.00	4.00	3.99	4.00
Ca	0.30	0.25	0.21	0.25	0.22	0.22	0.25	0.25	0.02	0.04	0.02	0.25	0.26	0.08	0.02	0.27
Na	0.70	0.75	0.80	0.76	0.78	0.78	0.75	0.76	0.95	0.99	0.99	0.74	0.71	0.91	0.97	0.73
K	0.00	0.00	0.00	0.00	0.00	0.00	0.01	0.01	0.03	0.00	0.00	0.01	0.01	0.00	0.00	0.01
Σ	1.01	1.01	1.01	1.02	1.01	1.00	1.01	1.01	1.00	1.04	1.01	1.00	0.98	1.00	1.00	1.00
Σ cat	5.00	5.01	5.01	5.02	5.01	5.00	5.01	5.00	5.00	5.02	5.00	5.00	4.99	5.00	4.99	5.00
XAn	0.30	0.25	0.21	0.25	0.22	0.22	0.25	0.25	0.02	0.04	0.02	0.25	0.27	0.08	0.02	0.27
XAb	0.70	0.75	0.79	0.75	0.78	0.78	0.75	0.75	0.98	0.96	0.98	0.75	0.73	0.92	0.98	0.73

Note: XAn = Ca/(Ca+Na); XAb = Na/(Ca+Na)



**Appendix 3.2: Major element content and structural formulae for chlorite from mafic rocks**

Sample Analysis	61406 chl gb1	61406 chl gb2	61406 chl gb3	61406 chl m1	61406 chl m2	61406 chl m3	Tj 3 chl1
SiO <sub>2</sub>	32.28	31.89	31.59	31.75	31.22	31.75	34.88
TiO <sub>2</sub>	0.14	0.13	0.13	0.12	0.24	0.12	1.03
Al <sub>2</sub> O <sub>3</sub>	24.94	24.90	24.78	25.09	25.23	25.39	19.61
Cr <sub>2</sub> O <sub>3</sub>	0.27	0.10	0.06	0.07	0.00	0.07	
FeO	21.03	22.73	22.65	22.03	21.97	21.55	32.55
MnO	0.32	0.42	0.43	0.36	0.46	0.35	0.49
MgO	20.96	19.79	20.37	20.63	20.86	20.76	10.93
K <sub>2</sub> O	0.06	0.05	0.00	0.00	0.03	0.02	0.52
Total	100.00	100.01	100.01	100.05	100.01	100.01	100.01
Si IV	2.86	2.84	2.82	2.82	2.78	2.82	3.25
Al IV	1.14	1.16	1.18	1.18	1.22	1.18	0.75
Σ IV	4.00	4.00	4.00	4.00	4.00	4.00	4.00
Al VI	1.46	1.46	1.43	1.45	1.43	1.47	1.41
Ti	0.01	0.01	0.01	0.01	0.02	0.01	0.07
Cr	0.02	0.01	0.00	0.00	0.00	0.00	0.00
Fe <sup>2+</sup>	1.56	1.70	1.69	1.64	1.64	1.60	2.54
Mn	0.02	0.03	0.03	0.02	0.03	0.02	0.03
Mg	2.76	2.63	2.71	2.73	2.77	2.74	1.52
Ca	0.00	0.00	0.00	0.00	0.00	0.00	0.00
Na	0.00	0.00	0.00	0.00	0.00	0.00	0.00
K	0.01	0.01	0.00	0.00	0.00	0.00	0.06
Σ	5.83	5.84	5.87	5.85	5.88	5.85	5.63
Σ cat	9.83	9.84	9.87	9.85	9.88	9.85	9.63
Mg#	63.98	60.81	61.58	62.53	62.85	63.19	37.44

Note: Mg# = 100 x Mg/(Mg+Fe)